

Analytical and Numerical Studies of Waveguiding and Coupling in Periodic Dielectric Materials

Thesis by
Yong Xu

In Partial Fulfillment of the Requirements
for the Degree of
Doctor of Philosophy



California Institute of Technology
Pasadena, California

2001
(Submitted May 7, 2001)

Acknowledgements

During the past few years at Caltech, many people have guided, encouraged, and supported me. Without them, my life at Caltech could not have been as stimulating and enriching as it was. I would like to take this opportunity to thank them. First and foremost, I am deeply indebted to my advisor Professor Amnon Yariv, who gave me the privilege of being a member of his research group. His deep physical insight has a profound impact on me. Without his guidance, I could not have appreciated the wondrous beauty of the world of optoelectronics as much as I do now. I would also like to thank Professor Axel Scherer, who generously gave me the access to his semiconductor fabrication lab in my non-theorist days.

I worked with many people in the field of photonic crystals. My collaboration with Dr. Reginald K. Lee, a senior member of Professor Yariv's group, has been particularly fruitful. I also appreciate the opportunity of working with Dr. John O'Brien, Dr. Ali Adibi, Dr. Chuan-Cheng Cheng, Dr. Oskar Painter, Jelena Vuckovic, Zhiwen Liu and George Ouyang.

I enjoyed discussions and friendships with many other members of Professor Yariv's group, even though we did not have the opportunity of direct collaboration. I have learned a great deal from the works of Drs. Doruk Engin, Xiaolin Tong, Dan Provenzano and Roger Koumans. I also want to thank John Choi, who has recently taken over the task of maintaining the computer systems in Professor Yariv's lab. Without his friendship, the many long nights in front of the flickering computer

screens could have been quite boring. I appreciate the help from former and current staff members, Jana Mercado, Connie Rodriguez, Kevin Cooper, and Ali Ghaffari.

Another art I learned at Caltech is karate. I greatly appreciated the instructions I received from Mr. Ohshima, Steve Bankes, Randy McClure, and Pamela Logan. They have made me a much stronger and better person. I also want to thank many other countless karate buddies of mine. We have sweated together, fought together, and laughed together. It is an experience I will treasure forever.

Finally, I would like to thank my parents. Without their love and sacrifice, I could not have the chance of studying at Caltech. I dedicate this thesis to them.

Abstract

Using both analytical approaches and finite difference time domain simulations, we investigate different types of waveguiding and coupling mechanisms, including direct coupling between the optical resonators, waveguide-resonator coupling, indirect resonator coupling via waveguide modes, and Bragg reflection in cylindrically symmetric geometries.

By coupling an array of high Q optical resonators together, we form a new type of waveguide, coupled resonator optical waveguide (CROW), where photons propagate by “hopping” from one resonator to its nearest neighbors. Using tight-binding approximation, we find that the CROW modes retain the symmetries of the isolated high Q optical modes and the CROW band dispersion can be simply characterized by a coupling coefficient κ . The tight-binding results are confirmed by using the finite difference time domain algorithms to analyze two examples of CROW’s: one is composed of coupled defect cavities in a two-dimensional triangular lattice photonic crystal, while the other is formed by coupling an array of dielectric microdisk cavities.

By coupling a resonator to a waveguide, we significantly change the reflection and transmission characteristics of the waveguide. The waveguide dispersion can also be drastically modified by coupling an array of resonators to the waveguide, due to indirect coupling between the resonators via waveguide modes. Using a formalism based on the quantum scattering theory, we investigate how the waveguide-resonator coupling, resonator gain (loss), degeneracy and symmetries of the resonator modes

influence the optical properties of such coupled waveguide-resonator systems.

Bragg guiding can be achieved in cylindrically symmetric geometries by using cladding media with alternating high and low refractive indices. Examples include Bragg fibers and dielectric coaxial fibers. An asymptotic formalism is developed to study the dispersion, propagation loss, and field distribution of guided modes in such fibers. The results are compared with those obtained from numerical calculations, where excellent agreement is found between the two approaches.

Contents

Acknowledgements	iii
Abstract	v
1 Introduction	1
1.1 One-Dimensional Bragg Reflection	1
1.2 Photonic Crystals and the Formation of Bandgap	3
1.3 Different Waveguiding Mechanisms	5
2 Finite Difference Time Domain (FDTD) Algorithm	7
2.1 FDTD Cells and Finite Difference Equations	7
2.1.1 Two-Dimensional Case	8
2.1.2 Three-Dimensional Case	11
2.2 Boundary Conditions	14
2.2.1 Bloch Boundary	14
2.2.2 Mirror Boundary	16
2.2.3 Perfectly Matched Layer (PML) Boundary	19
2.3 FDTD Algorithms and Their Applications	24
2.3.1 Simulation of High Q Optical Modes	24
2.3.2 Simulation of Waveguide Modes	28
2.3.3 Sources in FDTD Simulations and Their Applications	30

3	Coupled Resonator Optical Waveguide (CROW)	36
3.1	Introduction	36
3.2	Tight Binding Analysis of CROW	39
3.2.1	Non-degenerate CROW Band	39
3.2.2	Degenerate CROW Band	41
3.3	Coupled Defect Cavity Waveguide	43
3.4	Coupled Microdisk Waveguide	51
3.5	Second Harmonic Generation in CROW	57
4	Scattering Theory Analysis of Waveguide-Resonator Coupling	64
4.1	Introduction	64
4.2	Scattering Theory Formalism	66
4.2.1	Scattering Matrix	66
4.2.2	Green Function	69
4.3	Optical Scattering in Two Generic Coupled Waveguide-Resonator Systems	72
4.3.1	Side Coupling	73
4.3.2	Resonant Coupling	75
4.4	Critical Coupling in Coupled Waveguide-Resonator Systems	77
4.4.1	Single Mode Side Coupling	77
4.4.2	Side Coupling with Doubly Degenerate Modes	80
4.4.3	Single Mode Resonant Coupling	88
4.5	Dispersion Relation of Indirect CROW	91
4.6	Optical Transmission and Reflection Through Waveguide Coupled with Multiple Cavities	95
5	Bragg Fibers and Dielectric Coaxial Fibers	106
5.1	Introduction	106
5.2	Asymptotic Matrix Theory	109
5.2.1	Exact Solution in the Core Region	110
5.2.2	Asymptotic Approximation in the Cladding Region	112

5.2.3	Matrix Formalism	114
5.2.4	Surface Modes	120
5.3	Radiation Loss	122
5.4	Bragg Fiber Dispersion	130
5.5	Coaxial Fiber Dispersion	136
6	Conclusions	144
	Bibliography	147

List of Figures

1.1	(a) Distributed feedback provided by the periodic perturbation of the refractive index or gain. (b) Electromagnetic field in one-dimensional periodic stratified media.	2
1.2	A two-dimensional photonic crystal composed of a square lattice of air holes in a high refractive index dielectric medium.	3
2.1	Electromagnetic field components at the (i, j) th 2D FDTD cell. . . .	10
2.2	Electromagnetic field components at the (i, j, k) th 3D FDTD cell. . .	12
2.3	A two-dimensional FDTD computational domain with $(N_x + 1) \times (N_y + 1)$ FDTD cells.	15
2.4	A two-dimensional dielectric distribution with a mirror reflection symmetry plane $y = y_0$	17
2.5	(a) Absorption of light in a perfectly matched layer. (b) PML boundary condition in a 2D FDTD computational domain.	22
2.6	FFT spectrum of the temporal series of the electromagnetic field obtained using FDTD equations in Sec. 2.1.	26
2.7	Schematic of the FDTD mode filtering algorithm.	27
2.8	Boundary conditions for the FDTD calculation of photonic crystal waveguide modes.	30
2.9	Huygens Source that excites the TE mode of an infinite dielectric slab waveguide.	32

2.10 Huygens source.	35
3.1 Three types of waveguiding: a) the waveguiding by total internal reflection at the interface between the high index medium and low index medium. b) the “Bragg waveguiding” achieved by reflection from the periodic Bragg stacks. c) the coupled resonators optical waveguide-CROW, with waveguiding due to the coupling between the individual microdisks. R is the size of a unit cell and \mathbf{e}_x is the direction of the periodicity for the coupled resonators. d) the CROW realized by coupling the individual defect cavities in a 2D photonic crystal.	37
3.2 The FDTD computational domain. a) For a single defect cavity in a 2D photonic crystal. Mirror boundary condition is used at the bottom y boundary. For other three boundaries, the first order Mur absorbing boundary is used. b) For the CROW composed of coupled defect cavities with 4 air holes in between. The PML absorbing boundary condition and the mirror boundary condition are respectively used for the top and bottom y boundaries. At both of the x boundaries, $x = 0$ and $x = R$, the Bloch boundary condition is used.	45
3.3 The single defect cavity modes. (a) The even defect mode. (b) The odd defect mode.	46
3.4 The even CROW modes with (a) 2 inter-cavity hole spacing and (b) 4 inter-cavity hole spacing. The Bloch vector K of both modes is $K = 0.6\pi/R$	47
3.5 The dispersion of the even defect cavity CROW band. The symbols represent the results calculated from FDTD algorithm using different values of inter-cavity hole spacing. The solid lines are the least square fits of the numerical results using Eq. (3.19).	47
3.6 The odd defect cavity CROW mode with 3 inter-cavity hole spacing and Bloch vector $K = 0.6\pi/R$	49

3.7	The dispersion of the odd defect cavity CROW band of coupled defect cavities. The symbols represent the results calculated from FDTD algorithm using different values of inter-cavity hole spacing: The solid lines are the least square fits of the numerical results using Eq. (3.19).	49
3.8	The $TE(7, 1)$ whispering gallery modes in a single microdisk cavity. The even mode is shown in a) and the odd mode is shown in (b).	52
3.9	The even microdisk CROW mode formed by coupling the even $TE(7, 1)$ modes together. We use $R/2r = 1.1$ and $K = 0.5\pi/R$.	52
3.10	The effective Q factors of the even microdisk CROW modes with $R/2r = 1.17$.	53
3.11	The dispersion of the even microdisk CROW band. The FDTD results are represented by asterisks. The error bars refer to the frequency error caused by the finite decay rate of the CROW modes and are estimated to be $\omega/2Q_{eff}$. The solid lines are the least square fits of the numerical results using Eq. 3.19. The dispersion diagrams for $R/2r = 1.1, 1.17$ and 1.23 are shown respectively in a), b) and c).	54
3.12	The odd microdisk CROW mode formed by coupling the odd $TE(7, 1)$ modes together. We use $R/2r = 1.1$ and $K = 0.5\pi/R$.	55
3.13	The dispersion of the odd microdisk CROW band. The FDTD results are represented by asterisks. The error bars refer to the frequency error caused by the finite decay rate of the CROW modes and are estimated to be $\omega/2Q_{eff}$. The solid lines are the least square fits using Eq. (3.19). The dispersion diagrams for $R/2r = 1.1, 1.17$ and 1.23 are shown respectively in (a), (b) and (c).	56
3.14	SHG in CROW. The fundamental frequency modes propagate from one defect cavity to another along the x axis. The second harmonic mode can either propagate in CROW along x axis or leak out of CROW along z axis.	61

4.1	(a) The general geometry of a waveguide coupled with a cavity. (b) Example of a CROW with indirect coupling.	65
4.2	(a) The “side coupling” case, where a cavity is side coupled to a waveguide. (b) The “resonant coupling” case, where two waveguides are coupled by a high Q cavity.	73
4.3	(a) A single mode resonator side coupled to a single mode waveguide. Γ_-^c and Γ_+^c are respectively the cavity decay rate in the $-\hat{x}$ and $+\hat{x}$ direction. For a resonator with mirror reflection symmetry with respect to $x = 0$ plane, $\Gamma_-^c = \Gamma_+^c$. (b) The resonant ($\Delta\omega = 0$) reflection and transmission coefficient for the geometry shown in (a). Γ^0 represents the intrinsic cavity loss (gain), and Γ^c is the decay rate of the cavity mode into the waveguide. (c) Reflection and transmission spectrum for four different values of Γ^0/Γ^c	78
4.4	(a) A waveguide side coupled with a cavity supporting two degenerate modes. The cavity is symmetric with respect to $x = 0$ plane and support two degenerate modes with opposite parity under mirror reflection. The even mode is $ e\rangle$ and the odd mode is $ o\rangle$. (b) The side coupling geometry with two degenerate traveling wave modes in the cavity. The mode traveling in the clockwise direction is $ +\rangle$ and the mode traveling in the counterclockwise direction is $ -\rangle$. (c) The resonant transmission coefficient as a function of Γ^0/Γ^c . (d) The transmission spectrum for different values of Γ^0/Γ^c	81
4.5	Reflection/Transmission spectrum of a waveguide coupled to a resonator that supports two counter-propagating traveling modes, as described in Eq. (4.82) and (4.83). The coupling between the two traveling modes is given by κ	86
4.6	Resonant reflection/transmission coefficient of a waveguide coupled to a resonator with two coupled, lossless ($\Gamma^0 = 0$), counter-propagating traveling modes.	86

4.7	Reflection/Transmission spectrum of a waveguide coupled to a resonator with two coupled traveling wave modes, using different values of κ/Γ^c	87
4.8	Reflection spectrum of a waveguide coupled to a resonator with two coupled traveling wave modes. In this case, we use different values of Γ^0/Γ^c but keep $\kappa = \Gamma^c$	87
4.9	(a) Two waveguides of the same type coupled together via a high Q resonator supports a single mode. (b) The resonant reflection and transmission coefficients of the “resonant coupling” geometry shown in (a). (c) The reflection and transmission spectrum with different parameters of Γ^0/Γ^c	89
4.10	An example of indirect CROW, which consists of a waveguide side coupled to an array of high Q resonators.	91
4.11	The uncoupled waveguide band and the photonic band of the indirect CROW calculated from Eq. (4.99). In (a) $k_0R = \pi/2$ and in (b) $k_0R = 5\pi/6$. We choose the parameter $R\Gamma^c/v_g = 0.05$. The justification of this value is given in the text.	94
4.12	Dispersion relations of the indirect CROW bands. The solid lines are the exact solutions of Eq. (4.99) with $R\Gamma^c/v_g = 0.05$. The dash line represents the uncoupled waveguide band and the stars are the approximate solutions given by Eq. (4.100). In (a), we use (a) $k_0R = \pi/2$ and in (b) $k_0R = 5\pi/6$	96
4.13	Near horizontal indirect CROW band. Photon group velocity is greatly reduced for the middle band shown above. The dashed line is the unperturbed waveguide band. We use $k_0R = 3.0$ and $R\Gamma^c/v_g = 0.05$	96
4.14	(a) A straight waveguide side coupled to N resonators. The incident optical wave is described by $[a_i \ b_i]$, the output optical wave is given by $[a_o \ b_o]$. (b) A straight waveguide coupled to a resonator that possesses mirror reflection symmetry with respect to plane $x = x_o$	97

4.15 The transmission and reflection coefficient of a straight waveguide side coupled to N resonators, with $N = 2$ and $N = 6$ respectively. $\Gamma^0/\Gamma^c = 0$, $k_0R = \pi/2$, $R\Gamma^c/v_g = 0.05$ are used. 102

4.16 (a) The transmission spectrum of a straight waveguide side coupled to N resonators, with $N = 2$, $N = 6$ and $N = 20$ respectively. $\Gamma^0/\Gamma^c = 0$ and $k_0R = 0$, and $R\Gamma^c/v_g = 0.05$ are used in the calculations. (b) The photonic band of a straight waveguide side coupled to an infinite array of resonators the same as those in (a). The band structures are calculated using Eq. (4.99), with $k_0R = 0$ and $R\Gamma^c/v_g = 0.05$. The bandgap in (b) corresponds to the transmission dip for the case of $N = 20$ in (a). 102

4.17 The transmission spectrum of a straight waveguide side coupled to N resonators, with $N = 2$ and $N = 10$ respectively. We use $\Gamma^0/\Gamma^c = 0$, $k_0R = 3.0$, and $R\Gamma^c/v_g = 0.05$ 103

4.18 The transmission and reflection spectrum of a waveguide coupled to N resonators with loss ($\Gamma^0/\Gamma^c > 0$) or gain ($\Gamma^0/\Gamma^c < 0$). We use $N = 6$, $k_0R = \pi/2$, and $R\Gamma^c/v_g = 0.05$ in the calculations. 103

4.19 The transmission spectrum of a waveguide coupled to 20 resonators with loss or gain. $k_0R = 0$, and $R\Gamma^c/v_g = 0.05$ are used in the calculations. 105

4.20 The transmission spectrum of a waveguide coupled to 6 resonators. $k_0R = 3.0$, and $R\Gamma^c/v_g = 0.05$ are used in the calculations. 105

5.1 Schematic of (a) a Bragg fiber, (b) a dielectric coaxial fiber, and (c) a metallic coaxial cable. 107

5.2 Schematic of the $r - z$ cross-section of a fiber with Bragg cladding. The dielectric layers of the Bragg fiber are classified into two regions: the core region and the cladding region, which are separated by the dash line in the figure. 109

- 5.3 The radiation loss of an air core Bragg fiber with N cladding pairs. P_z is the power flux inside the air core. P_r represents the outgoing radiation power flux through a cylindrical surface with radius R and height dz 123
- 5.4 The number of Bragg cladding pairs necessary to achieve 0.2dB/km radiation loss. Δn is the index contrast between the two cladding dielectric media $n_{cl}^1 - n_{cl}^2$, with $n_{cl}^2 = 1.5$. The solid line gives the minimum Bragg pairs for TE modes to 0.2dB/km, while the dash line gives the corresponding quantity for the TM modes. 129
- 5.5 The dispersion of an air core Bragg fiber with a single $m = 1$ mode. The Bragg fiber parameters are: $n_{co}^1 = 1.0$, $\rho_{co}^1 = 1.0\Lambda$, $n_{cl}^1 = 4.6$, $l_{cl}^1 = 0.25\Lambda$, $n_{cl}^2 = 1.5$ and $l_{cl}^2 = 0.75\Lambda$. The solid line is from the asymptotic analysis, while the dots represent the 2D FDTD results. The effective indices n_{eff} is defined as $\beta c/\omega$ 131
- 5.6 The H_z field distribution of a guided Bragg fiber mode at $\omega = 0.291(2\pi c/\Lambda)$ and $\beta = 0.143(2\pi/\Lambda)$. The parameters of the Bragg fiber are given in caption of Fig. 5.5. 131
- 5.7 The deviation of the effective indices obtained using various inner core region layers. We use n_{eff}^N to denote the effective index obtained using a N layer core region. The curves labeled with "1 layer," "3 layers," and "5 layers" represent respectively $|n_{eff}^1 - n_{eff}^7|$, $|n_{eff}^3 - n_{eff}^7|$, and $|n_{eff}^5 - n_{eff}^7|$. The parameters of the Bragg fiber are given in the caption of Fig. 5.5. 133
- 5.8 The electromagnetic field distribution of the guided Bragg fiber mode at $\omega = 0.286(2\pi c/\Lambda)$. The interface between the core region and cladding region is indicated by dash line. The exact solutions are obtained using Eq. (5.6) and (5.8) only. The asymptotic solutions are obtained using Eq. (5.6) and Eq. (5.8) in the core region, and Eq. (5.10) and (5.11) in the cladding region. 135

- 5.9 Dispersion of the coaxial fiber. The points in the shaded region indicate the existence of propagating TM cladding modes in the omnidirectional reflector. The thick solid lines are results obtained from asymptotic analysis. The dots represent the 2D FDTD results. The light lines in air ($\beta = \omega/c$) and in the low index medium of the Bragg cladding ($\beta = n_{cl}^2\omega/c$) are also shown. If the omnidirectional cladding is taken away, the center core of the coaxial fiber resembles a conventional optical fiber and supports three guided modes: HE, TE and TM modes. Their dispersions are calculated using the formulae for conventional optical fibers and are shown as dash lines. The single mode windows for the TM band are illustrated in the figure as two boxes. 137
- 5.10 The H_z field distributions of the lower $m = 1$ band. In (a), the guided mode has $\beta = 0.153(2\pi/\Lambda)$ and $\omega = 0.187(2\pi c/\Lambda)$. In (b), the guided mode has $\beta = 0.611(2\pi/\Lambda)$ and $\omega = 0.229(2\pi c/\Lambda)$ 139
- 5.11 Dispersion parameter D of the coaxial fiber TM band. At $\lambda = 1.598\mu m$ [or $\omega = 0.202(2\pi c/\Lambda)$], the dispersion parameter D becomes zero, which is shown as the dash line. In the upper diagram, the absolute values of D are shown in a log scale. The two single mode windows in Fig. 5.9 are shown as shaded regions. To the left of the dash line, D is negative, whereas D is positive to the right of the dash line. In the lower diagram, D is shown in the linear scale. 141
- 5.12 The E_z and H_θ fields of the TM coaxial fiber mode at $\omega = 0.202(2\pi c/\Lambda)$. The unshaded, light, and dark regions respectively represent air ($n_{coax} = 1$), low index dielectric medium ($n_{cl}^2 = 1.6$) and high index dielectric medium ($n_{cl}^1 = 4.6$). The units for electric field and magnetic field are chosen such that $\epsilon_0 = 1$ and $\mu_0 = 1$. The asymptotic solutions and the exact solutions are obtained in the same way as in the caption of Fig. 5.8. 142

List of Tables

3.1	The coupling coefficient κ_l of the coupled defect cavities. The hole number refers to the numbers of air holes between the adjacent defect cavities. The fitting results are obtained from fitting the FDTD dispersion results using using Eq. (3.19). The integral results are obtained from the overlap integral in Eq. (3.20).	50
-----	---------------------------------------------------------------------------------------------------------------------------------------------------------------------------------------------------------------------------------------------------------------------------------------------------------------------------------------------------	----

Chapter 1

Introduction

1.1 One-Dimensional Bragg Reflection

In a 1972 paper entitled “Coupled wave theory of distributed feedback lasers” [1], H. Kogelnik and C. V. Shank proposed using a spatially periodic modulation of the refractive index or gain to provide optical feedback for laser oscillation, as shown in Fig. (1.1a). In this case, the coupling between the counter-propagating waves can be well described by the coupled mode theory [2], and the condition of optical feedback requires that the spatial period of the modulation Λ equals to some integral multiple of half the guiding wavelength

$$\Lambda = m \frac{\lambda}{2}, \quad m = 1, 2, \dots \quad (1.1)$$

An optical bandgap, which is defined as a frequency zone where no propagating waveguide mode exists, is formed in the vicinity of this Bragg condition, i.e., Eq. (1.1). The magnitude of this bandgap was shown to be proportional to the strength of the index perturbation [2]. These types of one-dimensional (1D) dielectric structures with weak periodic index perturbation, which include fiber Bragg gratings [3] and semiconductor distributed feedback (DFB) lasers [4], have found wide applications in

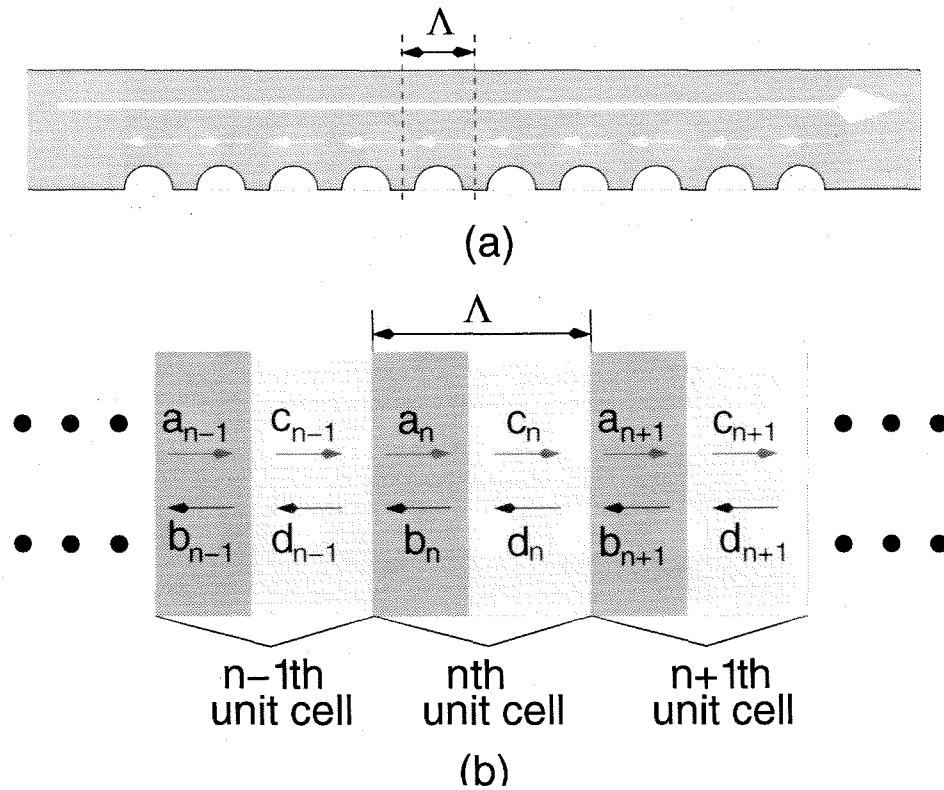


Figure 1.1: (a) Distributed feedback provided by the periodic perturbation of the refractive index or gain. (b) Electromagnetic field in one-dimensional periodic stratified media.

optoelectronics and telecommunications.

Another example of the 1D periodic dielectric structures is the planar Bragg stack shown in Fig. (1.1b), which consists of alternating dielectric layers with different refractive indices. For Bragg stacks with large enough index contrast, it is more appropriate to analyze them using the transfer matrix method as developed in Ref. [5], instead of the coupled mode theory. These planar Bragg stacks have found wide applications as vertical cavity surface emitting lasers (VCSEL) [6], light emitting diodes (LED) [7], anti-resonant reflecting optical waveguides (ARROW) [8], and Bragg waveguides [9, 10].

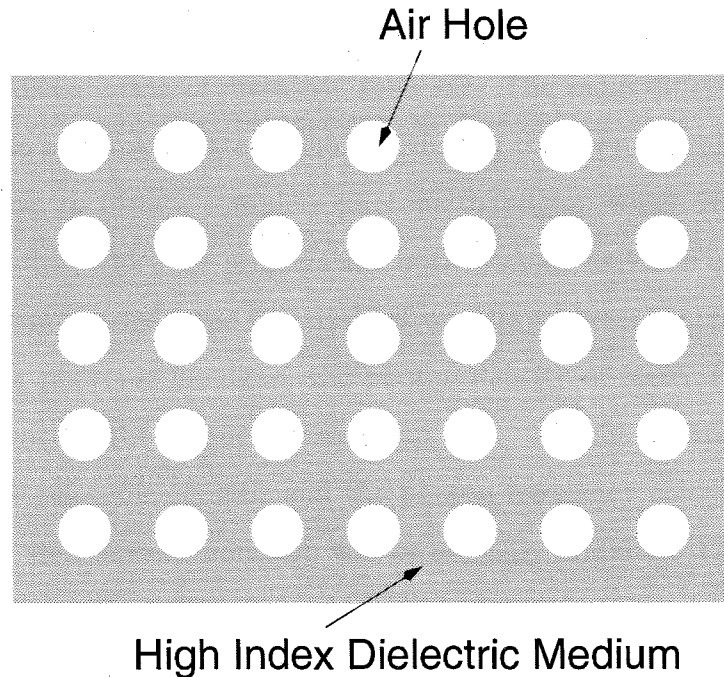


Figure 1.2: A two-dimensional photonic crystal composed of a square lattice of air holes in a high refractive index dielectric medium.

1.2 Photonic Crystals and the Formation of Bandgap

In the 1D periodic dielectric structures, the prohibition of wave propagation generally occurs in the direction perpendicular to the layers, which makes them highly valuable as ideal reflective mirrors. However, it can also be shown that for these 1D structures, no matter how we choose the index contrast and layer thickness, at any given frequency there exist some propagating electromagnetic modes within the dielectric structures, i.e., the photonic bandgap is not complete. To form a bandgap that prohibits light propagation in every direction, it is necessary to utilize dielectric structures periodic in multiple spatial dimensions, which are generally referred as photonic crystals in the literature [11]. This was first suggested in 1987 independently by E. Yablonovitch [12] and S. John [13]. In Fig. 1.2, a two-dimensional square lattice photonic crystal is shown.

The spatial periodicity of photonic crystals leads to a natural analogy with solid state crystals. For example, the Bloch theorem can be applied to classify optical

bands in photonic crystals, and the formation of an optical bandgap is directly due to the periodic distribution of dielectric constant. The main difference between the photonic crystals and solid state crystals is due to the vectorial nature of photons. As a consequence, to form a complete photonic bandgap, which is defined as a frequency range within which no propagating optical mode exists in every direction, it is necessary to employ dielectric materials of very large index contrast [13].

By forming a photonic bandgap, the photon density of states (DOS) is dramatically reduced within the frequency bandgap [14]. If light emitting materials are embedded in the photonic crystals and the photon frequency coincides with the frequency gap, the spontaneous emission will be strongly inhibited [12]. In some applications, it may be sufficient, or even desirable, to form a partial bandgap [15]-[17]. Until recently, much of the research in photonic crystals focused on the fabrication of dielectric structures exhibiting optical bandgap [18, 19] and the physics within the frequency bandgap [20].

The spatially periodic dielectric structures have much to offer besides the formation of a bandgap. It was demonstrated that the dispersion of light outside of the gap region can be 500 times stronger than the dispersion in conventional prisms [21], which can be attributed to the large normal and anomalous dispersion near the photonic bandedges [22]. In the long-wavelength limit where the photon frequency is far below the optical bandgap, the photonic crystals can be viewed as uniaxial or biaxial media and explicit formulas have been derived for the effective dielectric constants [23]. Above the bandgap, it was also shown that the photonic bands can be well described by the tight-binding approximation [24]. Thus it is obvious that in periodic dielectric materials, a different mechanism is responsible for photon guiding at different frequencies. To fully understand the complex behavior of the photonic dispersion in periodic dielectric materials, it is necessary to study in depth the different guiding mechanisms.

1.3 Different Waveguiding Mechanisms

The most widely used guiding mechanism in optoelectronics is the total internal reflection. One prominent example is the optical telecommunication fibers, where photons are confined in the silica core with refractive index slightly higher than that of the cladding medium. A far less obvious, but very interesting case of total internal reflection guiding is a 2D square lattice photonic crystal waveguide. In Ref. [25], we demonstrate that the propagating modes within the PBG waveguide can be regarded as a slab waveguide mode, and the photonic crystals surrounding the core region can be well approximated using an effective index lower than the core region index. However, since the total internal reflection is well understood, with simple analytical solutions easily available, the following chapters shall concentrate on evanescent guiding and Bragg guiding.

The evanescent coupling between individual optical resonators, as a guiding mechanism, is very similar to the tight-binding propagation in the solid state physics [26]. In Chapter 3, we utilize evanescent coupling to construct a new type of waveguide, coupled resonator optical waveguide (CROW), whose unique symmetry and dispersion properties allow for many potential applications in optoelectronics, especially nonlinear optics. It should be mentioned that this type of evanescent guiding is quite common in photonic crystals [24, 27].

As we shall see in Chapter 4, another type of evanescent coupling, the waveguide-resonator coupling, is also of great interest. For a waveguide coupled to a single resonator, a scattering theory is used to analyze the transmission and reflection characteristics of the coupled system, which are shown to depend strongly on the characteristics of the cavity modes and the waveguide-resonator coupling. The evanescent coupling between the waveguide and the resonator leads to the formation of indirect CROW.

Bragg guiding is considered in Chapter 5. The effects of Bragg guiding in planar geometries have been extensively studied [28]. The Bragg guiding in cylindrically symmetric geometries, on the other hand, is not well understood. In Chapter 5, we

developed an asymptotic matrix theory to analytically find the photonic dispersion and guided mode distribution in the cylindrically symmetric geometries.

Most of the dielectric structures considered in later chapters are quite complicated. And the analytical theories developed for them usually involve approximations. Therefore, it is necessary to develop numerical algorithms capable of solving Maxwell equations exactly. One such numerical method, finite difference time domain (FDTD) method, is discussed in the next chapter in detail, and is applied to various dielectric structures. The numerical results are compared with those obtained from analytical theories.

Chapter 2

Finite Difference Time Domain (FDTD) Algorithm

2.1 FDTD Cells and Finite Difference Equations

The original finite difference time domain (FDTD) algorithm was proposed by Yee in 1966 [29]. Since then, it has found wide applications in numerical electromagnetic simulations and is extensively reviewed in Ref. [30]. With its versatility and relatively easy implementation, the FDTD analysis becomes a powerful numerical tool in optoelectronics. In this method, we introduce a lattice of computational grids to discretize the spatial domain and transform Maxwell equations into a set of finite difference equations. Unlike the beam propagation method [31], the FDTD method does not involve the paraxial approximation. Consequently, FDTD algorithms are of special importance for dielectric structures with large index contrast and complicated dielectric constant distribution, such as photonic crystals.

According to the coordinate systems, FDTD algorithms can be generally classified into the two-dimensional (2D) FDTD algorithm [32, 33], the three-dimensional (3D) FDTD algorithm [29], and the cylindrical one [34]. In this chapter, we discuss the 2D and 3D FDTD algorithms in detail. The cylindrical FDTD algorithm has relatively

limited applications and is not considered here. Readers interested in the cylindrical FDTD algorithm should consult Ref. [34].

To speed up FDTD simulations, in this chapter, we adopt a normalized unit in which $\epsilon_0 = 1$ and $\mu_0 = 1$. With this convention, the vacuum speed of light $c = 1$, while time and space have the same unit.

2.1.1 Two-Dimensional Case

For a given dielectric structure infinite in the z axis, the z dependence of the electromagnetic field can be written as $e^{-i\beta z}$, which is directly due to continuous translational symmetry in the z direction. Consequently, we can write the electric field $\mathcal{E}(x, y, z, t)$ and magnetic field $\mathcal{H}(x, y, z, t)$ in the form of

$$\mathcal{E}(x, y, z, t) = e^{-i\beta z} \begin{bmatrix} E_x(x, y, t) \\ E_y(x, y, t) \\ iE_z(x, y, t) \end{bmatrix}, \quad (2.1)$$

$$\mathcal{H}(x, y, z, t) = e^{-i\beta z} \begin{bmatrix} iH_x(x, y, t) \\ iH_y(x, y, t) \\ H_z(x, y, t) \end{bmatrix}. \quad (2.2)$$

Substituting them into Maxwell equations, we find

$$\frac{\partial H_x}{\partial t} = -\frac{\partial E_z}{\partial y} - \beta E_y, \quad (2.3)$$

$$\frac{\partial H_y}{\partial t} = \frac{\partial E_z}{\partial x} + \beta E_x, \quad (2.4)$$

$$\frac{\partial H_z}{\partial t} = \frac{\partial E_x}{\partial y} - \frac{\partial E_y}{\partial x}, \quad (2.5)$$

$$\frac{\partial E_x}{\partial t} = \frac{1}{c} \left(\frac{\partial H_z}{\partial y} - \beta H_y \right), \quad (2.6)$$

$$\frac{\partial E_y}{\partial t} = \frac{1}{c} \left(-\frac{\partial H_z}{\partial x} + \beta H_x \right), \quad (2.7)$$

$$\frac{\partial E_z}{\partial t} = \frac{1}{\epsilon} \left(\frac{\partial H_y}{\partial x} - \frac{\partial H_x}{\partial y} \right), \quad (2.8)$$

where ϵ represents the distribution of dielectric constant in the xy plane.

In order to discretize Eq. (2.3) to Eq. (2.8), we introduce a two-dimensional lattice of computational cells (2D FDTD lattice), on which for an arbitrary function $F(x, y, t)$ we define

$$F^n(i, j) = F(i\Delta, j\Delta, n\Delta t), \quad (2.9)$$

where Δ is the grid size and Δt is the time step. The FDTD cell itself is labeled according to the position of its lower-left corner. For example, the lower-left corner of the (i, j) th FDTD cell, as seen in Fig. 2.1, should be located at the spatial point $(i\Delta, j\Delta)$. On each FDTD cell, we arrange the components of the electromagnetic field as shown in Fig. 2.1. Following the convention in Eq. (2.9) and take cell size $\Delta = 1$, we can transform Eq. (2.3) to Eq. (2.8) into the finite difference form [32, 33]:

$$\begin{aligned} H_x^{n-\frac{1}{2}}(i, j - \frac{1}{2}) &= H_x^{n-\frac{1}{2}}(i, j + \frac{1}{2}) - \Delta t \\ &\times \left[E_z^n(i, j + 1) - E_z^n(i, j) + \beta E_y^n(i, j + \frac{1}{2}) \right], \end{aligned} \quad (2.10)$$

$$\begin{aligned} H_y^{n+\frac{1}{2}}(i + \frac{1}{2}, j) &= H_y^{n-\frac{1}{2}}(i + \frac{1}{2}, j) + \Delta t \\ &\times \left[E_z^n(i + 1, j) - E_z^n(i, j) + \beta E_x^n(i + \frac{1}{2}, j) \right], \end{aligned} \quad (2.11)$$

$$\begin{aligned} H_z^{n+\frac{1}{2}}(i - \frac{1}{2}, j + \frac{1}{2}) &= H_z^{n-\frac{1}{2}}(i + \frac{1}{2}, j + \frac{1}{2}) + \Delta t \\ &\times \left[E_x^n(i + \frac{1}{2}, j + 1) - E_x^n(i + \frac{1}{2}, j) + E_y^n(i, j + \frac{1}{2}) - E_y^n(i + 1, j + \frac{1}{2}) \right], \end{aligned} \quad (2.12)$$

$$\begin{aligned} E_x^{n+1}(i + \frac{1}{2}, j) &= E_x^n(i + \frac{1}{2}, j) + \frac{\Delta t}{\epsilon(i, j)} \\ &\times \left[H_z^{n+\frac{1}{2}}(i + \frac{1}{2}, j + \frac{1}{2}) - H_z^{n+\frac{1}{2}}(i - \frac{1}{2}, j - \frac{1}{2}) + \beta H_y^{n+\frac{1}{2}}(i + \frac{1}{2}, j) \right], \end{aligned} \quad (2.13)$$

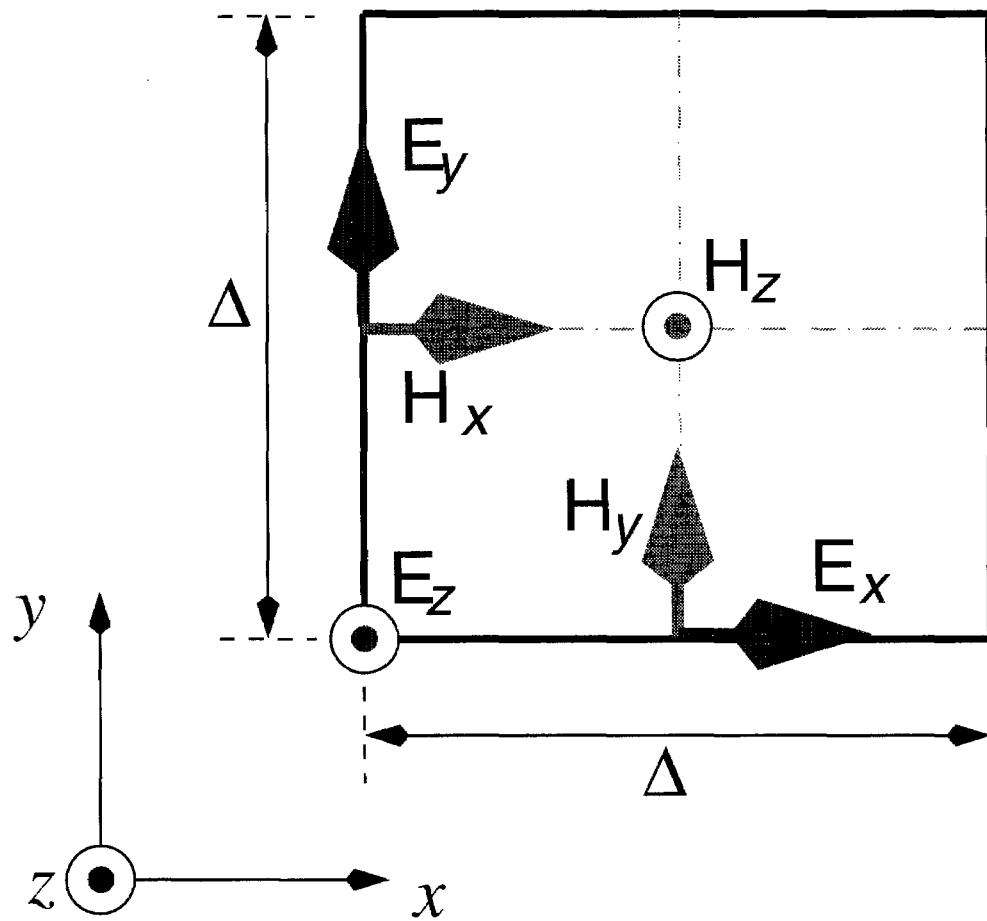


Figure 2.1: Electromagnetic field components at the (i, j) th 2D FDTD cell.

$$E_y^{n+1}(i, j - \frac{1}{2}) = E_y^n(i, j + \frac{1}{2}) + \frac{\Delta t}{\epsilon(i, j)} \quad (2.14)$$

$$\times \left[-H_z^{n+\frac{1}{2}}(i + \frac{1}{2}, j + \frac{1}{2}) + H_z^{n+\frac{1}{2}}(i - \frac{1}{2}, j + \frac{1}{2}) + \beta H_x^{n+\frac{1}{2}}(i, j + \frac{1}{2}) \right],$$

$$E_z^{n+1}(i, j) = E_z^n(i, j) + \frac{\Delta t}{c(i, j)} \quad (2.15)$$

$$\times \left[-H_x^{n+\frac{1}{2}}(i, j + \frac{1}{2}) + H_x^{n+\frac{1}{2}}(i, j - \frac{1}{2}) + H_y^{n+\frac{1}{2}}(i + \frac{1}{2}, j) - H_y^{n+\frac{1}{2}}(i - \frac{1}{2}, j) \right],$$

In this approach, we assume that the propagation constant β is already known, and its value is substituted into Eq. (2.10) to Eq. (2.15). Using these FDTD equations, we can evolve any electromagnetic field distribution within a given spatial domain. Based on the time evolution results, we can find the frequency and the field distribution of the resonant modes within the 2D dielectric structures.

2.1.2 Three-Dimensional Case

Without the continuous translational symmetry of the 2D case, here we start from the complete Maxwell equations for electric field \vec{E} and magnetic field \vec{H} :

$$\frac{\partial \vec{H}}{\partial t} = -\vec{\nabla} \times \vec{E}, \quad (2.16)$$

$$\epsilon \frac{\partial \vec{E}}{\partial t} = \vec{\nabla} \times \vec{H}. \quad (2.17)$$

As before, we introduce a three-dimensional lattice of cubic cells and attach a label to each FDTD cell according to the position of the corner closest to the origin of the coordinate system. The (i, j, k) th cell in the FDTD lattice is shown in Fig. 2.2, where we also indicate the arrangement of electromagnetic field components at this FDTD cell. Adopting a similar convention as that in the 2D case, for an arbitrary function $F(x, y, z, t)$, we have

$$F^n(i, j, k) = F(i\Delta, j\Delta, k\Delta, n\Delta t). \quad (2.18)$$

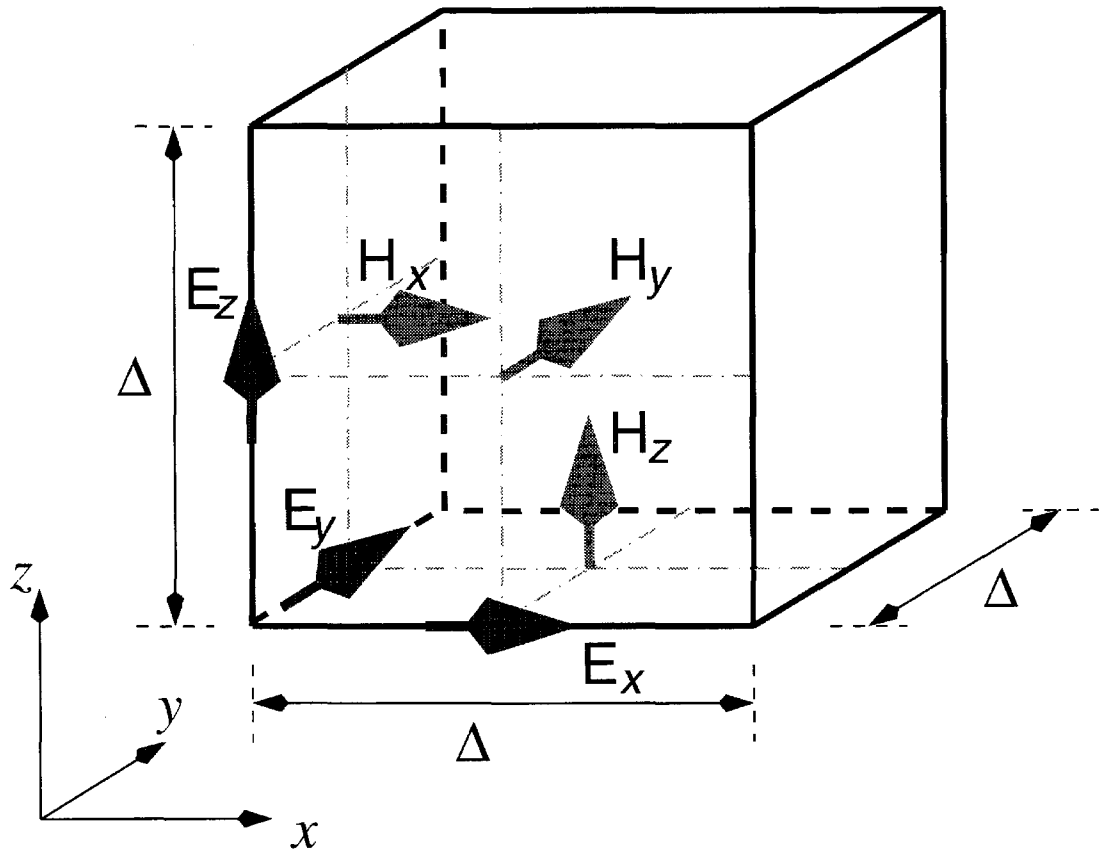


Figure 2.2: Electromagnetic field components at the (i, j, k) th 3D FDTD cell.

Using this notation and taking the cell size $\Delta = 1$, we can discretize Eq. (2.16) and Eq. (2.17), which gives us [29]

$$H_x^{n+\frac{1}{2}}(i, j + \frac{1}{2}, k + \frac{1}{2}) = H_x^{n-\frac{1}{2}}(i, j + \frac{1}{2}, k + \frac{1}{2}) - \Delta t \quad (2.19)$$

$$\times \left[E_y^n(i, j + \frac{1}{2}, k) - E_y^n(i, j + \frac{1}{2}, k + 1) - E_z^n(i, j, k + \frac{1}{2}) + E_z^n(i, j + 1, k + \frac{1}{2}) \right],$$

$$H_y^{n+\frac{1}{2}}(i + \frac{1}{2}, j, k + \frac{1}{2}) = H_y^{n-\frac{1}{2}}(i + \frac{1}{2}, j, k + \frac{1}{2}) - \Delta t \quad (2.20)$$

$$\times \left[E_x^n(i + \frac{1}{2}, j, k + 1) - E_x^n(i + \frac{1}{2}, j, k) + E_z^n(i, j, k + \frac{1}{2}) - E_z^n(i + 1, j, k + \frac{1}{2}) \right],$$

$$H_z^{n-\frac{1}{2}}(i + \frac{1}{2}, j + \frac{1}{2}, k) = H_z^{n-\frac{1}{2}}(i + \frac{1}{2}, j + \frac{1}{2}, k) - \Delta t \quad (2.21)$$

$$\times \left[E_y^n(i + 1, j + \frac{1}{2}, k) - E_y^n(i, j + \frac{1}{2}, k) - E_x^n(i + \frac{1}{2}, j + 1, k) + E_x^n(i + \frac{1}{2}, j, k) \right],$$

$$E_x^{n+1}(i + \frac{1}{2}, j, k) = E_x^n(i + \frac{1}{2}, j, k) - \frac{\Delta t}{\epsilon(i, j, k)} \left[H_y^{n+\frac{1}{2}}(i + \frac{1}{2}, j, k - \frac{1}{2}) \quad (2.22)$$

$$- H_y^{n+\frac{1}{2}}(i + \frac{1}{2}, j, k + \frac{1}{2}) + H_z^{n+\frac{1}{2}}(i + \frac{1}{2}, j - \frac{1}{2}, k) - H_z^{n+\frac{1}{2}}(i + \frac{1}{2}, j - \frac{1}{2}, k) \right],$$

$$E_y^{n+1}(i, j + \frac{1}{2}, k) = E_y^n(i, j + \frac{1}{2}, k) + \frac{\Delta t}{\epsilon(i, j, k)} \left[H_x^{n-\frac{1}{2}}(i, j - \frac{1}{2}, k + \frac{1}{2}) \quad (2.23)$$

$$- H_x^{n+\frac{1}{2}}(i, j + \frac{1}{2}, k - \frac{1}{2}) + H_z^{n-\frac{1}{2}}(i - \frac{1}{2}, j + \frac{1}{2}, k) - H_z^{n+\frac{1}{2}}(i + \frac{1}{2}, j + \frac{1}{2}, k) \right],$$

$$E_z^{n+1}(i, j, k + \frac{1}{2}) = E_z^n(i, j, k + \frac{1}{2}) + \frac{\Delta t}{\epsilon(i, j, k)} \left[H_y^{n+\frac{1}{2}}(i + \frac{1}{2}, j, k + \frac{1}{2}) \quad (2.24)$$

$$- H_y^{n+\frac{1}{2}}(i - \frac{1}{2}, j, k + \frac{1}{2}) + H_x^{n+\frac{1}{2}}(i, j - \frac{1}{2}, k + \frac{1}{2}) - H_x^{n-\frac{1}{2}}(i, j + \frac{1}{2}, k + \frac{1}{2}) \right].$$

Eq. (2.19) to Eq. (2.24) are the finite difference equivalence of 3D Maxwell equations. They can be used to evolve an arbitrary three-dimensional electromagnetic field distribution, and form the basis of 3D FDTD algorithm.

2.2 Boundary Conditions

One important question associated with any FDTD simulation is how to terminate the computational domain. Take the 2D case for example. In Fig. 2.3; we showed a 2D FDTD computational domain with $(N_x - 1) \times (N_y + 1)$ FDTD cells. As can be seen from Eq. (2.10) to Eq. (2.15), the electromagnetic fields at the (i, j) th cell depend on those at the four neighboring cells. Thus for some field components at the boundary cells, such as $E_z^n(i, 0)$, we can no longer use the FDTD equations to update their values. Consequently, it is necessary to use various boundary conditions to provide values for electromagnetic fields located at the boundaries of the computational domain.

There is no unique way to terminate the FDTD computational domain, and the solution generally depends on the physical nature of the problem. For example, if we want to know the electromagnetic modes within a cube bound by perfect metal, we can simply take all the electromagnetic fields at the FDTD boundary cells to be zero. Symmetry considerations can also be applied to terminate computational boundaries, such as the Bloch boundary condition and the mirror boundary condition, as we shall see shortly hereafter. For some other problems, the boundary conditions are more difficult to find. An example is the problem of finding the mode frequency and quality (Q) factor of a high Q mode in an optical resonator. In this case, we are required to find an absorbing boundary condition that imitates open space, i.e., it should absorb all the outgoing electromagnetic radiation without reflection. Of all the absorbing boundary conditions available in the literature, the perfectly matched layer (PML) boundary condition [35, 36] provides the best performance and has found wide applications in FDTD simulations.

2.2.1 Bloch Boundary

For any dielectric structure with discrete translational symmetry with spatial periodicity R in the x direction, we can classify the electromagnetic modes according to

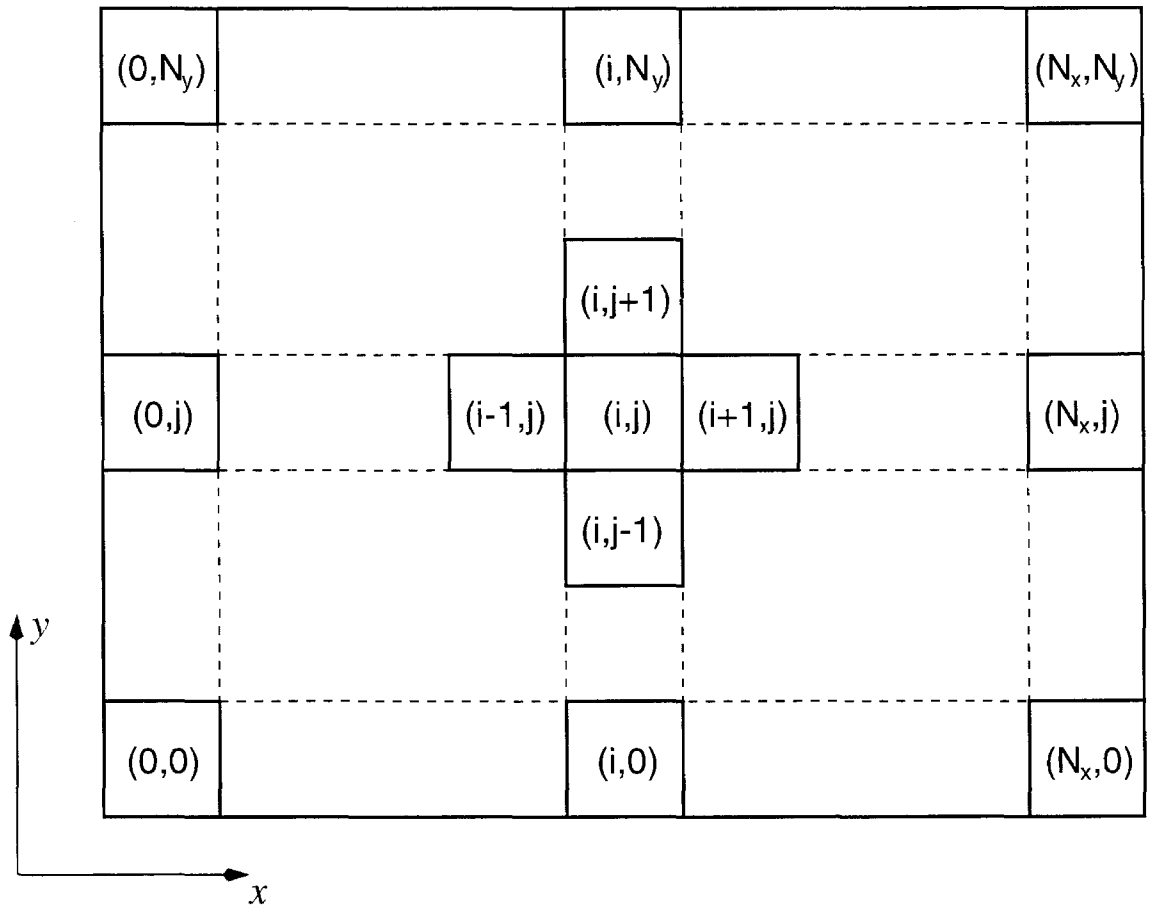


Figure 2.3: A two-dimensional FDTD computational domain with $(N_x+1) \times (N_y+1)$ FDTD cells.

the Bloch vector K . In the 2D case, the Bloch theorem requires

$$\vec{E}(x = R, y) = e^{-iKR} \vec{E}(x = 0, y) , \quad (2.25)$$

$$\vec{H}(x = R, y) = e^{-iKR} \vec{H}(x = 0, y) . \quad (2.26)$$

However, we cannot directly apply these relations to the $(0, j)$ th cell and the (N_x, j) th cell FDTD domain in Fig. 2.3, since electromagnetic fields at both the $(0, j)$ th cell and the (N_x, j) th cell are unknown. Instead, we should relate the electromagnetic fields at the (N_x, j) th cell to those at the $(1, j)$ th cell:

$$H_x^{n+\frac{1}{2}}(N_x, j + \frac{1}{2}) = e^{-iK(N_x-1)} H_x^{n-\frac{1}{2}}(1, j + \frac{1}{2}) . \quad (2.27)$$

$$H_y^{n+\frac{1}{2}}(N_x + \frac{1}{2}, j) = e^{-iK(N_x-1)} H_y^{n+\frac{1}{2}}(\frac{3}{2}, j) , \quad (2.28)$$

$$H_z^{n+\frac{1}{2}}(N_x + \frac{1}{2}, j + \frac{1}{2}) = e^{-iK(N_x-1)} H_z^{n+\frac{1}{2}}(\frac{3}{2}, j + \frac{1}{2}) , \quad (2.29)$$

$$E_x^n(N_x, j + \frac{1}{2}) = e^{-iK(N_x-1)} E_x^n(1, j + \frac{1}{2}) , \quad (2.30)$$

$$E_y^n(N_x + \frac{1}{2}, j) = e^{-iK(N_x-1)} E_y^n(1 + \frac{1}{2}, j) , \quad (2.31)$$

$$E_z^n(N_x, j) = e^{-iK(N_x-1)} E_z^n(1, j) , \quad (2.32)$$

where we use the fact that cell size $\Delta = 1$. In the same way, we can relate the $(0, j)$ th cell to the $(N_x - 1, j)$ th cell, which completes the construction of the Bloch boundary condition for the x direction in the 2D case. We can treat the 2D Bloch boundary condition along the y axis, and the 3D Bloch boundary condition in a similar fashion.

2.2.2 Mirror Boundary

Another symmetry property that is useful in FDTD simulations is the mirror reflection symmetry. Many dielectric structures possess mirror reflection symmetry with respect to a given symmetry plane, from which we can derive the mirror boundary conditions for FDTD simulations. One advantage of the mirror boundary conditions is that they

can lead to the reduction of the computational domain by a factor of 2 or even more. This can be very helpful for the 3D simulations, where limited computer memory often limits the size of dielectric structure that can be calculated. As an additional advantage, the mirror boundary conditions can also be used to resolve the modal degeneracy dictated by the symmetry properties of the dielectric structures.

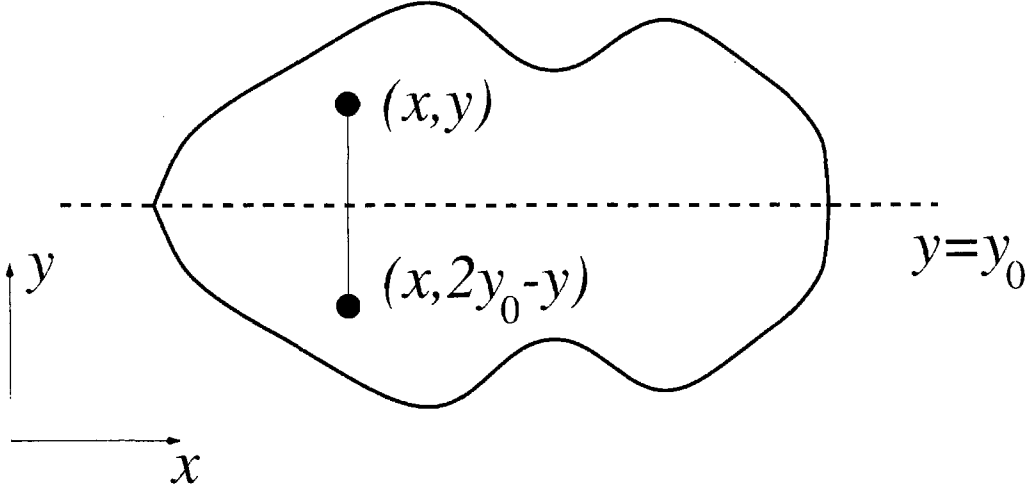


Figure 2.4: A two-dimensional dielectric distribution with a mirror reflection symmetry plane $y = y_0$.

Take the 2D case as shown in Fig. 2.4, for example, where the dielectric structure is symmetric with respect to the plane $y = y_0$. Due to the mirror reflection symmetry, the optical modes in this structure can be classified according to their parity P [11]:

$$H_x(x, y) = -PH_x(x, 2y_0 - y) , \quad (2.33)$$

$$H_y(x, y) = PH_y(x, 2y_0 - y) , \quad (2.34)$$

$$H_z(x, y) = -PH_z(x, 2y_0 - y) , \quad (2.35)$$

$$E_x(x, y) = PE_x(x, 2y_0 - y) , \quad (2.36)$$

$$E_y(x, y) = -PE_y(x, 2y_0 - y) , \quad (2.37)$$

$$E_z(x, y) = PE_z(x, 2y_0 - y) , \quad (2.38)$$

where the parity P can take the value of ± 1 . The modes with $P = 1$ and $P = -1$ shall be called, respectively, the even modes and the odd modes.

If the FDTD domain in Fig. 2.3 is used to calculate the even symmetry modes ($P = 1$), we choose the mirror reflection plane located at $y_0 = 1/2$. Applying Eq. (2.33) through Eq. (2.38) to the $(i, 0)$ th cell and $(i, 1)$ th cell, we find

$$H_x^{n+\frac{1}{2}}(i, \frac{1}{2}) = 0, \quad (2.39)$$

$$H_y^{n+\frac{1}{2}}(i + \frac{1}{2}, 0) = H_y^{n+\frac{1}{2}}(i + \frac{1}{2}, 1), \quad (2.40)$$

$$H_z^{n+\frac{1}{2}}(i + \frac{1}{2}, \frac{1}{2}) = 0, \quad (2.41)$$

$$E_x^n(i + \frac{1}{2}, 0) = E_x^n(i + \frac{1}{2}, 1), \quad (2.42)$$

$$E_y^n(i, \frac{1}{2}) = 0, \quad (2.43)$$

$$E_z^n(i, 0) = E_z^n(i, 1). \quad (2.44)$$

The above six equations give the even mirror boundary condition at $y = 1/2$. For the odd symmetry modes with $P = -1$, we choose the mirror reflection plane at $y_0 = 1$ and transform Eq. (2.33) to Eq. (2.38) into

$$H_x^{n+\frac{1}{2}}(i, \frac{1}{2}) = H_x^{n-\frac{1}{2}}(i, \frac{3}{2}), \quad (2.45)$$

$$H_y^{n-\frac{1}{2}}(i + \frac{1}{2}, 0) = -H_y^{n-\frac{1}{2}}(i + \frac{1}{2}, 2), \quad (2.46)$$

$$H_y^{n+\frac{1}{2}}(i + \frac{1}{2}, 1) = 0. \quad (2.47)$$

$$H_z^{n+\frac{1}{2}}(i + \frac{1}{2}, \frac{1}{2}) = H_z^{n-\frac{1}{2}}(i + \frac{1}{2}, \frac{3}{2}), \quad (2.48)$$

$$E_x^n(i + \frac{1}{2}, 0) = -E_x^n(i + \frac{1}{2}, 2), \quad (2.49)$$

$$E_x^n(i + \frac{1}{2}, 1) = 0, \quad (2.50)$$

$$E_y^n(i, \frac{1}{2}, 0) = E_y^n(i, \frac{3}{2}), \quad (2.51)$$

$$E_z^n(i, 0) = -E_z^n(i, 2), \quad (2.52)$$

$$E_z^n(i, 1) = 0. \quad (2.53)$$

Similarly, we can construct even and odd symmetry boundary conditions for 3D cases.

2.2.3 Perfectly Matched Layer (PML) Boundary

In reality, almost all dielectric structures are located in free space and are of finite size. To analyze such structures, it is often necessary to use absorbing boundary conditions to simulate free space at the boundaries of the FDTD domain. Among various absorbing boundary conditions, the perfectly matched layer (PML) boundary condition is relatively complicated in construction but offers superior absorption characteristics.

In 2D case, the perfectly matched layer can be viewed as a lossy uniaxial medium characterized by parameters (σ_x, σ_y) . Following Gedney [36], for a monochromatic electromagnetic field with frequency ω , we can write Maxwell equations in PML region to be

$$\vec{\nabla} \times \vec{H} = i\omega\epsilon\vec{E}, \quad (2.54)$$

$$\vec{\nabla} \times \vec{E} = -i\omega\bar{\mu}\vec{H}, \quad (2.55)$$

where we have chosen $\epsilon_0 = \mu_0 = 1$ and use ϵ to represent the distribution of dielectric constant, whereas $\bar{\epsilon}$ and $\bar{\mu}$ are defined as

$$\bar{\epsilon} = \bar{\mu} = \begin{bmatrix} s_y/s_x & 0 & 0 \\ 0 & s_x/s_y & 0 \\ 0 & 0 & s_x s_y \end{bmatrix}, \quad (2.56)$$

with s_x and s_y being

$$s_x = 1 + \frac{\sigma_x(x)}{i\omega}, \quad (2.57)$$

$$s_y = 1 + \frac{\sigma_y(y)}{i\omega} . \quad (2.58)$$

The parameters σ_x and σ_y have, respectively, only x and y dependence [36].

Eqs. (2.54) and Eq. (2.55) are both in the frequency domain. To transform them into the time domain, we introduce two auxiliary vectorial quantities \vec{D} and \vec{B} . Take the x component of Eq. (2.55) for example:

$$-i\omega \frac{s_y}{s_x} H_x = \vec{e}_x \cdot (\vec{\nabla} \times \vec{E}) . \quad (2.59)$$

We introduce B_x which is defined as

$$B_x = \frac{H_x}{s_x} , \quad (2.60)$$

and write Eq. (2.59) as

$$-i\omega s_y B_x = \vec{e}_x \cdot (\vec{\nabla} \times \vec{E}) . \quad (2.61)$$

Substituting the definitions of s_x and s_y , as given in Eq. (2.57) and Eq. (2.58), into Eq. (2.61) and Eq. (2.60), we respectively find

$$\frac{\partial B_x}{\partial t} + \sigma_y(y) B_x = -\vec{e}_x \cdot (\vec{\nabla} \times \vec{E}) , \quad (2.62)$$

$$\frac{\partial H_x}{\partial t} = \frac{\partial B_x}{\partial t} + \sigma_x(x) B_x , \quad (2.63)$$

where we have replaced $i\omega$ by $\partial/\partial t$. Following the same steps, we can derive similar equations for other components.

As in Sec. 2.1.1, we observe that in 2D case, the z dependence of the fields is simply $e^{-i\beta z}$. Thus Eq. (2.62), Eq. (2.63), and similar equations for other electromagnetic field components can be transformed into:

$$\frac{\partial B_x}{\partial t} + \sigma_y(y) B_x = -\frac{\partial E_z}{\partial y} - \beta E_y , \quad (2.64)$$

$$\frac{\partial H_x}{\partial t} = \frac{\partial B_x}{\partial t} + \sigma_x(x) B_x , \quad (2.65)$$

$$\frac{\partial B_y}{\partial t} + \sigma_x(x)B_y = \frac{\partial E_z}{\partial x} + \beta E_x, \quad (2.66)$$

$$\frac{\partial H_y}{\partial t} = \frac{\partial B_y}{\partial t} + \sigma_y(y)B_y, \quad (2.67)$$

$$\frac{\partial B_z}{\partial t} + \sigma_y(y)B_z = -\frac{\partial E_y}{\partial x} + \frac{\partial E_x}{\partial y}, \quad (2.68)$$

$$\frac{\partial H_z}{\partial t} + \sigma_x(x)H_z = \frac{\partial B_z}{\partial t}, \quad (2.69)$$

$$\frac{\partial D_x}{\partial t} + \sigma_y(y)D_x = \frac{1}{\epsilon(x, y)}\left(\frac{\partial H_z}{\partial y} - \beta H_y\right), \quad (2.70)$$

$$\frac{\partial E_x}{\partial t} = \frac{\partial D_x}{\partial t} + \sigma_x(x)D_x, \quad (2.71)$$

$$\frac{\partial D_y}{\partial t} + \sigma_x(x)D_y = \frac{1}{\epsilon(x, y)}\left(-\frac{\partial H_z}{\partial x} + \beta H_x\right), \quad (2.72)$$

$$\frac{\partial E_y}{\partial t} = \frac{\partial D_y}{\partial t} + \sigma_y(y)D_y, \quad (2.73)$$

$$\frac{\partial D_z}{\partial t} + \sigma_y(y)D_z = \frac{1}{\epsilon(x, y)}\left(\frac{\partial H_y}{\partial x} - \frac{\partial H_x}{\partial y}\right), \quad (2.74)$$

$$\frac{\partial E_z}{\partial t} + \sigma_x(x)E_z = \frac{\partial D_z}{\partial t}. \quad (2.75)$$

It is relatively easy to derive the finite difference form of Eq. (2.64) to Eq. (2.75). We will give the explicit finite difference equation for the H_x component only. Within the FDTD cell shown in Fig. 2.1, we put the components of the \vec{B} field at the same location as those of the \vec{H} field, while the \vec{D} components occupy the same position of the \vec{E} components. With such an FDTD cell, Eq. (2.64) and Eq. (2.65) are transformed into:

$$\begin{aligned} B_x^{n+\frac{1}{2}}(i, j + \frac{1}{2}) &= \frac{1 - \frac{\sigma_y(j+\frac{1}{2})\Delta t}{2}}{1 + \frac{\sigma_y(j+\frac{1}{2})\Delta t}{2}} B_x^{n-\frac{1}{2}}(i, j + \frac{1}{2}) \\ &- \frac{\Delta t}{1 + \frac{\sigma_y(j+\frac{1}{2})\Delta t}{2}} \left[E_z^n(i, j + 1) - E_z^n(i, j) + \beta E_y^n(i, j + \frac{1}{2}) \right], \end{aligned} \quad (2.76)$$

$$H_x^{n-\frac{1}{2}}(i, j - \frac{1}{2}) = H_x^{n+\frac{1}{2}}(i, j + \frac{1}{2}) - \left[1 - \frac{\sigma_x(i)\Delta t}{2} \right] B_x^{n+\frac{1}{2}}(i, j + \frac{1}{2}) \quad (2.77)$$

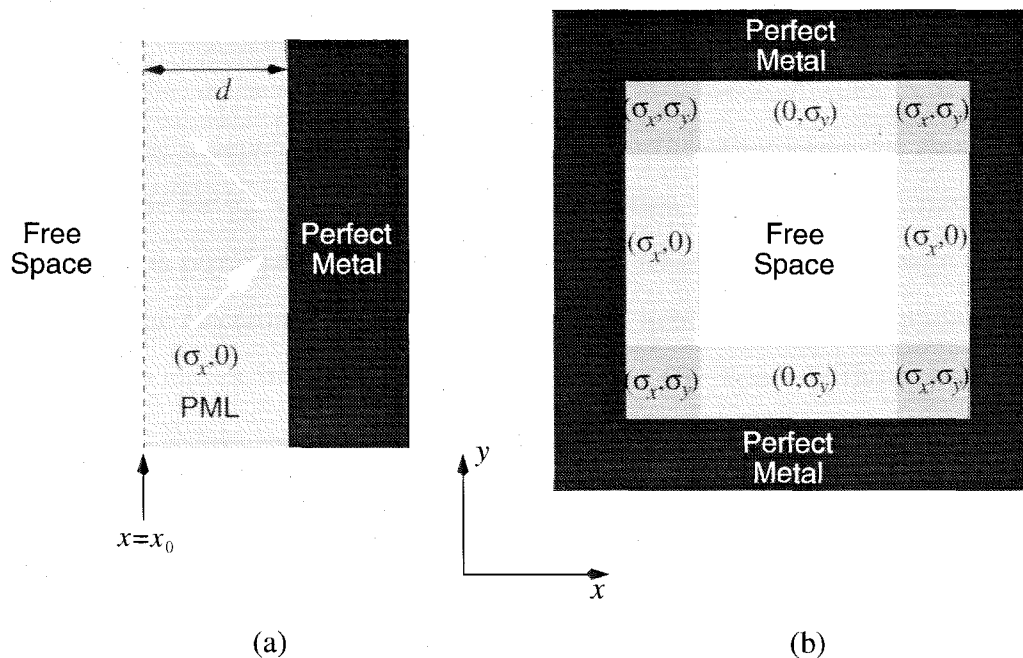


Figure 2.5: (a) Absorption of light in a perfectly matched layer. (b) PML boundary condition in a 2D FDTD computational domain.

$$- \left[1 - \frac{\sigma_x(i)\Delta t}{2} \right] B_x^{n+\frac{1}{2}}(i, j + \frac{1}{2}).$$

Finite difference equations for other components can also be similarly derived.

As demonstrated by Eq. (2.54) and Eq. (2.55), the PML medium can be regarded as an artificial dielectric medium characterized by the parameters (σ_x, σ_y) . In fact, if we substitute $\sigma_x = 0$ and $\sigma_y = 0$ into Eq. (2.56), Eq. (2.57) and Eq. (2.58), it is obvious that free space can be viewed as a special case of the PML medium with $(\sigma_x, \sigma_y) = (0, 0)$. In Ref. [36], it has been shown that if σ_x varies only along the x direction and σ_y has only y dependence, any incident electromagnetic radiation shall enter into the PML medium without reflection, irrespective of the incident angle. Within the PML medium itself, the radiation attenuates exponentially, with the absorption constant depending on the values of σ_x and σ_y .

In Fig. (2.5a), we illustrate how the PML works as an absorbing boundary condition. We take the PML boundary to be perpendicular to the x axis, while the unshaded region to the left of the plane $x = x_0$ represents the free space and the

shaded region to the right is the PML medium terminated by perfect metal. Therefore, in Fig. (2.5a) σ_y must remain zero within the PML medium, since σ_y is zero in the free space and is independent of the variable x . On the other hand, we should choose a non-zero value for σ_x , which provides the absorption within the PML medium. The PML medium is terminated by the perfect metal, where we simply assign zero to all the values of the electromagnetic field. Under this arrangement, the incident electromagnetic wave enters into the PML medium from free space without encountering any reflection. While the incoming wave propagates in PML medium, it attenuates both before and after being reflected by the perfect metal. With the thickness of the PML medium and the value of σ_x properly chosen, the residual radiation reflected back into the free space can be reduced to negligible level.

In Fig. (2.5b), we show how to arrange the (σ_x, σ_y) parameters of the PML medium to effectively absorb the outgoing radiation from the 2D computational domain. All the PML medium, with the exception of the four corners, has only one of the σ_x and σ_y non-zero, directly due to the requirement that σ_x and σ_y should be, respectively, independent of y and x . As discussed before, such arrangement insures the radiation incident on the PML medium does not encounter reflection. As the electromagnetic radiation enters into PML medium close to the four corners, some may penetrate into the corner region. Still, the (σ_x, σ_y) are arranged such that the radiation field continues its attenuation without suffering back reflection.

Due to discretization error in actual simulations, it was found that σ_x can be chosen to take the following form to minimize the numerical back reflection [36]

$$\sigma_x(x) = \sigma_{max} \frac{(x - x_0)^4}{d^4}, \quad x > x_0, \quad (2.78)$$

where d is the total thickness of the PML layer and x_0 is the coordinate of the interface between free space and PML medium, as shown in Fig. (2.5a). We can choose σ_y to be of similar dependence on y .

In concluding this section, we remark that PML layers can be similarly constructed for 3D cases. The main difference is that we have to introduce a third parameter σ_z .

For more details, the readers should consult Ref. [36].

2.3 FDTD Algorithms and Their Applications

2.3.1 Simulation of High Q Optical Modes

One important application of the FDTD analysis is to find the resonant frequency ω and the quality factor Q of the optical modes within a dielectric resonator. For a dielectric structure with dielectric constant distribution $\epsilon(\vec{r})$, we can define the vector potential $\vec{A}_n(\vec{r})$ of the n th mode as the eigensolutions of the following equation [37]

$$\nabla \times [\nabla \times \vec{A}_n(\vec{r})] = \omega_n^2 \epsilon(\vec{r}) \vec{A}_n(\vec{r}) , \quad (2.79)$$

where ω_n is the eigenvalue for the n th eigenmode. The eigenmodes are orthonormal

$$\int d^3r \epsilon(\vec{r}) \vec{A}_m^*(\vec{r}) \cdot \vec{A}_n(\vec{r}) = \delta_{mn} , \quad (2.80)$$

and complete

$$\delta_{\alpha\beta} \delta(\vec{r}, \vec{r}') = \epsilon(\vec{x}) \sum_n A_{n\alpha}(\vec{r}) A_{n\beta}^*(\vec{r}') , \quad (2.81)$$

where $A_{n,\alpha}(\vec{r})$ is the α th components of the vector eigenmode $\vec{A}_n(\vec{r})$. Notice that in Eq. (2.79), we have used the convention of $c = 1$.

At the frequency ω , we introduce the Green function $G_{\alpha\beta}^\omega$ of Maxwell equations defined as [38, 39]:

$$-\nabla \times [\nabla \times (\sum_\alpha G_{\alpha\beta}^\omega(\vec{r}, \vec{r}') \vec{e}_\alpha)] + \epsilon(\vec{r}) \omega^2 \sum_\alpha G_{\alpha\beta}^\omega(\vec{r}, \vec{r}') \vec{e}_\alpha = \delta(\vec{r} - \vec{r}') \vec{e}_\beta , \quad (2.82)$$

where α and β are the subscripts of the Cartesian coordinate. As clear from this definition, $\sum_\alpha G_{\alpha\beta}^\omega(\vec{r}, \vec{r}') \vec{e}_\alpha$ represents the electromagnetic field excited by a δ -function source $\delta(\vec{r} - \vec{r}') \vec{e}_\beta$. We can expand the Green function in terms of the complete set

of the eigenmodes [39]:

$$G_{\alpha\beta}^{\omega}(\vec{r}, \vec{r}') = \sum_n \frac{1}{2\omega_n} \frac{A_{n,\alpha}(\vec{r})A_{n,\beta}^*(\vec{r}')}{\omega - \omega_n + i\Gamma_n}, \quad (2.83)$$

where Γ_n is the amplitude decay rate of the n th electromagnetic mode, from which we can define the quality factor Q_n as

$$Q_n = \frac{\omega_n}{2\Gamma_n}. \quad (2.84)$$

As can be seen from Eq. (2.83) and Eq. (2.84), for a high Q optical mode, the Green function becomes very large at the resonant frequency $\omega = \omega_n$. From the observation, we can build a FDTD algorithm to calculate the modal frequencies and spatial profiles of high Q modes.

Take the problem of finding mode resonant frequency for example. First we introduce an initial distribution of electromagnetic field and evolve the initial field using the appropriate FDTD equations as given in Sec. 2.1 and the PML boundary conditions as given in Sec. 2.2. We record the values of the electromagnetic field at a given “observation” point \vec{r}_0 as a function of time and denote the results as $\vec{E}(\vec{r}_0, t)$ and $\vec{H}(\vec{r}_0, t)$. We take one component of the electromagnetic field, say $E_x(\vec{r}_0, t)$, and transform the temporal series into the frequency domain via fast Fourier transform (FFT) [40], which gives us $E_x(\vec{r}_0, \omega)$. As obvious from the definition of Green function, the result $E_x(\vec{r}_0, \omega)$ is essentially the frequency domain Green function with some average over the initial field distribution. As a consequence, the peaks in the frequency spectrum of the temporal series can be identified as corresponding to the high Q optical modes. The position of the frequency peaks gives the resonant frequency of the modes, while the width of the peaks is inversely proportional to the Q factor of the modes. In Fig. 2.6 we show a typical FFT spectrum of the electromagnetic field at the “observation” point, where the three peaks in the figure indicate the existence of three high Q modes within this frequency range.

If we know *a priori* the resonant frequency ω of a particular high Q mode, the

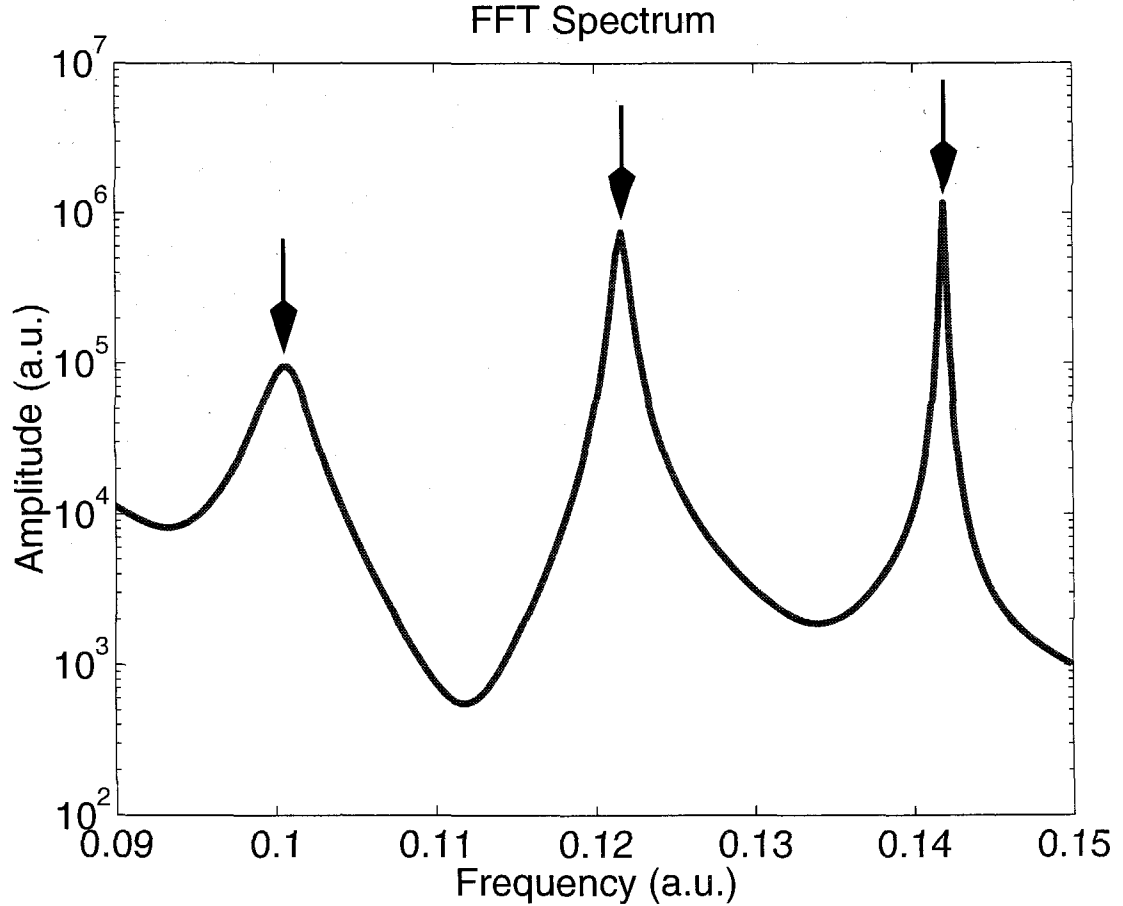


Figure 2.6: FFT spectrum of the temporal series of the electromagnetic field obtained using FDTD equations in Sec. 2.1.

mode's spatial profile can be simply found by using the following mode filtering technique. As before, we start from an arbitrary initial field distribution and use the FDTD equations to evolve the initial field to find a time-varying electromagnetic field $\vec{E}(\vec{r}, t)$ and $\vec{H}(\vec{r}, t)$. The difference is that here we need the electromagnetic field at every spatial point instead of just a single observation point \vec{r}_0 . This time-varying field generally contains a broad frequency spectrum, which depends on the choice of the initial field. By applying a narrow bandwidth frequency filter centered at ω to the temporal field, we filter out $\vec{E}(\vec{r}, \omega)$ and $\vec{H}(\vec{r}, \omega)$ at every spatial point \vec{r} , which gives us the electromagnetic mode at frequency ω . In our algorithm, this mode filtering process is simply achieved by applying a temporal Fourier transformation at the given

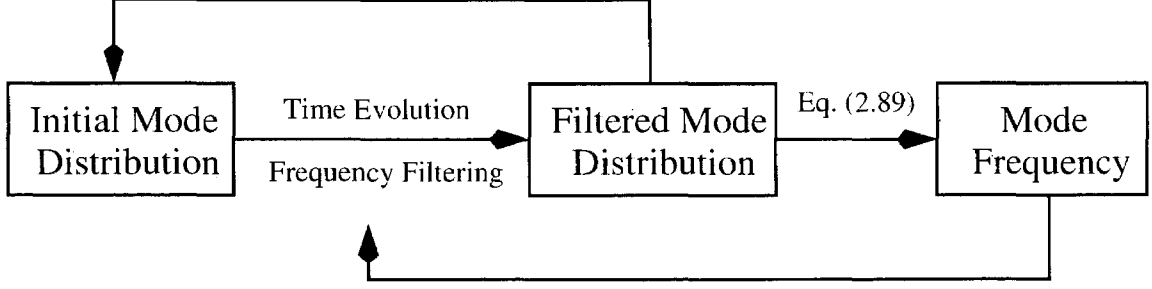


Figure 2.7: Schematic of the FDTD mode filtering algorithm.

frequency ω :

$$\vec{E}(\vec{r}, \omega) = \int_0^T dt e^{-i\omega t} \vec{E}(\vec{r}, t), \quad (2.85)$$

$$\vec{H}(\vec{r}, \omega) = \int_0^T dt e^{-i\omega t} \vec{H}(\vec{r}, t). \quad (2.86)$$

It should also be noted that the mode $\vec{E}(\vec{r}, \omega)$ and $\vec{H}(\vec{r}, \omega)$ has a frequency uncertainty of the order of $1/T$, since the temporal integration in Eq. (2.85) and Eq. (2.86) has a frequency bandwidth of the order of $1/T$.

In most cases, however, we do not know the mode frequency ω in advance. But if we know the spatial distribution of a high Q mode to be $\vec{E}(\vec{r})$ and $\vec{H}(\vec{r})$, the mode resonant frequency ω can be found by noticing that [11]

$$\nabla \times \left[\frac{1}{\epsilon(\vec{r})} \nabla \times \vec{H}(\vec{r}) \right] = \omega^2 \vec{H}(\vec{r}), \quad (2.87)$$

$$\nabla \times [\nabla \times \vec{E}(\vec{r})] = \omega^2 \epsilon(\vec{r}) \vec{E}(\vec{r}). \quad (2.88)$$

Consequently, the resonant frequency ω and the spatial distribution $\vec{E}(\vec{r})$ and $\vec{H}(\vec{r})$ of the given high Q mode satisfy

$$\omega^2 = c^2 \frac{\int_V d\vec{r} \left\{ \vec{H}^*(\vec{r}) \cdot \left[\nabla \times \left[\frac{1}{\epsilon(\vec{r})} \nabla \times \vec{H}(\vec{r}) \right] \right] + \vec{E}^*(\vec{r}) \cdot [\nabla \times [\nabla \times \vec{E}(\vec{r})]] \right\}}{\int_V d\vec{r} \left\{ \vec{H}^*(\vec{r}) \cdot \vec{H}(\vec{r}) + \epsilon(\vec{r}) \vec{E}^*(\vec{r}) \cdot \vec{E}(\vec{r}) \right\}}, \quad (2.89)$$

where the spatial integration is over the whole computational domain V .

Combining the mode filtering technique, i.e., Eq. (2.85) and Eq. (2.86), and the ability to find the resonant frequency of a given mode, i.e., Eq. (2.89), we can itera-

tively find the high Q mode of interest and its resonant frequency, starting from a good initial guess of the field distribution $\mathcal{E}_0(\vec{r})$, $\mathcal{H}_0(\vec{r})$ and the mode frequency Ω_0 . First we evolve the “guess” field $\mathcal{E}_0(\vec{r})$ and $\mathcal{H}_0(\vec{r})$ using the FDTD equations in Sec. 2.1. Then from Eq. (2.85) and Eq. (2.86), we can filter out a mode $\mathcal{E}_1(\vec{r})$ and $\mathcal{H}_1(\vec{r})$ from the time evolution of the initial field $\mathcal{E}_0(\vec{r})$ and $\mathcal{H}_0(\vec{r})$, using the “guess” frequency Ω_0 . Next the “average” frequency Ω_1 of the mode $\mathcal{E}_1(\vec{r})$ and $\mathcal{H}_1(\vec{r})$ is obtained from Eq. (2.89). Subsequently, we can use $\mathcal{E}_1(\vec{r})$ and $\mathcal{H}_1(\vec{r})$ as the initial field distribution and Ω_1 as the “guess” mode frequency, and resume the iteration. This process is repeated until it converges and gives the desired high Q mode. This iteration algorithm is also summarized in Fig. 2.7.

To evaluate the quality factor of a single resonator mode, we use the definition

$$Q = \frac{E_{mode}^{avg}}{E_{mode}(0) - E_{mode}(T)} \Omega_{mode} T, \quad (2.90)$$

where $E_{mode}(T)$ is the total energy of that mode at time T (the end of evolution), $E_{mode}(0)$ is the mode energy at time 0 (the beginning of evolution), E_{mode}^{avg} is the average mode energy during the time evolution, and Ω_{mode} is the frequency of the mode.

The decay of the modes leads to an uncertainty of the mode resonant frequency, which can become the dominant source for the frequency errors in our simulations, especially when the Q factor is not very large. Consider a mode with a mode frequency of Ω and quality factor of Q. Since the mode evolves temporally according to $e^{(-1/2Q+i)\Omega t}$, the calculated mode frequency will bear an uncertainty of order of $\Omega/2Q$.

2.3.2 Simulation of Waveguide Modes

Depending on whether the waveguide possesses continuous translational symmetry along the direction of propagation or not, we can classify the FDTD waveguide simulations into two types. If the waveguides are spatially invariant along propagation direction (such as in optical fibers), we follow the analysis in Sec. 2.1 and use Eq. (2.10) to Eq. (2.15) for time evolution in FDTD calculations. The PML boundary

conditions as developed in Sec. 2.2.3 can be directly applied here to terminate the FDTD computational domain. At any given value of propagation constant β , we can use the algorithms discussed in Sec. 2.3.1 to find the frequency and spatial distribution of the waveguide modes. The dispersion relation of the waveguide modes is subsequently obtained by varying propagation constant β and calculating mode frequency ω for each β . In Chapter 5, this method is applied to analyze Bragg fibers and dielectric coaxial fibers.

For waveguides with dielectric constant varying along the propagation direction, we can no longer take advantage of the continuous translational symmetry. In many cases, however, the waveguides possess discrete translational symmetry, and we can easily use the Bloch boundary condition in Sec. 2.2.1 to restrict the FDTD calculation within one unit cell of the waveguides. Take the triangular lattice photonic crystal waveguide as shown in Fig. (2.8a) for example. In this case, the discrete translational symmetry in the x direction allows us to use Bloch boundary condition to reduce the modal analysis within a single unit cell. The photonic crystal waveguide is defined by 3 layers of air holes in an infinite dielectric medium. Thus the PML boundary condition is applied to terminate the FDTD computational domain in the y direction. Consequently, we can reduce the original infinite waveguide to its single unit cell in the FDTD simulations, as shown in Fig. (2.8b). This problem can be further simplified by introducing the mirror boundary at the center of the photonic crystal waveguide, as in Fig. (2.8c).

An important parameter of waveguides is their propagation loss. Since the simulations of waveguides and simulations of optical resonators are quite similar, we can define an effective Q factor as

$$Q_{eff} = \frac{E_{mode}^{avg}}{E_{mode}(0) - E_{mode}(T)} \Omega_{mode} T. \quad (2.91)$$

This definition is the same as that of the Q factor of an optical resonator mode, as can be seen from Eq. (2.90). From the effective Q factor, we can easily get the waveguide decay rate, which after being divided by group velocity gives the propagation

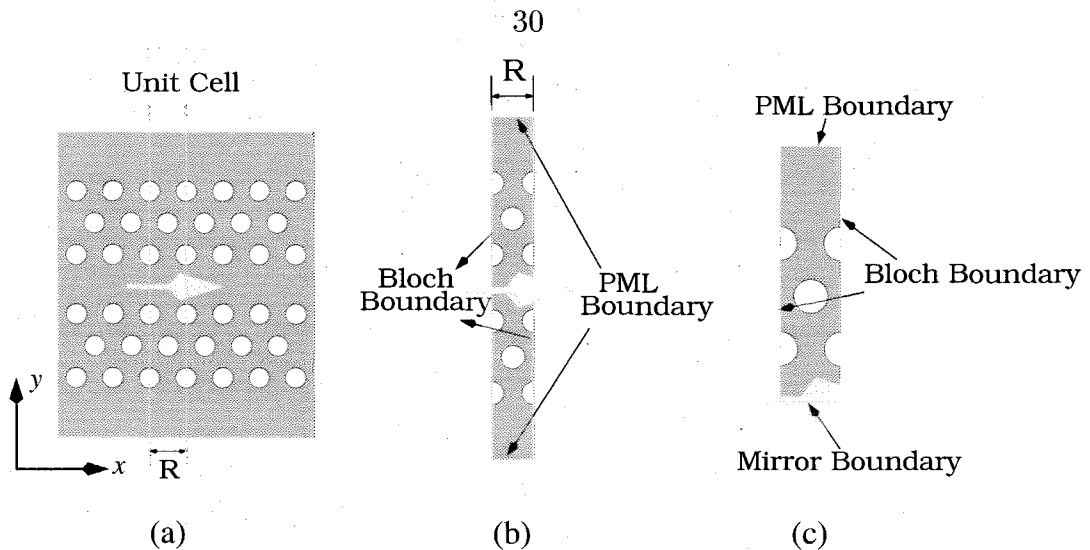


Figure 2.8: Boundary conditions for the FDTD calculation of photonic crystal waveguide modes.

loss of waveguide modes.

As mentioned at the end of Sec. 2.3.1, for any waveguide mode with effective Q factor Q_{eff} , it has a frequency uncertainty of the order of $\Omega/2Q_{eff}$. This may become the dominant contribution to the frequency errors in our FDTD analysis, especially when Q_{eff} is not very large.

2.3.3 Sources in FDTD Simulations and Their Applications

All the applications of FDTD algorithms discussed so far can be characterized as “passive” simulations, since there is no radiation source within the FDTD computational domain. For many applications such as microwave antenna design, it is necessary to include some radiation sources into the FDTD simulations. In this section, we introduce two types of FDTD radiation sources: the point dipole source, and the Huygens source.

The simplest radiation source in FDTD analysis is a point dipole source, which can be included in Maxwell equations simply by adding an additional dipole term \vec{P} as [41, 42]

$$\frac{\partial \vec{H}}{\partial t} = -\vec{\nabla} \times \vec{E}, \quad (2.92)$$

$$\epsilon \frac{\partial \vec{E}}{\partial t} = \vec{\nabla} \times \vec{H} - \frac{\partial \vec{P}}{\partial t}, \quad (2.93)$$

with \vec{P} defined as

$$\vec{P} = d(t) \hat{d} \delta(\vec{r} - \vec{r}_0), \quad (2.94)$$

where $d(t)$ and \hat{d} are, respectively, the magnitude and the polarization of the oscillating dipole. In translating Eq. (2.93) into the finite difference form, we basically follow the same steps outlined in Sec. 2.1. The only difference is that the δ -function in Eq. (2.94) is approximated by a dipole source with uniform distribution in a unit FDTD cell. The components of the dipole vector is allocated in the same as those of the electric field. For example, for a z -polarized dipole located at the (i, j, k) th FDTD cell, only $P(i, j, k + \frac{1}{2})$ is non-zero; all P_x , P_y , and other P_z are zero.

It is well known that spontaneous emission characteristics can be dramatically modified by complicated dielectric structures such as photonic crystals [12] or high Q cavities [43]. As shown by us in Ref. [39] and [41], the modification of spontaneous emission can be modeled using FDTD simulations with point dipole sources. Take the spontaneous emission rate for example. For a light source placed at the position \vec{r}_0 of an arbitrary dielectric structure, its spontaneous emission rate modification is related to radiation power of a classical dipole, placed at the same position in the same dielectric structure [41]:

$$\frac{\Gamma_{mod}}{\Gamma_{free}} = \frac{P_{mod}}{P_{free}}, \quad (2.95)$$

where Γ_{mod} and Γ_{free} represent, respectively, the spontaneous emission rate in the dielectric structure and that in free space, whereas P_{mod} and P_{free} correspond to, respectively, the classical dipole emission power in the same dielectric structure and that in free space. This algorithm has been used to simulate spontaneous emission modification in dielectric slab waveguides [41], microdisk cavities [42], and triangular lattice photonic crystal slabs [44].

Another very useful radiation source in FDTD simulations is the Huygens source [45, 46]. More specifically, suppose we know that at a given Huygens surface S , the field distribution of an optical mode is given by \vec{E}^{inc} and \vec{H}^{inc} . We can introduce an

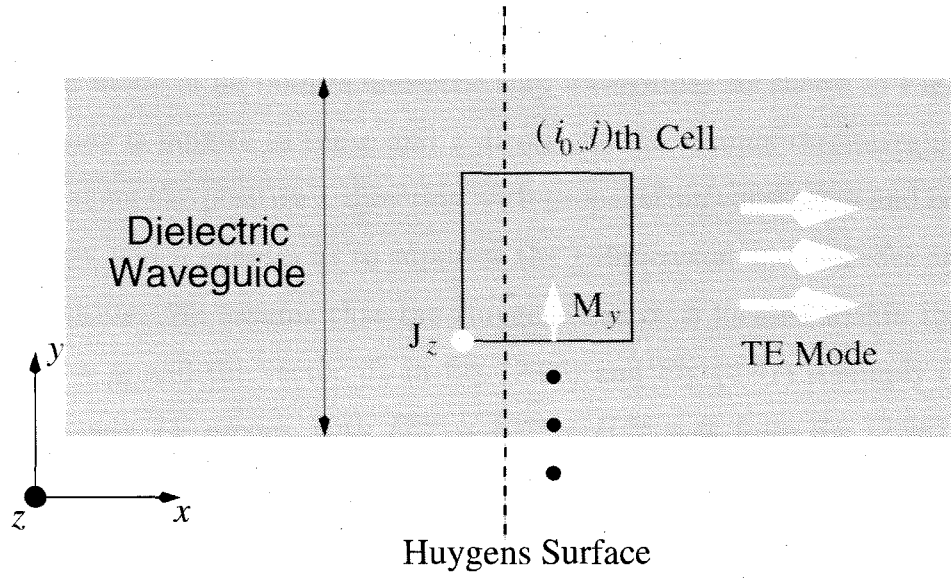


Figure 2.9: Huygens Source that excites the TE mode of an infinite dielectric slab waveguide.

electric surface current \vec{J}^{inc} and a magnetic surface current \vec{M}^{inc} (Huygens source) at the surface S , which are defined as

$$\vec{J}^{inc} = \vec{n}_S \times \vec{H}^{inc}, \quad (2.96)$$

$$\vec{M}^{inc} = -\vec{n}_S \times \vec{E}^{inc}, \quad (2.97)$$

where \vec{n}_S is a unit vector normal to the surface S and points towards one side of the surface S . With this Huygens source, Maxwell equations become

$$\nabla \times \vec{E} = -\frac{\partial \vec{H}}{\partial t} - \vec{M}^{inc}, \quad (2.98)$$

$$\nabla \times \vec{H} = \epsilon \frac{\partial \vec{E}}{\partial t} + \vec{J}^{inc}. \quad (2.99)$$

In Ref. [45] and [46], it was shown that the Huygens source as defined in Eq. (2.96) and Eq. (2.97) excites the desired optical mode at one side of the Huygens surface S , whereas it does not excite any electromagnetic field at the other side of the surface S .

As an example, we describe in detail how to construct a Huygens source that excites a TE mode in an infinite dielectric slab waveguide. As shown in Fig. 2.9, the slab waveguide is infinite in the x and z direction. We assume the waveguide mode propagates along the positive x direction with propagation constant β and is uniform in z direction, which enables us to suppress the z dimension and consider only the x and y dimension. We assume that the Huygens source is located within the FDTD cells with $i = i_0$ and the vector \vec{n}_S in Eq. (2.96) and Eq. (2.97) is simply \vec{e}_x . Since we consider only TE modes, with $E_x^{inc} = E_y^{inc} = H_z^{inc} = 0$, from Eq. (2.96) and Eq. (2.97) we can write

$$\vec{J}^{inc} = J_z^{inc} \vec{e}_z, \quad (2.100)$$

$$\vec{M}^{inc} = M_y^{inc} \vec{e}_y. \quad (2.101)$$

Consequently, we only need to consider the y component of Eq. (2.98) and z component of Eq. (2.99), while the rest of the FDTD equations are the same as those for Maxwell equations without Huygens source. In the finite difference form, y component of Eq. (2.98) and z component of Eq. (2.99) become:

$$\begin{aligned} & E_z^n(i_0 + 1, j) - E_z^n(i_0, j) \\ &= \frac{1}{\Delta t} \left[H_y^{n+\frac{1}{2}}(i_0 + \frac{1}{2}, j) - H_y^{n-\frac{1}{2}}(i_0 + \frac{1}{2}, j) \right] + M_y^{n,inc}(i_0 + \frac{1}{2}, j), \end{aligned} \quad (2.102)$$

$$\begin{aligned} & H_x^{n+\frac{1}{2}}(i_0, j - \frac{1}{2}) - H_x^{n+\frac{1}{2}}(i_0, j + \frac{1}{2}) + H_y^{n+\frac{1}{2}}(i_0 + \frac{1}{2}, j) - H_y^{n+\frac{1}{2}}(i_0 - \frac{1}{2}, j) \\ &= \frac{\epsilon(i_0, j)}{\Delta t} \left[E_z^{n+1}(i_0, j) - E_z^n(i_0, j) \right] + J_z^{n+\frac{1}{2},inc}(i_0, j). \end{aligned} \quad (2.103)$$

We require that the electromagnetic fields to the left of the Huygens surface are zero, while the fields to the right of the Huygens surface take the values of the propagating TE mode. Therefore, in Eq. (2.102) $E_z^n(i_0, j)$ equals zero, whereas the rest of the field components take the values of the TE mode components at the particular

FDTD grid point:

$$\begin{aligned} & E_z^{n,TE}(i_0 + 1, j) \\ &= \frac{1}{\Delta t} \left[H_y^{n+\frac{1}{2},TE}(i_0 + \frac{1}{2}) - H_y^{n-\frac{1}{2},TE}(i_0 + \frac{1}{2}, j) \right] + M_y^{n,inc}(i_0 + \frac{1}{2}, j), \end{aligned} \quad (2.104)$$

where the field quantities with superscript TE refer to those of the TE modes. On the other hand, without the Huygens source, Eq. (2.102) still holds if we substitute all the field quantities with the values of the propagating TE modes:

$$E_z^{n,TE}(i_0 + 1, j) - E_z^{n,TE}(i_0, j) = \frac{1}{\Delta t} \left[H_y^{n+\frac{1}{2},TE}(i_0 + \frac{1}{2}) - H_y^{n-\frac{1}{2},TE}(i_0 + \frac{1}{2}, j) \right] \quad (2.105)$$

Comparing Eq. (2.104) with Eq. (2.105), we find

$$M_y^{n,inc}(i_0 + \frac{1}{2}, j) = E_z^{n,TE}(i_0, j). \quad (2.106)$$

Similarly, by requiring the field components to the left of the Huygens source to be zero, we find that in Eq. (2.103) all components except $H_y^{n+\frac{1}{2},TE}(i_0 + \frac{1}{2}, j)$ and $J_z^{n+\frac{1}{2},inc}(i_0, j)$ are zero:

$$J_z^{n+\frac{1}{2},inc}(i_0, j) = H_y^{n+\frac{1}{2},TE}(i_0 + \frac{1}{2}, j), \quad (2.107)$$

where it is understood that $H_y^{n+\frac{1}{2},TE}(i_0 + \frac{1}{2}, j)$ takes the value of H_y component of the TE mode at point $(i_0 + \frac{1}{2}, j)$.

For the TE mode of the dielectric slab, we can write its field distribution as

$$H_y(x, y, t) = h_y^{TE}(y) \sin(\omega t - \beta x), \quad (2.108)$$

$$E_z(x, y, t) = e_z^{TE}(y) \sin(\omega t - \beta x), \quad (2.109)$$

where ω and β represent, respectively, the frequency and the propagation constant of the TE mode, while the exact form of h_y^{TE} and e_z^{TE} can be found from the standard text book on optoelectronics [28]. Here it suffices to notice that they have only y

dependence. Combining Eq. (2.106) and Eq. (2.109), we find

$$M_y^{n,inc}(i_0 + \frac{1}{2}, j) = e_z^{TE}(j) \sin [\omega n \Delta t - \beta i_0]. \quad (2.110)$$

Similarly, from Eq. (2.107) and Eq. (2.108), we find

$$J_z^{n+\frac{1}{2},inc}(i_0, j) = h_y^{TE}(j) \sin [\omega(n + \frac{1}{2})\Delta t - \beta(i_0 + \frac{1}{2})]. \quad (2.111)$$

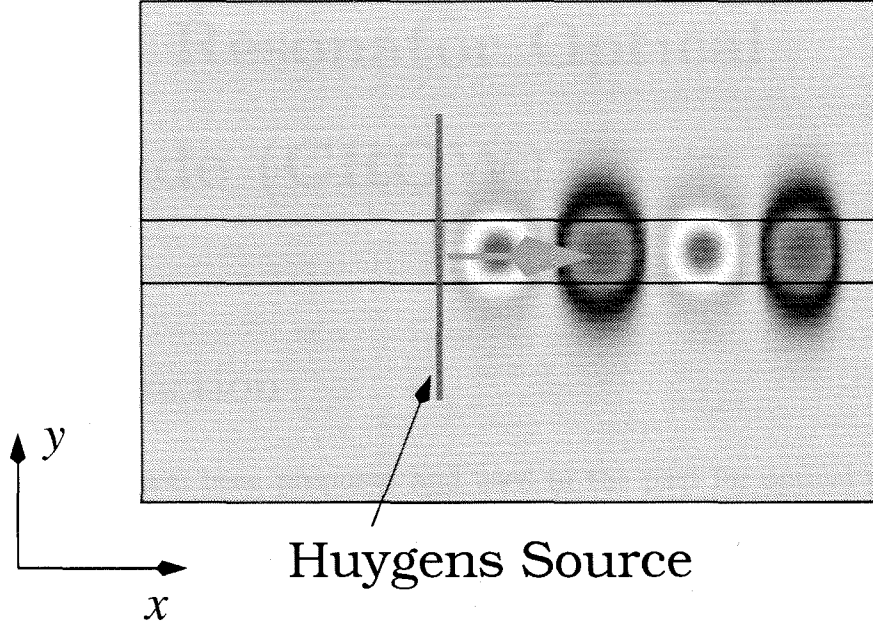


Figure 2.10: Huygens source.

In Fig. 2.10, we show the E_z field of the fundamental TE slab mode excited by a Huygens source according to Eq. (2.110) and Eq. (2.111). As seen from Fig. 2.10, the Huygens source produces the fundamental TE mode that exists only to the right of the Huygens surface. We have used such Huygens source to investigate the coupling between a dielectric slab waveguide and an air-core photonic crystal waveguide, and also the coupling between a dielectric slab waveguide [47] and a dielectric-core photonic crystal waveguide [25].

Chapter 3

Coupled Resonator Optical Waveguide (CROW)

3.1 Introduction

Two mechanisms have been proposed and used in the past for optical waveguiding [28]. The most widely used is the waveguiding by total internal reflection, as illustrated in Fig. (3.1a). Another mechanism—“Bragg waveguiding,” where waveguiding is achieved through Bragg reflection from a periodic structure, has also been demonstrated [9]. Fig. (3.1b) illustrate an example of Bragg reflection provided by a periodic Bragg stack.

There exists, however, a third approach in photon guiding [48, 49]. Fig. (3.1c) shows such a possibility: a waveguide based on the evanescent field coupling between the high Q whispering gallery modes of the individual microdisk cavities [50, 51]. Another possible realization is shown in Fig. (3.1d), where the individual resonators consist of the “defect” cavities [52, 53] embedded in a 2D triangular lattice photonic crystal. These defect resonators are designed such that their resonant frequency falls within the “forbidden gap” of the surrounding 2D structure which enables high Q optical modes. The coupling in this case is due to the evanescent Bloch waves. In

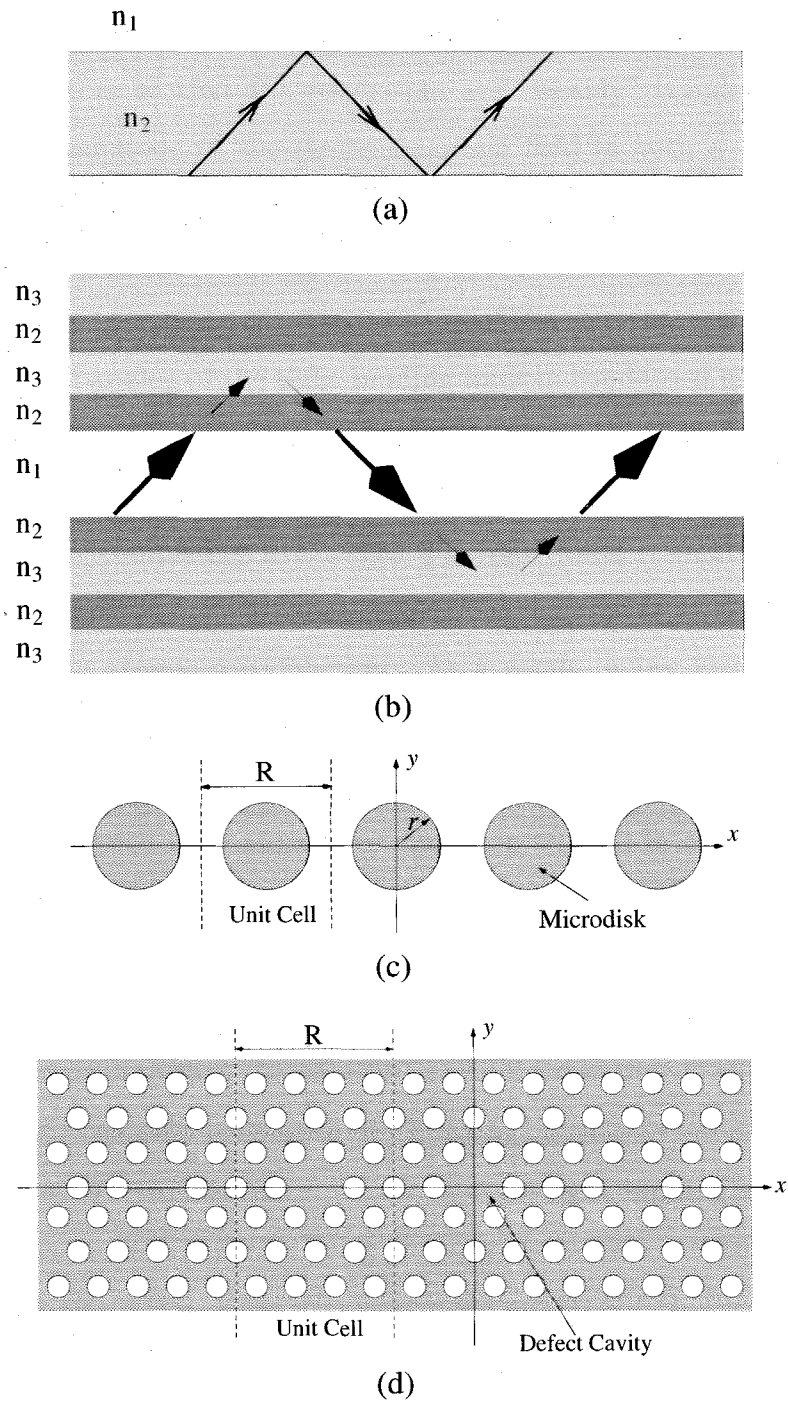


Figure 3.1: Three types of waveguiding: a) the waveguiding by total internal reflection at the interface between the high index medium and low index medium. b) the “Bragg waveguiding” achieved by reflection from the periodic Bragg stacks. c) the coupled resonators optical waveguide—CROW, with waveguiding due to the coupling between the individual microdisks. R is the size of a unit cell and \mathbf{e}_x is the direction of the periodicity for the coupled resonators. d) the CROW realized by coupling the individual defect cavities in a 2D photonic crystal.

both realizations of CROW, we assume a sufficiently large separation between the individual resonators so that the resonators are “weakly” coupled. Consequently, we expect the eigenmode of the electromagnetic field in such a coupled resonator waveguide should remain essentially the same as the high Q mode in a single resonator. Yet at the same time the coupling between the individual high Q modes must be taken into account to explain the transmission of the electromagnetic waves. This is exactly the optical analog of the tight-binding limit in condensed matter physics [26], in which the overlap of atomic wavefunctions is large enough to require corrections to the picture of isolated atoms, yet at the same time not large enough to render the atomic description completely irrelevant. The individual resonators in CROW are the optical counterpart of the isolated atoms, and the high Q mode in the resonators corresponds to the atomic wavefunction. As a result, many features of the tight-binding theory in solids remain the same in the coupled resonators waveguide. We call such waveguide the coupled resonators optical waveguide (CROW) [48, 49]. Some special cases of coupled resonators have also been studied in the literature, such as photonic molecules [54, 55, 56], and the “impurity band” in an infinite chain of spheres with negative dielectric constant [57].

In both realizations of CROW, we assume a sufficiently large separation between the high Q resonators so that the photons are “tightly confined” within each individual resonator and can only propagate by “hopping” from one resonator to its nearest neighbor. Under this circumstance, we can use the tight binding approach to study the waveguide mode in CROW’s. Using this approximation, we show two important properties of CROW’s [48]. First, the waveguide modes of CROW remain essentially the same as those of the high Q modes in a single resonator and have the same symmetry characteristics. This unique property can be utilized to construct reflectionless bends [48] and as well as CROW intersections without cross-talk [49]. Second, the dispersion relation of CROWs is greatly different from that of conventional dielectric waveguides. In a weakly coupled CROW, the optical waves are dramatically slowed down, a property which can be used to enhance the efficiency of nonlinear optical processes [48]. Take the second harmonic generation (SHG) process for example. In

photonic crystals, it has been shown that the second harmonic field can be enhanced at the band edge of the photonic crystals, where the group velocity tends to zero [58]-[61]. In the case of defect cavities, the enhancement of SHG efficiency is achieved as a result of the large optical field amplitude of the localized defect cavity modes [62]-[64]. Both the two properties, the low group velocity and large optical field amplitude, can be simultaneously achieved in CROW.

3.2 Tight Binding Analysis of CROW

3.2.1 Non-degenerate CROW Band

We first study the case where the isolated resonator supports only a single high Q mode. In the spirit of the tight-binding approximation, we take the eigenmode $\mathbf{E}_K(\mathbf{r}, t)$ of a coupled resonator waveguide as a linear combination of the high Q modes $\mathcal{E}_\Omega(\mathbf{r})$ of the individual resonators along a straight line parallel to \mathbf{e}_x axis (see Fig. 3.1). Denoting the coordinate of the center of the n th resonator as $x = nR$, we have

$$\mathbf{E}_K(\mathbf{r}, t) = A e^{i\omega_K t} \sum_n e^{-inKR} \mathbf{E}_\Omega(\mathbf{r} - nR\mathbf{e}_x). \quad (3.1)$$

It is straightforward to show that the waveguide mode $\mathbf{E}_K(\mathbf{r}, t)$ satisfies the Bloch theorem. Consequently, we can limit the Bloch vector K to the first Brillouin zone, i.e., $-\pi/R \leq K \leq \pi/R$.

$\mathbf{E}_K(\mathbf{r}, t)$ satisfies Maxwell equations, which lead to (in Gaussian units)

$$\nabla \times [\nabla \times \mathbf{E}_K] = \epsilon(\mathbf{r}) \frac{\omega_K^2}{c^2} \mathbf{E}_K, \quad (3.2)$$

where $\epsilon(\mathbf{r})$ is the dielectric constant of the system (of coupled resonators) and ω_K is the eigenfrequency of the waveguide mode. Similarly, $\mathcal{E}_\Omega(\mathbf{r})$ satisfies the same equation, but with $\epsilon(\mathbf{r})$ replaced by $\epsilon_0(\mathbf{r})$, the dielectric constant of the single resonator:

$$\nabla \times [\nabla \times \mathcal{E}_K] = \epsilon_0(\mathbf{r}) \frac{\Omega^2}{c^2} \mathcal{E}_K. \quad (3.3)$$

In the case of high Q modes, we can take $\mathcal{E}_\Omega(\mathbf{r})$ to be real and normalize it to unity according to $\int d\mathbf{r}\epsilon_0(\mathbf{r})\mathcal{E}_\Omega \cdot \mathcal{E}_\Omega = 1$.

After substituting Eq. (3.1) into Eq. (3.2), multiplying both sides from left by $\mathcal{E}_\Omega(\mathbf{r})$ and spatially integrating, we find the dispersion relation for the waveguide mode $\mathbf{E}_K(\mathbf{r}, t)$ to be

$$\omega_K^2 = \Omega^2 \frac{[1 + \sum_{n \neq 0} e^{inKR} \beta_n]}{[1 + \Delta\alpha + \sum_{n \neq 0} e^{-inKR} \alpha_n]}, \quad (3.4)$$

where α_n , β_n and $\Delta\alpha$ are defined as

$$\alpha^n = \int d^3\mathbf{r} \epsilon(\mathbf{r}) \mathcal{E}_\Omega(\mathbf{r}) \cdot \mathcal{E}_\Omega(\mathbf{r} - nR\mathbf{e}_z) \quad n \neq 0, \quad (3.5)$$

$$\beta^n = \int d^3\mathbf{r} \epsilon_0(\mathbf{r} - nR\mathbf{e}_z) \mathcal{E}_\Omega(\mathbf{r}) \cdot \mathcal{E}_\Omega(\mathbf{r} - nR\mathbf{e}_z) \quad n \neq 0, \quad (3.6)$$

$$\Delta\alpha = \int d^3\mathbf{r} [\epsilon(\mathbf{r}) - \epsilon_0(\mathbf{r})] \mathcal{E}_\Omega(\mathbf{r}) \cdot \mathcal{E}_\Omega(\mathbf{r}). \quad (3.7)$$

If the coupling between the resonators is sufficiently weak, we can keep only the nearest neighbor coupling, i.e.. $\alpha^n = 0$, $\beta^n = 0$ if $n \neq 1, -1$. From symmetry considerations, we also require $\alpha^1 = \alpha^{-1}$ and $\beta^1 = \beta^{-1}$. Finally we assume α^1 , β^1 and $\Delta\alpha$ to be small. Putting all these observations together, we simplify Eq. (3.4) to

$$\omega_K = \Omega \left\{ 1 - \frac{\Delta\alpha}{2} + \kappa \cos(KR) \right\}, \quad (3.8)$$

where we define the coupling factor κ as

$$\kappa = \beta^1 - \alpha^1 = \int d^3r [\epsilon_0(\mathbf{r} - R\mathbf{e}_z) - \epsilon(\mathbf{r} - R\mathbf{e}_z)] \mathcal{E}_\Omega(\mathbf{r}) \cdot \mathcal{E}_\Omega(\mathbf{r} - R\mathbf{e}_z). \quad (3.9)$$

This dispersion relation defines a photonic band formed by the coupling of the high Q modes in the individual resonators, which can be denoted as the CROW band. From Eq. (3.8), the group velocity is found to be

$$v_g(K) = \frac{d\omega_K}{dK} = -\Omega R \kappa \sin(KR), \quad (3.10)$$

which can be quite small for weakly coupled CROW. Notice that both the dispersion and the group velocity are only characterized by κ .

3.2.2 Degenerate CROW Band

If the single high Q optical resonator supports multiple modes, the l th eigenmode $\mathcal{E}_l(\mathbf{r})$ satisfies (in Gaussian units)

$$\nabla \times [\nabla \times \mathcal{E}_l(\mathbf{r})] = \epsilon_0(\mathbf{r}) \frac{\Omega_l^2}{c^2} \mathcal{E}_l(\mathbf{r}), \quad (3.11)$$

where Ω_l is the eigenfrequency of the l th mode, and $\epsilon_0(\mathbf{r})$ represents the dielectric constant of the single resonator. The eigenmodes $\mathcal{E}_l(\mathbf{r})$ are also orthonormal:

$$\int d\mathbf{r} \epsilon_0(\mathbf{r}) \mathcal{E}_l(\mathbf{r}) \cdot \mathcal{E}_m(\mathbf{r}) = \delta_{l,m}, \quad (3.12)$$

where as in the previous section we take the Q factors of the resonator modes to be very high and assume the mode function $\mathcal{E}_l(\mathbf{r})$ to be real.

As in the non-degenerate case, we take the waveguide mode $\mathbf{E}_K(\mathbf{r}, t)$ of the CROW as a linear combination of the high Q modes $\mathcal{E}_l(\mathbf{r})$ within the individual resonators along the \mathbf{e}_x axis, which gives us

$$\mathbf{E}_K(\mathbf{r}, t) = A e^{i\omega_K t} \sum_{n,l} e^{-inKR} b_l \mathcal{E}_l(\mathbf{r} - nR\mathbf{e}_x). \quad (3.13)$$

After substituting Eq. (3.13) into Eq. (3.2), multiplying both sides from left by $\mathcal{E}_m(\mathbf{r})$ and spatially integrating, we find the following eigenequation for the mode expansion coefficient b_l

$$\sum_l b_l \Omega_l^2 [\delta_{m,l} + \sum_{n \neq 0} e^{-inKR} \beta_{m,l}^n] = \omega_K^2 \sum_l b_l [\delta_{m,l} + \Delta\alpha_{m,l} + \sum_{n \neq 0} e^{-inKR} \alpha_{m,l}^n], \quad (3.14)$$

where $\alpha_{m,l}^n$, $\beta_{m,l}^n$ and $\Delta\alpha_{m,l}$ are defined as

$$\alpha_{m,l}^n = \int d\mathbf{r} \epsilon(\mathbf{r}) \mathcal{E}_m(\mathbf{r}) \cdot \mathcal{E}_l(\mathbf{r} - nR\mathbf{e}_x) \quad n \neq 0, \quad (3.15)$$

$$\beta_{m,l}^n = \int d\mathbf{r} \epsilon_0(\mathbf{r} - nR\mathbf{e}_x) \mathcal{E}_m(\mathbf{r}) \cdot \mathcal{E}_l(\mathbf{r} - nR\mathbf{e}_x) \quad n \neq 0, \quad (3.16)$$

$$\Delta\alpha_{m,l} = \int d\mathbf{r} [\epsilon(\mathbf{r}) - \epsilon_0(\mathbf{r})] \mathcal{E}_m(\mathbf{r}) \cdot \mathcal{E}_l(\mathbf{r}). \quad (3.17)$$

If the coupling between the resonators is sufficiently weak, we can keep only the nearest neighbor coupling, which means $\alpha_{m,l}^n = \beta_{m,l}^n = 0$ if $n \neq \pm 1$. From symmetry considerations, we also require $\alpha_{m,l}^1 = \alpha_{m,l}^{-1}$ and $\beta_{m,l}^1 = \beta_{m,l}^{-1}$. Putting these observations together, Eq. (3.14) becomes

$$\sum_l b_l \Omega_l^2 [\delta_{m,l} + 2\beta_{m,l}^1 \cos(KR)] = \omega_K^2 \sum_l b_l [\delta_{m,l} + \Delta\alpha_{m,l} + 2\alpha_{m,l}^1 \cos(KR)]. \quad (3.18)$$

Generally, if the single resonator has N degenerate or nearly degenerate high Q modes $\mathcal{E}_l(\mathbf{r})$, with $l = 1, \dots, N$, we need to diagonalize the $N \times N$ matrix of Eq. (3.18) to find the dispersion relations of the CROW. The result generally depends on all the parameters $\alpha_{m,l}^1, \beta_{m,l}^1, \Delta\alpha_{m,l}$, with $m, l = 1, \dots, N$.

However, if a single resonator possesses certain symmetries, the solution is usually much simpler. For example, the individual microdisks and defect cavities shown in Fig. 3.1 each possess a mirror reflection symmetry with respect to the $y = 0$ plane. Therefore, the single resonator modes can be classified according to the parity P of this mirror reflection symmetry, as defined in Eq. (2.33) to Eq. (2.38) of Sec. 2.2.2. The parity P of the eigenmode can take the value of ± 1 . The modes with $P = 1$ and $P = -1$ shall be called respectively the even modes and the odd modes.

It has been shown that the high Q modes in both the microdisk cavity and the single defect cavity are doubly degenerate and have opposite parity [50, 65]. Consequently, for the CROW's in Fig. 3.1, we can limit the mode expansion of Eq. (3.13) to the subspace spanned by these two degenerate modes $\mathcal{E}_l(\mathbf{r})$ with $l = \pm 1$, where the subscript l refers to the parity of the mode and can only take the value of ± 1 . The degeneracy of the two modes gives $\Omega_l = \Omega$ for $l = \pm 1$. The symmetry of the modes also leads to $\alpha_{m,l}^1, \beta_{m,l}^1, \Delta\alpha_{m,l} = 0$, if $m \neq l$, which is obvious from Eq. (3.15) to (3.17). To further simplify Eq. (3.18), we also assume the frequency difference between ω_K and Ω to be small. Finally, the dispersion relations for the coupled resonator modes

are found to be

$$\omega_K^l = \Omega \left\{ 1 - \frac{\Delta\alpha_{l,l}}{2} + \kappa_l \cos(KR) \right\}, \quad (3.19)$$

where l denotes the parity of the mode and the coupling coefficients κ_l are defined as

$$\kappa_l = \beta_{l,l}^1 - \alpha_{l,l}^1 = \int d\mathbf{r} [\epsilon_0(\mathbf{r} - R\mathbf{e}_x) - \epsilon(\mathbf{r} - R\mathbf{e}_x)] \mathcal{E}_l(\mathbf{r}) \cdot \mathcal{E}_l(\mathbf{r} - R\mathbf{e}_x). \quad (3.20)$$

For a given parity l , this dispersion relation defines a CROW band with the same parity as that of the single resonator mode. Therefore, they can also be denoted as the even band and the odd band according to their parity.

From Eq. (3.19), the group velocity is found to be

$$v_g^l(K) = \frac{d\omega_K^l}{dK} = -\Omega R \kappa_l \sin(KR), \quad (3.21)$$

which can be made small by reducing the coupling coefficient κ_l . It is also interesting to observe that the dispersion and the group velocity of the two CROW bands, given in Eq. (3.19) and Eq. (3.21), are exactly the same as the results of the non-degenerate analysis. This is directly due to the fact that the two degenerate single resonator modes have opposite parity and cannot couple to each other.

3.3 Coupled Defect Cavity Waveguide

For the numerical calculations in this chapter, we consider only 2D structures, which can give a good approximation of the original 3D problem if an appropriate effective refractive index is used [67]. Here we use an effective refractive index $n = 2.65$ for the dielectric medium to simulate a half-wavelength-thick slab waveguide with refractive index $n = 3.4$ [65]. A major advantage of this 2D approximation is that it speeds up the numerical simulations and renders them more memory efficient. We use the 2D FDTD algorithm as described in Sec. 2.1.1, and choose $\beta = 0$. Under this condition, the electromagnetic modes can be classified into TE modes and TM modes [11]. The TE modes consist of only E_x, E_y, H_z components, and TM modes

have only E_z, H_x, H_y components. In our FDTD analysis, we shall restrict ourselves to the TE modes, which can be achieved by using an initial field whose only non-zero component is the H_z component.

In this section, we use the 2D FDTD algorithm to analyze both the single defect cavity mode in a triangular lattice photonic crystal and the CROW band formed from such coupled defect cavities. Due to the mirror reflection symmetry, we can reduce the FDTD computational domain as that shown in Fig. 3.2. The 2D single defect cavity, formed by “plugging” an air hole from the 2D triangular lattice photonic crystal, is illustrated in Fig. (3.2a). The properties of this 2D triangular lattice photonic crystal are determined by the ratio of r/a , where r is the radius of the air hole and a is the inter-hole distance. In all the calculations of this section, we choose $a = 15$, $r/a = 0.3$ and use a/λ as the unit for frequency. Notice that here we use Mur absorbing boundary condition [66].

The 2D photonic crystal with $r/a = 0.3$ has a bandgap for TE modes in the frequency range of a/λ from 0.28 to 0.35 [65]. Within this TE bandgap, the single defect cavity can support two degenerate high Q modes. Classified according to the mirror reflection symmetry, the two modes possess opposite parities with respect to the lower y boundary in Fig. (3.2a). The mode with $P = 1$ is called the even defect mode and that with $P = -1$ is called the odd defect mode. These two modes are numerically calculated and the results are shown in Fig. 3.3. The field distribution in Fig. 3.3 is that of the H_z component. (In fact, all the figures of mode spatial profile in this chapter show the H_z component.) However, since the \vec{H} field transforms like a pseudo-vector under mirror reflection, the H_z field of the even defect mode actually is antisymmetric with respect to the lower y boundary, as in Fig. (3.3a). For the same reason, the H_z field of the odd defect mode is actually symmetric with respect to the lower y boundary. The frequency and the Q factor of the even mode are respectively 0.301 and 840, while the frequency and the Q factor of the odd mode are 0.310 and 780. The degeneracy of the two modes is broken due to the fact that the air holes in the numerical simulation are not ideally circular. It should be emphasized that this degeneracy splitting has no significant influence on the CROW

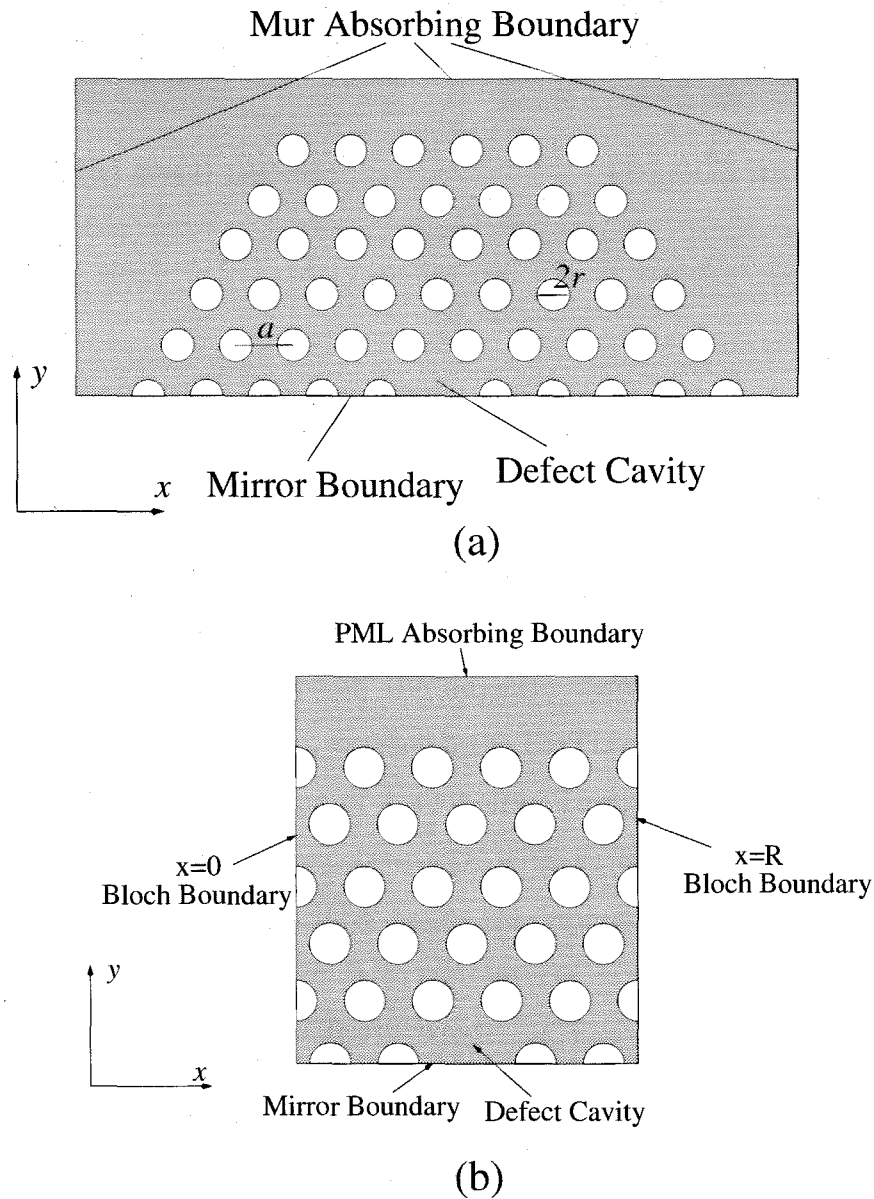


Figure 3.2: The FDTD computational domain. a) For a single defect cavity in a 2D photonic crystal. Mirror boundary condition is used at the bottom y boundary. For other three boundaries, the first order Mur absorbing boundary is used. b) For the CROW composed of coupled defect cavities with 4 air holes in between. The PML absorbing boundary condition and the mirror boundary condition are respectively used for the top and bottom y boundaries. At both of the x boundaries, $x = 0$ and $x = R$, the Bloch boundary condition is used.

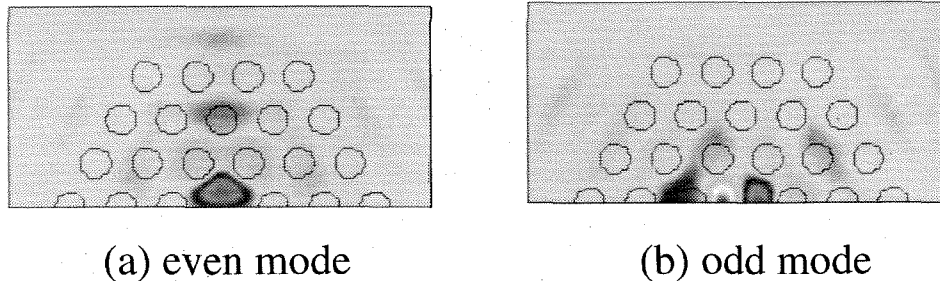


Figure 3.3: The single defect cavity modes. (a) The even defect mode. (b) The odd defect mode.

mode characteristics, since the two defect cavity modes still possess opposite parity and remains orthonormal to each other. As clear from the analysis leading to Eq. (3.19), each of the two CROW bands remains independent of each other and can still be characterized by a single coupling coefficient κ_l .

Using the 2D FDTD algorithm, three cases are studied for the defect cavity CROW, with the spacings between the adjacent defect cavities being 2, 3 and 4 holes respectively. In Fig. (3.2b), we sketch the FDTD computational domain for the CROW with inter-cavity spacing of 4 air holes. To map out the CROW band, we increase the Bloch vector K from 0 to π/R with an increment of $0.1\pi/R$. Due to symmetry considerations, the CROW bands are symmetric with respect to the $K = 0$ axis. Therefore, it is sufficient for us to concentrate on the half with $K \geq 0$.

First we consider the even CROW bands. In Fig. 3.4, we show two waveguide modes with inter-cavity spacing of 2 and 4 air holes and $K = 0.6\pi/R$. Comparing Fig. 3.4 with Fig. (3.3a), we clearly see that the waveguide modes in CROW closely resemble the single resonator mode. As expected from the tight binding analysis, this similarity is not restricted to this particular K value and holds through the whole CROW bands.

The dispersion curves for the even CROW bands are shown in Fig. 3.5. Using the least square method [68], we fit the calculated frequency versus K to Eq. (3.19) and obtain three coupling coefficients κ_1 . For the inter-cavity spacing of 2, 3 and 4 holes, κ_1 is respectively 5.6×10^{-3} , -1.4×10^{-3} and -2.9×10^{-4} . It is obvious from Fig. 3.5 that the coupling coefficient decreases with the inter-cavity distance and changes

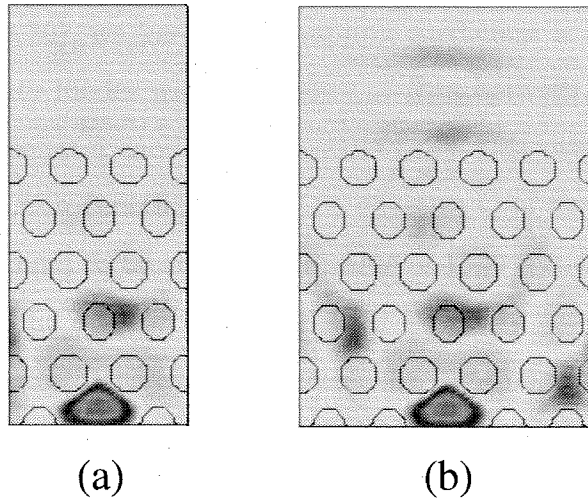


Figure 3.4: The even CROW modes with (a) 2 inter-cavity hole spacing and (b) 4 inter-cavity hole spacing. The Bloch vector K of both modes is $K = 0.6\pi/R$.

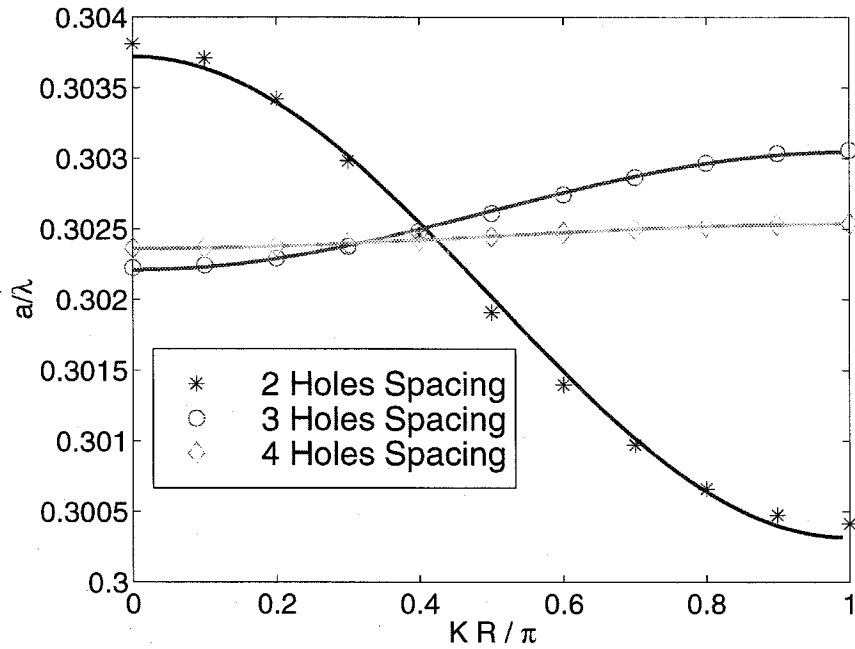


Figure 3.5: The dispersion of the even defect cavity CROW band. The symbols represent the results calculated from FDTD algorithm using different values of inter-cavity hole spacing. The solid lines are the least square fits of the numerical results using Eq. (3.19).

sign for the CROW band with 3 holes spacing. Such results can be understood as follows. From Eq. (3.20), we know the coupling coefficient is an overlap integral of two single defect cavity modes with a distance of R in between. Since the evanescent field of the single resonator mode decay oscillatorily, this overlap integral will also decrease oscillatorily as a function of R . The effective Q of the even CROW band is also calculated and found to be close to the value of 1500 through the CROW bands.

Next we analyze the odd CROW band, and as before, use three different inter-cavity spacings: 2 holes, 3 holes and 4 holes. In Fig. 3.6, we show the waveguide modes with $K = 0.6\pi/R$ and 3 air holes spacing. This CROW mode is qualitatively the same as the odd defect mode in Fig. 3.3b. As before, this similarity holds through the whole CROW bands.

The dispersion relations of the odd CROW modes are shown in Fig. 3.7. The numerical calculated mode frequency as a function of K is then fitted into Eq. (3.19), using least square method. From this fitting, the coupling coefficients κ_{-1} are found to be respectively 1.24×10^{-2} , 4.5×10^{-3} and 1.7×10^{-3} for spacings of 2, 3 and 4 holes. Again as expected, the coupling decreases as the inter-cavity spacing increases. It should also be noticed that the coupling coefficients of the odd CROW modes are larger than that of the even CROW modes with the same hole spacing. This is due to the fact that the even defect mode radiates stronger along the \mathbf{e}_y direction than the \mathbf{e}_x direction, while the opposite holds true for the odd defect mode, as can be seen from Fig. 3.3. Another consequence of this fact is that the effective Q of the odd CROW modes should be much larger than the corresponding even CROW modes, which is also confirmed by our numerical calculations and obvious by comparing Fig. 3.4 and Fig. 3.6. In fact, all the Q_{eff} of the odd CROW modes are found to be larger than 10^6 . Unfortunately, these results are only qualitatively correct, since a precise calculation of Q factor requires the time evolution of order of Q optical periods, which is impractical for Q factors large as those.

We also calculate the coupling coefficient using the overlap integral in Eq. (3.20). We choose the $\epsilon_0(\mathbf{r})$ to be a single defect cavity surrounded by 5 layers of air holes in the \mathbf{e}_y direction and 9 layers of air holes in the \mathbf{e}_x direction. Then we calculate

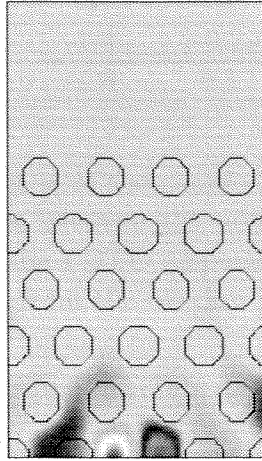


Figure 3.6: The odd defect cavity CROW mode with 3 inter-cavity hole spacing and Bloch vector $K = 0.6\pi/R$.

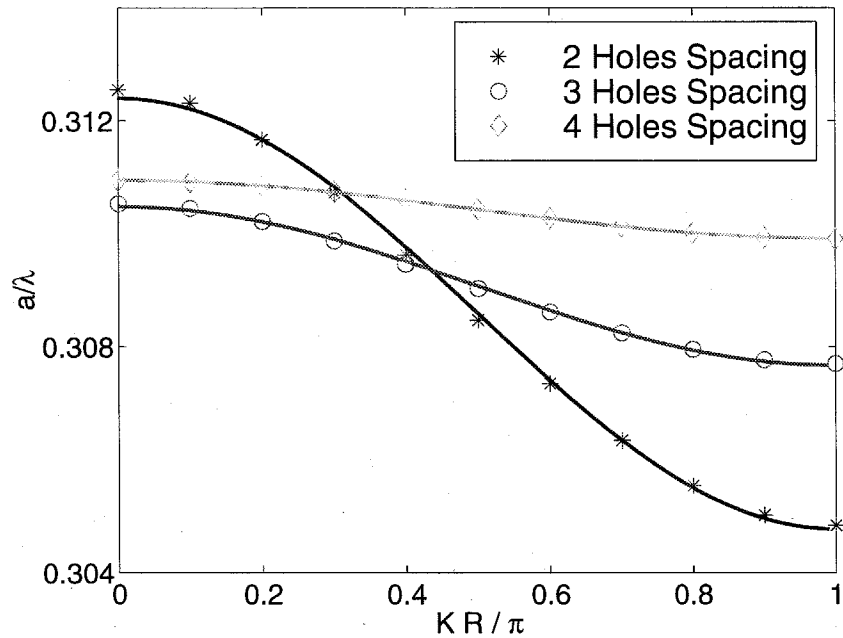


Figure 3.7: The dispersion of the odd defect cavity CROW band of coupled defect cavities. The symbols represent the results calculated from FDTD algorithm using different values of inter-cavity hole spacing. The solid lines are the least square fits of the numerical results using Eq. (3.19).

Coupling Coefficient	$\kappa_1 (\times 10^{-3})$			$\kappa_{-1} (\times 10^{-3})$		
	Hole Number	2	3	4	2	3
Fitting Results	5.6	-1.4	-0.29	12.4	4.5	1.7
Integral Results	5.4	-1.3	0.17	7.3	0.70	-0.90

Table 3.1: The coupling coefficient κ_l of the coupled defect cavities. The hole number refers to the numbers of air holes between the adjacent defect cavities. The fitting results are obtained from fitting the FDTD dispersion results using Eq. (3.19). The integral results are obtained from the overlap integral in Eq. (3.20).

the even and odd defect modes of such a single defect cavity and use them to obtain κ_1 and κ_{-1} . They are shown in Tab. 3.1 as theoretical results, together with the coupling coefficients from least square fitting. The results for relatively large κ_1 agrees well with those obtained from least square fitting. However, the deviation is larger for κ_{-1} . For both κ_1 and κ_{-1} , as the coupling between the individual resonators becomes weaker, the discrepancy between the tight binding results and the FDTD results is more pronounced. The difference between these two results, we believe, is likely caused by the fact that we assume the single resonator mode $\mathcal{E}_l(\mathbf{r})$ to be a real function (see Eq. (3.12)), which only holds when the loss of the cavity mode can be ignored. However, as the distance between the neighboring resonators becomes larger, the mode radiation loss, even though relatively small, will introduce a phase shift to the electromagnetic field that can no longer be ignored. This fact also helps to explain why the tight binding results for κ_1 agree better with the FDTD results than in the case of κ_{-1} . Previously, we have shown that the even defect cavity mode radiates primarily along the \mathbf{e}_y direction; therefore, the phase shift in the \mathbf{e}_x direction is relatively small. On the other hand, the odd cavity mode radiates more strongly along the \mathbf{e}_x direction, which inevitably introduces a larger phase shift. In this case, assuming the mode function to be real causes larger deviations between the tight binding results and the FDTD results.

3.4 Coupled Microdisk Waveguide

It is well known that a dielectric microdisk cavity can support high Q whispering gallery modes, which can be classified according to their polarization (TE or TM), their azimuthal mode number m and their radial mode number l [50, 51]. A TE whispering gallery mode $TE(m, l)$ has $2m$ nodes in the azimuthal direction and $l - 1$ nodes in the radial direction. It is also doubly degenerate and can be classified into an even or odd mode according to its mirror reflection symmetry. By coupling the microdisks together as in Fig. (3.1b), we can form the even and odd CROW bands from such whispering gallery modes. In this section, we study the CROW bands formed by the $TE(7, 1)$ whispering gallery modes.

In these calculations, we choose the radius r of the microdisk to be 30 FDTD cells and use three parameters for the inter-microdisk spacing R , which is normalized as $R/2r$ and takes the value of $R/2r = 1.1, 1.17$ and 1.23 . r/λ is used as the unit of frequency.

The $TE(7, 1)$ even mode and odd mode of a single microdisk are shown in Fig. 3.8. The frequency and Q factor of the even $TE(7, 1)$ mode are found to be 0.645 and 1500. For the odd $TE(7, 1)$ mode, the frequency and the Q factor are 0.639 and 1200 respectively. The degeneracy of the two $TE(7, 1)$ modes is broken, due to the deviation of the dielectric microdisk from an ideal circular shape in our 2D simulation. As in the case of photonic crystal defect cavities, such degeneracy splitting will not cause significant change on the dispersion and mode characteristics of the CROW band, since the even and odd CROW modes remain orthonormal to each other.

The even CROW bands are calculated for three microdisk spacing parameter $R/2r$. Shown in Fig. 3.9 is the mode profile of a waveguide mode with $R/2r = 1.1$ and $K = 0.5\pi/R$. It is qualitatively the same as that of the even $TE(7, 1)$ mode in Fig. (3.8a). This suggests that the tight binding approximation is still valid, even for the close distance between the microdisks.

The CROW loss can be characterized by its effective Q, as defined in Sec. 2.3.2. We find that the effective Q factors of the even CROW bands depend strongly on

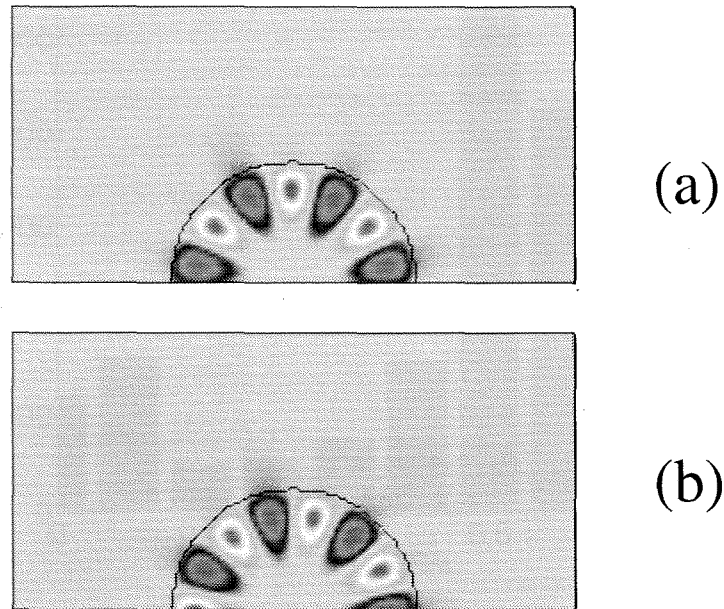


Figure 3.8: The $TE(7, 1)$ whispering gallery modes in a single microdisk cavity. The even mode is shown in a) and the odd mode is shown in (b).

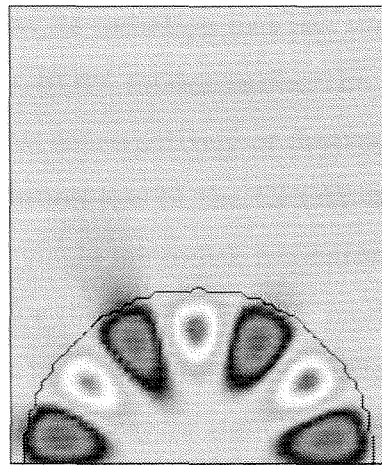


Figure 3.9: The even microdisk CROW mode formed by coupling the even $TE(7, 1)$ modes together. We use $R/2r = 1.1$ and $K = 0.5\pi/R$.

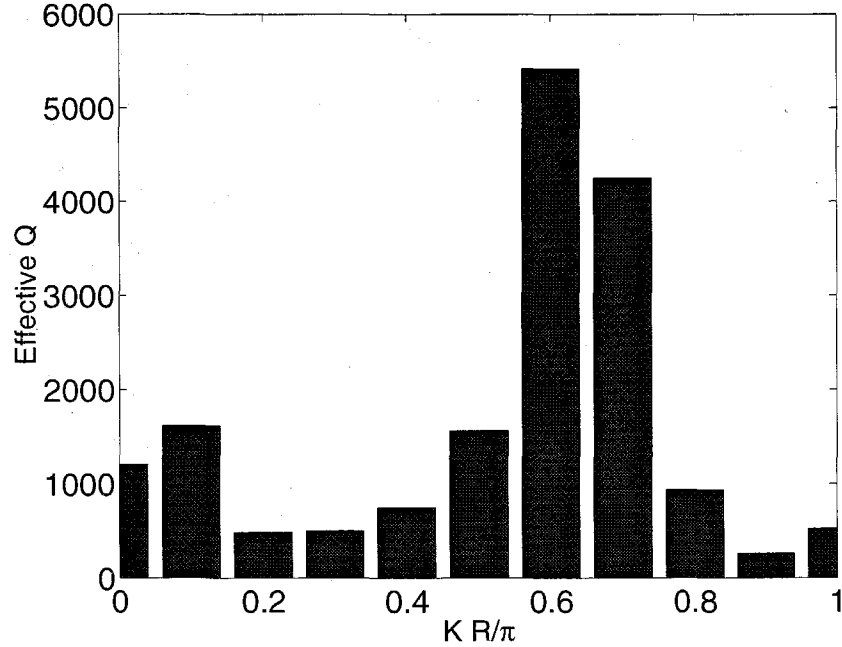


Figure 3.10: The effective Q factors of the even microdisk CROW modes with $R/2r = 1.17$.

the Bloch vector K . The $Q_{eff}(K)$ of the CROW band with $R/2r = 1.17$ is shown in Fig. 3.10 as a function of K . The fact that effective Q depends on K is not surprising and can be explained intuitively. The $TE(m, l)$ mode has an azimuthal dependence of $e^{im\phi}$ [50], which means that its radiation loss has similar angular dependence. As K , the Bloch vector of the CROW modes varies, the radiation field from different individual resonators interferes constructively or destructively with each other, which consequently causes the radiation loss of the CROW modes to increase or decrease and deviate from that of the single microdisk resonator.

The dispersion relations for the “even” CROW modes with three different values of $R/2r$ are shown in Fig. 3.11. The error bars in Fig. 3.11 refer to the frequency uncertainty due to the radiation decay of the CROW modes, which is estimated to be $\omega_K/2Q_{eff}$ as in section 2.1.1. Within the limit of these frequency errors, the numerical data agree well with the tight-binding results.

These frequency errors are also taken into account when we fit the numerical results into Eq. (3.19) using the least-square method. We no longer treat the numeri-

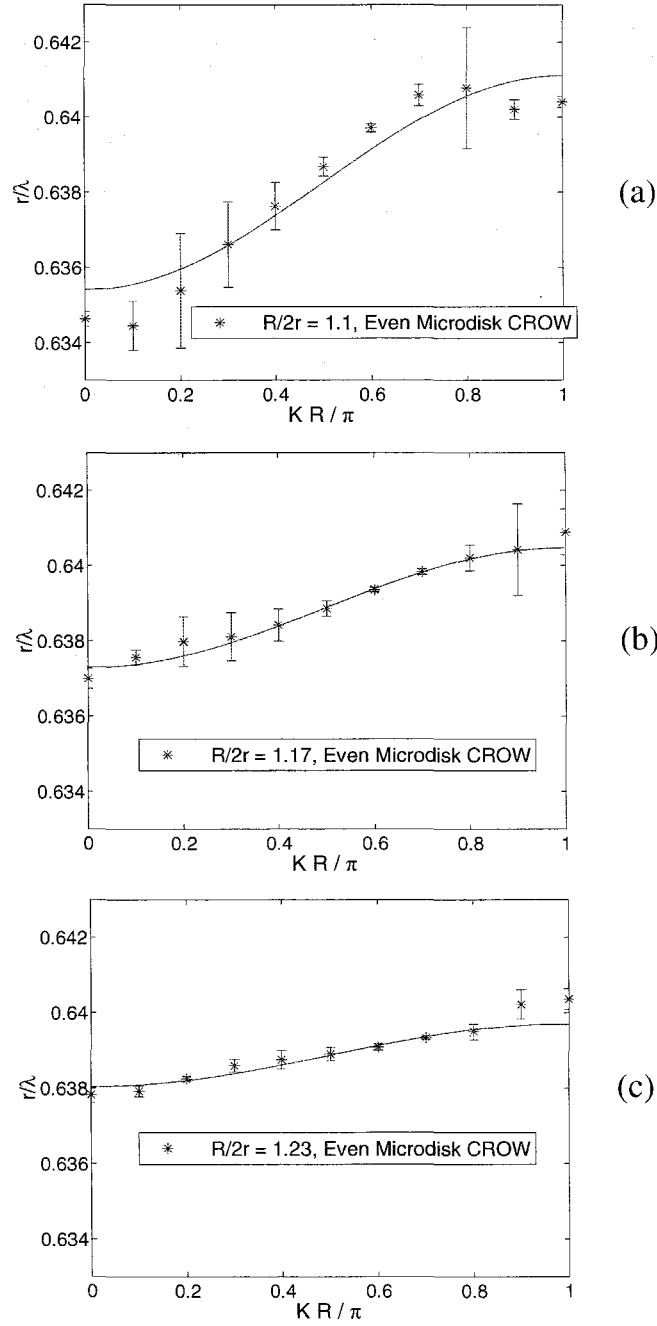


Figure 3.11: The dispersion of the even microdisk CROW band. The FDTD results are represented by asterisks. The error bars refer to the frequency error caused by the finite decay rate of the CROW modes and are estimated to be $\omega/2Q_{eff}$. The solid lines are the least square fits of the numerical results using Eq. 3.19. The dispersion diagrams for $R/2r = 1.1$, 1.17 and 1.23 are shown respectively in a), b) and c).

cally calculated mode frequencies equally and weigh them by the frequency deviation of $\omega_K/2Q_{eff}$. The coupling coefficient κ_1 obtained from this fitting are respectively -4.5×10^{-3} , -2.5×10^{-3} and -1.3×10^{-3} for different values of $R/2r = 1.1, 1.17$ and 1.23 . As expected, κ_1 decreases as the inter-microdisk spacing increases.

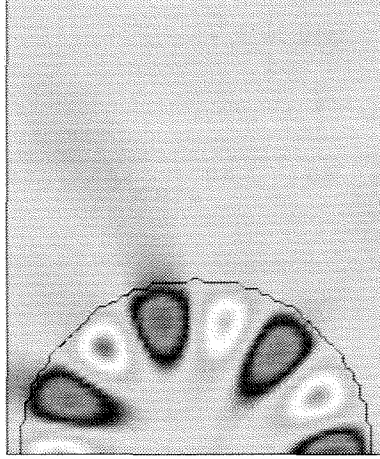


Figure 3.12: The odd microdisk CROW mode formed by coupling the odd $TE(7,1)$ modes together. We use $R/2r = 1.1$ and $K = 0.5\pi/R$.

The odd CROW bands are also calculated using the same set of values for $R/2r$. The CROW mode shown in Fig. 3.12 is calculated with $R/2r = 1.1$ and $K = 0.5\pi/R$, and as before, is similar to the odd $TE(7,1)$ mode shown in Fig. (3.8b). The odd CROW bands are shown in Fig. 3.13 for $R/2r = 1.1, 1.17$ and 1.23 . Again after considering the frequency deviation due to the decay of CROW modes, the numerical results agree well with the theoretical fits. The results for κ_{-1} obtained from the theoretical fitting are respectively 4.8×10^{-3} , 2.9×10^{-3} and 1.4×10^{-3} for $R/2r = 1.1, 1.17$ and 1.23 .

In the case of coupled microdisks, it is difficult to calculate the coupling coefficient using the overlap integral in Eq. (3.20). One reason is that the electromagnetic field outside the microdisk depends strongly on the boundary conditions of the computational domain, especially in the regions far from the microdisk. This is quite different from the case of the defect cavity in 2D photonic crystal, where the photonic crystal can effectively block much of the influence of the absorbing boundaries. Another

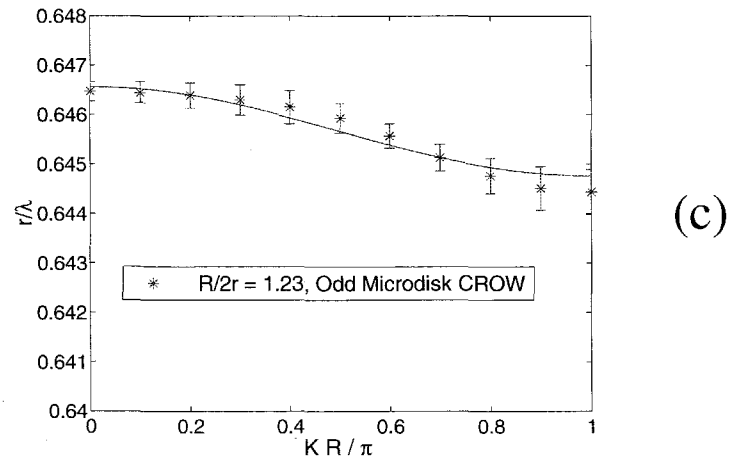
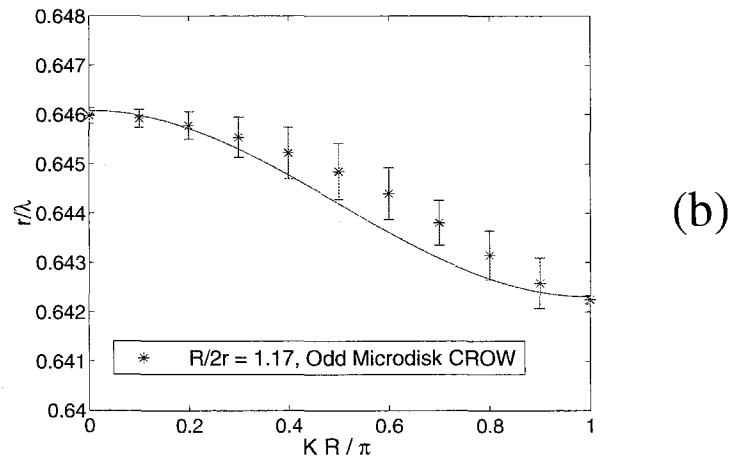
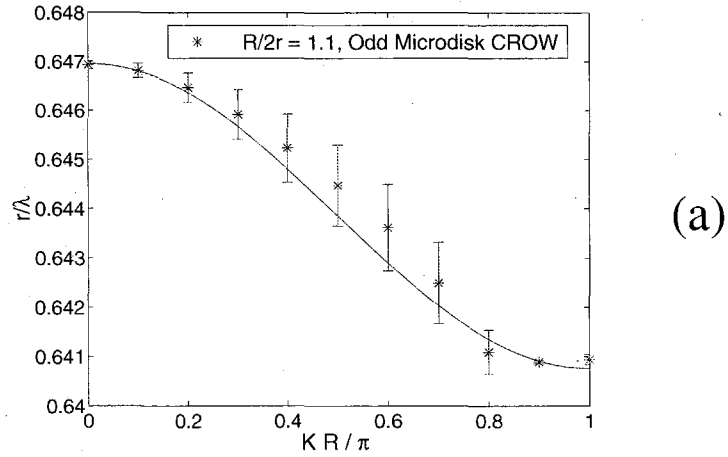


Figure 3.13: The dispersion of the odd microdisk CROW band. The FDTD results are represented by asterisks. The error bars refer to the frequency error caused by the finite decay rate of the CROW modes and are estimated to be $\omega/2Q_{eff}$. The solid lines are the least square fits using Eq. (3.19). The dispersion diagrams for $R/2r = 1.1, 1.17$ and 1.23 are shown respectively in (a), (b) and (c).

reason is that the electromagnetic field does not decay exponentially away from the microdisk, and therefore creates a normalization problem.

3.5 Second Harmonic Generation in CROW

An important application envisaged for CROW is nonlinear optics [48]. In CROW's, the propagating power flux P is proportional to the group velocity of the CROW band [48]

$$P \propto \frac{1}{8\pi R} v_{\omega,g} |A|^2, \quad (3.22)$$

where A is the amplitude of the CROW mode as defined in Eq. (3.1) and Eq. (3.13). Consequently, the small group velocity of the CROW band can result in a large optical field with only modest amount of power flux. Since the efficiency of nonlinear optical processes is proportional to some power of the electric field strength [69], it is possible to use the CROW band to greatly enhance the efficiency of these processes. Here we shall analyze in detail the second harmonic generation (SHG) process in CROW. This analysis, however, is not limited by the tight binding approximation of CROW and in principle can be applied to any dielectric structures with one-dimensional discrete translational symmetry.

Using the Bloch theorem, we can express the waveguide mode of a CROW in terms of a periodic Bloch wavefunction. Assume that the waveguide is periodic in x direction with a spatial period of R (see Fig. 3.1 for example); the waveguide mode $\mathbf{E}_K(\mathbf{r}, t)$ can be written as

$$\mathbf{E}_K(\mathbf{r}, t) = e^{(-\Gamma_\omega + i\omega)t} e^{-iK\mathbf{e}_x \cdot \mathbf{r}} \mathbf{u}_K(\mathbf{r}), \quad (3.23)$$

where the Bloch wavefunction $\mathbf{u}_K(\mathbf{r})$ is periodic: $\mathbf{u}_K(\mathbf{r} + R\mathbf{e}_x) = \mathbf{u}_K(\mathbf{r})$ and normalized within a unit cell:

$$\int_{u.c.} d\mathbf{r} \epsilon(\mathbf{r}) \mathbf{u}_K^*(\mathbf{r}) \cdot \mathbf{u}_K(\mathbf{r}) = 1. \quad (3.24)$$

The frequency and the decay rate of this mode are represented by ω and Γ_ω respec-

tively.

The waveguide mode $\mathbf{E}_K(\mathbf{r}, t)$ satisfies

$$\nabla \times [\nabla \times \mathbf{E}_K] + \frac{4\pi}{c^2} \sigma(\mathbf{r}) \frac{\partial \mathbf{E}_K}{\partial t} = -\frac{\epsilon(\mathbf{r})}{c^2} \frac{\partial^2 \mathbf{E}_K}{\partial t^2}, \quad (3.25)$$

where $\sigma(\mathbf{r})$ is introduced to account for the radiation loss of the waveguide mode. By substituting Eq. (3.23) into Eq. (3.25), we can separate the above wave equation into an imaginary part and a real part. From the imaginary part, we can derive an expression for the mode decay rate Γ_ω

$$\Gamma_\omega = 2\pi \int_{u.c.} d\mathbf{r} \sigma(\mathbf{r}) \mathbf{u}_K^*(\mathbf{r}) \cdot \mathbf{u}_K(\mathbf{r}). \quad (3.26)$$

From the real part, an eigenequation for the Bloch wavefunction \mathbf{u}_K is found:

$$\mathcal{H}_K \mathbf{u}_K(\mathbf{r}) = \frac{\omega^2}{c^2} \epsilon(\mathbf{r}) \mathbf{u}_K(\mathbf{r}), \quad (3.27)$$

$$\mathcal{H}_K \mathbf{u}_K = \nabla \times [\nabla \times \mathbf{u}_K] - iK \{ \nabla \times [\mathbf{e}_x \times \mathbf{u}_K] + \mathbf{e}_x \times [\nabla \times \mathbf{u}_K] \} - K^2 \mathbf{e}_x \times [\mathbf{e}_x \times \mathbf{u}_K]. \quad (3.28)$$

It can be easily shown that \mathcal{H}_K is a Hermitian operator. The derivative of the normalization relation Eq. (3.24) gives

$$\int_{u.c.} d\mathbf{r} \epsilon(\mathbf{r}) \left[\frac{d\mathbf{u}_K^*}{dK} \cdot \mathbf{u}_K + \mathbf{u}_K^* \cdot \frac{d\mathbf{u}_K}{dK} \right] = 0. \quad (3.29)$$

The derivative of ω^2/c^2 can also be found from Eq. (3.27) to be

$$\frac{d}{dK} \left(\frac{\omega^2}{c^2} \right) = \int_{u.c.} d\mathbf{r} \left[\frac{d\mathbf{u}_K^*}{dK} \cdot \mathcal{H}(K) \mathbf{u}_K + \mathbf{u}_K^* \cdot \mathcal{H}(K) \frac{d\mathbf{u}_K}{dK} + \mathbf{u}_K^* \cdot \frac{\mathcal{H}(K)}{dK} \mathbf{u}_K \right]. \quad (3.30)$$

Using Eq. (3.29) and the fact that $\mathcal{H}(K)$ is a Hermitian operator, this equation is reduced to

$$\frac{d}{dK} \left(\frac{\omega^2}{c^2} \right) = \int_V d\mathbf{r} \mathbf{u}_K^* \cdot \frac{\mathcal{H}(K)}{dK} \mathbf{u}_K. \quad (3.31)$$

In fact, this result is a direct generalization of the Hellman-Feynman theorem [70]. Substituting Eq. (3.28) into Eq. (3.31), we find an expression for the group velocity

$v_{\omega,g}$ at frequency ω :

$$v_{\omega,g} = \frac{c^2}{2\omega} \int_{u.c.} d\mathbf{r} \mathbf{u}_K^* \cdot \{-2K\mathbf{e}_x \times [\mathbf{e}_x \times \mathbf{u}_K] - i\mathbf{e}_x \times [\nabla \times \mathbf{u}_K] - i\nabla \times [\mathbf{e}_x \times \mathbf{u}_K]\} . \quad (3.32)$$

Having found the mode decay rate in Eq. (3.26) and the group velocity in Eq. (3.32), we can proceed to analyze the second harmonic generation in CROW. First let us limit our consideration to an electromagnetic field with three components: two fundamental frequency modes $\mathbf{E}_1(\mathbf{r}, t)$, $\mathbf{E}'_1(\mathbf{r}, t)$ and a second harmonic mode $\mathbf{E}_2(\mathbf{r}, t)$

$$\mathbf{E}_1(\mathbf{r}, t) = \frac{1}{2} \{ E_1 e^{i\omega t} e^{-iK_1(\omega)x} \mathbf{u}_{K_1(\omega)}(\mathbf{r}) + c.c. \} , \quad (3.33)$$

$$\mathbf{E}'_1(\mathbf{r}, t) = \frac{1}{2} \{ E_1 e^{i\omega t} e^{-iK_2(\omega)x} \mathbf{u}_{K_2(\omega)}(\mathbf{r}) + c.c. \} , \quad (3.34)$$

$$\mathbf{E}_2(\mathbf{r}, t) = \frac{1}{2} \{ E_2(x) e^{i2\omega t} e^{iK(2\omega)x} \mathbf{u}_{K(2\omega)}(\mathbf{r}) + c.c. \} . \quad (3.35)$$

For simplicity, we assume that the two fundamental frequency modes have the same amplitude E_1 throughout the region of second harmonic generation (undepleted pump) [69] and also require the amplitude of the second harmonic mode $E_2(x)$ to be a slowly varying function.

The second harmonic mode is generated according to the following equation [69]

$$\nabla \times [\nabla \times \mathbf{E}_2] + \frac{4\pi}{c^2} \sigma(\mathbf{r}) \frac{\partial \mathbf{E}_2}{\partial t} + \frac{\epsilon(\mathbf{r})}{c^2} \frac{\partial^2 \mathbf{E}_2}{\partial t^2} = -\frac{1}{c^2} \frac{\partial^2}{\partial t^2} \mathbf{P}_{NL}(\mathbf{r}, t) , \quad (3.36)$$

where the nonlinear polarization term $\mathbf{P}_{NL}(\mathbf{r}, t)$, the source of the second harmonic mode, is given by

$$\mathbf{P}_{NL}(\mathbf{r}, t) = \frac{1}{2} \{ E_1^2 e^{i2\omega t} e^{-i[K_1(\omega) - K_2(\omega)]x} \tilde{d}_{2\omega}(\mathbf{r}) \mathbf{u}_{K_1(\omega)}(\mathbf{r}) \mathbf{u}_{K_2(\omega)}(\mathbf{r}) + c.c. \} . \quad (3.37)$$

The tensor $\tilde{d}(\mathbf{r})$ represents the second order nonlinear coefficient of the dielectric medium. Multiplying Eq. (3.36) from the left by $\mathbf{u}_{K(2\omega)}^*(\mathbf{r})$ and integrating spatially within a unit cell, after a long but straightforward derivation, we obtain an equation

for $E_2(x)$

$$v_{2\omega,g} \frac{dE_2(x)}{dx} + \Gamma_{2\omega} E_2(x) = -i\omega E_1^2 \int_{u.c.} d\mathbf{r} e^{-i[K_1(\omega)+K_2(\omega)-K(2\omega)]x} \mathbf{u}_{K(2\omega)}^* \cdot \tilde{\mathbf{d}} \mathbf{u}_{K_1(\omega)} \mathbf{u}_{K_2(\omega)}, \quad (3.38)$$

where $v_{2\omega,g}$ is the group velocity of the second harmonic mode, and $\Gamma_{2\omega}$ is the corresponding decay rate. It is clear that $E_2(x)$ will always be small unless there exists an integer n such that the difference of the Bloch vectors $K_1(\omega) + K_2(\omega) - K(2\omega) + n2\pi/R$ becomes very small. In such case, the above equation is simplified as

$$v_{2\omega,g} \frac{dE_2(x)}{dx} + \Gamma_{2\omega} E_2(x) = -i\omega D_n E_1^2 e^{-i\Delta K_n x}, \quad (3.39)$$

$$\Delta K_n = K_1(\omega) + K_2(\omega) - K(2\omega) + n \frac{2\pi}{R}, \quad n = 0, \pm 1, \pm 2 \dots, \quad (3.40)$$

$$D_n = \int_{u.c.} d\mathbf{r} e^{in(2\pi/R)x} \mathbf{u}_{K(2\omega)}^*(\mathbf{r}) \cdot \tilde{\mathbf{d}}(\mathbf{r}) \mathbf{u}_{K_1(\omega)}(\mathbf{r}) \mathbf{u}_{K_2(\omega)}(\mathbf{r}). \quad (3.41)$$

According to this equation, a large E_2 is only possible under the condition of $\Delta K_n = 0$, which is the phase matching condition in CROW

$$K(2\omega) = K_1(\omega) + K_2(\omega) + n \frac{2\pi}{R}, \quad n = 0, \pm 1, \pm 2 \dots. \quad (3.42)$$

This phase matching condition in CROW is very similar to that in the bulk medium, except the appearance of the term $n2\pi/R$ [58]. This is to be expected, since only the Bloch vector, instead of the true photon wave vector, is conserved in CROW.

Eq. (3.39) are our master equations for the analysis of second harmonic generation. As an example, we shall use them to study two cases of phase-matched second harmonic generation configurations in CROW. Unlike the previous 2D cases, here we consider a three-dimensional (3D) geometry as sketched in Fig. 3.14. This CROW is still composed of defect cavities in 2D triangular lattice photonic crystal. But instead of being infinite in the third direction, it is confined in a slab waveguide along the z axis.

In the first case, we assume both the fundamental frequency modes propagate

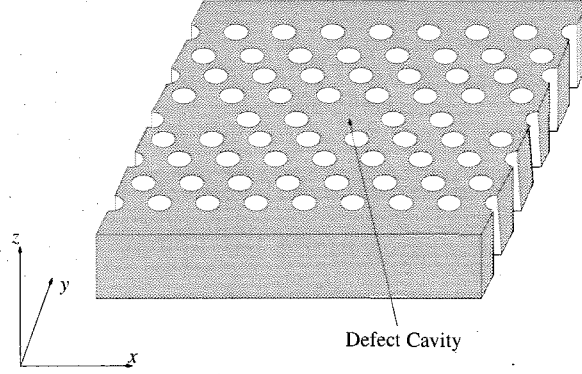


Figure 3.14: SHG in CROW. The fundamental frequency modes propagate from one defect cavity to another along the x axis. The second harmonic mode can either propagate in CROW along x axis or leak out of CROW along z axis.

along the positive x direction and satisfy $K_1(\omega) = K_2(\omega) = K(\omega)$, $K(2\omega) = 2K(\omega)$. The second harmonic photons also propagate along the x axis but can either be collected along the x direction, or collected after “leaking” out along the z direction. We call this case SHG configuration I.

Assuming the CROW begins at $x = 0$, we can require $E_2(0) = 0$. From Eq. (3.39), $E_2(x)$ is found to be

$$E_2(x) = -i \frac{\omega E_1^2 D_0}{\Gamma_{2\omega}} (1 - e^{-\Gamma_{2\omega} x / v_{2\omega, g}}). \quad (3.43)$$

From this relation, it is obvious that the SHG process falls into two distinctive limits, with $x \ll v_{2\omega, g} / \Gamma_{2\omega}$ (the unsaturated limit) and $x \gg v_{2\omega, g} / \Gamma_{2\omega}$ (the saturated limit) respectively. Defining a saturation length $L_s = v_{2\omega, g} / \Gamma_{2\omega}$, the amplitude of the second harmonic mode becomes

$$E_2(x) = -i \frac{\omega E_1^2 D_0}{v_{2\omega, g}} x, \quad x \ll L_s, \quad (3.44)$$

$$E_2(x) = -i \frac{\omega E_1^2 D_0}{\Gamma_{2\omega}}, \quad x \gg L_s. \quad (3.45)$$

In the unsaturated limit, we collect light along the x direction. In the saturated limit, however, we let the photons “leak” through and then collect them along the z

direction.

In the second case, the two fundamental frequency modes propagate along opposite x direction, $K_1(\omega) = -K_2(\omega)$ and $K(2\omega) = 0$ and the second harmonic photons are collected after “leaking” out along the z direction. We shall call this case SHG configuration II. Due to the undepleted pump approximation and symmetry considerations, we can require $E_2(x)$ to be a constant and obtain

$$E_2 = -i \frac{\omega E_1^2 D_0}{\Gamma_{2\omega}}. \quad (3.46)$$

Notice that this result is the same as that of the saturated SHG configuration I.

To calculate the efficiency of the second harmonic generation in CROW, we still need to relate the power flux to the amplitude of the waveguide mode. Recall that the electromagnetic energy density for a waveguide mode [see Eq. (3.33) to Eq. (3.35)] is $|E|^2 \epsilon(\mathbf{r}) \mathbf{u}_K^*(\mathbf{r}) \cdot \mathbf{u}_K(\mathbf{r}) / 8\pi$. After integration, the energy stored in a unit cell is found to be simply $|E|^2 / 8\pi$. Consequently, for the waveguide mode propagating along the x direction, the power flux P is given by

$$P = \frac{1}{8\pi} \frac{v_g}{R} |E|^2. \quad (3.47)$$

On the other hand, for the mode leaking through the z direction, the power flux is

$$P = \frac{1}{8\pi} N \Gamma |E|^2, \quad (3.48)$$

where N is the total number of the resonators in CROW. Finally, assuming the total length of CROW is L and combining Eq. (3.47) and Eq. (3.48) with Eq. (3.44), Eq. (3.45), and Eq. (3.46), we can obtain the second harmonic generation efficiency η_{SHG} . For the unsaturated limit of SHG configuration I, η_{SHG} is

$$\eta_{SHG} = \frac{P_{2\omega}}{P_\omega} = \frac{1}{v_{2\omega,g} v_{\omega,g}^2} \omega^2 |D_0|^2 8\pi R P_\omega L^2. \quad (3.49)$$

The η_{SHG} for both the saturated SHG configuration I and SHG configuration II

becomes

$$\eta_{SHG} = \frac{P_{2\omega}}{P_{\omega}} = \frac{1}{\Gamma_{2\omega} v_{\omega,g}^2} \omega^2 |D_0|^2 8\pi R P_{\omega} L . \quad (3.50)$$

In the above results for η_{SHG} , the factors $1/v_{\omega,g}^2$, $1/v_{2\omega,g}$, and $1/\Gamma_{2\omega}$ come directly from the relation between group velocity and field intensity, as shown in Eq. (3.22) at the beginning of this section. It suggests that SHG efficiency can be enhanced by slowing down the fundamental mode, the second harmonic mode or making the effective Q of the second harmonic mode very high. Another interesting point is that η_{SHG} is proportional to L^2 in Eq. (3.49) and is only proportional to L in Eq. (3.50). The reason is that if we collect second harmonic photons along the x axis, the phase matching condition guarantees that the photons generated at different resonators interfere coherently with each other. On the other hand, such phase matching cannot be obtained along the z direction.

Chapter 4

Scattering Theory Analysis of Waveguide-Resonator Coupling

4.1 Introduction

The coupling between high Q optical resonators is investigated in the previous chapter, with particular emphasis on the waveguiding induced by such resonator-resonator coupling. A related and equally interesting subject is the coupling between waveguides and resonators, which has received considerable attention in recent years [71]-[86]. For example, the resonant tunneling through the photonic crystal via the localized defect modes has been numerically analyzed [71, 72] and experimentally observed [73, 74]. Recently, a channel add-drop filter based on coupled waveguide-resonator systems in photonic crystal was proposed [75, 76, 77]. It was shown that for defect cavities satisfying certain symmetry and degeneracy conditions, optical signals can be completely transferred from one waveguide to another. Waveguide-resonator coupling has also been explored in many other geometries, such as coupled fiber-ring geometry [79], coupled fiber-sphere geometry [80]-[83], or coupled semiconductor slab waveguide-microring geometry [84, 85, 86]. It is intuitively clear that the presence of resonator should have profound impact on the reflection and transmission characteristics of the

waveguide. For a system composed of a waveguide and a resonator that supports traveling wave modes, it was recently demonstrated that the transmission characteristics depend critically on the balance between waveguide-resonator coupling and cavity loss, thus it was named “critical coupling” [87]. In Ref. [88], we use scattering theory to show that for the general system of coupled waveguide-resonator as in Fig. (4.1a), the reflection and transmission coefficients depend critically on the waveguide-resonator coupling, the symmetry and degeneracy of the resonant modes, cavity loss (gain), and the mode resonant frequency.

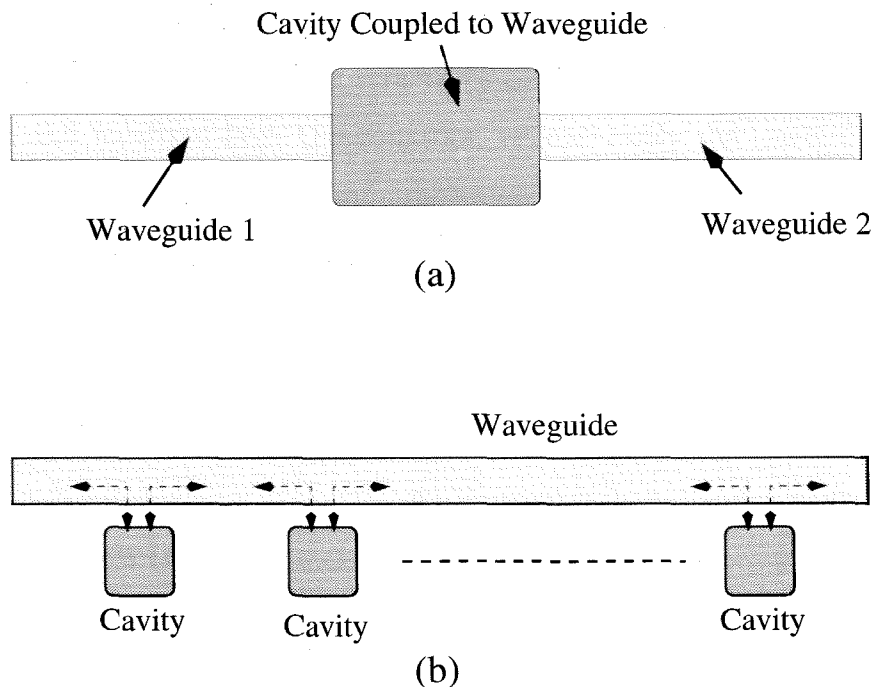


Figure 4.1: (a) The general geometry of a waveguide coupled with a cavity. (b) Example of a CROW with indirect coupling.

Similar to the CROW's, if we couple multiple resonators with a waveguide as shown in Fig. (4.1b), the composite structure also serves as a waveguide whose properties can be drastically different from those of the conventional waveguides. In this case, besides direct resonator-resonator coupling, the resonators can also be indirectly coupled together by the propagating modes within the waveguide. We call this new type of waveguides indirect CROW's since the cavities are indirectly coupled together. A unique feature of such indirect CROW's is that the tight-binding approximation

no longer applies, since any two resonators (not just the neighbor resonators) in Fig. (4.1b) are coupled through the waveguide modes.

It is possible to numerically calculate the transmission and reflection characteristics of waveguides coupled to other complicated dielectric structures [89, 90, 91]. In fact, the Huygens source as developed in Sec. 2.3.3 is ideal for this purpose, and has been applied for us to analyze the coupling between a slab waveguide and a photonic crystal waveguide [47, 25]. The benefit of the numerical approach is that it is capable of analyzing dielectric structures of complicated geometries. On the other hand, the numerical calculations are often time consuming and cannot be easily generalized. Since the dielectric structures considered here can be separated into waveguides and localized high Q resonators, we can apply the quantum scattering theory [92] to find the reflection and transmission coefficients for complicated coupled waveguide-resonator systems and dispersion properties of indirect CROW's. It is also worth mentioning that the coupled mode theory has also been used to treat the coupled waveguide-resonator systems, if the resonators support only one high Q mode [77, 93].

4.2 Scattering Theory Formalism

4.2.1 Scattering Matrix

Maxwell equations can be rewritten in the following form:

$$i \frac{\partial}{\partial t} \psi = \mathbf{H} \psi, \quad (4.1)$$

$$\psi = \begin{bmatrix} \vec{E} \\ \vec{H} \end{bmatrix}, \quad \mathbf{H} = \begin{bmatrix} 0 & (i/\epsilon) \nabla \times \\ (-i/\mu_0) \nabla \times & 0 \end{bmatrix}. \quad (4.2)$$

If we introduce the inner product as

$$\langle \psi_2 | \psi_1 \rangle = \frac{1}{2} \left[\int d^3r \epsilon(\vec{r}) \vec{E}_2^* \cdot \vec{E}_1 + \mu_0 \int d^3r \vec{H}_2^* \cdot \vec{H}_1 \right], \quad (4.3)$$

it is easy to verify that the Hamiltonian \mathbf{H} is a Hermitian operator. For the weakly coupled waveguide-resonator system as shown in Fig. (4.1a), the Hamiltonian \mathbf{H} can be separated into a 0th order approximation \mathbf{H}_0 where the waveguide modes and the localized high Q modes are independent, and a perturbation term \mathbf{V} that couples them together [76],

$$\mathbf{H} = \mathbf{H}_0 + \mathbf{V} , \quad (4.4)$$

$$\mathbf{H}_0 = \sum_{k_i} \omega_{k_i} |k_i\rangle \langle k_i| + \sum_n \Omega_n |n\rangle \langle n| , \quad (4.5)$$

$$\mathbf{V} = \sum_{m \neq n} V_{m,n} |m\rangle \langle n| + \sum_{n, k_i} (V_{n, k_i} |n\rangle \langle k_i| + V_{k_i, n} |k_i\rangle \langle n|) . \quad (4.6)$$

In this Hamiltonian we use $|n\rangle$ to represent the n th high Q optical mode with “bare” resonant frequency Ω_n , and $|k_i\rangle$ to represent the waveguide mode with wave vector k_i . Here we assume the waveguide supports only one propagating mode, since multimode waveguides are usually undesirable in applications. Both $|k_i\rangle$ and $|n\rangle$ are normalized to 1 according to Eq. (4.3). We also require $V_{m,n} = V_{n,m}^*$ and $V_{n, k_i} = V_{k_i, n}^*$, since the Hamiltonian is Hermitian. In Eq. (4.4) to (4.6), we ignore the direct coupling between the waveguide modes (i.e., $V_{k_i, k_j} = 0$), which will be justified later. An explicit form for the perturbation term $V_{j,i}$ can be obtained from Eq. (4.1) to Eq. (4.3)

$$V_{j,i} = \langle \psi_j | \mathbf{V} | \psi_i \rangle = \frac{\omega_i}{2} \int d^3r [\epsilon_0(\vec{r})]^2 \Delta \left[\frac{1}{\epsilon(\vec{r})} \right] \vec{E}_j^* \cdot \vec{E}_i , \quad (4.7)$$

where \vec{E}_i and \vec{E}_j are respectively the electric field associated with mode $|\psi_i\rangle$ and $|\psi_j\rangle$, ω_i is the resonant frequency of mode $|\psi_i\rangle$, $\epsilon_0(\vec{r})$ refers to the dielectric constant of the unperturbed Hamiltonian \mathbf{H}_0 , and $\Delta \left[\frac{1}{\epsilon(\vec{r})} \right]$ is the difference of $1/\epsilon(\vec{r})$ between the full Hamiltonian \mathbf{H} and its 0th order approximation \mathbf{H}_0 .

Following Ref. [76], we use the waveguide mode $|k_i\rangle$ as the incident optical wave, and assume that the total wavefunction is given by $|\psi_{total}\rangle$. These two states $|k_i\rangle$ and $|\psi_{total}\rangle$ are related via the scattering matrix \mathbf{T} [92]

$$|\psi_{total}\rangle = |k_i\rangle + \frac{1}{\omega_{k_i} - \mathbf{H}_0 + i\epsilon} \mathbf{V} |\psi_{total}\rangle = \mathbf{T} |k_i\rangle , \quad (4.8)$$

where ϵ is a positive infinitesimal number to enforce the outgoing boundary condition.

From Eq. (4.8), we can express the term $\mathbf{T}|k_i\rangle$ as the sum of an infinite series

$$\mathbf{T}|k_i\rangle = \left[\sum_{l=0}^{\infty} \left(\frac{1}{\omega_{k_i} - \mathbf{H}_0 + i\epsilon} \mathbf{V} \right)^l \right] |k_i\rangle. \quad (4.9)$$

We define the renormalized Green function \mathbf{G} as

$$G_{m,n}(\omega) = \langle m | \mathbf{G} | n \rangle = \langle m | \sum_{l=0}^{\infty} \frac{1}{\omega - \mathbf{H}_0 + i\epsilon} \left(\mathbf{V} \frac{1}{\omega - \mathbf{H}_0 + i\epsilon} \right)^l | n \rangle. \quad (4.10)$$

Multiplying Eq. (4.9) from left by $|k_j\rangle$ and using the above definition for \mathbf{G} , we find

$$T_{k_j, k_i} = \langle k_j | \mathbf{T} | k_i \rangle = \delta_{k_j, k_i} + \frac{1}{\omega_{k_i} - \omega_{k_j} + i\epsilon} \sum_{m,n} V_{k_j, m} G_{m, n}(\omega_{k_i}) V_{n, k_i}. \quad (4.11)$$

Similarly, we have

$$T_{n, k_i} = \langle n | \mathbf{T} | k_i \rangle = \sum_m G_{n, m}(\omega_{k_i}) V_{m, k_i}. \quad (4.12)$$

In Eq. (4.11), δ_{k_j, k_i} is 1 if $k_i = k_j$ and zero if otherwise. The physical meaning of Eq. (4.11) is clear: The state $|k_i\rangle$ can be scattered into the state $|k_j\rangle$ in two ways, the direct transition as represented by δ_{k_j, k_i} , and the indirect transition through the localized high Q modes $|n\rangle$ as represented by the second term at the right-hand side of Eq. (4.11).

Now we can justify the absence of the direct waveguide mode interaction term V_{k_j, k_i} in the Hamiltonian. If we include such term, the scattering matrix will have an additional non-resonant contribution $T_{k_j, k_i}^{nr} \sim V_{k_j, k_i} / (\omega_{k_i} - \omega_{k_j} + i\epsilon)$ [see Eq. (4.8)]. Comparing this quantity with the resonant scattering amplitude T_{k_j, k_i}^r due to the n th mode, we have

$$\frac{T_{k_j, k_i}^r}{T_{k_j, k_i}^{nr}} \sim \frac{V_{k_j, n} G_{n, n} V_{n, k_i}}{V_{k_j, k_i}}, \quad (4.13)$$

where we have used Eq. (4.11). If the waveguide length is L , V_{k_j, k_i} is of the order of ω_{k_i}/L according to Eq. (4.7), while $V_{k_j, n} V_{n, k_i}$ is of the order of $\omega_{k_i}^2/L$. In the next section, we show that the Green function is of the form $G_{n, n}(\omega_{k_i}) = 1/(\omega_{k_i} - \omega_n + i\Gamma_n)$, with ω_n being the ‘‘renormalized’’ resonant frequency and Γ_n the mode decay

rate. Substituting these observations into Eq. (4.13), it is obvious that the indirect scattering via the n th high Q modes has an enhancement factor of $\omega_{k_i}/(\omega_{k_i}-\omega_n+i\Gamma_n)$. Therefore, if we are interested in the resonant behavior, the direct waveguide mode interaction V_{k_j,k_i} can be safely ignored.

Once the scattering matrix \mathbf{T} is known, the optical reflection and transmission coefficients can be easily found as follows. If we respectively use $\psi_i(\vec{r})$, $\psi_r(\vec{r})$, and $\psi_t(\vec{r})$ to represent the incident wave, the reflected wave, and the transmitted wave, then they can be related to the \mathbf{T} matrix through the following simple relations:

$$\psi_i(\vec{r}) + \psi_r(\vec{r}) = \langle x \rightarrow -\infty | T | k_i \rangle = \sum_{k_j} \langle x \rightarrow -\infty | k_j \rangle T_{k_j,k_i}, \quad (4.14)$$

$$\psi_t(\vec{r}) = \langle x \rightarrow +\infty | T | k_i \rangle = \sum_{k_j} \langle x \rightarrow +\infty | k_j \rangle T_{k_j,k_i}. \quad (4.15)$$

From this expression, we can easily find the reflection coefficient and transmission coefficient. This method is essentially the same as that in Ref. [76].

4.2.2 Green Function

In Eq. (4.10), $G_{m,n}$ is expressed as the sum of an infinite series and is quite complicated. To simplify this expression, we notice that for any matrix \mathbf{B} , whose eigenvalues are all less than one, we have the following identity:

$$\frac{1}{\mathbf{I} - \mathbf{B}} = \sum_{l=0}^{\infty} \mathbf{B}^l, \quad (4.16)$$

where \mathbf{I} is an identity matrix. Applying this relation to Eq. (4.10), we find

$$\begin{aligned} \mathbf{G} &= \frac{1}{\omega - \mathbf{H}_0 + i\epsilon} \sum_{l=0}^{\infty} \left(\mathbf{V} \frac{1}{\omega - \mathbf{H}_0 + i\epsilon} \right)^l \\ &= \frac{1}{\omega - \mathbf{H}_0 + i\epsilon} \cdot \frac{1}{\mathbf{I} - \mathbf{V} \frac{1}{\omega - \mathbf{H}_0 + i\epsilon}} \\ &= \frac{1}{\omega - \mathbf{H} + i\epsilon}, \end{aligned} \quad (4.17)$$

Thus the term $G_{m,n}$, which represents the matrix element of the “renormalized” Green function \mathbf{G} , can be simplified as

$$G_{m,n}(\omega) = \langle m | \frac{1}{\omega - \mathbf{H} + i\epsilon} | n \rangle. \quad (4.18)$$

It is also of use to find an expression for $(G^{-1})_{m,n}$, the matrix elements of the inverse of the Green function. We start by rewriting Eq. (4.10) as

$$G_{m,n} = \langle m | \mathbf{G} | n \rangle = \frac{1}{\omega - \Omega_n + i\epsilon} \sum_{l=0}^{\infty} a_{m,n}^l = \frac{1}{\omega - \Omega_n + i\epsilon} \sum_{l=0}^{\infty} \langle m | \mathbf{A}_l | n \rangle, \quad (4.19)$$

where the index m and n refers to the optical modes within the high Q resonator, Ω_n is the frequency of mode $|n\rangle$ as given by the unperturbed Hamiltonian \mathbf{H}_0 , and the matrix \mathbf{A}_l is defined as

$$\mathbf{A}_l = \left(\frac{1}{\omega - \mathbf{H}_0 + i\epsilon} \mathbf{V} \right)^l. \quad (4.20)$$

We can express $a_{m,n}^l$ in terms of its lower order terms

$$\begin{aligned} a_{m,n}^l &= \sum_p \langle m | \frac{1}{\omega - \mathbf{H}_0 + i\epsilon} \mathbf{V} | p \rangle \langle p | \frac{1}{\omega - \mathbf{H}_0 + i\epsilon} \mathbf{V}^{l-1} | n \rangle \\ &+ \sum_{k,p} \langle m | \frac{1}{\omega - \mathbf{H}_0 + i\epsilon} \mathbf{V} | k \rangle \langle k | \frac{1}{\omega - \mathbf{H}_0 + i\epsilon} \mathbf{V} | p \rangle \langle p | \frac{1}{\omega - \mathbf{H}_0 + i\epsilon} \mathbf{V}^{l-2} | n \rangle \\ &= \frac{1}{\omega - \Omega_m + i\epsilon} \left(\sum_p V_{m,p} a_{p,n}^{l-1} + \sum_{k,p} V_{m,k} \frac{1}{\omega - \omega_k + i\epsilon} V_{k,p} a_{p,n}^{l-2} \right). \end{aligned} \quad (4.21)$$

To cast this relation in a simpler form, we define the following matrix operator within the subspace expanded by the high Q modes in the resonator:

$$\langle m | \mathbf{G}_0 | n \rangle = \frac{\delta_{m,n}}{\omega - \Omega_n + i\epsilon}, \quad (4.22)$$

$$\langle m | \mathbf{V}_d | n \rangle = V_{m,n}, \quad (4.23)$$

$$\langle m | \mathbf{V}_i | n \rangle = \sum_k V_{m,k} \frac{1}{\omega - \omega_k + i\epsilon} V_{k,n}, \quad (4.24)$$

where the term \mathbf{V}_d and \mathbf{V}_i respectively represent the direct and the indirect interac-

tion between the cavity modes. Using these notations, the matrix form of Eq. (4.19) is

$$\mathbf{G} = \left(\sum_{l=0}^{\infty} \mathbf{A}_l \right) \mathbf{G}_0, \quad (4.25)$$

while Eq. (4.21) can be written as

$$\mathbf{A}_l = \mathbf{G}_0 [\mathbf{V}_d \mathbf{A}_{l-1} + \mathbf{V}_i \mathbf{A}_{l-2}]. \quad (4.26)$$

Substituting Eq. (4.26) into Eq. (4.25), we find

$$\mathbf{G} = \mathbf{G}_0 + \mathbf{G}_0 (\mathbf{V}_d + \mathbf{V}_i) \mathbf{G}, \quad (4.27)$$

where we used $\mathbf{A}_0 = \mathbf{I}$ and $\mathbf{A}_1 = \mathbf{G}_0 \mathbf{V}_d$ [see the definition in Eq. (4.20)].

From Eq. (4.27), we find that the inverse of the renormalized Green function is

$$\mathbf{G}^{-1} = \mathbf{G}_0^{-1} - (\mathbf{V}_d + \mathbf{V}_i), \quad (4.28)$$

and its matrix elements are given by [76]

$$(G^{-1})_{m,n} = (\omega - \Omega_n) \delta_{m,n} - \Sigma_{m,n}, \quad (4.29)$$

$$\Sigma_{m,n}(\omega) = V_{m,n} + \sum_{k_i} V_{m,k_i} \frac{1}{\omega - \omega_{k_i} + i\epsilon} V_{k_i,n}. \quad (4.30)$$

Generally, the Σ matrix has some off-diagonal elements, so that finding the renormalized Green function \mathbf{G} can be quite involved. However, in some cases where the high Q resonators have definite symmetry properties, Σ is already diagonalized by the unperturbed states $|n\rangle$. Therefore, the renormalized green function can be simply written as

$$G_{m,n}(\omega) = \frac{1}{\omega - \omega_n + i\Gamma_n} \delta_{m,n}, \quad (4.31)$$

where ω_n is the renormalized frequency of mode $|n\rangle$, and Γ_n is the mode decay rate.

Besides enhanced scattering amplitude, the optical intensity in the resonators is also increased. From Eq. (4.12) and Eq. (4.31), we find the localized mode amplitude

to be

$$T_{n,k_i} = \langle n | \mathbf{T} | k_i \rangle = \frac{V_{n,k_i}}{\omega_{k_i} - \omega_n + i\Gamma_n}, \quad (4.32)$$

which means that the mode amplitude at the resonance is inversely proportional to the mode decay rate.

The mode decay rate Γ_n plays an important role in the problem of waveguide-resonator coupling and can be calculated as follows. Using Eq. (4.30), we find

$$\Sigma_{n,n}(\omega) = \sum_{k_i} |V_{n,k_i}|^2 \frac{1}{\omega - \omega_{k_i} + i\epsilon} = \frac{L}{2\pi} \int d\omega_{k_i} \frac{1}{v_g} (|V_{n,k_i}|^2 + |V_{n,-k_i}|^2) \frac{1}{\omega - \omega_{k_i} + i\epsilon}, \quad (4.33)$$

where k_i is the wave vector of the propagating mode, v_g represents the photon group velocity and is assumed to be positive for any $k_i > 0$. Evaluating the integral, we find

$$\text{Im}(\Sigma_{n,n}) = -\frac{L}{2v_g} (|V_{n,k_i}|^2 + |V_{n,-k_i}|^2). \quad (4.34)$$

If the mode representation $|n\rangle$ is chosen such that only the diagonal elements of Σ are nonzero, the total decay rate of the mode $|n\rangle$ is simply

$$\Gamma_n = \Gamma_n^0 + \frac{L}{2v_g} (|V_{n,k_i}|^2 + |V_{n,-k_i}|^2), \quad (4.35)$$

where Γ_n^0 is the intrinsic cavity decay rate. We should notice that in Eq. (4.35), the decay rate is actually independent of the waveguide length L , since $\langle k_i | k_i \rangle = 1$ and thus V_{n,k_i} is proportional to $1/\sqrt{L}$.

4.3 Optical Scattering in Two Generic Coupled Waveguide-Resonator Systems

We study two generic cases of coupled waveguide-resonator systems as illustrated in Fig. 4.2. The case in Fig. (4.2a) is denoted as the ‘‘side coupling’’ case, since the resonator is located at the side of an infinite waveguide. For the geometry shown in Fig. (4.2b), the two half-infinite waveguides are coupled together via resonant

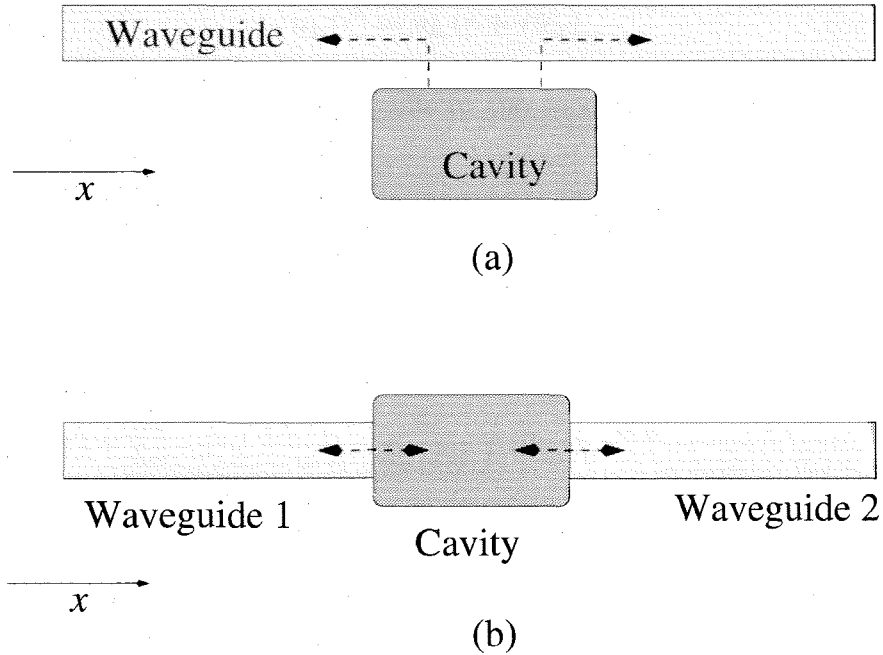


Figure 4.2: (a) The “side coupling” case, where a cavity is side coupled to a waveguide. (b) The “resonant coupling” case, where two waveguides are coupled by a high Q cavity.

tunneling through the center cavity. Consequently we call it the “resonant coupling” case. It should be noticed that the waveguides and resonators in Fig. 4.2 can be of any type. In particular, the analysis of this section applies to photonic crystal waveguides and defect cavities. Therefore, we assume that the waveguides possess a one-dimensional discrete translational symmetry. The waveguides with continuous translational symmetry, such as slab waveguides or optical fibers, can be regarded as special cases.

4.3.1 Side Coupling

First let us consider the “side coupling” case. We assume that the waveguide mode $|k_i\rangle$ has the following general form (using Bloch theorem)

$$\phi_{k_i}(\vec{r}) = \frac{1}{\sqrt{N}} u_{k_i}(\vec{r}) e^{ik_i x}, \quad (4.36)$$

$$u_{k_i}(\vec{r}) = u_{k_i}(\vec{r} + R\hat{e}_x), \quad (4.37)$$

where N is the total number of unit cells in the waveguide and $u_{k_i}(\vec{r})$ is normalized to 1 within a unit cell. R is the length of a unit cell.

We assume that the incoming wave is the waveguide mode $|k_i\rangle$. Therefore, the incident wave $\psi_i(\vec{r})$ in Eq. (4.14) is simply $\phi_{k_i}(\vec{r})$ and the transmitted wave $\psi_t(\vec{r})$ at $x \rightarrow +\infty$, as defined in Eq. (4.15), is

$$\psi_t(\vec{r}) = \phi_{k_i}(\vec{r}) + \sum_n \frac{V_{n,k_i}}{\omega_{k_i} - \omega_n + i\Gamma_n} \frac{L}{2\pi\sqrt{N}} \int dk_j u_{k_j} e^{ik_j x} \frac{V_{k_j,n}}{-v_g(k_j - k_i) - i\epsilon}, \quad (4.38)$$

where Eq. (4.11) and Eq. (4.31) are used, and we transform the the summation over k_j into an integral. Evaluating the integral, we find the transmitted wave to be

$$\psi_t(\vec{r}) = \frac{1}{\sqrt{N}} u_{k_i}(\vec{r}) e^{ik_i x} \left[1 - i \sum_n \frac{1}{\omega_{k_i} - \omega_n + i\Gamma_n} \frac{L|V_{k_i,n}|^2}{v_g} \right], \quad (4.39)$$

$$\Gamma_n = \Gamma_n^0 + \frac{L(|V_{k_i,n}|^2 + |V_{-k_i,n}|^2)}{2v_g}. \quad (4.40)$$

In a similar way, we use Eq. (4.14) and find the optical wave at $x \rightarrow -\infty$ to be

$$\psi_i(\vec{r}) + \psi_r(\vec{r}) = \phi_{k_i}(\vec{r}) + \sum_n \frac{V_{n,k_i}}{\omega_{k_i} - \omega_n + i\Gamma_n} \sum_{k_j} \phi_{k_j}(\vec{r}) \frac{V_{k_j,n}}{\omega_{k_i} - \omega_{k_j} - i\epsilon}. \quad (4.41)$$

We transform the summation over k_j into an integral and find $\psi_r(\vec{r})$ to be

$$\psi_r(\vec{r}) = -i \sum_n \frac{1}{\omega_{k_i} - \omega_n + i\Gamma_n} \frac{LV_{-k_i,n}V_{n,k_i}}{v_g} \left[\frac{1}{\sqrt{N}} u_{-k_i}(\vec{r}) e^{-ik_i x} \right]. \quad (4.42)$$

If we respectively use r and t to denote the amplitude reflection and transmission coefficient, the above results can be summarized as

$$r = -i \sum_n \frac{1}{\omega_{k_i} - \omega_n + i\Gamma_n} \frac{LV_{-k_i,n}V_{n,k_i}}{v_g}, \quad (4.43)$$

$$t = 1 - i \sum_n \frac{1}{\omega_{k_i} - \omega_n + i\Gamma_n} \frac{L|V_{k_i,n}|^2}{v_g}, \quad (4.44)$$

$$\Gamma_n = \Gamma_n^0 + \frac{L(|V_{k_i,n}|^2 - |V_{-k_i,n}|^2)}{2v_g}. \quad (4.45)$$

The side coupling geometry can actually be regarded as part of the photonic crystal add-drop filter considered in Ref. [75] to [77]. The above results are also similar to those in Ref. [76]. However, there is a subtle but important difference: we consider the possibility of gain or loss in the cavity, which is represented by Γ_n^0 in Eq. (4.45). More detailed discussion will be given in the next section.

4.3.2 Resonant Coupling

Next we study the case of “resonant coupling” as shown in Fig. (4.2b). Here for the notational convenience, we assume that both waveguides are along the x direction, even though the results do not depend on this assumption. In reality, the two waveguides can have an arbitrary bending angle, as long as the direct interaction between them can be ignored.

We assume that both waveguides consist of N unit cells, the normalized waveguide modes in waveguide 1 and waveguide 2 are uncoupled and can be expressed respectively as

$$\langle \vec{r} | k_i \rangle = \frac{1}{\sqrt{2N}} [u_{k_i}(\vec{r})e^{ik_i x} + u_{k_i}^*(\vec{r})e^{-ik_i x}], \quad \text{in waveguide 1}; \quad (4.46)$$

$$\langle \vec{r} | q_j \rangle = \frac{1}{\sqrt{2N}} [v_{q_j}(\vec{r})e^{iq_j x} + v_{q_j}^*(\vec{r})e^{-iq_j x}], \quad \text{in waveguide 2}; \quad (4.47)$$

We respectively use $|k_i\rangle$ and $|q_j\rangle$ to represent modes in waveguide 1 and waveguide 2, with k_i and q_j referring to their wave vectors. As before, both $u_{k_i}(\vec{r})$ and $v_{q_j}(\vec{r})$ are normalized within a unit cell. We assume that the unit cell length in waveguide 1 is R_1 , and the total waveguide length is $L_1 = NR_1$. For waveguide 2, the unit cell length is R_2 and the total length is $L_2 = NR_2$.

According to Eq. (4.14), the optical wave at $x \rightarrow -\infty$ (in waveguide 1) consists

of the incident wave $\psi_i(\vec{r})$ and the reflected wave $\psi_r(\vec{r})$:

$$\psi_i(\vec{r}) + \psi_r(\vec{r}) = \int dk_j \frac{L_1}{\pi\sqrt{2N}} [u_{k_j} e^{ik_j x} + c.c.] \left[\delta_{k_j, k_i} + \frac{1}{\omega_{k_i} - \omega_{k_j} + i\epsilon} \sum_n \frac{V_{k_j, n} V_{n, k_i}}{\omega_{k_i} - \omega_n + i\Gamma_n} \right]. \quad (4.48)$$

Evaluating the integral, we find

$$\psi_i(\vec{r}) = \frac{1}{\sqrt{2N}} u_{k_i}(\vec{r}) e^{ik_i x} \quad (4.49)$$

$$\psi_r(\vec{r}) = \frac{1}{\sqrt{2N}} u_{k_i}^*(\vec{r}) e^{-ik_i x} \left[1 - i \sum_n \frac{|V_{k_i, n}|^2}{\omega_{k_i} - \omega_n + i\Gamma_n} \frac{2L_1}{v_g^1} \right], \quad (4.50)$$

where v_g^1 is the photon group velocity in waveguide 1 and is assumed to be positive. The transmitted wave $\psi_t(\vec{r})$ at $x \rightarrow +\infty$ (in waveguide 2) can be found similarly from Eq. (4.15):

$$\begin{aligned} \psi_t(\vec{r}) &= \frac{L_2}{\pi\sqrt{2N}} \int dq_j (v_{q_j} e^{iq_j x} + c.c.) \frac{1}{\omega_{k_i} - \omega_{q_j} + i\epsilon} \sum_n \frac{V_{q_j, n} V_{n, k_i}}{\omega_{k_i} - \omega_n + i\Gamma_n} \\ &= \frac{1}{\sqrt{2N}} v_{q_j}(\vec{r}) e^{iq_j x} \left[-2i \sum_n \frac{1}{\omega_{k_i} - \omega_n + i\Gamma_n} \frac{L_2 V_{q_j, n} V_{n, k_i}}{v_g^2} \right], \end{aligned} \quad (4.51)$$

where q_j is the wave vector of the propagating mode in waveguide 2 and is determined by the condition $\omega_{q_j} = \omega_{k_i}$, v_g^2 is the corresponding photon group velocity and is assumed to be positive.

Since the photons in the high Q cavity can independently decay into both waveguide 1 and waveguide 2, the decay rate of the n th mode Γ_n will simply be the sum of the two processes. Collecting the results, for the ‘‘resonant coupling’’ case, we have

$$\psi_i(\vec{r}) = \frac{1}{\sqrt{2N}} u_{k_i}(\vec{r}) e^{ik_i x}, \quad (4.52)$$

$$\psi_r(\vec{r}) = \frac{1}{\sqrt{2N}} u_{k_i}^*(\vec{r}) e^{-ik_i x} \left[1 - i \sum_n \frac{1}{\omega_{k_i} - \omega_n + i\Gamma_n} \frac{2L_1 |V_{k_i, n}|^2}{v_g^1} \right], \quad (4.53)$$

$$\psi_t(\vec{r}) = \frac{1}{\sqrt{2N}} v_{q_j}(\vec{r}) e^{iq_j x} \left[-i \sum_n \frac{1}{\omega_{k_i} - \omega_n + i\Gamma_n} \frac{2L_2 V_{q_j, n} V_{n, k_i}}{v_g^2} \right], \quad (4.54)$$

$$\Gamma_n = \Gamma_n^0 + \frac{L_1 |V_{n,k_i}|^2}{v_g^1} + \frac{L_2 |V_{n,q_j}|^2}{v_g^2}. \quad (4.55)$$

The cavity mode decay rate Γ_n in Eq. (4.55) is different from Eq. (4.35), which is due to the fact that we assume the waveguide supports traveling wave in deriving Eq. (4.35), yet the waveguide modes we use in the “resonant coupling” case are essentially standing waves (see Eq. (4.47)). It is interesting to compare the above results, Eq. (4.52) to Eq. (4.54) with Eq. (4.43) and Eq. (4.44), and observe that the reflection and transmission in the “resonant” coupling cases correspond, respectively, to the transmission and reflection in the “side” coupling geometries.

The Bloch wavefunctions u_{k_i} or v_{q_j} in Eq. (4.46) and (4.47) are normalized to 1 within a unit cell. Thus the power flux P in the waveguide satisfies the following relation

$$P \propto |A|^2 \frac{v_g}{R}, \quad (4.56)$$

where R is the size of a unit cell, v_g is the photon group velocity, and A is the amplitude of the optical wave. As an example, $A = \exp(ik_i x) / \sqrt{2N}$ for the incident wave $\psi_i(\vec{r})$ in Eq. (4.52). From Eq. (4.52) to Eq. (4.54) and applying Eq. (4.56), we find the power reflection coefficient R and transmission coefficient T to be

$$R = \left| 1 - i \sum_n \frac{1}{\omega_{k_i} - \omega_n + i\Gamma_n} \frac{2L_1 |V_{k_i,n}|^2}{v_g^1} \right|^2, \quad (4.57)$$

$$T = \left| \sum_n \frac{1}{\omega_{k_i} - \omega_n + i\Gamma_n} \frac{2L_2 V_{q_j,n} V_{n,k_i}}{v_g^2} \right|^2 \frac{v_g^2 R_1}{v_g^1 R_2}. \quad (4.58)$$

4.4 Critical Coupling in Coupled Waveguide-Resonator Systems

4.4.1 Single Mode Side Coupling

The simplest case of “side coupling” is a single mode resonator coupled with a single mode waveguide, as shown in Fig. (4.3a). A specific example of this side coupling

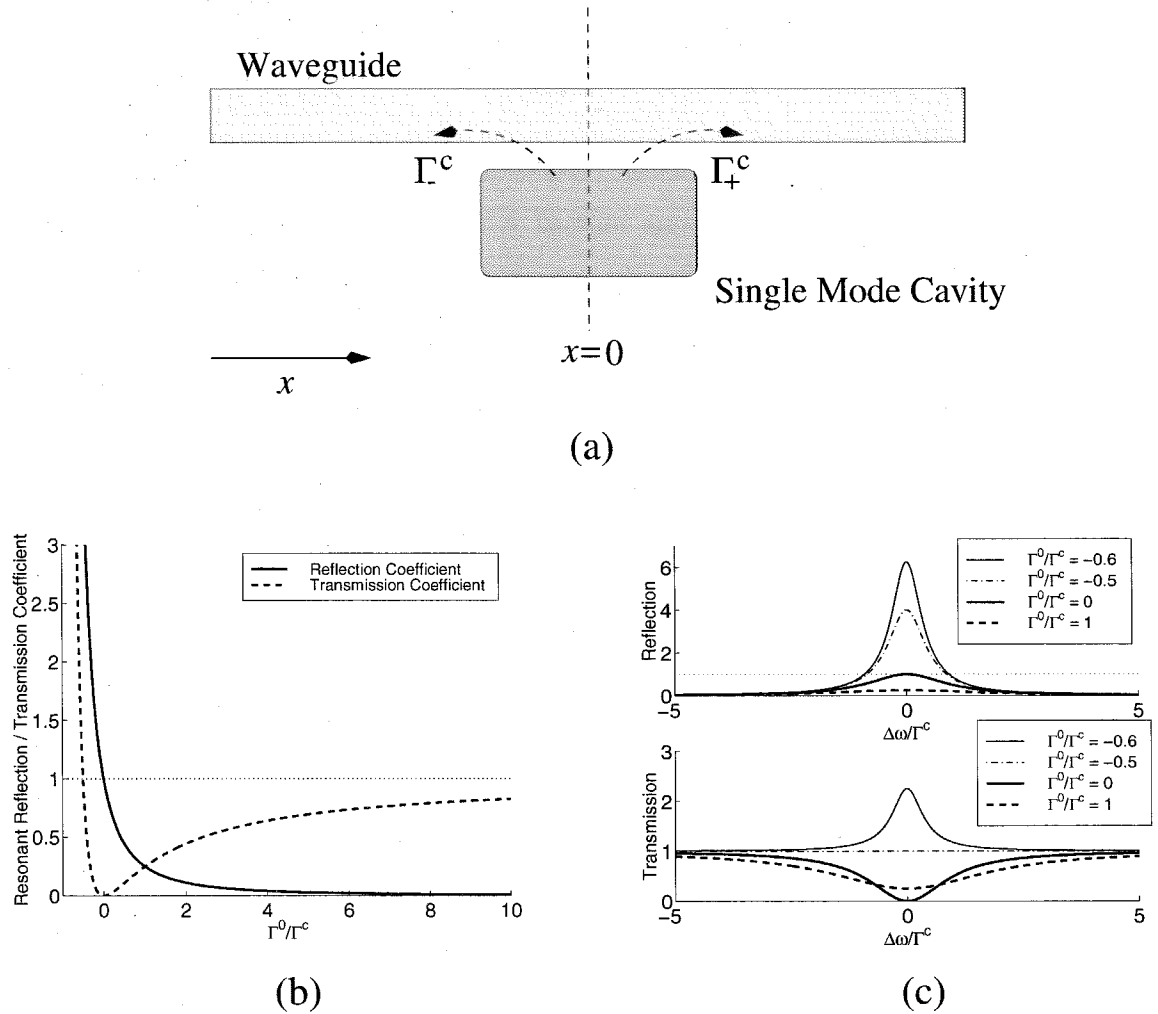


Figure 4.3: (a) A single mode resonator side coupled to a single mode waveguide. Γ_-^c and Γ_+^c are respectively the cavity decay rate in the $-\hat{x}$ and $+\hat{x}$ direction. For a resonator with mirror reflection symmetry with respect to $x = 0$ plane, $\Gamma_-^c = \Gamma_+^c$. (b) The resonant ($\Delta\omega = 0$) reflection and transmission coefficient for the geometry shown in (a). Γ^0 represents the intrinsic cavity loss (gain), and Γ^c is the decay rate of the cavity mode into the waveguide. (c) Reflection and transmission spectrum for four different values of Γ^0/Γ^c .

geometry has been investigated in Ref. [93], where the single mode resonator is the quarter wave shifted DFB resonator. In our case, the cavity decay rate Γ^c due to the presence of waveguide is given by Eq. (4.35)

$$\Gamma^c = \Gamma_-^c + \Gamma_+^c = \frac{L}{2v_g}|V_{n,-k}|^2 + \frac{L}{2v_g}|V_{n,k}|^2, \quad (4.59)$$

where we respectively use $\Gamma_-^c = \frac{L}{2v_g}|V_{n,-k}|^2$ and $\Gamma_+^c = \frac{L}{2v_g}|V_{n,k}|^2$ to represent the decay in the $-\hat{x}$ and $+\hat{x}$ direction. A further simplification is possible if the cavity possesses a mirror reflection symmetry with respect to the $x = 0$ plane, which gives $\Gamma_-^c = \Gamma_+^c = \Gamma_c/2$. From Eq. (4.43) and Eq. (4.44), we find the power reflection coefficient R and transmission coefficient T to be

$$R = |r|^2 = \frac{(\Gamma^c)^2}{\Delta\omega^2 + (\Gamma^0 + \Gamma^c)^2}, \quad (4.60)$$

$$T = |t|^2 = \frac{\Delta\omega^2 + (\Gamma^0)^2}{\Delta\omega^2 + (\Gamma^0 + \Gamma^c)^2}. \quad (4.61)$$

where Γ^0 represents the intrinsic loss (gain) of the resonator, $\Delta\omega$ is $\omega - \Omega$, with ω being the frequency of the incident light and Ω being the “renormalized” mode frequency.

In Fig. (4.3b), we show the resonant ($\Delta\omega = 0$) reflection coefficient R and transmission coefficient T as a function of Γ^0/Γ^c . Notice that at $\Gamma^0/\Gamma^c = 0$, the resonant transmission coefficient T becomes zero and the reflection coefficient R is 1. On the other hand, when the intrinsic cavity loss is much larger than the cavity-waveguide coupling, i.e. $\Gamma^0/\Gamma^c \gg 1$, the transmission coefficient approaches 1 and the reflection coefficient almost vanishes. If we introduce gain into the cavity and the lasing condition is approached, i.e. $\Gamma^0/\Gamma^c \rightarrow -1$, both R and T become very large. In Fig. (4.3c), we plot the transmission and reflection spectrum using different values of Γ^0/Γ^c , which clearly shows the critical dependence of the reflection and transmission characteristics on both $\Delta\omega$ and Γ^0/Γ^c . Of particular interest is the case of $\Gamma^0/\Gamma^c = -0.5$, which gives a flat transmission coefficient equal to 1. An obvious application of this critical dependence, similar to the phenomenon of “critical coupling” observed in Ref. [87], is the possibility of controlling optical transmission and reflection by tuning $\Delta\omega$, Γ^0 ,

or Γ^c .

In reality, it is difficult to fabricate a dielectric structure with perfect mirror reflection symmetry and there will always be some small difference between Γ_+^c and Γ_-^c . With symmetry broken, the reflection coefficient R and transmission coefficient T are

$$R = |r|^2 = \frac{4\Gamma_-^c\Gamma_+^c}{\Delta\omega^2 + (\Gamma^0 + \Gamma_-^c + \Gamma_+^c)^2}, \quad (4.62)$$

$$T = |t|^2 = \frac{\Delta\omega^2 - (\Gamma^0 + \Gamma_-^c - \Gamma_+^c)^2}{\Delta\omega^2 + (\Gamma^0 + \Gamma_-^c + \Gamma_+^c)^2}. \quad (4.63)$$

These results show that the general reflection and transmission features of the system is not significantly changed. We can still achieve zero resonant ($\Delta\omega = 0$) transmission by tuning $\Gamma^0 = \Gamma_+^c - \Gamma_-^c$. The unity transmission can also be achieved by choosing $\Gamma^0 = -\Gamma_-^c$.

4.4.2 Side Coupling with Doubly Degenerate Modes

Here we consider a side coupled cavity that supports two degenerate modes with frequency Ω . We rewrite Eq. (4.43) to Eq. (4.45) as

$$r = -i \sum_{n=1}^2 \frac{1}{\Delta\omega + i\Gamma_n} \frac{L}{v_g} V_{-k,n} V_{n,k}, \quad (4.64)$$

$$t = 1 - i \sum_{n=1}^2 \frac{1}{\Delta\omega + i\Gamma_n} \frac{L}{v_g} |V_{k,n}|^2, \quad (4.65)$$

$$\Gamma_n = \Gamma_n^0 + \Gamma_n^c = \Gamma_n^0 + \frac{L}{2v_g} |V_{k,n}|^2 + \frac{L}{2v_g} |V_{-k,n}|^2, \quad (4.66)$$

where we use the convention of $\Delta\omega = \omega - \Omega$, and Ω represents the “renormalized” frequency of the doubly degenerate modes.

For this doubly degenerate side coupling geometry, two simple cases are of special interest. The first example is when the resonator possesses a mirror reflection symmetry with respect to the $x = 0$ plane and the two degenerate modes have opposite parity, as shown in Fig. (4.4a). Assuming the even mode is $|e\rangle$ and the odd mode is

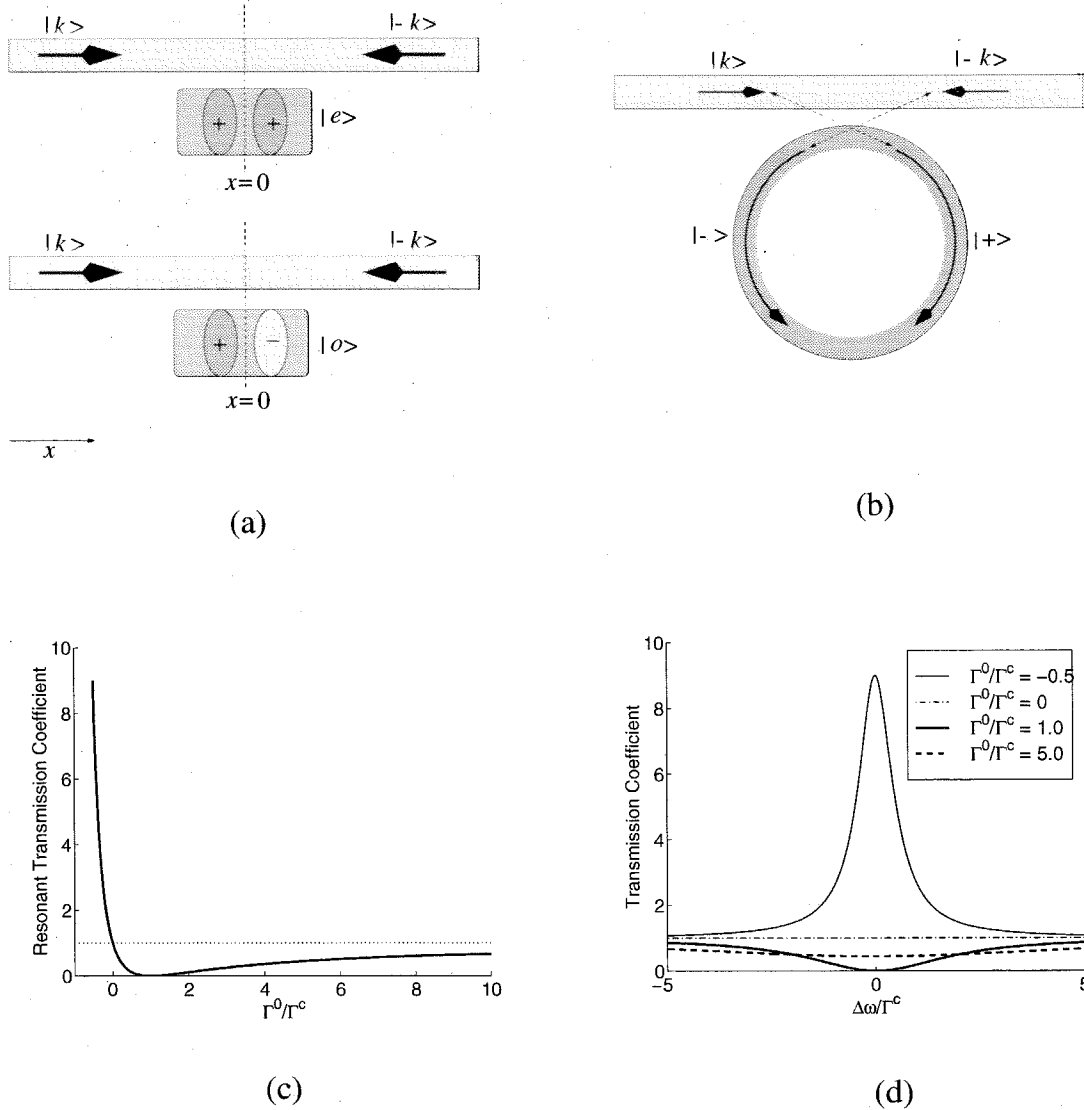


Figure 4.4: (a) A waveguide side coupled with a cavity supporting two degenerate modes. The cavity is symmetric with respect to $x = 0$ plane and support two degenerate modes with opposite parity under mirror reflection. The even mode is $|e\rangle$ and the odd mode is $|o\rangle$. (b) The side coupling geometry with two degenerate traveling wave modes in the cavity. The mode traveling in the clockwise direction is $|+\rangle$ and the mode traveling in the counterclockwise direction is $|-\rangle$. (c) The resonant transmission coefficient as a function of Γ^0/Γ^c . (d) The transmission spectrum for different values of Γ^0/Γ^c .

$|o\rangle$, Eq. (4.7) gives

$$V_{k,e} = V_{-k,e}, \quad V_{k,o} = -V_{-k,o}, \quad (4.67)$$

where $V_{k,e}$ represents the coupling between the incident wave $|k\rangle$ and the even cavity mode $|e\rangle$, and $V_{k,o}$ represents the coupling between $|k\rangle$ and the odd cavity mode $|o\rangle$. Following Ref. [75] and [76], we assume that the waveguide mode $|k\rangle$ couples equally strong with the even mode and the odd mode, i.e.

$$|V_{k,e}| = |V_{k,o}|. \quad (4.68)$$

Consequently, from Eq. (4.66) we obtain

$$R = 0, \quad T = \frac{\Delta\omega^2 + (\Gamma^0 - \Gamma^c)^2}{\Delta\omega^2 + (\Gamma^0 + \Gamma^c)^2}, \quad (4.69)$$

where Γ^c is $\Gamma^c = L|V_{k,e}|^2/v_g$. We notice the remarkable result that the reflection coefficient R remains 0 for all the frequencies. This is a direct consequence of the destructive interference between the reflected waves due to the two degenerate cavity modes, as was pointed out in Ref. [75]. In fact, this side coupling geometry can be regarded as half of the photonic crystal add-drop filters studied in Ref. [75] to [77]. Here the coupling to the second waveguide is represented by the ‘‘intrinsic’’ cavity decay rate Γ^0 .

In addition to the condition of frequency degeneracy and equal mode decay rate, Eq. (4.68) must also be strictly satisfied to eliminate reflection. It is very difficult to simultaneously realize these requirements during the fabrication processes. In practice, it is easier to fabricate semiconductor ring or disk resonators [84]-[86] and dielectric microspheres [80]-[83], which support two counter-propagating modes, as shown in Fig. (4.4b). In the following analysis, we show that the reflection and transmission coefficients of a waveguide coupled to this type of resonators are also described by Eq. (4.69).

If the waveguide mode and the traveling wave mode in the resonator are phase-matched, it is safe to assume that the waveguide mode can only induce the traveling

wave circulating in one direction, due to the requirement of phase matching. As shown in Fig. (4.4b), we denote the clockwise circulating mode as $|+\rangle$, and the counterclockwise mode as $|-\rangle$. Using these notations, the condition for phase-matched coupling is $V_{k,+} = 0$, and $V_{-k,+} = 0$. Furthermore, using Eq. (4.7) and the time reversal symmetry, we find $V_{k,+} = V_{-k,-}^*$. With these conditions, from Eq. (4.66) we have

$$R = |r|^2 = 0, \quad (4.70)$$

$$T = |t|^2 = \frac{\Delta\omega^2 + (\Gamma^0 - \Gamma^c)^2}{\Delta\omega^2 + (\Gamma^0 + \Gamma^c)^2}, \quad (4.71)$$

$$\Gamma^c = \frac{L}{2v_g} |V_{k,+}|^2 = \frac{L}{2v_g} |V_{-k,-}|^2. \quad (4.72)$$

The above results are the same as Eq. (4.69).

In Fig. (4.4c), the resonant ($\Delta\omega = 0$) transmission coefficient was plotted as a function of Γ^0/Γ^c . Notice that at $\Gamma^0/\Gamma^c = 1$, T is always equal to zero. This phenomenon is the principle behind many add-drop filters studied in the literature [75]-[77], [82]-[86], and was named “critical coupling” in Ref. [87]. The transmission spectrum is shown in Fig. (4.4d) for different values of Γ^0/Γ^c . We notice that when the lasing threshold is approached ($\Gamma^0/\Gamma^c \rightarrow -1$), the optical wave is amplified and the resonance width is narrowed.

The “critical coupling” condition depends on the assumption that the waveguide mode couples to only one of the traveling wave modes, and the two counter-propagating traveling wave modes are independent. Under these two conditions, the transmitted wave is the superposition of two scattering waves: One due to the direct scattering where the photons propagate through the waveguide without interacting with the resonator, the other due to the indirect scattering where the photons are first coupled into the resonator, travel in the resonator while experiencing loss or gain, and are coupled back into the waveguide. At $\Delta\omega = 0$ and $\Gamma^0 = \Gamma^c$, the scattering amplitudes due to the direct scattering and the indirect scattering have equal amplitude but opposite sign, and cancel each other exactly.

In reality, the surface of the dielectric microring, microdisk, or microspheres would

not be ideally smooth and can cause coupling between the counter-propagating cavity modes [94, 95]. It is also conceivable that a Bragg grating is deliberately introduced into the resonator to couple the two counter-propagating modes together. In either scenario, it becomes essential to take the coupling between the resonator modes into account. Using the expression in Eq. (4.30), we can introduce a phenomenological parameter κ such that the Σ matrix can be written as

$$\Sigma = \begin{bmatrix} \bar{\omega} - i(\Gamma^0 + \Gamma^c) & \kappa \\ \kappa & \bar{\omega} - i(\Gamma^0 + \Gamma^c) \end{bmatrix}, \quad (4.73)$$

where $\bar{\omega}$ representing the difference between the “bare” resonant frequency and the “renormalized” resonant frequency. In reaching Eq. (4.73), we also keep the assumption of $V_{k,+} = V_{-k,-}^*$, $V_{k,-} = V_{-k,+} = 0$, and Γ^c is given by Eq. (4.72). With the relative phase of the two counter-propagating modes carefully chosen, κ can be assumed to be a positive number. To diagonalize the Σ matrix, we use a new representation

$$|1\rangle = \frac{1}{\sqrt{2}}[|-\rangle + |+\rangle], \quad (4.74)$$

$$|2\rangle = \frac{1}{\sqrt{2}}[|-\rangle - |+\rangle]. \quad (4.75)$$

In this representation, the Σ matrix becomes

$$\Sigma = \begin{bmatrix} \bar{\omega} + \kappa - i(\Gamma^0 + \Gamma^c) & 0 \\ 0 & \bar{\omega} - \kappa - i(\Gamma^0 + \Gamma^c) \end{bmatrix}. \quad (4.76)$$

From this expression and Eq. (4.29), we can read out the resonant frequencies of mode $|1\rangle$ and $|2\rangle$:

$$\omega_1 = \Omega + \kappa, \quad (4.77)$$

$$\omega_2 = \Omega - \kappa, \quad (4.78)$$

which clearly shows the splitting of the modal degeneracy due to the coupling term

κ . The decay rates of the two modes remain the same:

$$\Gamma_1 = \Gamma_2 = \Gamma^0 + \Gamma^c . \quad (4.79)$$

From the definitions in Eq. (4.74) and Eq. (4.75), we also find

$$V_{k,1} = \frac{1}{\sqrt{2}}V_{k,+} , \quad V_{-k,1} = \frac{1}{\sqrt{2}}V_{-k,-} , \quad (4.80)$$

$$V_{k,2} = -\frac{1}{\sqrt{2}}V_{k,+} , \quad V_{-k,2} = \frac{1}{\sqrt{2}}V_{-k,-} . \quad (4.81)$$

Combining Eq. (4.77) to Eq. (4.81) and substituting them into Eq. (4.43), we find

$$R = |r|^2 = \frac{4(\Gamma^c)^2\kappa^2}{\left[(\Delta\omega)^2 - \kappa^2 - (\Gamma^0 + \Gamma^c)^2\right]^2 + 4(\Delta\omega)^2(\Gamma^0 + \Gamma^c)^2} , \quad (4.82)$$

where $\Delta\omega = \omega - \Omega$, and Ω is the resonant frequency of the uncoupled traveling wave modes. Similarly from Eq. (4.44), we find

$$T = |t|^2 = \frac{\left[(\Delta\omega)^2 - \kappa^2 - (\Gamma^0)^2 + (\Gamma^c)^2\right]^2 + 4(\Delta\omega)^2(\Gamma^0)^2}{\left[(\Delta\omega)^2 - \kappa^2 - (\Gamma^0 + \Gamma^c)^2\right]^2 + 4(\Delta\omega)^2(\Gamma^0 + \Gamma^c)^2} . \quad (4.83)$$

Inspecting Eq. (4.82) and Eq. (4.83), we observe that the reflection/transmission characteristics of this particular coupled waveguide-resonator system depend critically on κ , Γ^0 , and Γ^c . A special case of particular interest is shown in Fig. 4.5, under the condition of $\Gamma^0 = 0$ and $\kappa = \Gamma^c$. Different from the previous case with doubly mode degeneracy, the reflection coefficient in Fig. 4.5 is not zero around the resonance. In fact, the photons are completely reflected at $\omega = \Omega$. Also notice that the reflection/transmission spectrum is much flatter than the typical Lorentzian lineshape as shown in Fig. (4.4d).

In Fig. 4.6, we show how the resonant reflection/transmission coefficients change as a function κ/Γ^c . At $\kappa = 0$, since the two traveling modes are decoupled, the reflection coefficient is zero. At $\kappa = \Gamma^c$, the reflection coefficient is 1 and the transmission

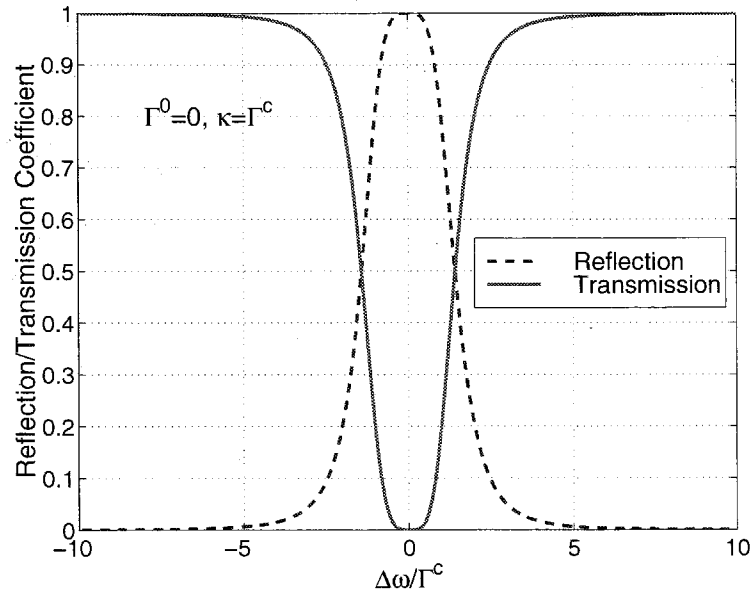


Figure 4.5: Reflection/Transmission spectrum of a waveguide coupled to a resonator that supports two counter-propagating traveling modes, as described in Eq. (4.82) and (4.83). The coupling between the two traveling modes is given by κ .

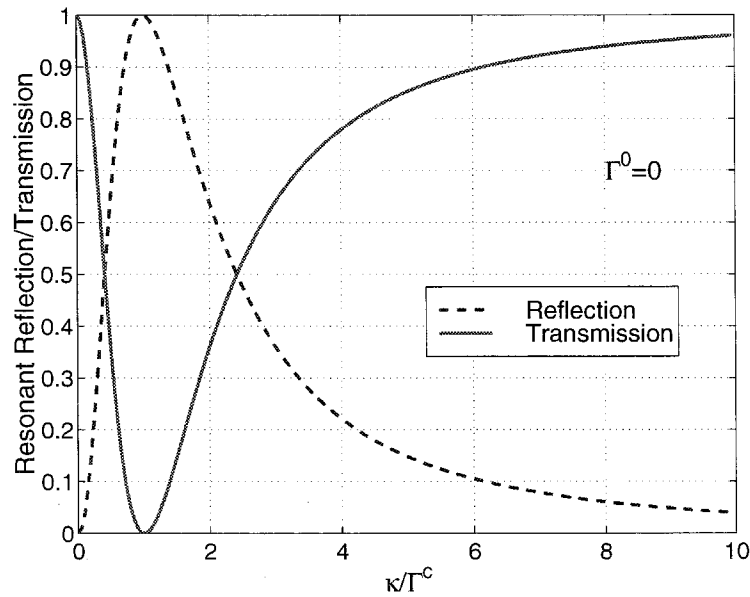


Figure 4.6: Resonant reflection/transmission coefficient of a waveguide coupled to a resonator with two coupled, lossless ($\Gamma^0 = 0$), counter-propagating traveling modes.

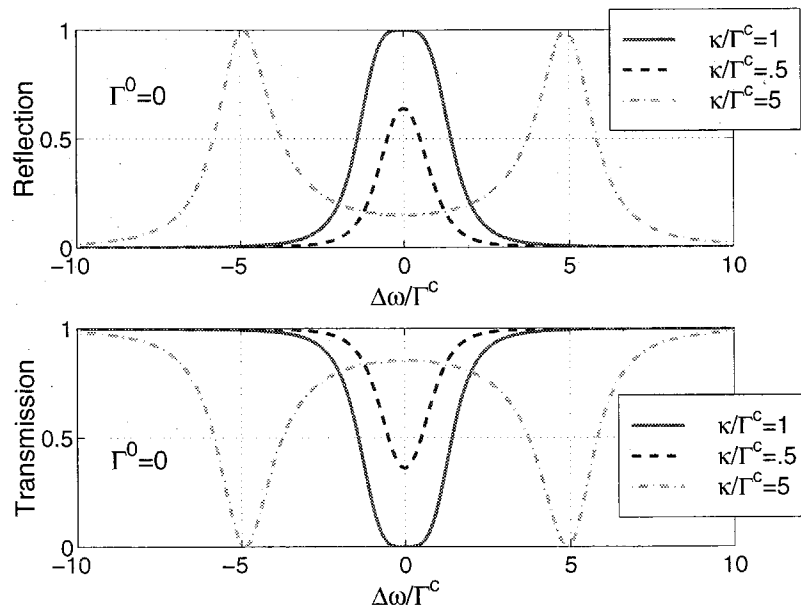


Figure 4.7: Reflection/Transmission spectrum of a waveguide coupled to a resonator with two coupled traveling wave modes, using different values of κ/Γ^c .

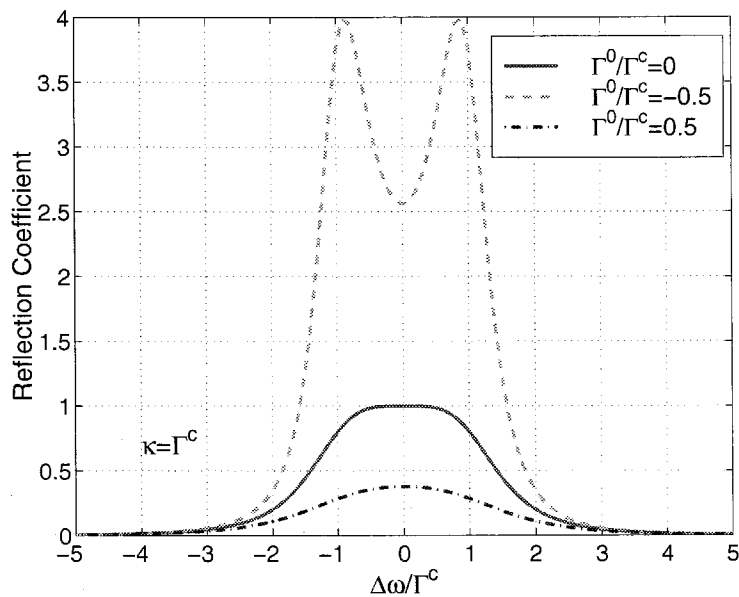


Figure 4.8: Reflection spectrum of a waveguide coupled to a resonator with two coupled traveling wave modes. In this case, we use different values of Γ^0/Γ^c but keep $\kappa = \Gamma^c$.

coefficient is zero, which is also consistent with Fig. 4.5. To gain more intuition into this result, let us consider photons propagating along $+\hat{x}$ direction in the waveguide shown in Fig. (4.4b). The photons are first coupled into the ring resonator in the form of clockwise traveling wave. As the photons propagate within the resonator, some of them are coupled into the counter-clockwise modes and can be counted as loss with respect to the clockwise traveling photons. The counter-clockwise photons are coupled back into the waveguide and propagate along $-\hat{x}$ direction. In the doubly degenerate case, at the “critical coupling” point, the waveguide-resonator coupling and resonator loss exactly balance against each other and cancel the transmitted wave. With the presence of coupling term κ and $\Gamma^0 = 0$, the coupling between the traveling wave modes takes a role similar to that of the resonator “loss” in the doubly degenerate case, and “critical coupling” point is defined by $\Gamma^c = \kappa$.

In Fig. 4.7, we change the value of κ/Γ^c and plot the reflection/transmission spectrum of the coupled system. As expected, in the “under-coupled” case ($\kappa < \Gamma^c$), the values of the reflection coefficient are less than the corresponding “critically-coupled” results ($\kappa = \Gamma^c$). When the two counter-propagating modes are “over-coupled” ($\kappa > \Gamma^c$), the reflection spectrum and the transmission spectrum clearly show two resonances, with one centered at $\omega = \Omega - \kappa$ and the other centered at $\omega = \Omega + \kappa$. In Fig. 4.8, we introduce loss/gain into the resonator and show the reflection spectrum. If the resonator is lossy ($\Gamma^0 > 0$), the reflection coefficients are smaller than those in the lossless case. With the presence of cavity gain, the reflection spectrum clearly shows double peaks, whose peak frequencies correspond to $\Omega - \kappa$ and $\Omega + \kappa$ respectively.

4.4.3 Single Mode Resonant Coupling

For the case of resonant coupling, we limit ourselves to the simplest case, which is composed of two waveguides coupled via a single mode high Q resonator, as shown in Fig. 4.9. As a further simplification, we assume that the two waveguides are the same type and have the same unit cell length R and total length L . Thus Eq. (4.57)

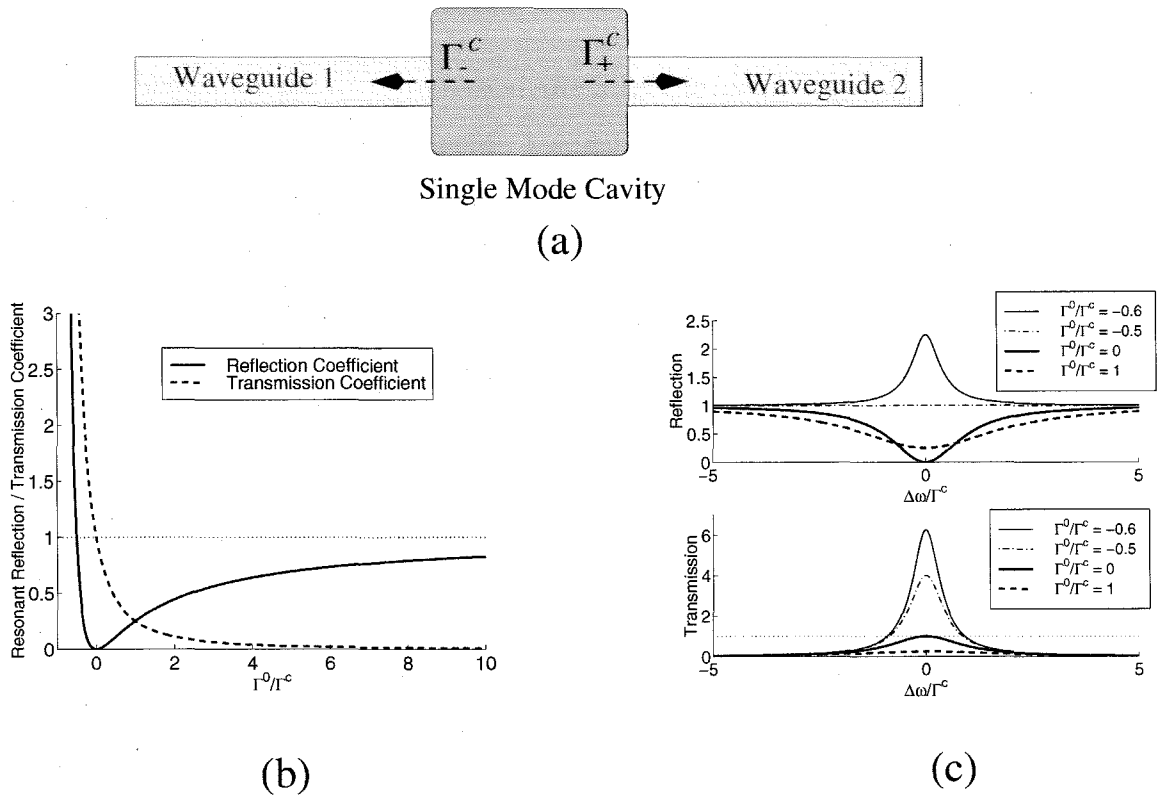


Figure 4.9: (a) Two waveguides of the same type coupled together via a high Q resonator supports a single mode. (b) The resonant reflection and transmission coefficients of the “resonant coupling” geometry shown in (a). (c) The reflection and transmission spectrum with different parameters of Γ^0/Γ^c .

and Eq. (4.58) become

$$R = \frac{(\Delta\omega)^2 + (\Gamma^0 + \Gamma_-^c - \Gamma_+^c)^2}{(\Delta\omega)^2 + (\Gamma^0 + \Gamma_+^c + \Gamma_-^c)^2} \quad (4.84)$$

$$T = \frac{4\Gamma_-^c\Gamma_+^c}{(\Delta\omega)^2 + (\Gamma^0 + \Gamma_+^c + \Gamma_-^c)^2} \quad (4.85)$$

$$\Gamma_-^c = \frac{L}{v_g} |V_{n,k_i}|^2, \quad \Gamma_+^c = \frac{L}{v_g} |V_{n,q_j}|^2, \quad (4.86)$$

where as before we use Γ^0 to represent the intrinsic cavity loss or gain, Γ_-^c represents the cavity decay rate into waveguide 1 and Γ_+^c represents the cavity decay rate into waveguide 2. From the above equations, we find that at resonance ($\Delta\omega = 0$), it is necessary to satisfy the condition of $\Gamma^0 = 0$ and $\Gamma_-^c = \Gamma_+^c$ to realize $R = 0$ and $T = 1$ (i.e., photon resonant tunneling).

To reduce the parameters in our analysis, we assume $\Gamma_-^c = \Gamma_+^c$, which allows us to use a single parameter $\Gamma^c = 2\Gamma_-^c$ and simplify Eq. (4.84) and Eq. (4.85) as

$$R = \frac{(\Delta\omega)^2 + (\Gamma^0)^2}{(\Delta\omega)^2 + (\Gamma^0 + \Gamma^c)^2}, \quad (4.87)$$

$$T = \frac{(\Gamma^c)^2}{(\Delta\omega)^2 + (\Gamma^0 + \Gamma^c)^2}. \quad (4.88)$$

It is interesting to notice that the above result is very similar to Eq. (4.60) and Eq. (4.61), which give the reflection and transmission coefficient for a waveguide side-coupled with a single mode waveguide. The only difference between the two cases is that the reflection coefficient in Eq. (4.60) corresponds to the transmission coefficient in Eq. (4.88), and the transmission coefficient in Eq. (4.61) corresponds to the reflection coefficient in Eq. (4.87).

In Fig. (4.9b), we show the resonant reflection and transmission coefficients as a function of Γ^0/Γ^c . In Fig. (4.9c), we plot the reflection and transmission spectrum using various parameters of Γ^0/Γ^c . As expected, we find that Fig. (4.9b) and (4.9c) is the same as Fig. (4.3b) and (4.3c), if we respectively identify the transmission and reflection in Fig. 4.9 with the reflection and transmission in Fig. 4.3.

4.5 Dispersion Relation of Indirect CROW

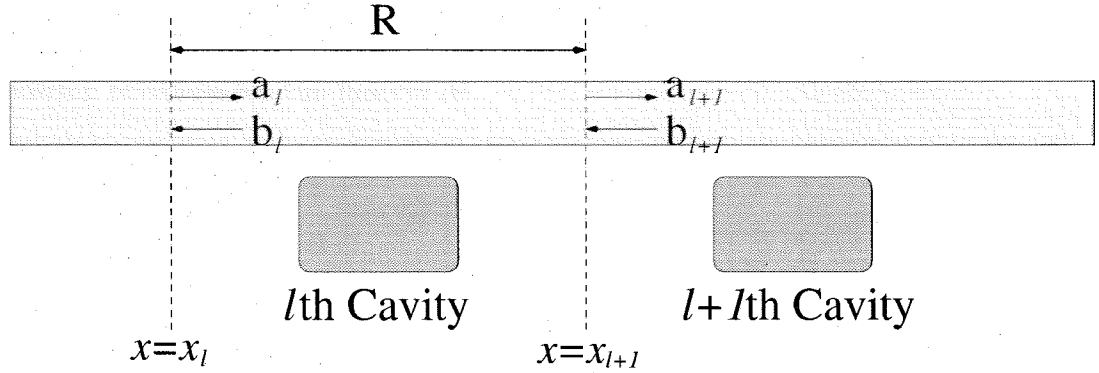


Figure 4.10: An example of indirect CROW, which consists of a waveguide side coupled to an array of high Q resonators.

As mentioned in Sec. 4.1, for the structure shown in Fig. 4.10, where a waveguide is side coupled to an array of high Q resonators, tight-binding approximation no longer applies, since any two resonators in this type of CROW are indirectly coupled to each other via the propagating modes in the waveguide. We shall name this type of CROW as indirect CROW. In this section, we develop a matrix formalism to analyze the indirect CROW's.

To simplify our analysis, we limit ourselves to the CROW's with large inter-cavity distance R , which enables us to ignore the direct coupling between the resonators. For the structure shown in Fig. 4.10, we write the optical wave to the immediate left of the l th unit cell as

$$\psi(\vec{r})|_{x=x_l} = A_l u_k(\vec{r}) + B_l u_k^*(\vec{r}) = a_l e^{ikx_l} u_k(\vec{r}) + b_l e^{-ikx_l} u_k^*(\vec{r}), \quad (4.89)$$

where $u_k(\vec{r})$ is the Bloch wavefunction defined in Eq. (4.37). We now introduce a matrix formalism, in which a matrix \mathbf{M} is used to relate the optical wave to the left and the optical wave to the right of the l th unit cell,

$$\begin{bmatrix} a_{l+1} \\ b_{l+1} \end{bmatrix} = \mathbf{M} \begin{bmatrix} a_l \\ b_l \end{bmatrix}. \quad (4.90)$$

We notice that this approach is similar to the transfer matrix method that was widely used to describe one-dimensional multilayer structures [28]. Using Eq. (4.39), Eq. (4.42), Eq. (4.43), Eq. (4.44), and applying time reversal symmetry, we have the following relations for the matrix M :

$$\begin{bmatrix} t \\ 0 \end{bmatrix} = \mathbf{M} \begin{bmatrix} 1 \\ r \end{bmatrix}, \quad \begin{bmatrix} 0 \\ t^* \end{bmatrix} = \mathbf{M} \begin{bmatrix} r^* \\ 1 \end{bmatrix}. \quad (4.91)$$

From these two equations, the matrix M is determined to be

$$\mathbf{M} = \begin{bmatrix} \frac{1}{t^*} & -\frac{r^*}{t^*} \\ -\frac{r}{t} & \frac{1}{t} \end{bmatrix}. \quad (4.92)$$

Combining Eq. (4.89), Eq. (4.90), and Eq. (4.92), we find

$$\begin{bmatrix} A_{l+1} \\ B_{l+1} \end{bmatrix} = \begin{bmatrix} \frac{1}{t^*} e^{ikR} & -\frac{r^*}{t^*} e^{ik(x_l+x_{l+1})} \\ -\frac{r}{t} e^{ik(x_l+x_{l+1})} & \frac{1}{t} e^{-ikR} \end{bmatrix} \begin{bmatrix} A_l \\ B_l \end{bmatrix}. \quad (4.93)$$

The eigenvalue equation for the matrix in the above equation is simply

$$\lambda^2 - \lambda \left(\frac{1}{t} e^{-ikR} + \frac{1}{t^*} e^{ikR} \right) + 1 = 0. \quad (4.94)$$

According to the Bloch theorem and the definition of A_l and B_l in Eq. (4.89), for any propagating wave inside a spatially periodic structure, the eigenvalue λ should be of the form $\exp(\pm i\beta R)$, with β being the Bloch wave vector. Consequently from Eq. (4.94), we find

$$2 \cos(\beta R) = \frac{1}{t} e^{-ikR} + \frac{1}{t^*} e^{ikR}. \quad (4.95)$$

We consider a simple case of CROW, where the resonator possesses mirror reflection symmetry and supports only a single mode. Under this assumption, the reflection coefficient t is given by Eq. (4.44),

$$t = \frac{\Delta\omega}{\Delta\omega + i\Gamma^c}, \quad (4.96)$$

where we assume the cavity has no loss or gain, i.e., $\Gamma^0 = 0$. We use the definition of $\Gamma^c = L|V_{k,n}|^2/v_g$, which represents the coupling between the cavity and the waveguide. Using Eq. (4.95) and Eq. (4.96), we obtain the dispersion relation for this indirect CROW

$$\cos(\beta R) = \cos(kR) + \frac{\Gamma^c}{\Delta\omega} \sin(kR). \quad (4.97)$$

Notice that k represents the wave vector of the pure waveguide, and β represents the wave vector of the compound system.

If the quantity $kR \neq n\pi$, a direct consequence of Eq. (4.97) is that no propagating mode exists at the renormalized resonance frequency $\omega = \Omega$. In fact, under the condition of $\sin(kR)$ not close to zero, for any $\Delta\omega$ within the range of Γ^c , the term $\Gamma^c/\Delta\omega$ will be larger than 1. According to Eq. (4.97), this means the formation a bandgap of the order of Γ^c that contains the renormalized resonator frequency Ω . If an unperturbed waveguide band traverses the renormalized resonance frequency at k_0 , it is necessary that this waveguide band is split and a bandgap is formed due to its coupling to the CROW structure. We assume a linear dispersion relation for the unperturbed waveguide mode

$$k = k_0 + \frac{1}{v_g} \Delta\omega, \quad (4.98)$$

where $\Delta\omega = \omega - \Omega$. This assumption simplifies Eq. (4.97) as

$$\cos(\beta R) = \cos\left(k_0 R + \frac{\Delta\omega}{\Gamma^c} \frac{R\Gamma^c}{v_g}\right) + \frac{\Gamma^c}{\Delta\omega} \sin\left(k_0 R + \frac{\Delta\omega}{\Gamma^c} \frac{R\Gamma^c}{v_g}\right). \quad (4.99)$$

From this expression, it is obvious that the photonic band structure of the compound waveguide depends critically on $k_0 R$, Γ^c and R . For many photonic crystals, the mid-gap frequency is typically of the value $\omega a/2\pi c = 0.3$, where a is the photonic lattice spacing and c is the light speed in free space [11]. If we consider a compound waveguide formed by a photonic crystal waveguide and defect cavities, we can choose $R = 5a$, $v_g = 0.3c$, the cavity Q (consequently ω/Γ^c) between 100 and 1000. From these estimates, we find that the parameter $R\Gamma^c/v_g$ is of the order of 0.05. In Fig.

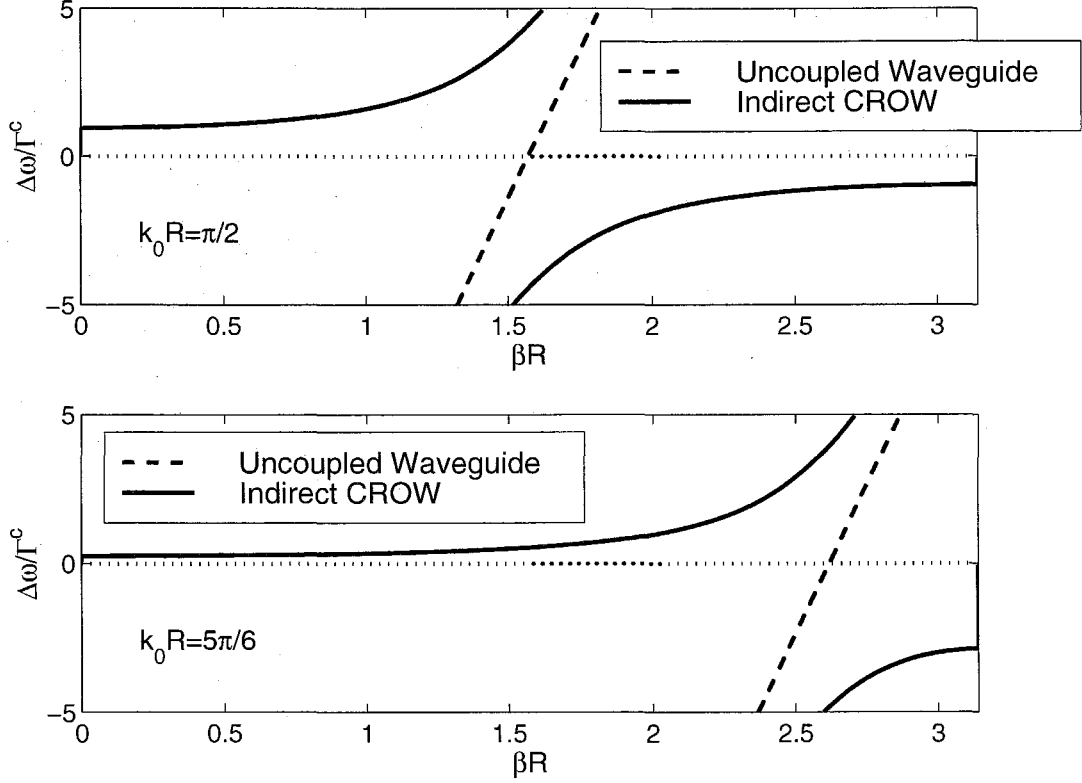


Figure 4.11: The uncoupled waveguide band and the photonic band of the indirect CROW calculated from Eq. (4.99). In (a) $k_0 R = \pi/2$ and in (b) $k_0 R = 5\pi/6$. We choose the parameter $R\Gamma^c/v_g = 0.05$. The justification of this value is given in the text.

4.11, we use $R\Gamma^c/v_g = 0.05$ and plot the indirect CROW band as calculated from Eq. (4.99). It is clearly demonstrated in Fig. 4.11 that the photonic band of the indirect CROW splits at $\Delta\omega = 0$ and its resonant band structure depends critically on the value of $k_0 R$.

On the other hand, if the propagating mode frequency is far away from resonance, Eq. (4.97) can be solved asymptotically. For $\Delta\omega \gg \Gamma^c$, β can be expanded around k to obtain an approximate solution

$$\beta R \simeq kR - \Gamma^c/\Delta\omega, \quad (4.100)$$

which can be easily verified by substituting this result into Eq. (4.97). Fig. 4.12 shows the uncoupled waveguide band, the split waveguide bands around ω_0 calculated from

Eq. (4.99), and the photonic bands obtained from the above asymptotic approximation. It is interesting to notice that the asymptotic approximation actually gives a fairly good description of the indirect CROW bands.

In closing this section, we remark that if $\cos(k_0R) \simeq \pm 1$, it is possible that one of the split bands becomes extremely flat. This scenario is illustrated in Fig. (4.13), where $k_0R = 3.0$ and $R\Gamma^c/v_g = 0.05$. The nearly horizontal band lies closely to the resonance frequency $\omega = \omega_0$. The flatness of the band indicates extremely low propagating group velocity. The group velocity is reduced to a large extent due to the fact that, when propagating through the indirect CROW structure, photons are trapped inside the resonance cavities most of the time. This property may find applications when low photon propagating velocity is desired, such as in the case of bandedge lasers [96].

4.6 Optical Transmission and Reflection Through Waveguide Coupled with Multiple Cavities

We have discussed the light reflection and transmission characteristics of some simple coupled waveguide-resonator system in Sec. 4.4. Yet it is of both theoretical and practical interest to investigate more complicated geometries. As an example, Fig. (4.14a) shows a structure composed of N identical resonators periodically side coupled to a straight waveguide. To simplify our analysis, we assume that each resonator is single mode and possesses mirror reflection symmetry.

First we reconsider the case where a straight waveguide is coupled to a single cavity. As shown in Fig. (4.14b), we choose the origin of the x coordinate such that $x = x_o$ is the mirror reflection symmetry plane of the system. As before, we express the propagating waveguide mode as

$$\psi(\vec{r}) = ae^{ik(x-x_o)}u_k(\vec{r}) + be^{-ik(x-x_o)}u_{-k}(\vec{r}), \quad (4.101)$$

where we choose the wavefunction of the propagating mode such that under mirror

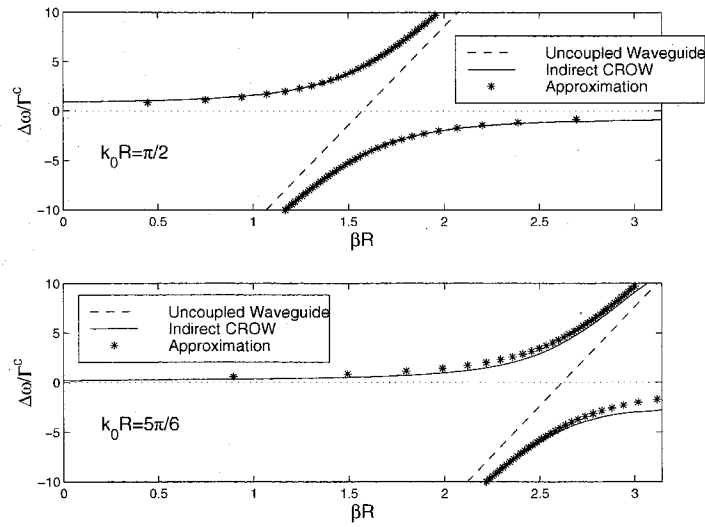


Figure 4.12: Dispersion relations of the indirect CROW bands. The solid lines are the exact solutions of Eq. (4.99) with $R\Gamma^c/v_g = 0.05$. The dash line represents the uncoupled waveguide band and the stars are the approximate solutions given by Eq. (4.100). In (a), we use (a) $k_0 R = \pi/2$ and in (b) $k_0 R = 5\pi/6$.

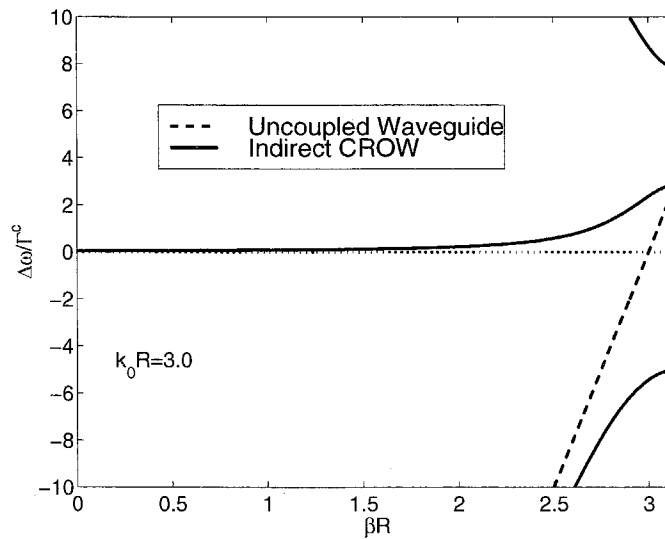


Figure 4.13: Near horizontal indirect CROW band. Photon group velocity is greatly reduced for the middle band shown above. The dashed line is the unperturbed waveguide band. We use $k_0 R = 3.0$ and $R\Gamma^c/v_g = 0.05$.

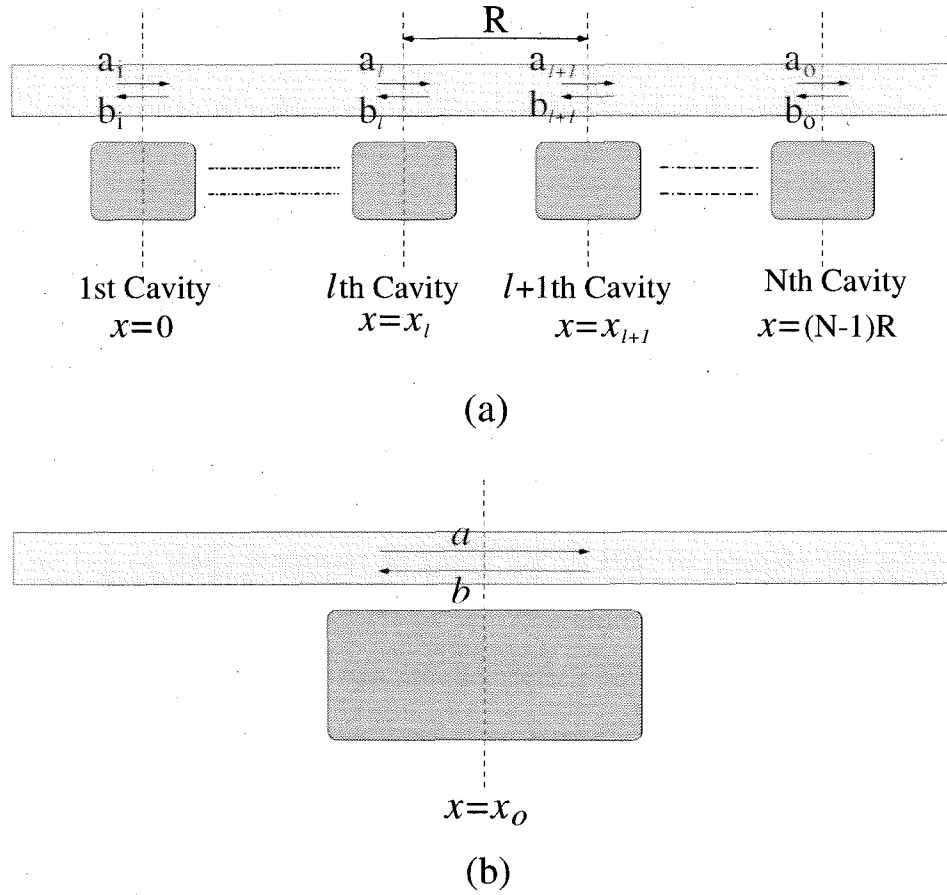


Figure 4.14: (a) A straight waveguide side coupled to N resonators. The incident optical wave is described by $[a_i \ b_i]$, the output optical wave is given by $[a_o \ b_o]$. (b) A straight waveguide coupled to a resonator that possesses mirror reflection symmetry with respect to plane $x = x_o$.

reflection operation $x - x_o \rightarrow -(x - x_o)$

$$\mathbf{O}_{x=x_o}[e^{ik(x-x_o)}u_k(\vec{r})] = e^{-ik(x-x_o)}u_{-k}(\vec{r}), \quad (4.102)$$

where the operator $\mathbf{O}_{x=x_o}$ represents the mirror reflection with respect to plane $x = x_o$. Using the same matrix formalism as in the previous section, from Eq. (4.45), we know that if the wave to the left of the resonator is described by $[1 \ r]$, then the wave to the right is given by $[t \ 0]$. On the other hand, if the wave to the right is $[r \ 1]$, the mirror reflection symmetry dictates that the wave to the left must be $[0 \ t]$. Since the

two waves can be related to each other via matrix \mathbf{M} , we have

$$\begin{bmatrix} t \\ 0 \end{bmatrix} = \mathbf{M} \begin{bmatrix} 1 \\ r \end{bmatrix}, \quad \begin{bmatrix} r \\ 1 \end{bmatrix} = \mathbf{M} \begin{bmatrix} 0 \\ t \end{bmatrix}, \quad (4.103)$$

which gives

$$\mathbf{M} = \begin{bmatrix} \frac{t^2-r^2}{t} & \frac{r}{t} \\ -\frac{r}{t} & \frac{1}{t} \end{bmatrix}. \quad (4.104)$$

When we study the case of a waveguide coupled to N identical resonators as shown in Fig. (4.14a), the scattering by each resonator can still be described by the matrix \mathbf{M} as given by Eq. (4.104). However, to apply Eq. (4.104) to describe the l th resonator, we need to choose x_o in Eq. (4.102) as x_l . Therefore, if the same \mathbf{M} matrix is used to describe the next resonator, we should switch to another basis of wavefunctions where x_o is $x_{l+1} = x_l + R$. Consequently, we have

$$\begin{bmatrix} a_{l+1} \\ b_{l+1} \end{bmatrix} = \mathbf{D} \begin{bmatrix} a_l \\ b_l \end{bmatrix}, \quad (4.105)$$

$$\mathbf{D} = \begin{bmatrix} e^{ikR} & 0 \\ 0 & e^{-ikR} \end{bmatrix} \begin{bmatrix} \frac{t^2-r^2}{t} & \frac{r}{t} \\ -\frac{r}{t} & \frac{1}{t} \end{bmatrix}. \quad (4.106)$$

It should be remembered that the wavefunction basis for $[a_{l+1} \ b_{l+1}]$ is *different* from that for $[a_l \ b_l]$.

Assuming the center of the first resonator is located at $x = 0$, and we choose the wavefunction basis according to Eq. (4.101) with $x_o = 0$. In the *same* wavefunction basis, the output optical wave $[a_o \ b_o]$ after the N th resonator is related to the incident wave $[a_i \ b_i]$ through

$$\begin{bmatrix} a_o \\ b_o \end{bmatrix} = \begin{bmatrix} e^{-iNkR} & 0 \\ 0 & e^{iNkR} \end{bmatrix} \mathbf{D}^N \begin{bmatrix} a_i \\ b_i \end{bmatrix}. \quad (4.107)$$

We consider the simplest case where the cavity possesses mirror reflection sym-

metry and supports only a single mode, where r can be found from Eq. (4.45)

$$r = \frac{-i}{\Delta\omega + i(\Gamma^0 + \Gamma^c)} \frac{L}{v_g} V_{-k,n} V_{n,k} . \quad (4.108)$$

Assuming the parity of the cavity mode is given by P , from Eq. (4.7), we have

$$V_{-k,n} = PV_{k,n} . \quad (4.109)$$

Using this relation, Eq. (4.108) is simplified as

$$r = -i \frac{P\Gamma^c}{\Delta\omega + i(\Gamma^0 + \Gamma^c)} . \quad (4.110)$$

The transmission coefficient is

$$t = \frac{\Delta\omega + i\Gamma^0}{\Delta\omega + i(\Gamma^0 + \Gamma^c)} . \quad (4.111)$$

Substituting Eq. (4.110) and Eq. (4.111) into Eq. (4.106), we find

$$\mathbf{D} = \frac{1}{\Delta\omega + i\Gamma^0} \begin{bmatrix} e^{ikR}[\Delta\omega + i(\Gamma^0 - \Gamma^c)] & -iP\Gamma^c e^{ikR} \\ iP\Gamma^c e^{-ikR} & e^{-ikR}[\Delta\omega + i(\Gamma^0 + \Gamma^c)] \end{bmatrix} . \quad (4.112)$$

To find the reflection and transmission coefficient, we calculate \mathbf{D}^N by using the procedure in Ref. [97]. First we obtain the eigenvalue equation of matrix \mathbf{D} :

$$\lambda^2 - 2\lambda \left[\cos(kR) + \frac{\Gamma^c}{\Delta\omega + i\Gamma^0} \sin(kR) \right] + 1 = 0 . \quad (4.113)$$

Then we use Hamilton-Cayley theorem [98], which says that the matrix obeys the same equation as its eigenvalue equation

$$\mathbf{D}^2 - 2\mathbf{D} \left[\cos(kR) + \frac{\Gamma^c}{\Delta\omega + i\Gamma^0} \sin(kR) \right] + 1 = 0 . \quad (4.114)$$

Thus, if we define β as

$$\cos(\beta R) = \cos(kR) + \frac{\Gamma^c}{\Delta\omega + i\Gamma^0} \sin(kR), \quad (4.115)$$

we find [97]

$$\mathbf{D}^N = \mathbf{D} \frac{\sin(N\beta R)}{\sin(\beta R)} - \mathbf{I} \frac{\sin(N-1)\beta R}{\sin(\beta R)}, \quad (4.116)$$

where \mathbf{I} is the identity matrix.

With the optical amplitude at the input and output given by Eq. (4.107) and the expression for \mathbf{D}^N given by Eq. (4.116), we can easily evaluate the optical transmission and reflection coefficients due to the presence of N resonators. The results in general depend critically on the values of $\Delta\omega$, Γ^0/Γ^c , N and k_0R . However, under the condition of $\Delta\omega = 0$ and $k_0R = n\pi$, the optical transmission and reflection coefficient are of simple form. In this case, \mathbf{D} and \mathbf{D}^N can be evaluated as

$$\mathbf{D} = (-1)^n \begin{bmatrix} 1 - \frac{\Gamma^c}{\Gamma^0} & -P \frac{\Gamma^c}{\Gamma^0} \\ P \frac{\Gamma^c}{\Gamma^0} & 1 + \frac{\Gamma^c}{\Gamma^0} \end{bmatrix}, \quad (4.117)$$

and

$$\mathbf{D}^N = (-1)^{Nn} \begin{bmatrix} 1 - \frac{N\Gamma^c}{\Gamma^0} & -P \frac{N\Gamma^c}{\Gamma^0} \\ P \frac{N\Gamma^c}{\Gamma^0} & 1 + \frac{N\Gamma^c}{\Gamma^0} \end{bmatrix}. \quad (4.118)$$

The power transmission and reflection coefficients of the whole system can readily be calculated as

$$T = \frac{1}{(1 + N\Gamma^c/\Gamma^0)^2}, \quad R = \left[\frac{N\Gamma^c/\Gamma^0}{1 + N\Gamma^c/\Gamma^0} \right]^2. \quad (4.119)$$

It is evident from (4.119) that under the condition of $k_0R = n\pi$, the resonant transmission and reflection characteristics of a waveguide coupled to N equally spaced single-mode resonators each with intrinsic loss Γ^0 are as if the waveguide is coupled to a *single* resonator with intrinsic loss Γ^0/N , which has been analyzed in section 4.4. In general, however, such scaling property with respect to N does not hold for arbitrary values of $\Delta\omega$ and k_0R . In the rest of this section, we shall use Eq. (4.107), Eq. (4.115) and Eq. (4.116) to find the transmission and reflection properties of such

coupled waveguide-resonator system. The parameter β as defined in Eq. (4.115) is very similar to the Bloch wavevector of the compound waveguide in the previous section and can be calculated using the same assumption of linear dispersion. In all the calculations of β , we choose the same $R\Gamma^c/v_g = 0.05$.

In Fig. 4.15, we show the transmission and reflection spectrums for a waveguide coupled to $N = 2$ and $N = 6$ resonators. We assume that there is no loss or gain and $k_0R = \pi/2$. It is interesting to notice that for only 2 resonators, the transmission dip and the reflection peak are no longer Lorentzian and relatively flat. For the case of $N = 6$, the transmission dip around $\Delta\omega = 0$ becomes extremely flat. We also observe the rapid oscillation of the transmission coefficient around the transmission dip, which is caused by the optical interference between the 6 resonators.

In Fig. (4.16a), we assume that $k_0R = 0$, $\Gamma^0/\Gamma^c = 0$ and show the transmission spectrum for a waveguide coupled to $N = 2$, $N = 6$, and $N = 20$ cavities. It is interesting to notice that only the case of $N = 20$ resonators produces flat transmission dip. In Fig. (4.16b), we show the photonic bands in the indirect CROW that corresponds to the coupled waveguide-resonator system in Fig. (4.16a). We notice the bandgap in the indirect CROW corresponds exactly to the transmission dip of $N = 20$ resonators in Fig. (4.16a). It is interesting that in Fig. 4.15 ($k_0R = \pi/2$), it only takes 6 resonators to produce a flat transmission dip, while under the condition of $k_0R = 0$, it requires 20 resonators.

We have observed in the previous section that it is possible to create a very flat photonic band close to $\Delta\omega = 0$ in an indirect CROW (see Fig. 4.13. where $k_0R = 3.0$ is used). We use the same value of k_0R to evaluate the optical transmission through a waveguide coupled to N lossless resonators, with N respectively equal to 2 and 10. The results are shown in Fig. 4.17. For the case of $N = 2$, we observe the presence of a narrow transmission peak around $\Delta\omega = 0$. For $N = 10$, multiple high transmission peaks are formed within the frequency range of $0 < \Delta\omega/\Gamma^c < 2.5$, which roughly corresponds to the flat CROW band observed in Fig. 4.13. The appearance of multiple peaks instead of a plateau of high transmission is likely due to the imperfect coupling between the unperturbed waveguide band and the flat CROW band.

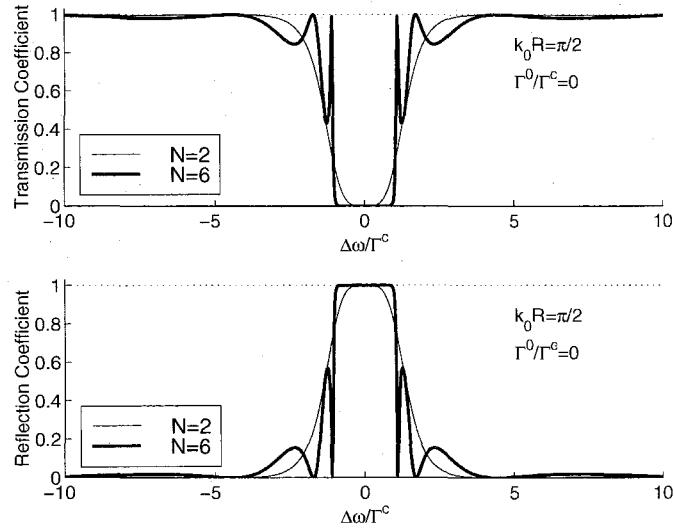


Figure 4.15: The transmission and reflection coefficient of a straight waveguide side coupled to N resonators, with $N = 2$ and $N = 6$ respectively. $\Gamma^0/\Gamma^c = 0$, $k_0 R = \pi/2$, $R\Gamma^c/v_g = 0.05$ are used.

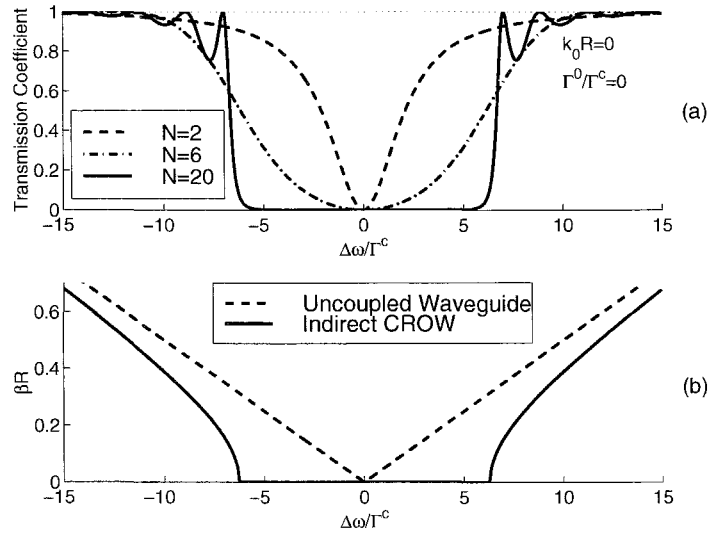


Figure 4.16: (a) The transmission spectrum of a straight waveguide side coupled to N resonators, with $N = 2$, $N = 6$ and $N = 20$ respectively. $\Gamma^0/\Gamma^c = 0$ and $k_0 R = 0$, and $R\Gamma^c/v_g = 0.05$ are used in the calculations. (b) The photonic band of a straight waveguide side coupled to an infinite array of resonators the same as those in (a). The band structures are calculated using Eq. (4.99), with $k_0 R = 0$ and $R\Gamma^c/v_g = 0.05$. The bandgap in (b) corresponds to the transmission dip for the case of $N = 20$ in (a).

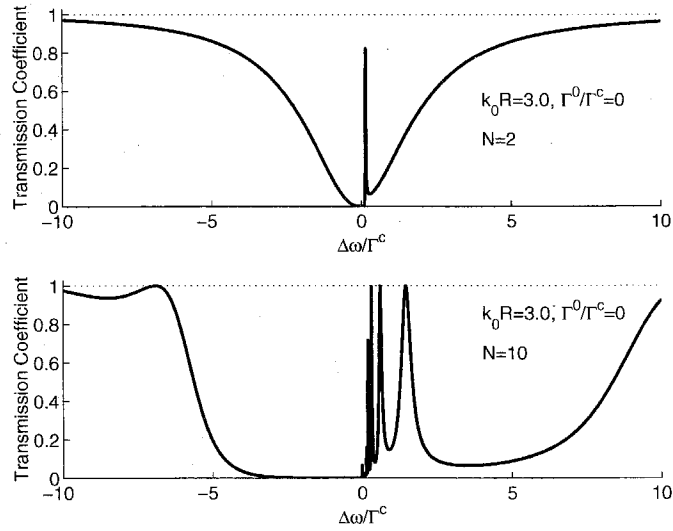


Figure 4.17: The transmission spectrum of a straight waveguide side coupled to N resonators, with $N = 2$ and $N = 10$ respectively. We use $\Gamma^0/\Gamma^c = 0$, $k_0 R = 3.0$, and $R\Gamma^c/v_g = 0.05$.

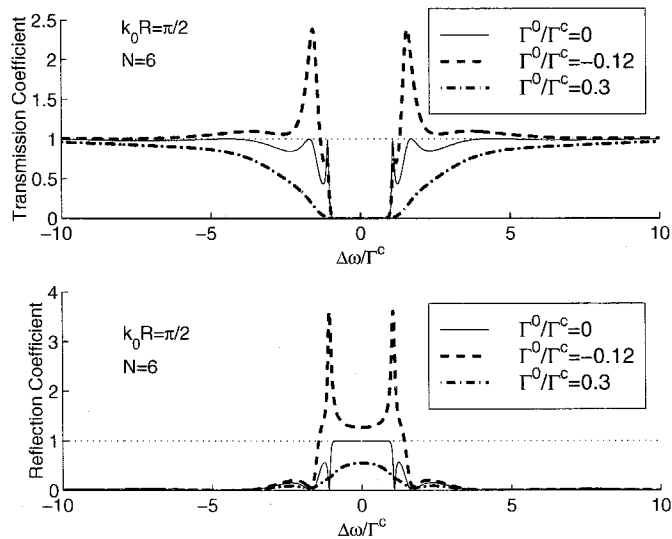


Figure 4.18: The transmission and reflection spectrum of a waveguide coupled to N resonators with loss ($\Gamma^0/\Gamma^c > 0$) or gain ($\Gamma^0/\Gamma^c < 0$). We use $N = 6$, $k_0 R = \pi/2$, and $R\Gamma^c/v_g = 0.05$ in the calculations.

In Sec. 4.4, we have found that the optical transmission and reflection depends critically on the cavity loss(gain). For a waveguide coupled to multiple resonators, we expect to see similar critical dependence. In Fig. 4.18, we calculate the optical transmission and reflection coefficient of a waveguide coupled to 6 resonators, with $k_0R = \pi/2$ and $R\Gamma^c/v_g = 0.05$. At the presence of cavity loss, we find that the rapid oscillation of the transmission coefficient vanishes around the edge of the transmission dip. This is due to the reduced interference between the lossy resonators. When cavity gain is introduced, we find that the transmission and reflection is greatly enhanced at frequencies corresponding to the bandedge of the indirect CROW band as shown in Fig. 4.11. This gain enhancement is a direct consequence of the slow group velocity at the edge of the indirect CROW band. In Fig. 4.19, where $N = 20$ and $k_0R = 0$, we also find diminished transmission side-lobe at the presence of cavity loss, and sharp enhancement of optical transmission at the bandedge when the cavities possess gain. However, comparing Fig. 4.19 to Fig. 4.18, we observe that it takes more cavities to obtain the same amount of optical enhancement when $k_0R = 0$. Finally, we study the case of $N = 6$ and $k_0R = 3.0$, which is shown in Fig. 4.20. With the presence of cavity loss $\Gamma^0/\Gamma^c = 0.3$, we find that the transmission peaks around $\Delta\omega = 0$ in the case of lossless cavities are greatly reduced. With cavity gain $\Gamma^0/\Gamma^c = -0.12$, we find that the sharp peak of enhanced optical transmission close to $\Delta\omega = 0$. Indeed, comparing Fig. 4.20 to Fig. 4.18, we find that the enhancement of the optical transmission for $k_0R = 3.0$ is much larger than the case of $k_0R = \pi/2$. As a concluding remark, we observe that the phenomenon of effective gain enhancement is a direct consequence of the reduced group velocity around bandedge [96].

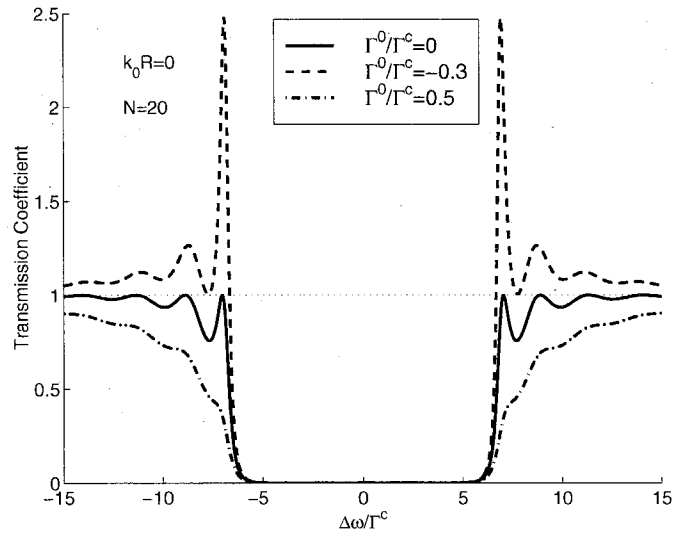


Figure 4.19: The transmission spectrum of a waveguide coupled to 20 resonators with loss or gain. $k_0R = 0$, and $R\Gamma^c/v_g = 0.05$ are used in the calculations.

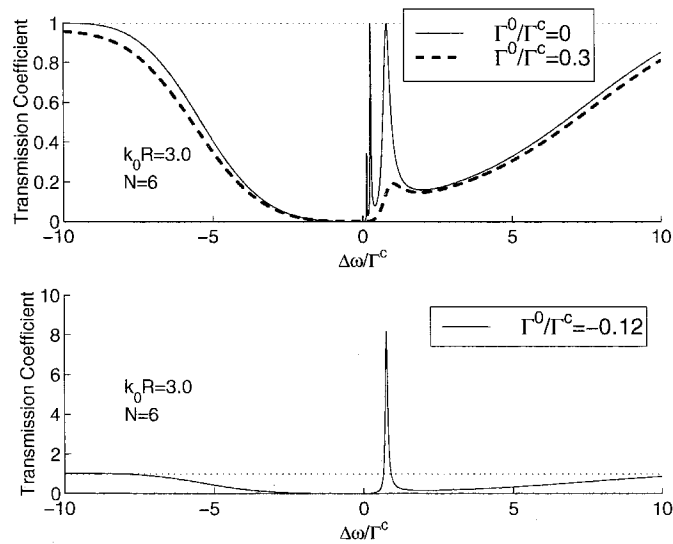


Figure 4.20: The transmission spectrum of a waveguide coupled to 6 resonators. $k_0R = 3.0$, and $R\Gamma^c/v_g = 0.05$ are used in the calculations.

Chapter 5

Bragg Fibers and Dielectric Coaxial Fibers

5.1 Introduction

In conventional optical fibers, the light confinement is achieved through total internal reflection and photons propagate mainly in the high index silica core. A completely different confinement mechanism, Bragg reflection, provides an alternative way of guiding photons, and has recently attracted a lot of attention [99]-[107]. Since Bragg reflection and total internal reflection are completely different guiding mechanisms, it is not surprising that fibers with Bragg confinement offer many possibilities that are difficult to achieve in conventional fibers. A particularly appealing application of Bragg confinement is the possibility of guiding light in air instead of silica glass, which can lead to lower propagation loss and reduce the threshold for nonlinear effects. We can also utilize Bragg reflection to design a fiber that supports a single guided mode without azimuthal dependence. In contrast with the fundamental mode in conventional fibers, which is always doubly degenerate, these guided fiber modes are truly single mode. Consequently, many undesirable polarization dependent effects, such as polarization mode dispersion (PMD) and polarization dependent loss (PDL),

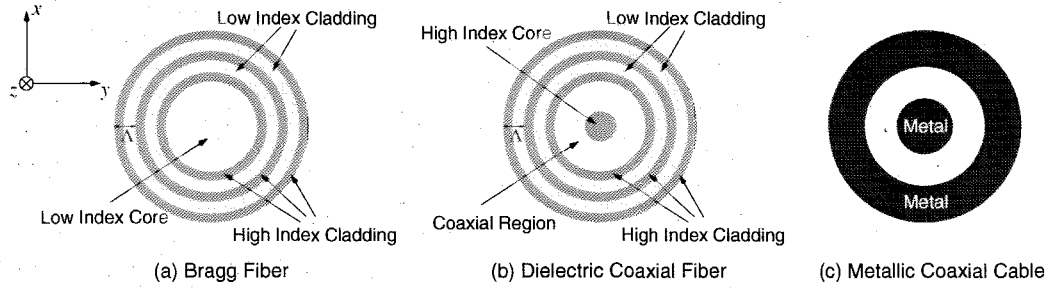


Figure 5.1: Schematic of (a) a Bragg fiber, (b) a dielectric coaxial fiber, and (c) a metallic coaxial cable.

can be completely eliminated [105].

The possibility of guiding light using Bragg confinement was first pointed out by Yeh et al. [99], where the concept of Bragg fibers was proposed. The experimental fabrication of Bragg fibers has been recently reported [102]. Fig. (5.1a) is the schematic of a Bragg fiber, which consists of a low index dielectric core surrounded by cladding layers with alternating high and low refractive indices. A new approach of using Bragg reflection to transmit optical signals was suggested in Ref. [105]. In this design, Ibanescu et al. proposed to use an all-dielectric coaxial fiber to overcome problems of polarization rotation and pulse broadening in high data rate telecommunication. The coaxial fiber is essentially a Bragg fiber with an extra high index core, as shown in Fig. (5.1b). The cladding of the coaxial fiber is a cylindrical omnidirectional mirror, which can be designed such that there is a frequency range within which light incident from the low index medium is completely reflected back irrespective of the incident angle and polarization [108, 109, 110]. Thus analogy can be drawn between dielectric coaxial fibers and metallic coaxial cables [see Fig. (5.1b) and Fig. (5.1c)]. Based on this analogy, Ibanescu et al. predicted small dispersion for dielectric coaxial fibers.

In both Bragg fibers and coaxial fibers, we use 1D Bragg reflection to achieve photon confinement. It is also possible to surround the fiber core region (silica glass or air) with silica glass patterned with two-dimensional arrays of air holes [101, 103, 104]. Such fibers are generally referred to as photonic crystal fibers, and shall not be considered here. However, we point out that as confinement mechanism, there

is no fundamental difference between 1D Bragg reflection and 2D Bragg reflection. Thus properties of photonic crystal fibers should qualitatively resemble those of Bragg fibers or coaxial fibers.

Due to the z translational symmetry of the aforementioned fibers, we can use the 2D FDTD algorithm in Sec. 2.1.1 and Sec. 2.3.2 to find dispersion and field distribution of the guided modes. This approach has the obvious advantage of being able to analyze fibers with complicated dielectric distribution. The drawback is that the numerical approach tends to be time consuming and physically less transparent. In this chapter, we shall develop an efficient analytical method for Bragg fibers and coaxial fibers by taking advantage of their cylindrical symmetry and radial periodicity of the cladding layers.

In the original matrix formalism [99], Yeh et al. used four independent parameters to describe the solution of Maxwell equations in each layer of the Bragg fiber, and the parameters in neighbor dielectric layers were related via a 4×4 matrix (see also Sec. 5.2.1). Unlike the case of conventional fibers, in this approach the confined modes in a Bragg fiber were treated as quasimodes whose propagation constant and field distribution were found by minimizing the radiation loss [99]. The extra complexity associated with this matrix approach is due to the difficulty in finding the eigenmode in fiber cladding layers. For a planar air core Bragg waveguide, the eigen solution that decays in the cladding structure can be easily found according to the Bloch theorem [9]. For a cylindrically symmetric geometry, which is strictly speaking not periodic and the Bloch theorem does not apply, we cannot single out an eigen solution that decays in the fiber cladding layers. As a result, it is no longer feasible to find an exact analytical equation that determines mode dispersion by matching the cladding solution and core solution at the waveguide core-cladding interface, as in the case of conventional optical fibers [69] or planar Bragg waveguides [9].

We observe that in the asymptotic limit, the exact solutions of Maxwell equations, which take the form of Bessel functions, can be approximated as $\exp(ikr)/\sqrt{r}$ and $\exp(-ikr)/\sqrt{r}$ [68]. In this form, the solutions in cylindrical Bragg cladding resemble those in planar Bragg stacks and eigen solutions in the fiber claddings can be similarly

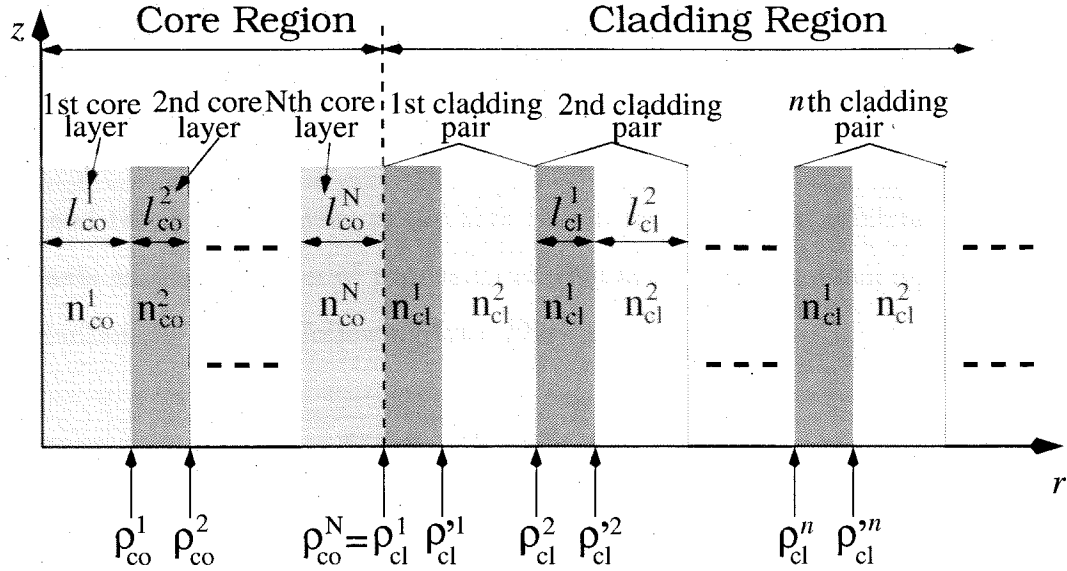


Figure 5.2: Schematic of the $r - z$ cross-section of a fiber with Bragg cladding. The dielectric layers of the Bragg fiber are classified into two regions: the core region and the cladding region, which are separated by the dash line in the figure.

found [106]. In Ref. [107], we treat the first several dielectric layers exactly and approximate the rest of the dielectric cladding structures in the asymptotic limit. We can use this method to find the dispersion relation of Bragg fibers within any desired precision simply by increasing the number of inner layers that are treated exactly. The accuracy of the asymptotic approximation can also be estimated by comparing results obtained from treating different number of inner layers exactly, as will be demonstrated shortly hereafter.

5.2 Asymptotic Matrix Theory

We begin the asymptotic analysis by separating the Bragg fiber or coaxial fiber into two regions: the core region and the cladding region. The core region consists of N concentric layers each with refractive index n_{co}^i and thickness l_{co}^i , $i = 1 \cdots N$. The fiber cladding region is composed of pairs of alternating layers of different dielectric materials. Layer type I has refractive index n_{cl}^1 and thickness l_{cl}^1 . Layer type II has refractive index n_{cl}^2 and thickness l_{cl}^2 , as shown in Fig. 5.2.

5.2.1 Exact Solution in the Core Region

In the asymptotic matrix formalism, we apply exact solutions of Maxwell equations to describe the fields in the core region. It should be emphasized that the refractive index and thickness of layers in the core region can be chosen arbitrarily. If we take the z axis as the direction of propagation, due to the translational symmetry, every field component has the following form [99]

$$\psi(r, \theta, z, t) = \psi(r, \theta)e^{i(\beta z - \omega t)}, \quad (5.1)$$

where ψ can be E_z , E_r , E_θ , H_z , H_r , and H_θ , ω is the mode frequency, and β is the propagation constant.

As in conventional fibers, the transverse field components can be represented by E_z and H_z [99]:

$$E_r = \frac{i\beta}{(\omega^2/c^2)n^2 - \beta^2} \left(\frac{\partial}{\partial r} E_z + \frac{\omega\mu_0}{\beta} \frac{\partial}{r\partial\theta} H_z \right), \quad (5.2)$$

$$E_\theta = \frac{i\beta}{(\omega^2/c^2)n^2 - \beta^2} \left(-\frac{\omega\mu_0}{\beta} \frac{\partial}{\partial r} H_z + \frac{\partial}{r\partial\theta} E_z \right), \quad (5.3)$$

$$H_r = \frac{i\beta}{(\omega^2/c^2)n^2 - \beta^2} \left(\frac{\partial}{\partial r} H_z - \frac{\omega\epsilon_0 n^2}{\beta} \frac{\partial}{r\partial\theta} E_z \right), \quad (5.4)$$

$$H_\theta = \frac{i\beta}{(\omega^2/c^2)n^2 - \beta^2} \left(\frac{\omega\epsilon_0 n^2}{\beta} \frac{\partial}{\partial r} E_z + \frac{\partial}{r\partial\theta} H_z \right), \quad (5.5)$$

where n is the refractive index of the dielectric medium.

Due to the cylindrical symmetry of Bragg fibers, we can take the azimuthal dependence of the field components as $\cos(m\theta)$ or $\sin(m\theta)$. For each m , the general solutions of E_z and H_z are the superposition of either $J_m(x)$ and $Y_m(x)$, or $I_m(x)$ and $K_m(x)$ [68]. In this section, we assume the solutions are given by $J_m(x)$ and $Y_m(x)$. As a result, the electromagnetic field at radius r , which is within the i th core layer,

can be written in the following matrix form [99]

$$\begin{bmatrix} E_z \\ \frac{1}{i\beta} H_\theta \\ H_z \\ -\frac{1}{i\beta} E_\theta \end{bmatrix} = M(n_{co}^i, k_{co}^i, r) \begin{bmatrix} A_i \\ B_i \\ C_i \\ D_i \end{bmatrix}. \quad (5.6)$$

The matrix $M(n_{co}^i, k_{co}^i, r)$ is defined as

$$M(n_{co}^i, k_{co}^i, r) = \begin{bmatrix} J_m(k_{co}^i r) & Y_m(k_{co}^i r) & 0 & 0 \\ \frac{\omega\epsilon_0(n_{co}^i)^2}{k_{co}^i\beta} J'_m(k_{co}^i r) & \frac{\omega\epsilon_0(n_{co}^i)^2}{k_{co}^i\beta} Y'_m(k_{co}^i r) & \frac{m}{(k_{co}^i)^2 r} J_m(k_{co}^i r) & \frac{m}{(k_{co}^i)^2 r} Y_m(k_{co}^i r) \\ 0 & 0 & J_m(k_{co}^i r) & Y_m(k_{co}^i r) \\ \frac{m}{(k_{co}^i)^2 r} J_m(k_{co}^i r) & \frac{m}{(k_{co}^i)^2 r} Y_m(k_{co}^i r) & \frac{\omega\mu_0}{k_{co}^i\beta} J'_m(k_{co}^i r) & \frac{\omega\mu_0}{k_{co}^i\beta} Y'_m(k_{co}^i r) \end{bmatrix}, \quad (5.7)$$

where $k_{co}^i = \sqrt{(n_{co}^i \omega/c)^2 - \beta^2}$. The coefficients A_i , B_i , C_i , and D_i are constant within the i th layer. We emphasize that as long as $\beta \leq n_{co}^i \omega/c$, Eq. (5.6) and Eq. (5.8) are the exact solution of Maxwell equations, with no approximation involved [99].

Once the electromagnetic field in the i th layer is known, we can easily find the field in the $(i+1)$ th layer by applying the condition that E_z , E_θ , H_z , H_θ are continuous at $r = \rho_{co}^i$, the interface between the i th and $(i+1)$ th layer:

$$\begin{bmatrix} A_{i+1} \\ B_{i+1} \\ C_{i+1} \\ D_{i+1} \end{bmatrix} = \mathbf{T}_i \begin{bmatrix} A_i \\ B_i \\ C_i \\ D_i \end{bmatrix}, \quad (5.8)$$

where the transfer matrix \mathbf{T}_i is

$$\mathbf{T}_i = \left[M(n_{co}^{i+1}, k_{co}^{i+1}, \rho_{co}^i) \right]^{-1} M(n_{co}^i, k_{co}^i, \rho_{co}^i). \quad (5.9)$$

It is important to notice that within the first core layer, the coefficients B_1 and D_1

are zero, since $Y_m(x)$ is infinite at $x = 0$.

5.2.2 Asymptotic Approximation in the Cladding Region

The electromagnetic fields in the cladding region can be described in the same way as the core regions fields, i.e., by Eq. (5.6) and Eq. (5.8). However, with a sufficiently large r , it suffices to approximate the exact solution in the asymptotic limit, which allows us to replace $J_m(x)$ and $Y_m(x)$ with $\exp(ix)/\sqrt{x}$ and $\exp(-ix)/\sqrt{x}$ [68]. Under this condition, the field distribution in type I layer of the n th cladding pair can be written as [107]:

$$\begin{cases} E_z = \frac{f_{TM}}{\sqrt{k_{cl}^1 r}} [a_n e^{ik_{cl}^1(r-\rho_{cl}^n)} + b_n e^{-ik_{cl}^1(r-\rho_{cl}^n)}] \\ H_\theta = -\frac{\omega\epsilon_0(n_{cl}^1)^2}{k_{cl}^1} \frac{f_{TM}}{\sqrt{k_{cl}^1 r}} [a_n e^{ik_{cl}^1(r-\rho_{cl}^n)} - b_n e^{-ik_{cl}^1(r-\rho_{cl}^n)}] \\ H_z = \frac{f_{TE}}{\sqrt{k_{cl}^1 r}} [c_n e^{ik_{cl}^1(r-\rho_{cl}^n)} + d_n e^{-ik_{cl}^1(r-\rho_{cl}^n)}] \\ E_\theta = \frac{\omega\mu_0}{k_{cl}^1} \frac{f_{TE}}{\sqrt{k_{cl}^1 r}} [c_n e^{ik_{cl}^1(r-\rho_{cl}^n)} - d_n e^{-ik_{cl}^1(r-\rho_{cl}^n)}] \end{cases} \quad \rho_{cl}^n \leq r < \rho_{cl}^n + l_{cl}^1. \quad (5.10)$$

Similarly, fields inside type II of the same cladding pair are given by

$$\begin{cases} E_z = \frac{f_{TM}}{\sqrt{k_{cl}^2 r}} [a'_n e^{ik_{cl}^2(r-\rho'_{cl}^n)} + b'_n e^{-ik_{cl}^2(r-\rho'_{cl}^n)}] \\ H_\theta = -\frac{\omega\epsilon_0(n_{cl}^2)^2}{k_{cl}^2} \frac{f_{TM}}{\sqrt{k_{cl}^2 r}} [a'_n e^{ik_{cl}^2(r-\rho'_{cl}^n)} - b'_n e^{-ik_{cl}^2(r-\rho'_{cl}^n)}] \\ H_z = \frac{f_{TE}}{\sqrt{k_{cl}^2 r}} [c'_n e^{ik_{cl}^2(r-\rho'_{cl}^n)} + d'_n e^{-ik_{cl}^2(r-\rho'_{cl}^n)}] \\ E_\theta = \frac{\omega\mu_0}{k_{cl}^2} \frac{f_{TE}}{\sqrt{k_{cl}^2 r}} [c'_n e^{ik_{cl}^2(r-\rho'_{cl}^n)} - d'_n e^{-ik_{cl}^2(r-\rho'_{cl}^n)}] \end{cases} \quad \rho_{cl}^m \leq r < \rho_{cl}^m + l_{cl}^2. \quad (5.11)$$

In Eq. (5.10) and (5.11), $k_{cl}^1 = \sqrt{(n_{cl}^1\omega/c)^2 - \beta^2}$, $k_{cl}^2 = \sqrt{(n_{cl}^2\omega/c)^2 - \beta^2}$, ρ_{cl}^n , ρ'_{cl}^m are defined in Fig. 5.2. It should be noted that TM component (including E_z and H_θ) and TE component (including H_z and E_θ) are decoupled in the asymptotic limit, with TM component amplitude being f_{TM} and TE component amplitude being f_{TE} . The values of f_{TE} and f_{TM} are constant within the whole Bragg cladding region.

The field amplitudes in type II layer of the n th cladding pair can be easily related to those in type I layer of the same cladding pair. By applying the condition of E_z ,

E_θ , H_z , H_θ being continuous at $r = \rho_{cl}^n$, we find

$$\begin{bmatrix} a'_n \\ b'_n \end{bmatrix} = \frac{1}{2} \sqrt{\frac{k_{cl}^2}{k_{cl}^1}} \begin{bmatrix} \left(1 + \frac{(n_{cl}^1)^2 k_{cl}^2}{(n_{cl}^2)^2 k_{cl}^1}\right) e^{ik_{cl}^1 l_{cl}^1} & \left(1 - \frac{(n_{cl}^1)^2 k_{cl}^2}{(n_{cl}^2)^2 k_{cl}^1}\right) e^{-ik_{cl}^1 l_{cl}^1} \\ \left(1 - \frac{(n_{cl}^1)^2 k_{cl}^2}{(n_{cl}^2)^2 k_{cl}^1}\right) e^{ik_{cl}^1 l_{cl}^1} & \left(1 + \frac{(n_{cl}^1)^2 k_{cl}^2}{(n_{cl}^2)^2 k_{cl}^1}\right) e^{-ik_{cl}^1 l_{cl}^1} \end{bmatrix} \begin{bmatrix} a_n \\ b_n \end{bmatrix}, \quad (5.12)$$

for the TM component, and

$$\begin{bmatrix} c'_n \\ d'_n \end{bmatrix} = \frac{1}{2} \sqrt{\frac{k_{cl}^2}{k_{cl}^1}} \begin{bmatrix} \left(1 + \frac{k_{cl}^2}{k_{cl}^1}\right) e^{ik_{cl}^1 l_{cl}^1} & \left(1 - \frac{k_{cl}^2}{k_{cl}^1}\right) e^{-ik_{cl}^1 l_{cl}^1} \\ \left(1 - \frac{k_{cl}^2}{k_{cl}^1}\right) e^{ik_{cl}^1 l_{cl}^1} & \left(1 + \frac{k_{cl}^2}{k_{cl}^1}\right) e^{-ik_{cl}^1 l_{cl}^1} \end{bmatrix} \begin{bmatrix} c_n \\ d_n \end{bmatrix} \quad (5.13)$$

for the TE component. Similarly, we can relate a'_n , b'_n , c'_n and d'_n to a_{n+1} , b_{n+1} , c_{n+1} , and d_{n+1} by applying the field continuity condition at $r = \rho_{cl}^{n+1}$. This allows us to express a_{n+1} , b_{n+1} , c_{n+1} and d_{n+1} in terms of the corresponding parameters in the n th layer:

$$\begin{bmatrix} a_{n+1} \\ b_{n+1} \end{bmatrix} = \begin{bmatrix} A_{TM} & B_{TM} \\ B_{TM}^* & A_{TM}^* \end{bmatrix} \begin{bmatrix} a_n \\ b_n \end{bmatrix}, \quad (5.14)$$

$$\begin{bmatrix} c_{n+1} \\ d_{n+1} \end{bmatrix} = \begin{bmatrix} A_{TE} & B_{TE} \\ B_{TE}^* & A_{TE}^* \end{bmatrix} \begin{bmatrix} c_n \\ d_n \end{bmatrix}. \quad (5.15)$$

The parameters A_{TE} , B_{TE} , A_{TM} and B_{TM} are respectively defined as [106]:

$$A_{TE} = e^{ik_{cl}^1 l_{cl}^1} \left[i \frac{(k_{cl}^1)^2 + (k_{cl}^2)^2}{2k_{cl}^1 k_{cl}^2} \sin(k_{cl}^2 l_{cl}^2) + \cos(k_{cl}^2 l_{cl}^2) \right], \quad (5.16)$$

$$B_{TE} = ie^{-ik_{cl}^1 l_{cl}^1} \frac{(k_{cl}^1)^2 - (k_{cl}^2)^2}{2k_{cl}^1 k_{cl}^2} \sin(k_{cl}^2 l_{cl}^2), \quad (5.17)$$

$$A_{TM} = e^{ik_{cl}^1 l_{cl}^1} \left[i \frac{(n_{cl}^2)^4 (k_{cl}^1)^2 + (n_{cl}^1)^4 (k_{cl}^2)^2}{2(n_{cl}^1)^2 (n_{cl}^2)^2 k_{cl}^1 k_{cl}^2} \sin(k_{cl}^2 l_{cl}^2) + \cos(k_{cl}^2 l_{cl}^2) \right], \quad (5.18)$$

$$B_{TM} = ie^{-ik_{cl}^1 l_{cl}^1} \frac{(n_{cl}^2)^4 (k_{cl}^1)^2 - (n_{cl}^1)^4 (k_{cl}^2)^2}{2(n_{cl}^1)^2 (n_{cl}^2)^2 k_{cl}^1 k_{cl}^2} \sin(k_{cl}^2 l_{cl}^2). \quad (5.19)$$

Since A_{TE} , B_{TE} , A_{TM} , and B_{TM} are the same for all cladding layers, we can apply

the Bloch theorem to the cladding fields:

$$\begin{bmatrix} a_n \\ b_n \end{bmatrix} = (\lambda_{TM})^{n-1} \begin{bmatrix} B_{TM} \\ \lambda_{TM} - A_{TM} \end{bmatrix}, \quad (5.20)$$

$$\begin{bmatrix} c_n \\ d_n \end{bmatrix} = (\lambda_{TE})^{n-1} \begin{bmatrix} B_{TE} \\ \lambda_{TE} - A_{TE} \end{bmatrix}, \quad (5.21)$$

$$\lambda_{TE} = \text{Re}(A_{TE}) \pm \sqrt{[\text{Re}(A_{TE})]^2 - 1}, \quad (5.22)$$

$$\lambda_{TM} = \text{Re}(A_{TM}) \pm \sqrt{[\text{Re}(A_{TM})]^2 - 1}. \quad (5.23)$$

These results clearly indicate that in the asymptotic limit, the properties of Bragg fiber cladding resemble those of planar Bragg stacks [9], which is directly due to the radial periodicity of the cladding layers and the fact that the asymptotic solutions in Eq. (5.10) and (5.11) takes the form of traveling plane waves. There are two solutions for λ_{TE} and λ_{TM} . In the Bragg bandgap, which is defined by the condition of $\text{Re}(A_{TE}) > 1$ or $\text{Re}(A_{TM}) > 1$, the two solutions of λ_{TE} and λ_{TM} are real numbers, with one having absolute value less than one and the other greater than one. We shall take the solutions of λ_{TE} and λ_{TM} with absolute values less than unity, since they correspond to modes decaying in the Bragg cladding.

Once we find the values of $a_n, b_n, c_n, d_n, a'_n, b'_n, c'_n, d'_n$ by combining Eq. (5.20) through Eq. (5.23), the only unknown quantities in Eq. (5.10) and Eq. (5.11), which give the electromagnetic field in the entire cladding region, are f_{TE} and f_{TM} , the amplitudes of the TE and TM components. The problem of finding them lies at the center of our asymptotic matrix formalism, and will be treated in detail in Sec. 5.2.3.

5.2.3 Matrix Formalism

The guided modes in a Bragg fiber are founded by matching the exact solution in the core region [i.e., Eq. (5.6)] with the asymptotic solution in the cladding region [i.e.,

Eq. (5.10)] at the interface $r = \rho_{co}^N = \rho_{cl}^1$ (see Fig. 5.2), which gives us

$$M(n_{co}^N, k_{co}^N, \rho_{co}^N) \begin{bmatrix} A_N \\ B_N \\ C_N \\ D_N \end{bmatrix} = \begin{bmatrix} \frac{f_{TM}}{\sqrt{k_{cl}^1 \rho_{cl}^1}} (\lambda_{TM} - A_{TM} + B_{TM}) \\ -\frac{i\omega\epsilon_0 (n_{cl}^1)^2}{k_{cl}^1 \beta} \frac{f_{TM}}{\sqrt{k_{cl}^1 \rho_{cl}^1}} (\lambda_{TM} - A_{TM} - B_{TM}) \\ \frac{f_{TE}}{\sqrt{k_{cl}^1 \rho_{cl}^1}} (\lambda_{TE} - A_{TE} + B_{TE}) \\ -\frac{i\omega\mu_0}{k_{cl}^1 \beta} \frac{f_{TE}}{\sqrt{k_{cl}^1 \rho_{cl}^1}} (\lambda_{TE} - A_{TE} - B_{TE}) \end{bmatrix}. \quad (5.24)$$

We then relate the amplitude coefficients in the N th core layer (i.e., A_N, B_N, C_N and D_N) to the coefficients in the first core layer (i.e., A_1, B_1, C_1 and D_1). We remember that in the first core layer $B_1 = D_1 = 0$ and we further denote A_1 as \mathcal{A}_{TM} , and C_1 as \mathcal{C}_{TE} . Applying Eq. (5.8) and (5.9) repeatedly, we have

$$\begin{bmatrix} A_N \\ B_N \\ C_N \\ D_N \end{bmatrix} = \mathbf{T}_{N-1} \cdots \mathbf{T}_2 [M(n_{co}^2, k_{co}^2, \rho_{co}^1)]^{-1} \begin{bmatrix} J_m(k_{co}^1 \rho_{co}^1) & 0 \\ \frac{\omega\epsilon_0 (n_{co}^1)^2}{k_{co}^1 \beta} J'_m(k_{co}^1 \rho_{co}^1) & \frac{m}{(k_{co}^1)^2 \rho_{co}^1} J_m(k_{co}^1 \rho_{co}^1) \\ 0 & J_m(k_{co}^1 \rho_{co}^1) \\ \frac{m}{(k_{co}^1)^2 \rho_{co}^1} J_m(k_{co}^1 \rho_{co}^1) & \frac{\omega\mu_0}{k_{co}^1 \beta} J'_m(k_{co}^1 \rho_{co}^1) \end{bmatrix} \times \begin{bmatrix} \mathcal{A}_{TM} \\ \mathcal{C}_{TE} \end{bmatrix}. \quad (5.25)$$

Substituting Eq. (5.25) into Eq. (5.24), we find the following matrix relation

$$\begin{bmatrix} J_m(k_{co}^1 \rho_{co}^1) & 0 \\ \frac{\omega\epsilon_0 (n_{co}^1)^2}{k_{co}^1 \beta} J'_m(k_{co}^1 \rho_{co}^1) & \frac{m}{(k_{co}^1)^2 \rho_{co}^1} J_m(k_{co}^1 \rho_{co}^1) \\ 0 & J_m(k_{co}^1 \rho_{co}^1) \\ \frac{m}{(k_{co}^1)^2 \rho_{co}^1} J_m(k_{co}^1 \rho_{co}^1) & \frac{\omega\mu_0}{k_{co}^1 \beta} J'_m(k_{co}^1 \rho_{co}^1) \end{bmatrix} \begin{bmatrix} \mathcal{A}_{TM} \\ \mathcal{C}_{TE} \end{bmatrix} = \mathbf{T} \begin{bmatrix} \frac{f_{TM}}{\sqrt{k_{cl}^1 \rho_{cl}^1}} (\lambda_{TM} - A_{TM} - B_{TM}) \\ -\frac{i\omega\epsilon_0 (n_{cl}^1)^2}{k_{cl}^1 \beta} \frac{f_{TM}}{\sqrt{k_{cl}^1 \rho_{cl}^1}} (\lambda_{TM} - A_{TM} - B_{TM}) \\ \frac{f_{TE}}{\sqrt{k_{cl}^1 \rho_{cl}^1}} (\lambda_{TE} - A_{TE} + B_{TE}) \\ -\frac{i\omega\mu_0}{k_{cl}^1 \beta} \frac{f_{TE}}{\sqrt{k_{cl}^1 \rho_{cl}^1}} (\lambda_{TE} - A_{TE} - B_{TE}) \end{bmatrix}, \quad (5.26)$$

where an overall transfer matrix \mathbf{T} is defined as

$$\begin{aligned}
\mathbf{T} &= \left[M(n_{co}^2, k_{co}^2, \rho_{co}^1) M^{-1}(n_{co}^2, k_{co}^2, \rho_{co}^2) \right] \cdots \left[M(n_{co}^N, k_{co}^N, \rho_{co}^{N-1}) M^{-1}(n_{co}^N, k_{co}^N, \rho_{co}^N) \right] \\
&= \prod_{i=2}^N \left[M(n_{co}^i, k_{co}^i, \rho_{co}^{i-1}) M^{-1}(n_{co}^i, k_{co}^i, \rho_{co}^i) \right] \\
&= \begin{bmatrix} t_{11} & t_{12} & t_{13} & t_{14} \\ t_{21} & t_{22} & t_{23} & t_{24} \\ t_{31} & t_{32} & t_{33} & t_{34} \\ t_{41} & t_{42} & t_{43} & t_{44} \end{bmatrix}.
\end{aligned} \tag{5.27}$$

In Eq. (5.26), \mathcal{A}_{TM} and \mathcal{C}_{TE} , which represent field in the first core layer, are linearly related to field in the first cladding layer (f_{TM} and f_{TE}) via a 4×4 transfer matrix \mathbf{T} as defined in Eq. (5.27). Eq. (5.26) gives us four equations with four independent variables \mathcal{A}_{TM} , \mathcal{C}_{TE} , f_{TM} , f_{TE} , and is sufficient to determine the propagation constant β and field distribution of guided modes. To see this more clearly, we introduce eight new parameters g_{TM}^j and g_{TE}^j , $j = 1, \dots, 4$ as

$$g_{TE}^j = t_{j3}(\lambda_{TE} - A_{TE} + B_{TE}) - \frac{i\omega\mu_0}{k_{cl}^1\beta} t_{j4}(\lambda_{TE} - A_{TE} - B_{TE}), \quad j = 1, \dots, 4, \tag{5.28}$$

$$g_{TM}^j = t_{j1}(\lambda_{TM} - A_{TM} + B_{TM}) - \frac{i\omega\epsilon_0(n_{cl}^1)^2}{k_{cl}^1\beta} t_{j2}(\lambda_{TM} - A_{TM} - B_{TM}), \quad j = 1, \dots, 4, \tag{5.29}$$

where t_{j1} , t_{j2} , t_{j3} and t_{j4} are the matrix elements given in Eq. (5.27). With these new parameters, we can split Eq. (5.26) into two equations:

$$\begin{aligned}
&\begin{bmatrix} J_m(k_{co}^1\rho_{co}^1) & 0 \\ \frac{\omega\epsilon_0(n_{co}^1)^2}{k_{co}^1\beta} J'_m(k_{co}^1\rho_{co}^1) & \frac{m}{(k_{co}^1)^2\rho_{co}^1} J_m(k_{co}^1\rho_{co}^1) \end{bmatrix} \begin{bmatrix} \mathcal{A}_{TM} \\ \mathcal{C}_{TE} \end{bmatrix} \\
&= \frac{1}{\sqrt{k_{cl}^1\rho_{cl}^1}} \begin{bmatrix} g_{TM}^1 & g_{TE}^1 \\ g_{TM}^2 & g_{TE}^2 \end{bmatrix} \begin{bmatrix} f_{TM} \\ f_{TE} \end{bmatrix},
\end{aligned} \tag{5.30}$$

$$\begin{aligned}
& \begin{bmatrix} 0 & J_m(k_{co}^1 \rho_{co}^1) \\ \frac{m}{(k_{co}^1)^2 \rho_{co}^1} J_m(k_{co}^1 \rho_{co}^1) & \frac{\omega \mu_0}{k_{co}^1 \beta} J'_m(k_{co}^1 \rho_{co}^1) \end{bmatrix} \begin{bmatrix} \mathcal{A}_{TM} \\ \mathcal{C}_{TE} \end{bmatrix} \\
&= \frac{1}{\sqrt{k_{cl}^1 \rho_{cl}^1}} \begin{bmatrix} g_{TM}^3 & g_{TE}^3 \\ g_{TM}^4 & g_{TE}^4 \end{bmatrix} \begin{bmatrix} f_{TM} \\ f_{TE} \end{bmatrix}. \tag{5.31}
\end{aligned}$$

These two equations lie at the center of our asymptotic matrix method. To fully understand their consequences, we consider two separate cases, the TE or TM modes with $m = 0$, and the mixed modes with $m \neq 0$.

For modes with $m = 0$, we first notice that the matrix $M(n_{co}^i, k_{co}^i, r)$ is block diagonalized into two 2×2 matrices. As a result, the transfer matrix \mathbf{T} , as defined in Eq. (5.27), is also block diagonalized into two 2×2 matrices with $t_{31} = t_{41} = t_{32} = t_{42} = t_{13} = t_{23} = t_{14} = t_{24} = 0$. According to the definitions in Eq. (5.28) and Eq. (5.29), we have $g_{TM}^3 = g_{TM}^4 = 0$, and $g_{TE}^1 = g_{TE}^2 = 0$.

By definition, the H_z component of any TM mode must remain zero in the entire Bragg fiber, i.e., $\mathcal{C}_{TE} = 0$ and $f_{TE} = 0$. With this condition in mind, from Eq. (5.30) we can easily find

$$\frac{\omega \epsilon_0 (n_{co}^1)^2 J'_0(k_{co}^1 \rho_{co}^1)}{k_{co}^1 \beta J_0(k_{co}^1 \rho_{co}^1)} = \frac{g_{TM}^2}{g_{TM}^1}. \tag{5.32}$$

Once we have specified the Bragg fiber parameters and chosen the frequency ω , the propagation constants of TM modes are found by solving for β_{TM} satisfying Eq. (5.32). We substitute the result β_{TM} back into Eq. (5.30), and obtain the following relation

$$\mathcal{A}_{TM} = \frac{g_{TM}^1}{J_0(k_{co}^1 \rho_{co}^1) \sqrt{k_{cl}^1 \rho_{cl}^1}} f_{TM}. \tag{5.33}$$

The importance of this result is that it relates the mode amplitude \mathcal{A}_{TM} in the first core layer to f_{TM} , which determines the fields within the entire fiber cladding region. We can choose the normalization factor of the guided mode such that $\mathcal{A}_{TM} = 1$. Combining this condition with Eq. (5.33), $f_{TE} = 0$, and Eq. (5.10) through Eq. (5.23) in Sec. 5.2, we obtain the TM field distribution in the cladding region. The TM field distribution in the core region can also be easily found. In the center core layer, we have $A_1 = \mathcal{A}_{TM} = 1$, and $B_1 = C_1 = D_1 = 0$. Applying Eq. (5.8) repeatedly,

where the transfer matrices \mathbf{T}_i are found from Eq. (5.8) and Eq. (5.9), we find all the mode coefficients A_i , B_i , C_i , and D_i in the N core layers. The TM field distribution in the core region is simply given by substituting these mode coefficients into Eq. (5.6) and applying Eq. (5.8).

For TE modes, we have $A_{TM} = 0$ and Eq. (5.31) gives us

$$\frac{\omega\mu_0}{k_{co}^1\beta} \frac{J'_0(k_{co}^1\rho_{co}^1)}{J_0(k_{co}^1\rho_{co}^1)} = \frac{g_{TE}^4}{g_{TE}^3}, \quad (5.34)$$

$$\mathcal{C}_{TE} = \frac{g_{TE}^3}{J_0(k_{co}^1\rho_{co}^1)\sqrt{k_{cl}^1\rho_{cl}^1}} f_{TE}. \quad (5.35)$$

Following the same procedure as for TM modes, we can find the propagation constant β and field distribution for TE modes from the above two results: Eq. (5.34) and Eq. (5.35).

For any mixed mode with $m \neq 0$, both Eq. (5.30) and Eq. (5.31) are needed and the solutions are more complicated. To simplify our final results, we introduce more definitions

$$H_{TE}^1 = -J_m(k_{co}^1\rho_{co}^1)g_{TE}^4 + \frac{\omega\mu_0}{k_{co}^1\beta} J'_m(k_{co}^1\rho_{co}^1)g_{TE}^3 + \frac{m}{(k_{co}^1)^2\rho_{co}^1} J_m(k_{co}^1\rho_{co}^1)g_{TE}^1, \quad (5.36)$$

$$H_{TE}^2 = J_m(k_{co}^1\rho_{co}^1)g_{TE}^2 - \frac{\omega\epsilon_0(n_{co}^1)^2}{k_{co}^1\beta} J'_m(k_{co}^1\rho_{co}^1)g_{TE}^1 - \frac{m}{(k_{co}^1)^2\rho_{co}^1} J_m(k_{co}^1\rho_{co}^1)g_{TE}^3, \quad (5.37)$$

$$H_{TM}^1 = J_m(k_{co}^1\rho_{co}^1)g_{TM}^4 - \frac{\omega\mu_0}{k_{co}^1\beta} J'_m(k_{co}^1\rho_{co}^1)g_{TM}^3 - \frac{m}{(k_{co}^1)^2\rho_{co}^1} J_m(k_{co}^1\rho_{co}^1)g_{TM}^1, \quad (5.38)$$

$$H_{TM}^2 = -J_m(k_{co}^1\rho_{co}^1)g_{TM}^2 + \frac{\omega\epsilon_0(n_{co}^1)^2}{k_{co}^1\beta} J'_m(k_{co}^1\rho_{co}^1)g_{TM}^1 + \frac{m}{(k_{co}^1)^2\rho_{co}^1} J_m(k_{co}^1\rho_{co}^1)g_{TM}^3. \quad (5.39)$$

To find the propagation constant β of any mixed mode, we first express \mathcal{A}_{TM} and \mathcal{C}_{TE} in terms of f_{TM} and f_{TE} by inverting the leftmost 2×2 matrix in Eq. (5.30). Substituting the results of \mathcal{A}_{TM} and \mathcal{C}_{TE} into Eq. (5.31), we find

$$\begin{bmatrix} H_{TM}^1 & -H_{TE}^1 \\ H_{TM}^2 & -H_{TE}^2 \end{bmatrix} \begin{bmatrix} f_{TM} \\ f_{TE} \end{bmatrix} = \mathbf{0}, \quad (5.40)$$

with H_{TE}^1 , H_{TE}^2 , H_{TM}^1 and H_{TM}^2 defined in Eq. (5.36) through Eq. (5.39). In order for Eq. (5.40) to have non-zero solutions, the determinant of the matrix must be zero, which gives

$$\frac{H_{TM}^1}{H_{TM}^2} = \frac{H_{TE}^1}{H_{TE}^2}. \quad (5.41)$$

As can be seen from the definitions in Eq. (5.36) to Eq. (5.39), Eq. (5.27) to Eq. (5.29) and Eq. (5.8), the parameters H_{TE}^1 , H_{TE}^2 , H_{TM}^1 , and H_{TM}^2 are complicated. However, once the Bragg fiber structure is chosen and the frequency is given, they only depend on β . Therefore, the solution of Eq. (5.41) gives us the propagation constant of any mixed mode.

After finding the solutions of Eq. (5.41) and choosing an appropriate normalization constant, we can determine the values of f_{TM} and f_{TE} from Eq. (5.40):

$$\begin{bmatrix} f_{TM} \\ f_{TE} \end{bmatrix} = \frac{m}{(k_{co}^1)^2 \rho_{co}^1} [J_m(k_{co}^1 \rho_{co}^1)]^2 \sqrt{k_{cl}^1 \rho_{cl}^1} \begin{bmatrix} H_{TE}^1 \\ H_{TM}^1 \end{bmatrix}. \quad (5.42)$$

As before, by combining this result with Eq. (5.10) to Eq. (5.23) in Sec. 5.2, we can find the whole cladding field distribution. To obtain the fields in the fiber core region, we substitute Eq. (5.42) into Eq. (5.31) and find

$$\begin{aligned} & \begin{bmatrix} \mathcal{A}_{TM} \\ \mathcal{C}_{TE} \end{bmatrix} \\ &= \begin{bmatrix} -\frac{\omega\mu_0}{k_{co}^1 \beta} J'_m(k_{co}^1 \rho_{co}^1) (g_{TM}^3 H_{TE}^1 + g_{TE}^3 H_{TM}^1) + J_m(k_{co}^1 \rho_{co}^1) (g_{TM}^4 H_{TE}^1 + g_{TE}^4 H_{TM}^1) \\ \frac{m}{(k_{co}^1)^2 \rho_{co}^1} J_m(k_{co}^1 \rho_{co}^1) (g_{TM}^3 H_{TE}^1 + g_{TE}^3 H_{TM}^1) \end{bmatrix}. \end{aligned} \quad (5.43)$$

Thus within the first core layer, we have $A_1 = \mathcal{A}_{TM}$, $C_1 = \mathcal{C}_{TE}$, and $B_1 = D_1 = 0$. By applying Eq. (5.6) to Eq. (5.9) in Sec. 5.2.1 throughout the entire core layers, we find the electromagnetic fields in the Bragg fiber core region.

5.2.4 Surface Modes

In the previous sections, we assume that general solutions in any layer are given by $J_m(x)$ and $Y_m(x)$, which only holds if $\beta \leq n_{co}^i \omega/c$ for all the core layers. In an air core Bragg fiber, a guided mode may have β exceeding ω/c , yet satisfying $\beta \leq n_{cl}^1 \omega/c$ and $\beta \leq n_{cl}^2 \omega/c$. Such mode is generally referred to as surface mode, since it decays both in the cladding layers (due to Bragg reflection) and in the air core (due to total internal reflection). In this case, we can still apply the asymptotic approximation to the cladding field and use results in Sec. 5.2.3. However, in the core region, there are some important differences between regular guided modes and surface modes, which shall be summarized in this section.

For the i th Bragg fiber layer in which $\beta > n_{co}^i \omega/c$, the solutions of E_z and H_z are given by $I_m(k_{co}^i r)$ and $K_m(k_{co}^i r)$ [68], with k_{co}^i defined as

$$k_{co}^i = \sqrt{\beta^2 - (n_{co}^i \omega/c)^2}. \quad (5.44)$$

We still use four parameters A_i , B_i , C_i and D_i to express field components in the i th layer, as in Eq. (5.6). However, the matrix M has a new definition:

$$M(n_{co}^i, k_{co}^i, r) \quad (5.45)$$

$$= \begin{bmatrix} I_m(k_{co}^i r) & K_m(k_{co}^i r) & 0 & 0 \\ -\frac{\omega \epsilon_0 (n_{co}^i)^2}{k_{co}^i \beta} I_m'(k_{co}^i r) & -\frac{\omega \epsilon_0 (n_{co}^i)^2}{k_{co}^i \beta} K_m'(k_{co}^i r) & -\frac{m}{(k_{co}^i)^2 r} I_m(k_{co}^i r) & -\frac{m}{(k_{co}^i)^2 r} K_m(k_{co}^i r) \\ 0 & 0 & I_m(k_{co}^i r) & K_m(k_{co}^i r) \\ -\frac{m}{(k_{co}^i)^2 r} I_m(k_{co}^i r) & -\frac{m}{(k_{co}^i)^2 r} K_m(k_{co}^i r) & -\frac{\omega \mu_0}{k_{co}^i \beta} I_m'(k_{co}^i r) & -\frac{\omega \mu_0}{k_{co}^i \beta} K_m'(k_{co}^i r) \end{bmatrix}.$$

If we use this new definition for $M(n_{co}^i, k_{co}^i, r)$ when $\beta > n_{co}^i \omega/c$, the overall transfer matrix \mathbf{T} is still the same as in Eq. (5.27), and g_{TE}^j , g_{TM}^j are still given by Eq. (5.28) and Eq. (5.29) respectively. If $\beta > n_{co}^1 \omega/c$ at the first core layer, Eq. (5.30) and Eq.

(5.31), which determine modal dispersion and field distribution, are replaced by

$$\begin{aligned}
& \begin{bmatrix} I_m(k_{co}^1 \rho_{co}^1) & 0 \\ -\frac{\omega \epsilon_0 (n_{co}^1)^2}{k_{co}^1 \beta} I'_m(k_{co}^1 \rho_{co}^1) & -\frac{m}{(k_{co}^1)^2 \rho_{co}^1} I_m(k_{co}^1 \rho_{co}^1) \end{bmatrix} \begin{bmatrix} \mathcal{A}_{TM} \\ \mathcal{C}_{TE} \end{bmatrix} \\
= & \frac{1}{\sqrt{k_{cl}^1 \rho_{cl}^1}} \begin{bmatrix} g_{TM}^1 & g_{TE}^1 \\ g_{TM}^2 & g_{TE}^2 \end{bmatrix} \begin{bmatrix} f_{TM} \\ f_{TE} \end{bmatrix}, \tag{5.46}
\end{aligned}$$

$$\begin{aligned}
& \begin{bmatrix} 0 & I_m(k_{co}^1 \rho_{co}^1) \\ -\frac{m}{(k_{co}^1)^2 \rho_{co}^1} I_m(k_{co}^1 \rho_{co}^1) & -\frac{\omega \mu_0}{k_{co}^1 \beta} I'_m(k_{co}^1 \rho_{co}^1) \end{bmatrix} \begin{bmatrix} \mathcal{A}_{TM} \\ \mathcal{C}_{TE} \end{bmatrix} \\
= & \frac{1}{\sqrt{k_{cl}^1 \rho_{cl}^1}} \begin{bmatrix} g_{TM}^3 & g_{TE}^3 \\ g_{TM}^4 & g_{TE}^4 \end{bmatrix} \begin{bmatrix} f_{TM} \\ f_{TE} \end{bmatrix}. \tag{5.47}
\end{aligned}$$

From the above two equations, for TM modes we find

$$-\frac{\omega \epsilon_0 (n_{co}^1)^2}{k_{co}^1 \beta} \frac{I'_0(k_{co}^1 \rho_{co}^1)}{I_0(k_{co}^1 \rho_{co}^1)} = \frac{g_{TM}^2}{g_{TM}^1}, \tag{5.48}$$

$$\mathcal{A}_{TM} = \frac{g_{TM}^1}{I_0(k_{co}^1 \rho_{co}^1) \sqrt{k_{cl}^1 \rho_{cl}^1}} f_{TM}, \tag{5.49}$$

which, respectively, give dispersion and field distribution of guided TM modes. The corresponding equations for TE modes are

$$-\frac{\omega \mu_0}{k_{co}^1 \beta} \frac{I'_0(k_{co}^1 \rho_{co}^1)}{I_0(k_{co}^1 \rho_{co}^1)} = \frac{g_{TE}^4}{g_{TE}^3}, \tag{5.50}$$

$$\mathcal{C}_{TE} = \frac{g_{TE}^3}{I_0(k_{co}^1 \rho_{co}^1) \sqrt{k_{cl}^1 \rho_{cl}^1}} f_{TE}. \tag{5.51}$$

The results for the mixed surface modes are more complicated. First, if $\beta > n_{co}^1 \omega/c$, the definitions of H_{TE}^1 , H_{TE}^2 , H_{TM}^1 , H_{TM}^2 must be changed accordingly:

$$H_{TE}^1 = -I_m(k_{co}^1 \rho_{co}^1) g_{TE}^4 - \frac{\omega \mu_0}{k_{co}^1 \beta} I'_m(k_{co}^1 \rho_{co}^1) g_{TE}^3 - \frac{m}{(k_{co}^1)^2 \rho_{co}^1} I_m(k_{co}^1 \rho_{co}^1) g_{TE}^1, \tag{5.52}$$

$$H_{TE}^2 = I_m(k_{co}^1 \rho_{co}^1) g_{TE}^2 + \frac{\omega \epsilon_0 (n_{co}^1)^2}{k_{co}^1 \beta} I'_m(k_{co}^1 \rho_{co}^1) g_{TE}^1 + \frac{m}{(k_{co}^1)^2 \rho_{co}^1} I_m(k_{co}^1 \rho_{co}^1) g_{TE}^3, \quad (5.53)$$

$$H_{TM}^1 = I_m(k_{co}^1 \rho_{co}^1) g_{TM}^4 + \frac{\omega \mu_0}{k_{co}^1 \beta} I'_m(k_{co}^1 \rho_{co}^1) g_{TM}^3 + \frac{m}{(k_{co}^1)^2 \rho_{co}^1} I_m(k_{co}^1 \rho_{co}^1) g_{TM}^1, \quad (5.54)$$

$$H_{TM}^2 = -I_m(k_{co}^1 \rho_{co}^1) g_{TM}^2 - \frac{\omega \epsilon_0 (n_{co}^1)^2}{k_{co}^1 \beta} I'_m(k_{co}^1 \rho_{co}^1) g_{TM}^1 - \frac{m}{(k_{co}^1)^2 \rho_{co}^1} I_m(k_{co}^1 \rho_{co}^1) g_{TM}^3. \quad (5.55)$$

With the new definitions, Eq. (5.41) still holds for surface modes and its solutions give the modal dispersion. However, the expressions for cladding field coefficients and core field coefficients are different, and are respectively given by

$$\begin{bmatrix} f_{TM} \\ f_{TE} \end{bmatrix} = \frac{m}{(k_{co}^1)^2 \rho_{co}^1} [I_m(k_{co}^1 \rho_{co}^1)]^2 \sqrt{k_{cl}^1 \rho_{cl}^1} \begin{bmatrix} H_{TE}^1 \\ H_{TM}^1 \end{bmatrix}, \quad (5.56)$$

$$\begin{aligned} & \begin{bmatrix} \mathcal{A}_{TM} \\ \mathcal{C}_{TE} \end{bmatrix} \\ & = \begin{bmatrix} -\frac{\omega \mu_0}{k_{co}^1 \beta} I'_m(k_{co}^1 \rho_{co}^1) (g_{TM}^3 H_{TE}^1 + g_{TE}^3 H_{TM}^1) - I_m(k_{co}^1 \rho_{co}^1) (g_{TM}^4 H_{TE}^1 + g_{TE}^4 H_{TM}^1) \\ \frac{m}{(k_{co}^1)^2 \rho_{co}^1} I_m(k_{co}^1 \rho_{co}^1) (g_{TM}^3 H_{TE}^1 + g_{TE}^3 H_{TM}^1) \end{bmatrix}. \end{aligned} \quad (5.57)$$

5.3 Radiation Loss

There are two sources that contribute to the propagation loss in Bragg fibers or coaxial fibers: the material absorption loss and the radiation loss. The material absorption loss depends on the choice of dielectric medium. The radiation loss mainly depends on the index contrast between the cladding media and the number of cladding pairs. In principle, the radiation loss can be reduced below any given number simply by using a large enough number of cladding pairs. In this case, the propagation loss in an air core fiber is mostly due to the residual absorption in the fiber cladding. Thus if appropriate cladding materials can be found, it is possible to reduce the propagation loss in an air core fiber below that of conventional optical fibers. In fact, this is one of the main reasons behind the recent interest in air core fibers [102, 104]. However, since using too many cladding pairs is generally undesirable or even impractical, it is

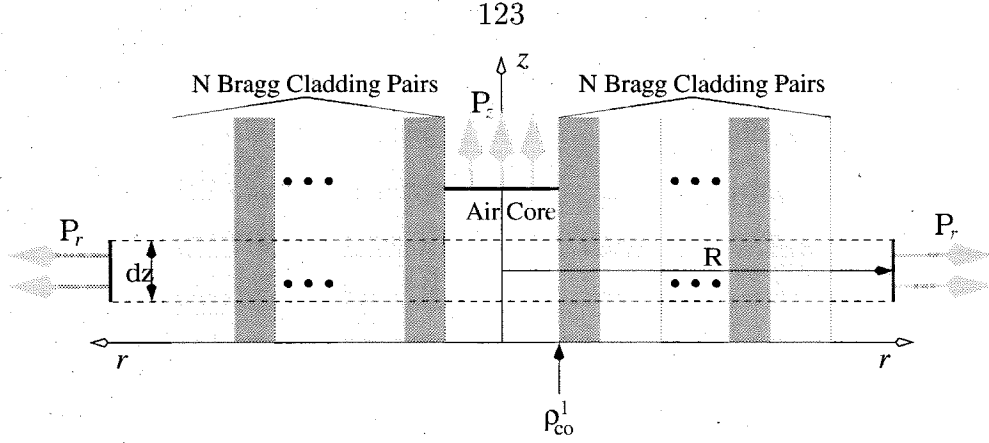


Figure 5.3: The radiation loss of an air core Bragg fiber with N cladding pairs. P_z is the power flux inside the air core. P_r represents the outgoing radiation power flux through a cylindrical surface with radius R and height dz .

important to know how many layers are required to reduce the radiation loss below a given number. Here we give an estimate about the number of cladding pairs necessary to achieve 0.2dB/km radiation loss, as a comparison with typical conventional fiber propagation loss.

To simplify our analysis, we study a Bragg fiber with a central air core bounded by N pairs of cladding layers, as shown in Fig. 5.3. We treat the air core exactly and apply the asymptotic approximation to the entire Bragg cladding structure. This means that the transfer matrix \mathbf{T} relating the cladding region to the core region is simply a 4×4 identity matrix whose diagonal terms are 1 and the off diagonal terms are 0. Following Eq. (5.28) and Eq. (5.29), we find

$$g_{TE}^3 = \lambda_{TE} - A_{TE} + B_{TE}, \quad (5.58)$$

$$g_{TE}^4 = -\frac{i\omega\mu_0}{k_{cl}^1\beta}(\lambda_{TE} - A_{TE} - B_{TE}), \quad (5.59)$$

$$g_{TM}^1 = \lambda_{TM} - A_{TM} + B_{TM}, \quad (5.60)$$

$$g_{TM}^2 = -\frac{i\omega\epsilon_0(n_{cl}^1)^2}{k_{cl}^1\beta}(\lambda_{TM} - A_{TM} - B_{TM}). \quad (5.61)$$

Other values of g_{TE}^i and g_{TM}^i are all zero. As a further simplification, we shall confine ourselves to the study of TE and TM modes. The reasons are two-fold. As we have

mentioned before, the modes with $m = 0$ are of special interest, since they do not have any polarization dependent effects. Secondly, in the asymptotic limit, the mixed modes ($m \neq 0$) in the cladding structure can always be classified into TE component and TM component. Therefore, we can expect the radiation loss of mixed modes to exhibit characteristics between those of TE and TM modes.

We first consider TE modes. According to Eq. (5.6), the $H_z(r)$ component in the Bragg fiber core is simply $H_z(r) = \mathcal{C}_{TE} J_0(k_{co}^1 r)$ and the other two components are [99]

$$E_\theta = -i \frac{\omega \mu_0}{k_{co}^1} \mathcal{C}_{TE} J_0'(k_{co}^1 r), \quad (5.62)$$

$$H_r = \frac{i\beta}{k_{co}^1} \mathcal{C}_{TE} J_0'(k_{co}^1 r). \quad (5.63)$$

From these expressions for E_θ and H_r , we find the power flux along the z direction in the low index core:

$$P_z^{TE} = |\mathcal{C}_{TE}|^2 \frac{\pi \omega \mu_0 \beta}{(k_{co}^1)^2} \int_0^{\rho_{co}^1} dr r [J_0'(k_{co}^1 r)]^2. \quad (5.64)$$

If the Bragg fiber consists of an infinite number of cladding pairs, the asymptotic fields in the $(N + 1)$ th cladding pair can be extracted from Eq. (5.10)

$$H_z = \frac{f_{TE}}{\sqrt{k_{cl}^1 r}} \left[c_{N+1} e^{ik_{cl}^1 (r - \rho_{cl}^{N+1})} + d_{N+1} e^{-ik_{cl}^1 (r - \rho_{cl}^{N+1})} \right], \quad (5.65)$$

$$E_\theta = \frac{\omega \mu_0}{k_{cl}^1} \frac{f_{TE}}{\sqrt{k_{cl}^1 r}} \left[c_{N+1} e^{ik_{cl}^1 (r - \rho_{cl}^{N+1})} - d_{N+1} e^{-ik_{cl}^1 (r - \rho_{cl}^{N+1})} \right]. \quad (5.66)$$

In the above expressions, we notice that the fields consist of two components: an outgoing wave with amplitude proportional to c_{N+1} , and an incoming wave with amplitude proportional to d_{N+1} . It can be shown that the two components are of equal value and cancel each other such that the Bragg fiber has no net radial power flux. This, however, is directly due to the assumption of infinite cladding pairs. In fact, we can regard the incoming component in the $(N + 1)$ th cladding pair as due to the reflection by the remaining Bragg cladding. Therefore, it is reasonable to

assume that if the Bragg fiber has only N cladding pairs, the radiation field outside the cladding structure can be well approximated by the outgoing component of Eq. (5.65) and Eq. (5.66) (i.e., we replace d_{N+1} with 0). To calculate the radial power flow, let us consider a cylindrical surface with radius R and height dz that encloses the Bragg fiber, as shown in Fig. 5.3. Using Eq. (5.65) and Eq. (5.66) and taking $d_{N+1} = 0$, we find the radial power flux through this surface to be

$$P_r^{TE} = \frac{\pi\omega\mu_0}{(k_{cl}^1)^2} |f_{TE}|^2 |c_{N+1}|^2 dz. \quad (5.67)$$

For TE modes propagating along the z direction of the Bragg fiber, with the presence of radiation loss, the optical power decays as $\exp(-\alpha_{TE}z)$. The parameter α_{TE} is the radiation loss constant, and from the definitions of P_z^{TE} and P_r^{TE} , we can identify α_{TE} as

$$\alpha_{TE} = \frac{P_r^{TE}}{P_z^{TE} dz} = \frac{1}{\beta} \left(\frac{k_{co}^1}{k_{cl}^1} \right)^2 \left| \frac{B_{TE}}{\lambda_{TE} - A_{TE} + B_{TE}} \right|^2 |\lambda_{TE}|^{2N} \frac{[J_0(k_{co}^1 \rho_{co})]^2 k_{cl}^1 \rho_{cl}^1}{\int_0^{\rho_{co}^1} dr r [J_0(k_{co}^1 r)]^2}, \quad (5.68)$$

where Eq. (5.21), (5.35), (5.58), (5.64), and (5.67) are used.

For TM modes, we can follow the same procedure to obtain the radiation loss constant α_{TM} . First, we find fields in the low index core and the corresponding power flux in z direction

$$H_\theta = \frac{i\omega\epsilon_0 (n_{co}^1)^2}{k_{co}^1} \mathcal{A}_{TM} J_0'(k_{co}^1 r), \quad (5.69)$$

$$E_r = \frac{i\beta}{k_{co}^1} \mathcal{A}_{TM} J_0'(k_{co}^1 r), \quad (5.70)$$

$$P_z^{TM} = |\mathcal{A}_{TM}|^2 \frac{\pi\omega\epsilon_0 (n_{co}^1)^2 \beta}{(k_{co}^1)^2} \int_0^{\rho_{co}^1} dr r [J_0'(k_{co}^1 r)]^2. \quad (5.71)$$

The outgoing radiation field outside the N th cladding pairs can also be identified from Eq. (5.10) as

$$E_z = \frac{f_{TM}}{\sqrt{k_{cl}^1 r}} a_{N+1} e^{ik_{cl}^1 (r - \rho_{cl}^{N+1})}, \quad (5.72)$$

$$H_\theta = -\frac{\omega\epsilon_0(n_{cl}^1)^2}{k_{cl}^1} \frac{f_{TM}}{\sqrt{k_{cl}^1 r}} a_{N+1} e^{ik_{cl}^1(r-\rho_{cl}^{N+1})}, \quad (5.73)$$

and correspondingly, the radial power flux is

$$P_r^{TM} = \frac{\pi\omega\epsilon_0(n_{cl}^1)^2}{(k_{cl}^1)^2} |f_{TM}|^2 |a_{N+1}|^2 dz, \quad (5.74)$$

which gives the radiation loss constant to be

$$\alpha_{TM} = \frac{P_r^{TM}}{P_z^{TM} dz} = \frac{1}{\beta} \left(\frac{n_{cl}^1 k_{co}^1}{n_{co}^1 k_{cl}^1} \right)^2 \left| \frac{B_{TM}}{\lambda_{TM} - A_{TM} + B_{TM}} \right|^2 |\lambda_{TM}|^{2N} \frac{[J_0(k_{co}^1 \rho_{co}^1)]^2 k_{cl}^1 \rho_{cl}^1}{\int_0^{\rho_{co}^1} dr r [J_0'(k_{co}^1 r)]^2}, \quad (5.75)$$

where Eq. (5.20), (5.33), (5.60), (5.71), and (5.74) are used.

To simplify our results for α_{TE} and α_{TM} , we introduce a new parameter $x = k_{co}^1 \rho_{co}^1$. For the fiber structure shown in Fig. 5.3, ρ_{cl}^1 is the same as ρ_{co}^1 , which gives

$$\frac{[J_0(k_{co}^1 \rho_{co}^1)]^2 k_{cl}^1 \rho_{cl}^1}{\int_0^{\rho_{co}^1} dr r [J_0'(k_{co}^1 r)]^2} = k_{co}^1 k_{cl}^1 \frac{x [J_0(x)]^2}{\int_0^x du u [J_1(u)]^2}, \quad (5.76)$$

where we have applied $J_0'(x) = -J_1(x)$ [68]. The exact value of this expression depends on our choice of x . But for an order of magnitude estimate, we can simply choose $x = 3.8317$, the first zero point of $J_1(x)$, and the integral $\int_0^x du u [J_1(u)]^2$ becomes $x^2 [J_2(x)]^2 / 2$ [68]. Combining these results, we find

$$\frac{[J_0(k_{co}^1 \rho_{co}^1)]^2 k_{cl}^1 \rho_{cl}^1}{\int_0^{\rho_{co}^1} dr r [J_0'(k_{co}^1 r)]^2} \approx 0.522 k_{co}^1 k_{cl}^1. \quad (5.77)$$

As can be seen from Eq. (5.16) to Eq. (5.23), A_{TE} , B_{TE} , λ_{TE} , A_{TM} , B_{TM} , and λ_{TM} have the same order of magnitude. Therefore, in our estimation of radiation loss, we take the values of $B_{TE}/(\lambda_{TE} - A_{TE} + B_{TE})$ and $B_{TM}/(\lambda_{TM} - A_{TM} + B_{TM})$ to be 1. Combining these approximations with Eq. (5.77), we find Eq. (5.68) and Eq. (5.75) become

$$\alpha_{TE} = 0.522 \frac{(k_{co}^1)^3}{\beta k_{cl}^1} |\lambda_{TE}|^{2N}, \quad (5.78)$$

$$\alpha_{TM} = 0.522 \left(\frac{n_{cl}^1}{n_{co}^1} \right)^2 \frac{(k_{co}^1)^3}{\beta k_{cl}^1} |\lambda_{TM}|^{2N}. \quad (5.79)$$

These two expressions can be further simplified by taking $n_{co}^1 = 1$ (air core), $\lambda = 2\pi c/\omega = 1.55\mu m$, and assuming $\beta = k_{co}^1 = \omega/\sqrt{2}c$, $k_{cl}^1 = n_{cl}^1\omega/c$:

$$\alpha_{TE}(\text{dB/km}) = 4.6 \times 10^9 \frac{1}{n_{cl}^1} |\lambda_{TE}|^{2N}, \quad (5.80)$$

$$\alpha_{TM}(\text{dB/km}) = 4.6 \times 10^9 n_{cl}^1 |\lambda_{TM}|^{2N}, \quad (5.81)$$

where the unit for radiation loss has been converted to dB/km.

Many assumptions are made to simplify Eq. (5.68) and (5.75) into Eq. (5.80) and (5.81). It is worthwhile to see how we can justify the simplified results from an intuitive point of view. Without the Bragg cladding, the light confinement can only be achieved on the order of the wavelength, which means that the radiation loss constant must be of the order of $\text{dB}/\mu m = 10^9 \text{dB/km}$. With the presence of Bragg cladding, the light amplitude reduction due to each cladding pair is λ_{TE} for TE modes and λ_{TM} for TM modes. Therefore, the radiation loss for a fiber with N Bragg cladding pairs should be of the order of $(\lambda_{TE})^{2N} \times 10^9 \text{dB/km}$ for TE modes and $(\lambda_{TM})^{2N} \times 10^9 \text{dB/km}$ for TM modes.

The values of λ_{TE} and λ_{TM} also have complicated dependence on β , n_{cl}^1 , l_{cl}^1 , n_{cl}^2 and l_{cl}^2 , as can be seen from Eq. (5.16) to Eq. (5.23). However, when the cladding layers form quarter wave stack (i.e., $k_{cl}^1 l_{cl}^1 = k_{cl}^2 l_{cl}^2 = \pi/2$) such that light is optimally confined, the expressions for $|\lambda_{TE}|$ and $|\lambda_{TM}|$ take simpler forms:

$$|\lambda_{TE}| = \min\left(\frac{k_{cl}^2}{k_{cl}^1}, \frac{k_{cl}^1}{k_{cl}^2}\right), \quad (5.82)$$

$$|\lambda_{TM}| = \min\left[\left(\frac{n_{cl}^2}{n_{cl}^1}\right)^2 \frac{k_{cl}^1}{k_{cl}^2}, \left(\frac{n_{cl}^1}{n_{cl}^2}\right)^2 \frac{k_{cl}^2}{k_{cl}^1}\right]. \quad (5.83)$$

We choose cladding layer II to be the low index medium with $n_{cl}^2 = 1.5$, typical of silica glass and polymers. With this value, it can be shown that for $0 < \beta < \omega/c$ the minimum value of $|\lambda_{TE}|$ is $\sqrt{[(n_{cl}^2)^2 - 1]/[(n_{cl}^1)^2 - 1]}$, and the minimum value of $|\lambda_{TM}|$ is n_{cl}^2/n_{cl}^1 . Substituting them into Eq. (5.80) and Eq. (5.81), we find the *minimum*

number of Bragg layer pairs required to achieve 0.2dB/km radiation loss is

$$N_{TE} = \frac{23.9 - \ln(n_{cl}^1)}{\ln[(n_{cl}^1)^2 - 1] - \ln[(n_{cl}^2)^2 - 1]} \quad (5.84)$$

for TE modes and

$$N_{TM} = \frac{23.9 + \ln(n_{cl}^1)}{2[\ln(n_{cl}^1) - \ln(n_{cl}^2)]} \quad (5.85)$$

for TM modes.

We plot Eq. (5.84) and Eq. (5.85) in Fig. 5.4. The top figure corresponds to the case of weak index contrast. For Δn less than 0.01, it takes 1000 or more cladding pairs to reach 0.2dB/km. Fabricating such large number of cladding pairs is likely to be very difficult in practice. For Δn between 0.1 and 1, we find that it takes less than 200 cladding pairs to reduce the radiation loss of TE and TM modes to 0.2dB/km. We notice that this index contrast range corresponds to what can be achieved in air core PBG fiber [104]. Of course, the light confinement in PBG fibers is achieved through two-dimensional Bragg reflection rather than one-dimensional Bragg reflection. However, if we take an effective index approach and approximate the 2D air hole patterns as alternating layers of concentric dielectric layers with high and low refractive index, the index contrast between the effective refractive indices should fall within the range of 0.1 to 1. Thus for air core PBG fibers, 0.2dB/km propagation loss can be achieved with 200 or less air hole layers. The bottom figure in Fig. 5.4 corresponds to the case of large index contrast. We notice that for Δn between 1 and 3 ($2.5 < n_{cl}^1 < 4.5$), 25 pairs may suffice to guide TE and TM modes with less than 0.2dB/km radiation loss.

We have only discussed radiation loss for TE and TM modes so far. According to the discussions in Sec. 5.2.3, modes with $m \neq 0$ are mixtures of TE and TM components in the Bragg cladding layers. Therefore, their radiation loss is determined by the TM component, since TM component is less confined and suffers more radiation loss compared with TE component, as can be seen from Fig. 5.4.

Since we use the smallest possible values for $|\lambda_{TE}|$ and $|\lambda_{TM}|$ in deriving Eq. (5.84) and Eq. (5.85), our results in Fig. 5.4 give the minimum number of Bragg pairs

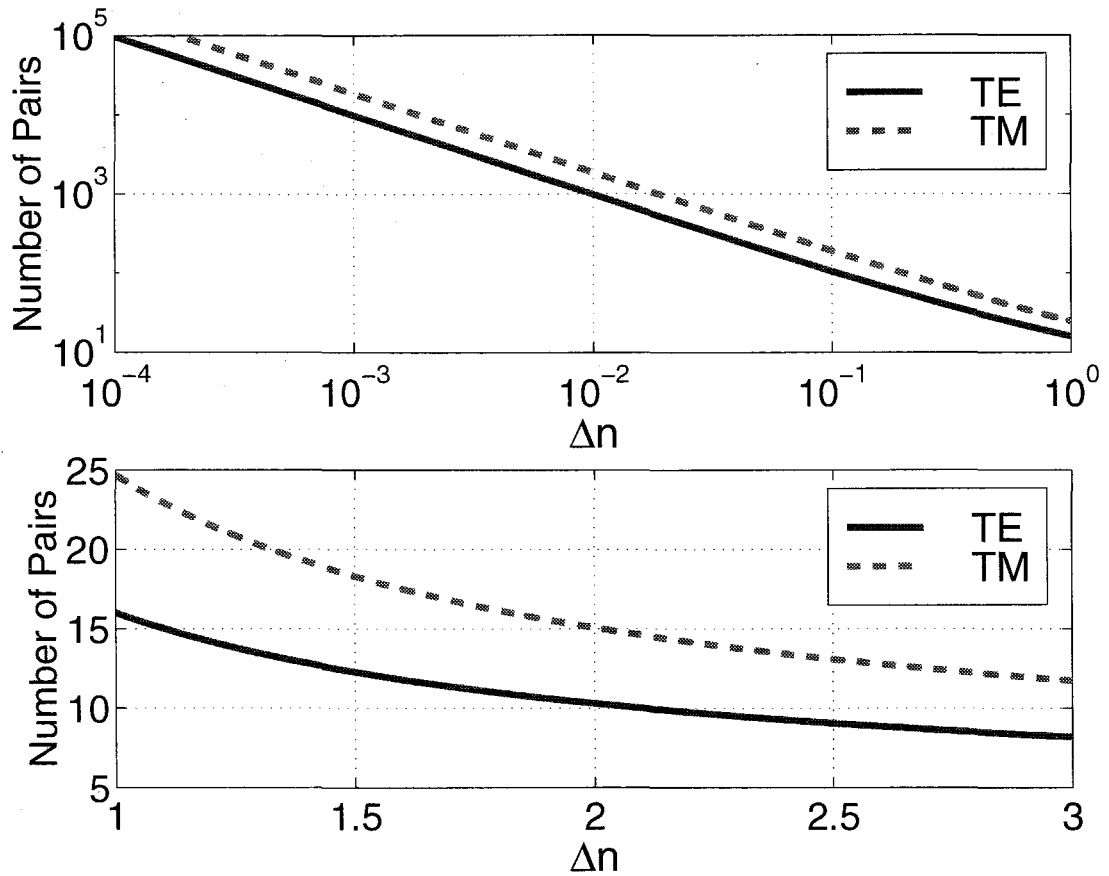


Figure 5.4: The number of Bragg cladding pairs necessary to achieve 0.2dB/km radiation loss. Δn is the index contrast between the two cladding dielectric media $n_{cl}^1 - n_{cl}^2$, with $n_{cl}^2 = 1.5$. The solid line gives the minimum Bragg pairs for TE modes to 0.2dB/km, while the dash line gives the corresponding quantity for the TM modes.

needed to achieve 0.2dB/km radiation loss and should serve as an order of magnitude estimate. Obtaining a better estimate of radiation loss requires values of β , n_{cl}^1 , l_{cl}^1 , n_{cl}^2 , and l_{cl}^2 . Once they are known, we can find λ_{TE} and λ_{TM} from Eq. (5.22) and (5.23), and substitute them into Eq. (5.78) and (5.79) for α_{TE} and α_{TM} .

One notable exception to the above estimate is worth mentioning. In an air core fiber, if β is only slightly less than ω/c , the value of k_{co}^1 can be very close to zero (whereas in deriving Eq. (5.84) and Eq. (5.85) we use $\beta = k_{co}^1 = \omega/\sqrt{2}c$). According to Eq. (5.68) and Eq. (5.75), a small k_{co}^1 can greatly reduce the radiation loss [100]. Therefore, when β becomes very close to ω/c , it may be necessary to use Eq. (5.68) and Eq. (5.75) to obtain accurate results of radiation loss.

5.4 Bragg Fiber Dispersion

Having developed the asymptotic formalism in the previous section, we shall apply it to study the dispersion properties of a Bragg fiber. The results will be compared with those obtained from 2D FDTD calculations to verify the validity of the asymptotic approach. We choose to study an air core ($n_{co}^1 = 1.0$) Bragg fiber with cladding parameters as follows: $n_{cl}^1 = 4.6$, $l_{cl}^1 = 0.25\Lambda$, $n_{cl}^2 = 1.5$ and $l_{cl}^2 = 0.75\Lambda$, where the parameters are defined in Fig. 5.2 and $\Lambda = l_{cl}^1 + l_{cl}^2$ is the total thickness of a Bragg cladding pair. We choose the air core radius to be $\rho_{co}^1 = 1.0\Lambda$. In the asymptotic calculations, the core region consists of 5 concentric dielectric layers. Using the notations in Fig. 5.2, we explicitly write out the core region parameters as $n_{co}^1 = 1.0$, $n_{co}^2 = n_{co}^4 = 4.6$, $n_{co}^3 = n_{co}^5 = 1.5$, $l_{co}^1 = 1.0\Lambda$, $l_{co}^2 = l_{co}^4 = 0.25\Lambda$, and $l_{co}^3 = l_{co}^5 = 0.75\Lambda$. In 2D FDTD calculations, we choose $\Lambda = 24$ computational cells and use 3 cladding pairs around the air core to define the Bragg fiber. In Fig. 5.4, we find that for index contrast we have chosen, 10 cladding pairs are enough to reduce the radiation loss to approximately 0.2dB/km. Not surprisingly, 3 cladding pairs should give us well defined guided modes.

Both the asymptotic results and the FDTD results are shown in Fig. 5.5, where in the top picture we plot the effective index $n_{eff} = \beta c/\omega$ as a function of ω , and in the

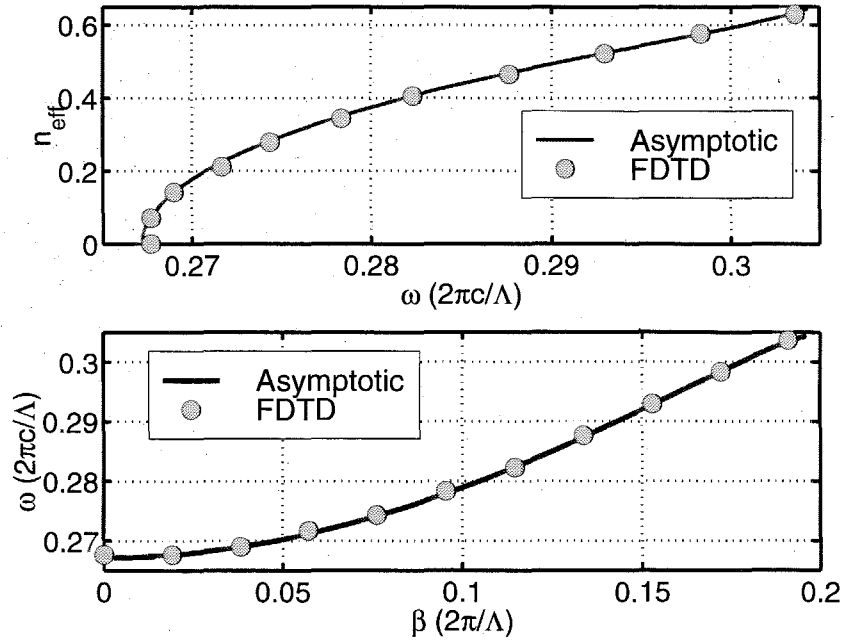


Figure 5.5: The dispersion of an air core Bragg fiber with a single $m = 1$ mode. The Bragg fiber parameters are: $n_{co}^1 = 1.0$, $\rho_{co}^1 = 1.0\Lambda$, $n_{cl}^1 = 4.6$, $l_{cl}^1 = 0.25\Lambda$, $n_{cl}^2 = 1.5$ and $l_{cl}^2 = 0.75\Lambda$. The solid line is from the asymptotic analysis, while the dots represent the 2D FDTD results. The effective indices n_{eff} is defined as $\beta c/\omega$.

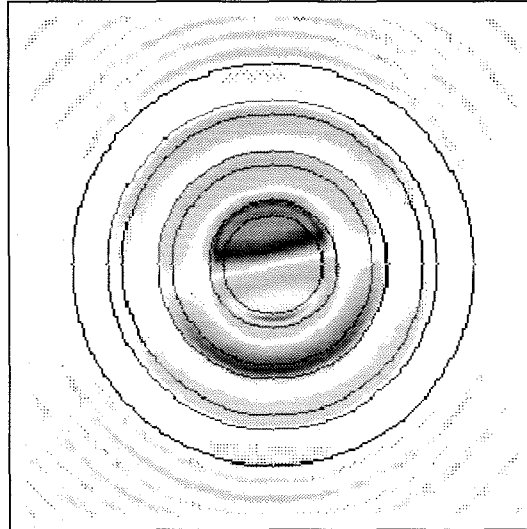


Figure 5.6: The H_z field distribution of a guided Bragg fiber mode at $\omega = 0.291(2\pi c/\Lambda)$ and $\beta = 0.143(2\pi/\Lambda)$. The parameters of the Bragg fiber are given in caption of Fig. 5.5.

bottom picture ω as a function of propagation constant β . Notice that the units for β and ω are respectively $2\pi/\Lambda$ and $2\pi c/\Lambda$. Within the frequency range shown in Fig. 5.5, both the asymptotic analysis and FDTD calculations show that the Bragg fiber supports a single guided mode with $m = 1$ propagating in the air core. In Fig. 5.5, the two approaches agree well with each other, while the small discrepancy can be attributed to the discretization error in the FDTD algorithm. In fact, if we consider that only 6 computational cells are used for l_{cl}^1 , the agreement between the asymptotic approach and FDTD approach is quite impressive.

In Fig. 5.6, we show the distribution of the H_z field obtained from FDTD calculation. The frequency and propagation constant of the mode are respectively $\omega = 0.291(2\pi c/\Lambda)$ and $\beta = 0.143(2\pi/\Lambda)$. Fig. 5.6 clearly shows that the guided mode has an azimuthal number $m = 1$ and most of the field is concentrated within the air core and the first cladding layer. The radiation field outside of the Bragg cladding can also be seen in Fig. 5.6.

As mentioned before, our asymptotic algorithm can be arbitrarily precise by incorporating more and more dielectric layers into the core region. More specifically, if we use a superscript N to denote the asymptotic results obtained using an inner core region consisting of N dielectric layers, the results should converge as a function of N to the exact solutions. With this expectation in mind, we analyze the same Bragg fiber described in the caption of Fig. 5.5 and study how the results depend on the number of inner core region layers. We first choose a core region consisting of 7 dielectric layers (including the center air core plus 3 cladding pairs) and calculate the effective index of the Bragg fiber. We denote the result as n_{eff}^7 and use this as the standard for comparison. Then we calculate the effective indices using 1, 3 and 5 inner core layers and respectively denote the results as n_{eff}^1 , n_{eff}^3 , and n_{eff}^5 . The absolute value of the difference of between these values and n_{eff}^7 are plotted in Fig. 5.7 (i.e., $|n_{eff}^1 - n_{eff}^7|$, $|n_{eff}^3 - n_{eff}^7|$, and $|n_{eff}^5 - n_{eff}^7|$).

We first notice that the difference between n_{eff}^1 , where the core region consists of only the air core, and the standard n_{eff}^7 is quite large. In fact, as frequency approaches $0.265(2\pi/\Lambda)$, the cutoff frequency of the guided mode, the difference between the two

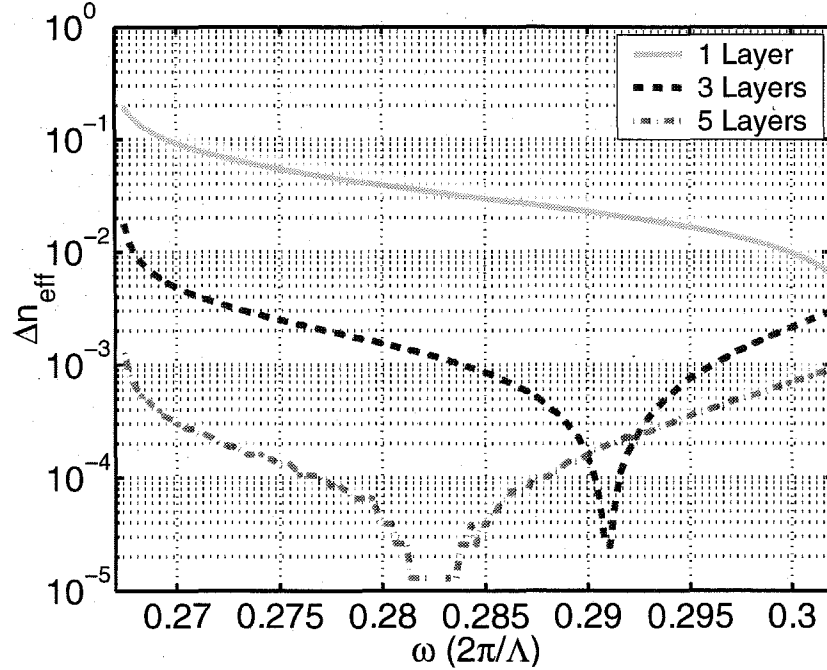


Figure 5.7: The deviation of the effective indices obtained using various inner core region layers. We use n_{eff}^N to denote the effective index obtained using a N layer core region. The curves labeled with “1 layer,” “3 layers,” and “5 layers” represent respectively $|n_{eff}^1 - n_{eff}^7|$, $|n_{eff}^3 - n_{eff}^7|$, and $|n_{eff}^5 - n_{eff}^7|$. The parameters of the Bragg fiber are given in the caption of Fig. 5.5.

values reaches 0.2, which is quite significant. On the other hand, with the addition of only one cladding pair into the core region, the deviation between the effective indices ($|n_{eff}^3 - n_{eff}^7|$) is reduced below 0.02, a $10\times$ reduction compared with $|n_{eff}^1 - n_{eff}^7|$. As one more cladding pair added into the core region, $|n_{eff}^5 - n_{eff}^7|$ is below 0.001. This suggests that the difference between asymptotic results and exact solutions should also be of the same order of magnitude. Thus we can conclude that asymptotic results with inner core region consisting of the first 5 dielectric layers offer an excellent approximation of the exact solution.

At the end of Sec. 5.2.3, we described how to find the field distribution using the asymptotic approach. Basically, we must first obtain the propagation constant using Eq. (5.41). Substituting the result into Eq. (5.42) and Eq. (5.43), we obtain the modal amplitude coefficients in the first layer of the cladding region (i.e., f_{TM} and f_{TE}) and those in the center air core (i.e., \mathcal{A}_{TM} and \mathcal{C}_{TE}), respectively. Then the cladding fields

are easily found from Eq. (5.10) and Eq. (5.11), while the core fields are obtained by applying Eq. (5.6) and Eq. (5.8) repeatedly. We apply this algorithm to study the field distribution of the guided Bragg fiber mode at $\omega = 0.286(2\pi c/\Lambda)$. Using a core region of 5 layers, we find the propagation constant to be $\beta = 0.128(2\pi/\Lambda)$. The field distribution given by this asymptotic approach is represented by the solid lines in Fig. 5.8.

Having obtained the field distribution using the asymptotic algorithm, naturally we would like to know how accurate the asymptotic approximation works *without* having to check asymptotic results using either the original algorithm by Yeh et al. or the FDTD method. We notice that the essence of the whole asymptotic algorithm is that the field distribution in the cladding region can be well described in the asymptotic limit. As long as this condition is satisfied, the asymptotic approach should provide a satisfactory description of the guided mode. To check the accuracy of the asymptotic approximation in the cladding region, we can calculate the *exact* field distribution in the cladding region by repeatedly applying Eq. (5.6) and (5.8). We use “exact solution” to denote results obtained this way. In other word, to find the “exact solution,” we still need to find \mathcal{A}_{TM} and \mathcal{C}_{TE} using Eq. (5.41), (5.42) and (5.43), as described in the previous paragraph. The only difference between the “exact solution” and the asymptotic solution is that for the “exact solution,” the field distribution in the entire Bragg fiber is obtained from Eq. (5.6) and (5.8). Consequently, within the core region, the “exact solution” and the asymptotic solution are the same. In the cladding region, the two solutions differ from each other, and their difference indicates how well the asymptotic approximation works. In Fig. 5.8, the “exact solutions” are represented by the dots. As expected, the “exact solution” and the asymptotic solution are the same within the core region. However, even in the cladding region, the difference between the two solutions are very small. Thus we can conclude that the asymptotic algorithm gives an accurate description of the field distribution of the guided mode.

We notice that the free space wavelength of the mode is $\lambda = 3.5\Lambda$, which means that the ratio of the air core radius and the photon wavelength is only 0.286. Inspect-

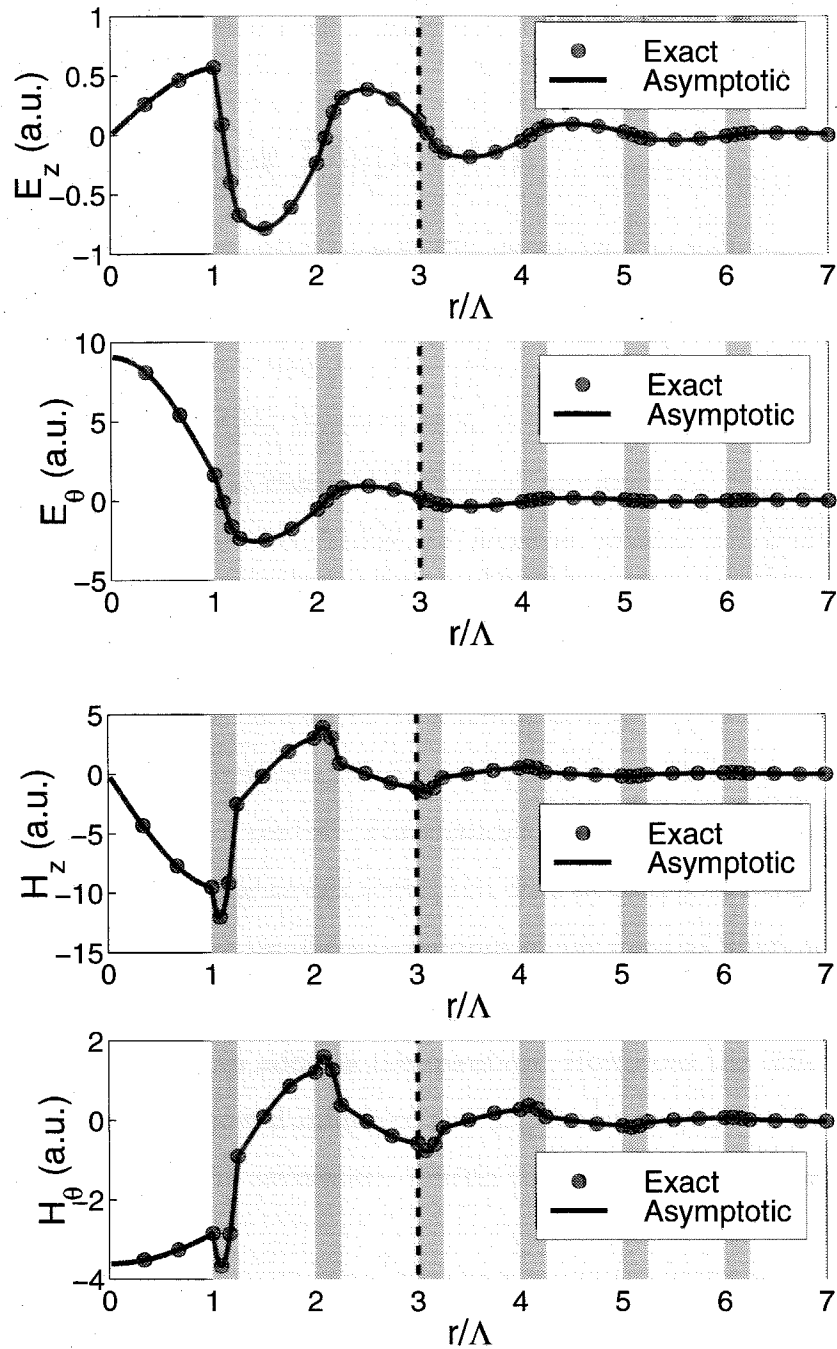


Figure 5.8: The electromagnetic field distribution of the guided Bragg fiber mode at $\omega = 0.286(2\pi c/\Delta)$. The interface between the core region and cladding region is indicated by dash line. The exact solutions are obtained using Eq. (5.6) and (5.8) only. The asymptotic solutions are obtained using Eq. (5.6) and Eq. (5.8) in the core region, and Eq. (5.10) and (5.11) in the cladding region.

ing Fig. 5.7 and Fig. 5.8, we find it quite amazing that for such small air core radius, the asymptotic approximation with 5 inner core layers works so well.

5.5 Coaxial Fiber Dispersion

It is well known that the fundamental TEM mode of a metallic coaxial cable has no polarization effect or any modal dispersion, which make it very attractive for transmitting electromagnetic signals. The problem is that metals are very lossy in the optical range. In Ref. [105], Ibanescu et al. drew an analogy between the metallic coaxial cables and dielectric coaxial fibers, and proposed to use dielectric coaxial fibers in optical communications. There are, however, several important problems to be solved before coaxial fibers can find wide applications in optical telecommunication. Firstly, it is critical that the coaxial fiber mode has small dispersion within the entire telecom frequency window instead of at a single point. Secondly, we should keep in mind that the analogy between omnidirectional mirrors and high refractive index materials with metals is not perfect. For example, if the outer cladding of a metallic coaxial cable is taken out, the center metal rod does not support lossless propagating mode. Yet if we take away the Bragg cladding of the coaxial fiber, the center high index dielectric rod resembles an optical fiber and supports at least one propagating mode. Naturally we need to address the question: How does the difference between high index dielectric and metal influence the dispersion properties of coaxial fibers? In this section, we apply the asymptotic matrix theory to address the aforementioned problems.

As in Bragg fibers, each guided coaxial fiber mode can be classified according to its propagation constant β (momentum in the z direction) and angular momentum m . Using the asymptotic method, we analyze one of the coaxial fibers studied in Ref. [105]. For the high index medium of the coaxial fiber cladding, we choose $n_{cl}^1 = 4.6$ and $l_{cl}^1 = (1/3)\Lambda$, whereas for the low index cladding medium we have $n_{cl}^2 = 1.6$ and $l_{cl}^2 = (2/3)\Lambda$. Λ is the total thickness of the Bragg cladding pair. The parameters of the Bragg stack are chosen such that it forms an omnidirectional reflector [105].

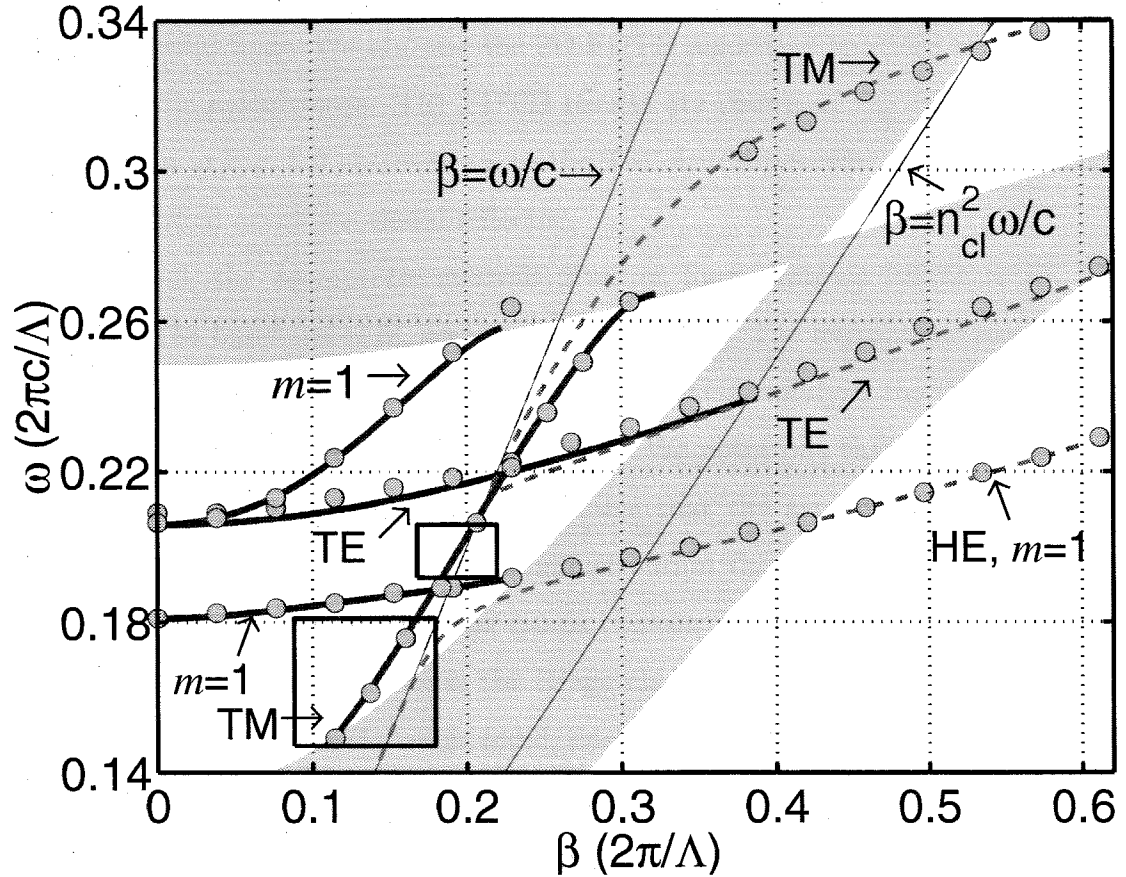


Figure 5.9: Dispersion of the coaxial fiber. The points in the shaded region indicate the existence of propagating TM cladding modes in the omnidirectional reflector. The thick solid lines are results obtained from asymptotic analysis. The dots represent the 2D FDTD results. The light lines in air ($\beta = \omega/c$) and in the low index medium of the Bragg cladding ($\beta = n_{cl}^2 \omega/c$) are also shown. If the omnidirectional cladding is taken away, the center core of the coaxial fiber resembles a conventional optical fiber and supports three guided modes: HE, TE and TM modes. Their dispersions are calculated using the formulae for conventional optical fibers and are shown as dash lines. The single mode windows for the TM band are illustrated in the figure as two boxes.

The refractive index and radius of the center core are respectively $n_{co} = 4.6$ and $l_{co} = 0.4\Lambda$. The refractive index and thickness of the coaxial region are respectively $n_{coax} = 1$ and $l_{coax} = 1.0\Lambda$. We use four core layers in our asymptotic calculations and normalize the results with respect to Λ . The asymptotic results are shown in Fig. 5.9 as thick solid lines. We also use the 2D FDTD algorithm to verify the validity of our asymptotic calculations. The FDTD results are shown in Fig. 5.9 as dots. The shaded region in Fig. 5.9 corresponds to the TM cladding modes that can propagate in the cylindrical omnidirectional reflector.

In Fig. 5.9, the asymptotic analysis gives us four photonic bands, a TE band ($m = 0$), a TM band ($m = 0$), and two $m = 1$ bands. The asymptotic results agree well with FDTD calculations, considering that in FDTD analysis the thickness of the high index cladding is only 8 calculation cells. We point out that the TE band was missed in the results in Ref. [105]. We notice that the asymptotic results for the TM band and two $m = 1$ bands are confined within the region of TM gap. This is simply due to the fact that all three bands contain TM components [106] and that the TM components must decay in the Bragg cladding to define guided coaxial fiber modes. The TE band, on the other hand, does not contain any TM component [106] and asymptotic analysis gives us guided TE modes up to the light line in cladding medium II ($\beta = n_{cl}^2\omega/c$). After crossing the light line, fields in cladding medium II can no longer be described by the asymptotic analysis in Sec. 5.2. The excellent agreement between the asymptotic analysis and FDTD calculations demonstrates the validity of asymptotic approach.

As mentioned before, if we take out the Bragg cladding, the center dielectric core becomes a conventional optical fiber whose modal dispersion is well known [69]. The dispersion of these conventional fiber modes was plotted in Fig. 5.9 as dash lines. Comparing the conventional fiber modes with the FDTD calculations of the full coaxial fiber, we find excellent correspondence between the two for the region below the air light line $\beta = \omega/c$. This strongly suggests that once the guided coaxial fiber modes pass through the air light line, the main confining mechanism is actually provided by the center high index core. To see this point more clearly, we show two

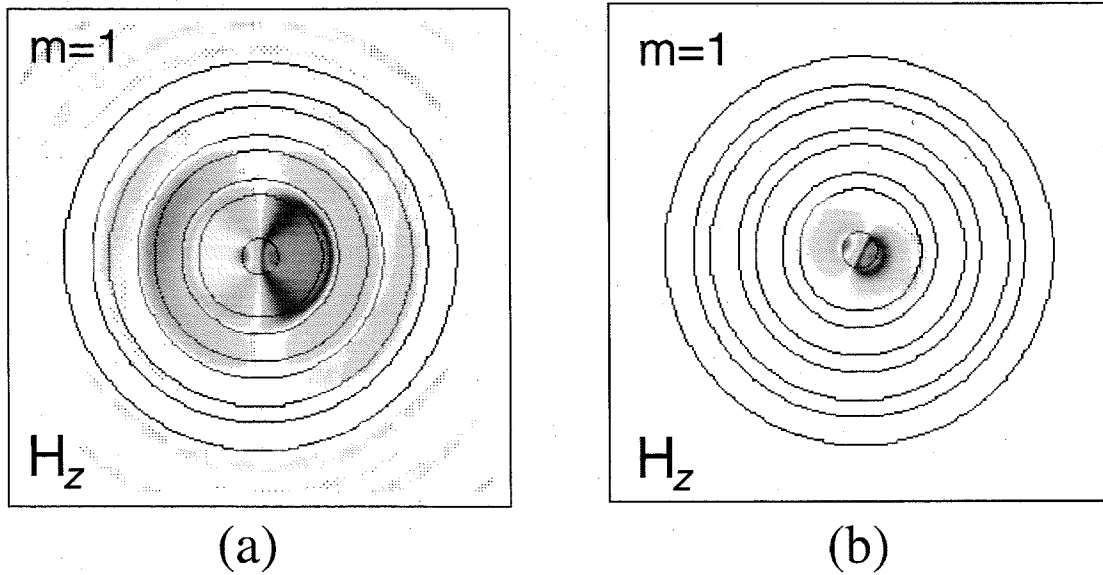


Figure 5.10: The H_z field distributions of the lower $m = 1$ band. In (a), the guided mode has $\beta = 0.153(2\pi/\Lambda)$ and $\omega = 0.187(2\pi c/\Lambda)$. In (b), the guided mode has $\beta = 0.611(2\pi/\Lambda)$ and $\omega = 0.229(2\pi c/\Lambda)$.

FDTD calculations of field distribution of the lower $m = 1$ band. The $m = 1$ mode in Fig. (5.10a) has $\beta = 0.153(2\pi/\Lambda)$, $\omega = 0.187(2\pi c/\Lambda)$ and belongs to the TM bandgap above the air light line. For any modes above light line, guiding cannot be achieved through total internal reflection and therefore in Fig. (5.10a) we observe a substantial field distribution in both the coaxial region (air) and the Bragg cladding. The $m = 1$ mode in Fig. (5.10b) has $\beta = 0.611(2\pi/\Lambda)$, $\omega = 0.229(2\pi c/\Lambda)$ and is clearly below the air light line. As expected, the guided coaxial fiber mode becomes essentially the HE mode of a conventional fiber, with optical fields concentrated in the center dielectric core and only a negligible amount in the Bragg cladding.

Not only does the total internal reflection play a significant role in the modal dispersion of the guided coaxial fiber below the light line, it also must be taken into account in determining the frequency window of single mode operation. The lower single mode window, as shown in Fig. 5.9, simply contains all the TM modes below the cutoff frequency of the lower $m = 1$ band. However, finding the higher single mode window is more trickier. As the lower $m = 1$ band enters the shaded region in Fig. 5.9, the TM field component loses confinement in the Bragg cladding and the

$m = 1$ band is no longer a well defined guided mode. Thus the second single TM mode window in Fig. 5.9 begins at the lower intersection of the $m = 1$ band and the TM gap, and ends at the smallest of the following frequencies: the cutoff frequency of the higher $m = 1$ band, the cutoff frequency of the TE band, and the higher intersection point of the lower $m = 1$ band and the TM gap where the lower $m = 1$ band enters again into the TM gap. The two single frequency windows are shown in Fig. 5.9 as two boxes. Within the higher single frequency window, the $m = 1$ quasi-band, even though not well confined, can still have low loss due to total internal reflection in the coaxial air region. In fact, that is exactly why FDTD algorithm can give us $m = 1$ and TM band outside of the TM gap. To study the influence of the $m = 1$ quasi-band on the single mode operation of TM band, however, is beyond the scope of this section.

For the long distance communication fibers, the dispersion parameter D , which is defined as $-\frac{2\pi c}{\lambda^2} \frac{d^2\beta}{d\omega^2}$ [69], should remain small within the entire telecommunication window. In Fig. 5.11, we show the dispersion parameter D calculated from the asymptotic results. The wavelength λ is normalized such that the TM band crosses air light line $\beta = \omega/c$ at $1.55\mu m$. The two single frequency windows are identified in Fig. 5.11 as shaded region. We immediately notice that the dispersion parameter D takes very large value at most frequencies and can be both positive and negative. Around $1.6\mu m$ [$\omega = 0.202(2\pi c/\Lambda)$], D crosses the point of zero dispersion but remains small only within a very small frequency range. In Ref. [105], Ibanescu et al. predicted a point of zero dispersion. Our results in Fig. 5.11 confirm their prediction, yet at the same time, point out an important problem: The frequency window of small D is too narrow for optical signal transmission.

In Fig. 5.12, we show E_z and H_θ components of the TM mode at the zero dispersion frequency $\omega = 0.202(2\pi c/\Lambda)$. Since the magnetic field of a TM mode contains only H_θ component, from Fig. 5.12 it is obvious that there is substantial presence of electromagnetic field in the high index core and the optical intensity in the high index core is comparable to that in the air coaxial region. As a result, using this coaxial fiber mode to guide light does not provide much benefit in terms of reducing material

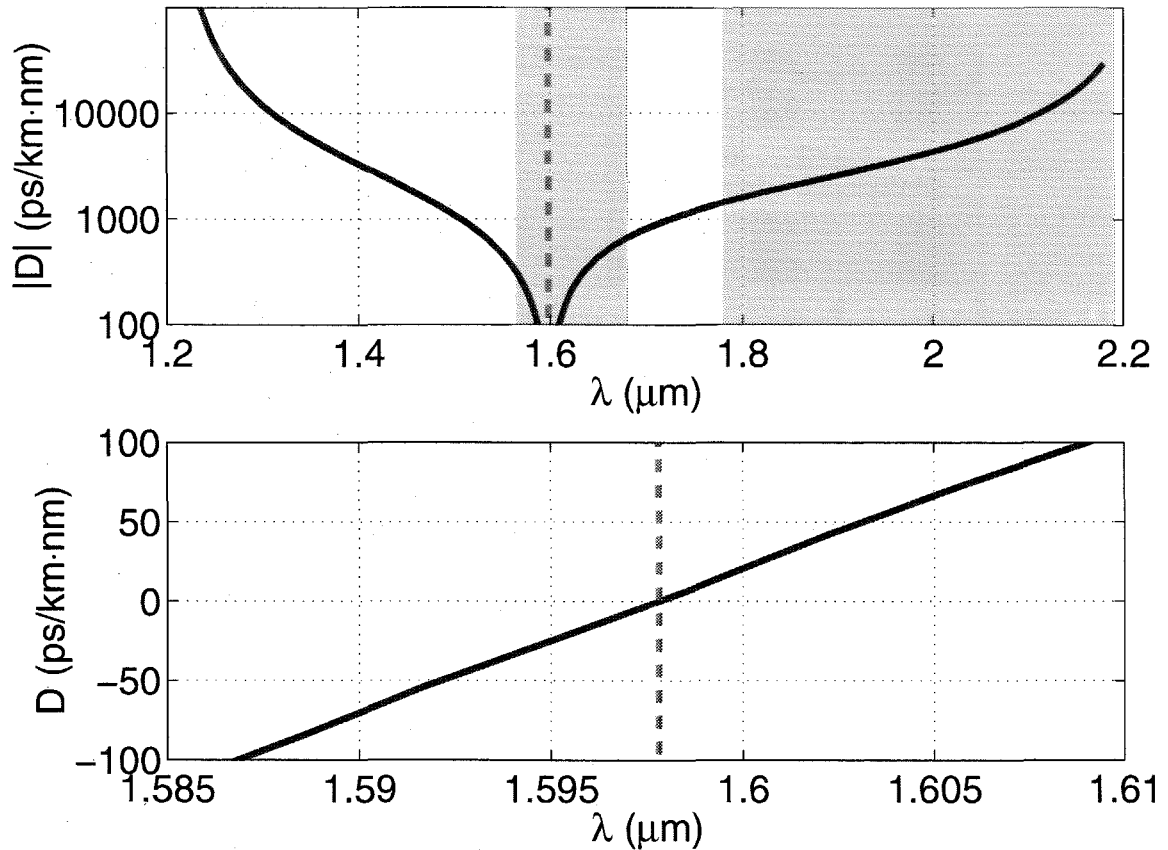


Figure 5.11: Dispersion parameter D of the coaxial fiber TM band. At $\lambda = 1.598\mu\text{m}$ [or $\omega = 0.202(2\pi c/\Lambda)$], the dispersion parameter D becomes zero, which is shown as the dash line. In the upper diagram, the absolute values of D are shown in a log scale. The two single mode windows in Fig. 5.9 are shown as shaded regions. To the left of the dash line, D is negative, whereas D is positive to the right of the dash line. In the lower diagram, D is shown in the linear scale.

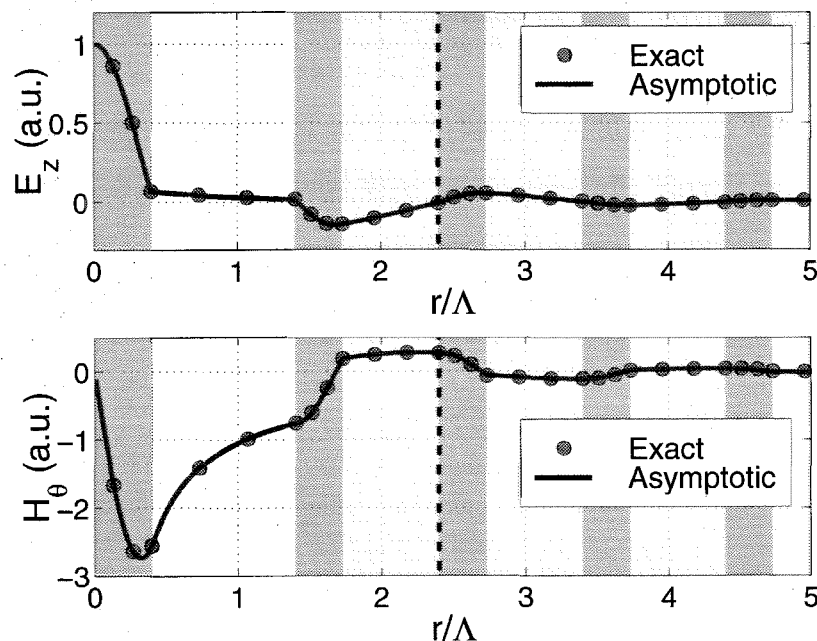


Figure 5.12: The E_z and H_θ fields of the TM coaxial fiber mode at $\omega = 0.202(2\pi c/\Lambda)$. The unshaded, light, and dark regions respectively represent air ($n_{coax} = 1$), low index dielectric medium ($n_{cl}^2 = 1.6$) and high index dielectric medium ($n_{cl}^1 = 4.6$). The units for electric field and magnetic field are chosen such that $\epsilon_0 = 1$ and $\mu_0 = 1$. The asymptotic solutions and the exact solutions are obtained in the same way as in the caption of Fig. 5.8.

absorption and nonlinear effects. This also illustrates that the analogy between dielectric coaxial fibers and metallic coaxial cables is not perfect. Turning our attention to the cladding field, we find that the field strength in the first cladding pairs, even though relatively small, is not negligible. In fact, the fields in the first Bragg pairs cannot be neglected, since optical fields must penetrate at least one cladding pair to experience Bragg confinement. This also explains the large modal dispersion we find in Fig. 5.11, since any guided coaxial fiber mode must “feel” several different dielectric media: the high index core, air in the coaxial region, the high index cladding, and the low index cladding. In contrast, for conventional optical fibers, the guided modes are defined by the silica core and cladding whose index difference is generally less than 0.01.

In conclusions, we find that both Bragg reflection and total internal reflection play

important roles in determining modal dispersion of the coaxial fiber. The analogy between dielectric coaxial fibers and metallic coaxial cable are not entirely accurate, and there is substantial amount of optical fields in the high index core and the Bragg cladding. As a result, guided coaxial fiber mode generally have large dispersion.

Chapter 6

Conclusions

In the previous chapters, it is demonstrated that evanescent coupling and Bragg reflection, as confinement mechanism, lead to many possibilities that are difficult to achieve using conventional guiding via total internal reflection.

In coupled resonator optical waveguides (CROW), the photons propagate by “hopping” from one resonator to its closest neighbors, which leads to substantially reduced group velocity and dramatically modified dispersion relation. Both these properties are very useful in nonlinear optics. In Sec. 3.5, we take second harmonic generation (SHG) as an example and derive expressions for the SHG efficiency. In the derivation, two observations are of special importance and can be applied to many other nonlinear optical processes besides SHG. First, we notice

$$P \propto |E|^2 v_g, \quad (6.1)$$

where $|E|$ stands for the strength of the electric field, P is the power flux, and v_g is the group velocity of the photons. Consequently, in CROW's with small group velocity, a modest power input can lead to a large electric field strength, which in turn leads to more efficient nonlinear optical processes. Another consequence of the slow group velocity is that photons become much heavier. Again take SHG as an example, when

both the fundamental mode photons and the second harmonic mode photons travel much slower, the effective interaction time between them becomes longer for a given traveling length, as can be seen from the factor $v_{2\omega,g}$ in Eq. (3.39). This also leads to an enhancement of the nonlinear efficiency. Secondly, we observe that for the SHG process, the phase matching condition is changed into

$$K_1(\omega) + K_2(\omega) = K(2\omega) + n\frac{2\pi}{R}, \quad n = 0, \pm 1, \pm 2 \dots, \quad (6.2)$$

as can be seen from Eq. (3.40). The term $n2\pi/R$ in Eq. (6.2) corresponds to the Bloch vector of the 1D periodic structures. It is easy to see that the appearance of the Bloch vector in any phase matching condition should be universal, since the “real” photon momentum in any periodic structures is always the “crystal” momentum within the first Brillouin zone plus some integral multiples of the Bloch vectors of the periodic media. For many nonlinear optical processes, the addition of the Bloch vectors should make the phase matching condition easier to achieve.

Even though only two examples of CROW’s are studied in Chapter 3, the CROW bands appear in many other cases. In photonic crystals, many optical bands above the bandgap have the characteristics of CROW bands [24, 27]. We can apply tight binding approximation to study many interesting phenomena of those bands, such as superprism effect [21] and soliton propagation in CROW-type bands.

To achieve low propagation loss in Bragg fibers and dielectric coaxial fibers, it is necessary to use dielectric materials with large index contrast. Consequently, the guided modes tend to have large modal dispersion, which makes this type of fibers very interesting for the purpose of dispersion compensation. However, further calculations are needed to understand the complex dispersion behavior of Bragg fibers and dielectric coaxial fibers. Another interesting phenomenon is that the effective index of guided modes in Bragg fibers and coaxial fibers can be less than one, where the phase velocity is greater than the speed of light in free space. This unique property cannot be achieved in conventional fibers, and may lead to many interesting applications.

In the scattering theory analysis of waveguide-resonator coupling, we find that

the reflection/transmission characteristics of the composite system depend strongly on the strength of the waveguide-resonator coupling, the gain/loss of the high Q mode, and various properties of the cavity modes such as degeneracy and symmetry. Such dependence provides an efficient way of controlling the waveguide transmission and reflection using nonlinear optical effects, such as electro-optical effects and Kerr nonlinearity [111]. The improved efficiency is mainly due to two effects. First, at the cavity resonance, the cavity field amplitude is enhanced by a factor of Q , as shown in Eq. (4.32). Second, both the waveguide-resonator coupling and the cavity loss can be made very small. In this case, to completely change the transmission and reflection coefficients of the coupled system, we only need to modify the waveguide-resonator coupling by a small amount comparable to the cavity loss and vice versa (i.e., “critical coupling” in Ref. [87]). Another possibility is to modify the group velocity of the indirect CROW through changing the waveguide-resonator coupling.

The above mentioned effects are all classical effects in the sense that they can be understood purely from Maxwell equations. However, by strongly modifying the photonic density of states, periodic dielectric materials can also fundamentally change the interaction between atoms and photons. A well know example is the enhancement or the inhibition of the spontaneous emission rate by embedding the atoms in a high Q cavity [43] or photonic crystals [12]. A fascinating consequence of the modified spontaneous emission rate is the dramatically reduced threshold for nonlinear optical phenomena [112]. It should be emphasized that this effect is completely different from the enhancement of nonlinear optical efficiency due to group velocity reduction. Another interesting application of photonic crystals is to introduce a high Q defect cavity to increase the atom-photon coupling. When the atom-photon coupling is much larger than the cavity photon decay rate and atomic dephasing rate, the atom-photon coupling enters into the strong-coupling regime, which is of great interest in cavity QED [113].

Bibliography

- [1] H. Kolgenik, and C. V. Shank, "Coupled wave theory of distributed feedback lasers," *J. Appl. Phys.*, vol. 43, pp. 2327-2335, 1972.
- [2] A. Yariv, "Coupled mode theory for guided wave optics," *IEEE J. Quantum Electron.*, vol. 9, pp. 919-933, 1973.
- [3] G. Meltz, W. W. Morey, and W. H. Glenn, "Formation of Bragg gratings in optical fibers by a transverse holographic method," *Opt. Lett.*, vol. 14, pp. 823-825, 1989.
- [4] H. W. Yen, M. Nakamura, E. Garmire, S. Somekh, A. Yariv, and H. L. Garvin, "Optically pumped GaAs waveguide lasers with a fundamental 0.11μ corrugated feedback," *Opt. Commun.*, vol. 9, pp. 35-37, 1973.
- [5] P. Yeh, A. Yariv, and C. S. Heng, "Electromagnetic propagation in periodic stratified media I: general theory," *J. Opt. Soc. Am.*, vol. 67, pp. 423-438, 1977.
- [6] G. A. Evans, and J. M. Hammer, Eds., *Surface emitting semiconductor lasers and arrays*, Quantum Electronics — Principles and Applications, Academic Press, New York, 1993.
- [7] E. F. Schubert, N. E. J. Hunt, M. Micovic, R. J. Malik, D. L. Sivco, A. Y. Cho and G. J. Zydzik, "Highly efficient light-emitting diodes with microcavities," *Science*, vol. 265, pp. 943-945. 1994.

- [8] M. A. Duguay, Y. Kokubun, T. L. Koch, and L. Pfeiffer, "Antiresonant reflecting optical wave-guiding in SiO₂-Si multilayer structures," *App. Phys. Lett.*, vol. 49, pp. 13-15, 1986.
- [9] P. Yeh, and A. Yariv, "Bragg reflection waveguides," *Opt. Commun.*, vol. 19, pp. 427-430, 1976.
- [10] A. Y. Cho, A. Yariv, and P. Yeh, "Observation of confined propagation in Bragg waveguides," *Appl. Phys. Lett.*, vol. 30, pp. 471-472, 1977.
- [11] J. D. Joannopoulos, R. D. Meade, and J. N. Winn, *Photonic Crystals*, Princeton, New Jersey, 1995.
- [12] E. Yablonovitch, "Inhibited spontaneous emission in solid-state physics and electronics," *Phys. Rev. Lett.*, vol. 58, pp. 2059-2062, 1987.
- [13] S. John, "Strong Localization of Photons in Certain Disordered Dielectric Superlattices," *Phys. Rev. Lett.*, vol. 58, pp. 2486-2489, 1987.
- [14] S. John, and K. Butsch, "Photonic bandgap formation and tunability in certain self-organizing systems," *J. Lightwave Technol.*, vol. 17, pp. 1931-1943, 1999.
- [15] S. Fan, P. R. Villeneuve, J. D. Joannopoulos, and E. F. Schubert, "High extraction efficiency of spontaneous emission from slabs of photonic crystals," *Phys. Rev. Lett.*, vol. 78, pp. 3294-3297, 1997.
- [16] M. Boroditsky, R. Vrijen, T. F. Krauss, R. Coccioli, R. Bhat, and E. Yablonovitch, "Spontaneous emission extraction and Purcell enhancement from thin-film 2D photonic crystals," *J. Lightwave Technol.*, vol. 17, pp. 2096-2112, 1999.
- [17] P. St. J. Russell, S. Tredwell, and P. J. Roberts, "Full photonic bandgaps and spontaneous emission control in 1D multilayer dielectric structures," *Opt. Commun.*, vol. 160, pp. 66-71, 1999.

- [18] S. Y. Lin, and J. G. Fleming, "A three-dimensional optical photonic crystal," *J. Lightwave Technol.*, vol. 17, pp. 1944-1947, 1999.
- [19] S. Noda, N. Yamamoto, M. Imada, H. Kobayashi, and M. Okano, "Alignment and stacking of semiconductor photonic bandgaps by wafer-fusion," *J. Lightwave Technol.*, vol. 17, pp. 1948-1955, 1999.
- [20] T. K. Krauss, and R. M. De La Rue, "Photonic crystals in the optical regime — past, present and future," *Prog. in Quantum Electron.*, vol. 23, pp. 51-96, 1999.
- [21] H. Kosaka, T. Kawashima, A. Tomita, M. Notomi, T. Tamamura, T. Sato, and S. Kawakami, "Superprism phenomena in photonic crystals: towards microscale lightwave circuits," *J. Lightwave Technol.*, vol. 17, pp. 2032-2038, 1999.
- [22] A. Imhof, W. L. Vos, R. Sprik, and A. Lagendijk, "Large dispersive effects near the band edges of photonic crystals," *Phys. Rev. Lett.*, vol. 83, pp. 2942-2945, 1999.
- [23] P. Halevi, A. A. Krokhin, and J. Arriaga, "Photonic crystal optics and homogenization of 2D preiodic composites," *Phys. Rev. Lett.*, vol. 82, pp. 719-722, 1999.
- [24] E. Lidorikis, M. M. Sigalas, E. N. Economou, and C. M. Soukoulis, "Tight-binding parameterization for photonic band gap materials," *Phys. Rev. Lett.*, vol. 81, pp. 1405-1408, 1998.
- [25] A. Adibi, Y. Xu, R. K. Lee, and A. Yariv, "Properties of the slab modes in photonic crystal optical waveguides," *J. Lightwave Technol.*, vol. 18, pp. 1554-1564, 2000.
- [26] N. W. Ashcroft, and N. D. Mermin, *Solid State Physics*, Saunders, Philadelphia, 1976.
- [27] T. J. Shepherd, P. J. Roberts, and R. Loudon, "Soluble two-dimensional photonic crystal model," *Phys. Rev. E*, vol. 55, pp. 6024-6038, 1997.
- [28] A. Yariv, and P. Yeh, *Optical Waves in Crystals*, Wiley, New York, 1984.

- [29] K. S. Yee, "Numerical solution of initial boundary value problems involving Maxwell's equations in isotropic media," *IEEE Trans. Antennas Propag.*, vol. AP-14, pp. 302-307, 1966.
- [30] A. Taflove, *ed.* "Advances in computational electromagnetics, the finite difference time domain method," (Artech House, Boston, 1998).
- [31] M. D. Feit, and J. A. Fleck, "Light propagation in graded-index optical fibers," *Appl. Opt.*, vol. 17, pp. 3990-3998, 1978.
- [32] A. Asi, L. Shafai, "Dispersion analysis of anisotropic inhomogeneous waveguide using compact 2D-FDTD," *Electron. Lett.*, vol. 28, pp. 1451-1452, 1992.
- [33] F. Zepparelli, P. Mezzanotte, F. Alimenti, L. Roselli, R. Sorrentino, G. Tartarini, and P. Bassi, "Rigorous analysis of 3D optical and optoelectronic devices by the compact-2D-FDTD method," *Opt. and Quantum Electron.*, vol. 31, pp. 827-841, 1999.
- [34] Y. Chen, R. Mittra, and P. Harms, "Finite-difference time domain algorithm for solving Maxwell's equations in rotationally symmetric geometries," *IEEE Trans. Microwave Theory Tech.* vol. 44, pp. 832-839, 1996.
- [35] J. P. Berenger, "A perfectly matched layer for the absorption of electromagnetic waves," *J. Computat. Phys.*, vol. 114, pp. 185-200, 1994.
- [36] S. D. Gedney, "An anisotropic perfectly matched layer-absorbing medium for the truncation of FDTD lattices," *IEEE Trans. Antennas Propag.*, vol. 44, pp. 1630-1639, 1996.
- [37] R. J. Glauber and M. L. Lewenstein, "Quantum optics of dielectric media," *Phys. Rev. A*, vol. 43, pp. 467-491, 1991.
- [38] C. H. Henry and R. F. Kazarinov, "Quantum noise in photonics," *Rev. Mod. Phys.*, vol. 68, pp. 801-853, 1996.

- [39] Y. Xu, R. K. Lee, and A. Yariv, "Quantum and the classical analysis of spontaneous emission in a microcavity - art. no. 033807," *Phys. Rev. A*, vol. 61, pp. 3807-+, 2000.
- [40] W. H. Press, S. A. Teukolsky, W. T. Vetterling, B. P. Flannery, *Numerical Recipes in C*, Cambridge University Press, New York, 1995.
- [41] Y. Xu, J. S. Vuckovic, R. K. Lee, O.J. Painter, A. Scherer, and A. Yariv, "Finite-difference time-domain calculation of spontaneous emission lifetime in a microcavity," *J. Opt. Soc. Am. B*, vol. 16, pp. 465-474, 1999.
- [42] Y. Xu, R. K. Lee, and A. Yariv, "Finite-difference time-domain analysis of spontaneous emission in a microdisk cavity - art. no. 033808," *Phys. Rev. A*, vol. 61, pp. 3808-+, 2000.
- [43] E. M. Purcell, "Spontaneous emission probabilities at radio frequencies," *Phys. Rev.*, vol. 69, pp. 681, 1946.
- [44] R. K. Lee, Y. Xu, and A. Yariv, "Modified spontaneous emission from a two-dimensional photonic bandgap crystal slab," *J. Opt. Soc. Amer. B*, vol. 17, pp. 1438-1442, 2000.
- [45] D. E. Merewether, R. Fisher, and F. W. Smith, "On implementing a numeric Huygen's source scheme in a finite difference program to illuminate scattering bodies," *IEEE. Trans. Nuc. Sci.*, vol. NS-27, pp. 1829-1833, 1980.
- [46] R. Holland, and J. W. Williams, "Total-field versus scattered-field finite-difference codes: a comparative assessment," *IEEE Trans. Nuc. Sci.*, vol. NS-30, pp. 4583-4588, 1983.
- [47] Y. Xu, R. K. Lee, and A. Yariv, "Adiabatic coupling between conventional dielectric waveguides and waveguides with discrete translational symmetry," *Opt. Lett.*, vol. 25, pp. 755-757, 2000.

- [48] A. Yariv, Y. Xu, R. K. Lee, and A. Scherer, "Coupled-resonator optical waveguide: a proposal and analysis," *Opt. Lett.*, vol. 24, pp. 711-713, 1999.
- [49] Y. Xu, R. K. Lee, and A. Yariv, "Propagation and second harmonic generation in a coupled-resonator optical waveguide," *J. Opt. Soc. Amer. B*, vol. 17, pp. 387-400, 2000.
- [50] S. L. McCall, A. F. Levi, R. E. Slusher, S. J. Pearton, and R. L. Logan, "Whispering-gallery mode microdisk lasers," *Appl. Phys. Lett.*, vol. 60, pp. 289-291, 1992.
- [51] N. C. Frateschi, and A. F. Levi, "The spectrum of microdisk lasers," *J. Appl. Phys.*, vol. 80, pp. 644-653, 1996.
- [52] R. D. Meade, A. Devenyi, J. D. Joannopoulos, O. L. Alerhand, D. A. Smith, and K. Kash, "Novel applications of photonic band gap materials: Low-loss bends and high Q cavities," *J. Appl. Phys.*, vol. 75, pp. 4753-4755, 1994.
- [53] P. R. Villeneuve, S. Fan, and J. D. Joannopoulos, "Microcavities in photonic crystals: Mode symmetry, tunability, and coupling efficiency," *Phys. Rev. B*, vol. 54, pp. 7837-7842, 1996.
- [54] K. Hayata, H. Yénaka, and M. Koshiha, "Theory of coherent optical coupling between dielectric microspheres," *Opt. Lett.*, vol. 18, pp. 1385-1387, 1993.
- [55] M. Bayer, T. Gutbrod, J. P. Reithmaier, A. Forchel, T. L. Reinecke, P. A. Knipp, A. A. Dremin, and V. D. Kulakovskii, "Optical modes in photonic molecules," *Phys. Rev. Lett.*, vol. 81, pp. 2582-2585, 1998.
- [56] T. Mukaiyama, K. Takeda, H. Miyazaki, Y. Jimba, and M. Kuwata-Gonokami, "Tight-binding photonic molecule modes of resonant bispheres," *Phys. Rev. Lett.*, vol. 82, pp. 4623-4626, 1999.
- [57] N. Stefanou, and A. Modinos, "Impurity bands in photonic insulators," *Phys. Rev. B*, vol. 57, pp. 12127-12133, 1998.

- [58] K. Sakoda, and K. Ohtaka, "Optical response of three-dimensional photonic lattices: Solutions of inhomogeneous Maxwell's equations and their applications," *Phys. Rev. A.*, vol. 54, pp. 5732-5741, 1996.
- [59] K. Sakoda, and K. Ohtaka, "Sum-frequency generation in a two-dimensional photonic lattice," *Phys. Rev. A*, vol. 54, pp. 5742-5749, 1996.
- [60] M. Scalora, M. J. Bloemer, A. S. Manka, J. P. Dowling, C. M. Bowden, R. Viswanathan, and J. W. Haus, "Pulsed second-harmonic generation in nonlinear, one-dimensional, periodic structures," *Phys. Rev. A*, vol. 56, pp. 3166-3174, 1997.
- [61] J. W. Haus, R. Viswanathan, M. Scalora, A. G. Kalocsai, J. D. Cole, and J. Theimer, "Enhanced second-harmonic generation in media with a weak periodicity," *Phys. Rev. A*, vol. 57, pp. 2120-2128, 1998.
- [62] J. Martorell, and R. Corbalan, "Enhancement of second harmonic generation in a periodic structure with a defect," *Opt. Comm.*, vol. 108, pp. 319-323, 1994.
- [63] J. Trull, R. Vilaseca, J. Martorell, and R. Corbalan, "Second-harmonic generation in local modes of a truncated periodic structure," *Opt. Lett.*, vol. 20, pp. 1746-1748, 1995.
- [64] T. Hattori, N. Tsurumachi, and H. Nakatsuka, "Analysis of optical nonlinearity by defect states in one-dimensional photonic crystals," *J. Opt. Soc. Amer. B*, vol. 14, pp. 348-355, 1997.
- [65] O. Painter, J. Vuckovic, and A. Scherer, "Defect modes of a two-dimensional photonic crystal in an optically thin dielectric slab," *J. Opt. Soc. Amer. B*, vol. 16, pp. 275-285, 1999.
- [66] G. Mur, "Absorbing boundary conditions for the finite-difference approximation of the time-domain electromagnetic-field equations," *IEEE Trans. Electromagn. Compat.*, vol. EMC-23, pp. 377-382, 1981.

- [67] X. Feng, and Y. Arakawa, "Off-plane angle dependence of photonic band gap in a two-dimensional photonic crystal," *IEEE J. Quantum Electron.*, vol. 32, pp. 535-542 1996.
- [68] J. Mathews, and R. L. Walker, *Mathematical methods of physics*, Addison-Wesley, 1970.
- [69] A. Yariv, *Optical electronics in modern communications*, Oxford University Press, New York, 1997.
- [70] C. Cohen-Tannoudji, B. Piu, and F. Laloe, *Quantum Mechanics*, Wiley, New York, 1977.
- [71] M. Sigalas, C. M. Soukoulis, E. N. Economou, C. T. Chan, and K. M. Ho, "Photonic band-gap and defects in 2 dimensions — studies of the transmission coefficient," *Phys. Rev. B*, vol. 48, pp. 14121-14126, 1993.
- [72] G. Tayeb, and D. Maystre, "Rigorous theoretical study of finite-size two-dimensional photonic crystals doped by microcavities," *J. Opt. Soc. Amer. A*, vol. 14, pp. 3323-3332, 1997.
- [73] D. R. Smith, S. Schultz, S. L. McCall, and P. M. Platzmann, "Defect studies in a 2-dimensional periodic photonic lattice," *J. Mod. Opt.*, vol. 41, pp. 395-404, 1994.
- [74] P. Sabouroux, G. Tayeb, D. Maystre, "Experimental and theoretical study of resonant microcavities in two-dimensional photonic crystals," *Opt. Commun.*, vol. 160, pp 33-36, 1999.
- [75] S. Fan, P. R. Villeneuve, J. D. Joannopoulos, and H. A. Haus, "Channel drop tunneling through localized states," *Phys. Rev. Lett.*, vol. 80, pp. 960-963, 1998.
- [76] S. Fan, P. R. Villeneuve, J. D. Joannopoulos, M. J. Khan, C. Manolatou, and H. A. Haus, "Theoretical analysis of channel drop tunneling processes," *Phys. Rev. B*, vol. 59, pp. 15882-15892, 1999.

- [77] C. Manolatou, M. J. Khan, S. Fan, P. R. Villeneuve, H. A. Haus, and J. D. Joannopoulos, "Coupling of modes analysis of resonant channel add-drop filters," *IEEE J. Quantum Electron.*, vol. 35, 1322-1331, 1999.
- [78] S. Noda, A. Chutinan, and M. Imada, "Trapping and emission of photons by a single defect in a photonic bandgap structure," *Nature*, vol. 407, pp. 608-610, 2000.
- [79] L. F. Stokes, M. Chodorow, and H. J. Shaw, "All-single-mode fiber resonator," *Opt. Lett.*, vol. 7, pp. 288-290, 1982.
- [80] A. Serpengüzel, S. Arnold, and G. Griffel, "Excitation of resonances of microspheres on an optical-fiber," *Opt. Lett.*, vol. 20, pp. 654-656, 1995.
- [81] J. C. Knight, N. Dubreuil, V. Sandoghdar, J. Hare, V. Lefèvre-Seguin, J. M. Raimond, and S. Haroche, "Characterizing whispering-gallery modes in microspheres by direct observation of the optical standing-wave pattern in the near field," *Opt. Lett.*, vol. 21, pp. 698-700, 1996.
- [82] M. Cai, G. Hunziker, and K. Vahala, "Fiber-optic add-drop device based on a silica microsphere-whispering gallery mode system," *IEEE Photon. Technol. Lett.*, vol. 11, pp. 686-687, 1999.
- [83] M. Cai, O. Painter, and K. Vahala, "Observation of critical coupling in a fiber taper to a silica-microsphere whispering-gallery mode system," *Phys. Rev. Lett.*, vol. 85, pp. 74-77, 2000.
- [84] B. E. Little, S. T. Chu, H. A. Haus, J. Foresi, and J.-P. Laine, "Microring resonator channel dropping filters," *J. Lightwave Technol.*, vol. 15, 998-1005, 1997.
- [85] F. C. Blom, D. R. van Dijk, H. J. W. M. Hoekstra, A. Driessen, and Th. J. A. Popma, "Experimental study of integrated-optics microcavity resonators: Toward an all-optical switching device," *Appl. Phys. Lett.*, vol. 71, pp. 747-749, 1997.

- [86] D. Rafizadeh, J. P. Zhang, S. C. Hagness, A. Taflove, K. A. Stair, S. T. Ho, and R. C. Tiberio, "Waveguide-coupled AlGaAs/GaAs microcavity ring and disk resonators with high finesse and 1.6-nm free spectral range," *Opt. Lett.*, vol. 22, pp. 1244-1246, 1997.
- [87] A. Yariv, "Universal relations for coupling of optical power between microresonators and dielectric waveguides," *Electron. Lett.*, vol. 36, pp. 321-322, 2000.
- [88] Y. Xu, Y. Li, R. K. Lee, and A. Yariv, "Scattering-theory analysis of waveguide-resonator coupling," *Phys. Rev. E*, vol. 62, pp. 7389-7404, 2000.
- [89] A. Mekis, J. C. Chen, I. Kurland, S. Fan, P. R. Villeneuve, and J. D. Joannopoulos, "High transmission through sharp bends in photonic crystal waveguides," *Phys. Rev. Lett.*, vol. 77, pp. 3787-3790, 1996.
- [90] S. C. Hagness, D. Rafizadeh, S. T. Ho, and A. Taflove, "FDTD microcavity simulations: Design and experimental realization of waveguide-coupled single-mode ring and whispering-gallery-mode disk resonators," *J. Lightwave Technol.*, vol. 15, pp. 2154-2165, 1997.
- [91] J. Yonekura, M. Ikeda, and T. Baba, "Analysis of finite 2-D photonic crystals of columns and lightwave devices using the scattering matrix method," *J. Lightwave Technol.*, vol. 17, pp. 1500-1508, 1999.
- [92] J. J. Sakurai, *Modern Quantum Mechanics* Addison-Wesley, 1994.
- [93] H. A. Haus, and Y. Lai, "Theory of cascaded quarter wave shifted distributed feedback resonators," *IEEE J. Quantum Electron.*, vol. 28, pp. 205-213, 1992.
- [94] B. E. Little, J. P. Laine, and S. T. Chu, "Surface-roughness-induced contradi-
rectional coupling in ring and disk resonators," *Opt. Lett.*, vol. 22, pp. 4-6, 1997.
- [95] B. E. Little, S. T. Chu, and H. A. Haus, "Second-order filtering and sensing with partially coupled traveling waves in a single resonator," *Opt. Lett.*, vol. 23, pp. 1570-1572, 1998.

- [96] J. P. Dowling, M. Scalora, M. J. Bloemer, and C. M. Bowden, "The photonic bandedge laser — A new approach to gain enhancement," *J. Appl. Phys.*, vol. 75, pp. 1896-1899, 1994.
- [97] J. M. Bendickson, J. P. Dowling, and M. Scalora, "Analytic expressions for the electromagnetic mode density in finite, one-dimensional, photonic bandgap structures," *Phys. Rev. E*, vol. 53, pp. 4107-4121, 1996.
- [98] G. E. Shilov, *Linear Algebra* Dover Publications, New York, 1977.
- [99] P. Yeh, A. Yariv, and E. Marom, "Theory of Bragg fiber," *J. Opt. Soc. Amer.*, vol. 68, pp. 1196-1201, 1978.
- [100] N. J. Doran, and K. J. Blow, "Cylindrical Bragg fibers: a design and feasibility study for optical communications," *J. Lightwave Technol.*, vol. LT-1, pp. 588-590, 1983.
- [101] J. C. Knight, T. A. Birks, P. St. J. Russell, and D. M. Atkin, "All-silica single-mode optical fiber with photonic crystal cladding," *Opt. Lett.*, vol. 21, pp. 1547-1549, 1996.
- [102] Y. Fink, D. J. Ripin, S. Fan, C. Chen, J. D. Joannopoulos, and E. L. Thomas, "Guiding optical light in air using an all-dielectric structure," *J. Lightwave Technol.*, vol. 17, pp. 2039-2041, 1999.
- [103] J. C. Knight, J. Broeng, T. A. Birks, and P. St. J. Russell, "Photonic band gap guidance in optical fibers," *Science*, vol. 282, pp. 1476-1478, 1998.
- [104] R. F. Cregan, B. J. Mangan, J. C. Knight, T. A. Birks, P. St. J. Russell, P. J. Roberts, and D. C. Allan, "Single-mode photonic band gap guidance of light in air," *Science*, vol. 285, pp. 1537-1539, 1999.
- [105] M. Ibanescu, Y. Fink, S. Fan, E. L. Thomas, and J. D. Joannopoulos, "An all-dielectric coaxial waveguide," *Science*, vol. 289, pp. 415-419, 2000.

- [106] Y. Xu, R. K. Lee, and A. Yariv, "Asymptotic analysis of Bragg fibers," *Opt. Lett.*, vol. 25, pp. 1756-1758, 2000.
- [107] Y. Xu, G. X. Ouyang, R. K. Lee, and A. Yariv, "Asymptotic matrix theory of Bragg fibers," submitted to *J. Lightwave Technol.* 2001.
- [108] J. N. Winn, Y. Fink, S. Fan, and J. D. Joannopoulos, "Omnidirectional reflections from a one-dimensional photonic crystal," *Opt. Lett.*, vol. 23, pp. 1573-1575, 1998.
- [109] Y. Fink, J. N. Winn, S. Fan, C. Chen, J. Michel, J. D. Joannopoulos, and E. L. Thomas, "A dielectric omnidirectional reflector," *Science*, vol. 282, pp. 1679-1682, 1998.
- [110] D. N. Chigrin, A. V. Lavvrinenko, D. A. Yarotsky, and S. V. Gaponenko, "Observation of total omnidirectional reflection from one-dimensional dielectric lattice," *Appl. Phys. A*, vol. 68, pp. 25-28, 1999.
- [111] R. W. Boyd, *Nonlinear Optics*, Academic Press, Boston, 1992.
- [112] S. John and T. Quang, "Resonant nonlinear dielectric response in a photonic band gap material," *Phys. Rev. Lett.*, vol. 76, pp. 2484, 1996.
- [113] P. R. Berman Ed., *Cavity Quantum Electrodynamics*, Academic Press, Boston, 1994.